Investigation of Compressed-Sensing for Acceleration of Magnetic Resonance Spectroscopic Imaging

---

By

Lara Worthington

A thesis submitted to the

University of Birmingham

For the degree of

DOCTOR OF PHILOSOPHY

Physical Sciences of Imaging in the Biomedical Sciences

University of Birmingham

March 2015

Abstract

Magnetic Resonance Spectroscopic Imaging (MRSI) is a functional MRI technique allowing non-invasive biochemical mapping of the brain. MRSI is advantageous for characterising many neurological conditions; however, its clinical application is limited by lengthy scan time and low spatial resolution, which are intrinsically linked.

This research investigated the potential of Compressed Sensing (CS) to speed-up MRSI or enhance spatial resolution. CS allows accelerated acquisition by reducing the data sampling requirements, whilst preserving image quality. The focus of this work was the effect of CS-MRSI at different acceleration factors upon spatial integrity.

CS reconstruction software was developed and applied to retrospective MRSI data. Imaging test objects and software simulations were developed to assess MRSI spatial resolution via metabolite edge response measurements. CS-MRSI was also investigated in realistic scenarios using data from healthy volunteers and a child with Optic Pathway Glioma (OPG). The potential of CS-MRSI to enable high-resolution MRSI in feasible scan times was investigated using simulations of focal and infiltrative OPG.

Results suggest that CS-MRSI can reduce scan duration by up to a factor of 5 whilst simultaneously eliminating ringing artefacts and increasing spatial resolution compared with conventionally filtered MRSI. Therefore, CS could greatly increase the clinical utility of MRSI.

Dedication

This work is dedicated to my family. To my husband Andrew who has provided constant support and enthusiasm for my work. My two daughters Stephanie and Amber who have all had to consistently put up with 'Mum on her laptop' during many family occasions, car journeys, and generally any spare moment available.

I would also like to extend great thanks to my PhD supervisors Nigel Davies, Martin Wilson, Andrew Peet and Theodoros Arvanitis who have guided and provided valuable input over the last three years. I would especially like to thank Nigel who has been a great source of encouragement and academic advice throughout.

Declaration

I declare that the work presented in this thesis is entirely my own.

The following aspects of this study were performed in collaboration:

1) Clinical MRSI investigations were acquired by the radiographers in the Radiology department at Birmingham Children's hospital.
2) Dr Martin Wilson developed the TARQUIN metabolite quantification software.

Acknowledgments

This work was funded by the EPSRC as part of the Physical Sciences of Imaging in the Biomedical Sciences (PSIBS) Doctoral Training centre at the University of Birmingham (EP/F50053X/1). Imaging was performed at the NIHR 3T MR Research Centre, at Birmingham Children's Hospital NHS Foundation Trust. Funding was also received from an NIHR Research Professorship (13-0053) and the CR-UK & EPSRC Cancer Imaging Programme at the CCLG, in association with the MRC and Department of Health (England), (C7809/A10342).

First Author Poster presentations

1) Lara Worthington, Martin Wilson, Theodoros N. Arvanitis, Andrew C. Peet, and Nigel P. Davies, 'Investigation of spatial resolution in magnetic resonance spectroscopic Imaging reconstructed with compressed sensing.' British chapter ISMRM, Cambridge 2012.

2) Lara Worthington, Martin Wilson, Theodoros N. Arvanitis, Andrew C. Peet, and Nigel P. Davies, 'Investigation of spatial resolution in clinical magnetic resonance spectroscopic Imaging reconstructed with compressed sensing.' ISMRM 21st Annual meeting, Salt Lake City 2013.

First Author publications in Submission

1) Lara Worthington, Martin Wilson, Theodoros N. Arvanitis, Andrew C. Peet, and Nigel P. Davies, 'An Investigation into the Effect of Compressed Sensing Reconstruction on the Spatial Integrity of Magnetic Resonance Spectroscopic Imaging.' JMRI, 2015.- In preparation.

Abbreviations

MRI	**Magnetic Resonance Imaging**
FID	**Free Induction Decay**
NMR	**Nuclear Magnetic resonance**
SVS	**Single Voxel Spectroscopy**
MRSI	**Magnetic Resonance Spectroscopic Imaging**
CSI	**Chemical Shift Imaging**
PRESS	**Point Resolved Spectroscopy**
SE	**Spin Echo**
SENSE	**Sensitivity Encoding**
CS	**Compressed Sensing**
TARQUIN	**Totally Automatic Robust Quantitation in NMR**
TSI	**Turbo Spectroscopic Imaging**
VOI	**Volume of Interest**
SNR	**Signal to Noise Ratio**
MTF	**Modulation Transfer Function**
DC	**Direct Current**
FOV	**Field of View**
CT	**Computerised Tomography**
EPI	**Echo Planar Imaging**
PEPSI	**Proton Echo Planar Spectroscopic Imaging**
PSF	**Point Spread Function**
CS-MRSI	**Compressed Sensing Magnetic Resonance Spectroscopic Imaging**
TV	**Total Variation**
TR	**MRSI/MRI sequence repetition time**

TE	**MRSI/MRI sequence echo time**
OPG	**Optic Pathway Glioma**
FSSR	**Fully Sampled Standard Reconstruction**
LRR	**Low resolution Reconstruction**
NSA	**Number of Signal Averages**

Glossary of Terms

K-space	**The spatial frequency domain, indicating the spatial frequencies present in an image.**
Voxel	**Three dimensional cube from which spectroscopic data is acquired.**
SVS	**NMR Spectrum obtained from a single voxel.**
MRSI	**NMR spectra obtained from multiple adjacent voxels.**
CSI	**A previous term for MRSI called Chemical Shift Imaging.**
VOI	**three dimensional volumes containing multiple voxels from which spectroscopic data is acquired.**
Phantom	**A test object device suitable to be imaged, or which mimics an image to provide a means of verifying data quality.**
FID	**The decay of magnetisation with time after the excitation of nuclear spins with a radio frequency pulse.**
Shim	**Method to ensure the main magnetic field is kept uniform. This is particularly required at air/tissue boundaries where this field becomes distorted.**
MTF	**The quantification of the spatial frequencies presented or modulated by an imaging system.**
DC	**Represents zero frequency, or the origin of k-space.**
TARQUIN	**A piece of software which enables the quantification of individual metabolites present in an NMR spectrum.**
Metabolite	**Chemical metabolized in human brain tissue.**
FOV	**The entire area over which imaging is achieved.**
Nyquist Sampling	**The theory which states that a signal will be fully represented as long as it is sampled at a rate twice the highest frequency present.**
PSF	**The result from an imaging system of imaging a single point in space, usually resulting in a sinc function.**
Phantom	**A man-made construction used for the assessment of image quality.**
FSSR	**The fully sampled reconstructed MRSI data as achieved as standard on MRI scanner**
LRR	**Low resolution reconstruction. Data samples are uniformly sampled from an ellipse or circle at the centre of k-space. The number of data**

points included in the ellipse being the same as the CS acceleration factor it is being compared to.

CS-MRSI **MRSI reconstructed using compressed sensing**

CS-MRSI(identity) **CS reconstructed using the identity function as its sparse domain**

CS-MRSI(wavelets) **CS reconstructed using the wavelets as its sparse domain**

In-vivo **Subject is whole and living.**

In-vitro **Subject is not whole and living.**

Digital phantom **A software simulation of an MRSI dataset for use in retrospective reconstructions.**

TABLE OF CONTENTS

LIST OF FIGURES

LIST OF TABLES

1 Introduction

1.1 Magnetic Resonance Spectroscopic Imaging (MRSI)

1.1.1 What is MRSI?

MRSI is a non-invasive, Magnetic Resonance (MR) imaging technique providing spatial mappings of metabolite concentrations within tissue.

Nuclei possessing half-integer spin when placed in an external magnetic field will tend to align with the field. Such nuclei within a tissue are also subject to local magnetic field variations resulting from the specific molecular environment. The effect of this is to produce an amplitude and frequency variation of the MR signal from a volume (voxel) of tissue which reveals a profile of content and structure of the chemical species within it. Acquisition of a spectrum from a single voxel is known as Magnetic Resonance Spectroscopy (MRS). Since the human body is 70% water, most commonly proton (1H) MRS is used although phosphorous (31P) and carbon (13C) MRS is also achievable with specific hardware. A proton MRS profile from a voxel located within brain tissue at magnetic field strength 3 Tesla (T) is depicted in Figure 2-4.

MRSI is a multi-voxel technique allowing the spatial distribution of the metabolite profiles present in human tissue to be acquired simultaneously. Unlike conventional proton imaging which disregards spectroscopic information, MRSI preserves this information to provide a unique insight into tissue function at a biochemical level. The value of MRSI is its ability to reveal variations in metabolite profiles between healthy and diseased tissue which may not be seen in conventional MRI (Nelson 2001; Spratlin, Serkova et al. 2009; Posse, Otazo et al.

2013). This research focusses on proton MRSI although it is equally applicable to other nuclei.

MRSI is a valuable technique in aiding diagnosis and monitoring of many neurological conditions. It has been applied to dementia, multiple sclerosis, stroke and brain injury (Ashwal, Babikian et al. ; Friedman, Brooks et al. 1999; Chard, Griffin et al. 2002; Schuff, Capizzano et al. 2003; Muñoz Maniega, Cvoro et al. 2008). It is also widely utilised in oncology (Golder 2004; Barker 2014).

1.1.2 The limitations of MRSI

Single and multi-voxel spectroscopy are available alongside the conventional anatomical imaging on most clinical MR scanners. Despite being a well-established research tool and there being evidence of a broad range of clinical applications, MRSI is not routinely used in every hospital. This is primarily due to technical and practical challenges which hinder its ease of use, (section 2.2 and section 2.3). Magnetic field inhomogeneity, low Signal to Noise (SNR) ratio, inter-voxel contamination, and problematic coverage of larger areas of the brain are some of the difficulties also outlined in this section. One of the biggest challenges to the routine application of MRSI in the clinic is the long acquisition time (typically 5-10mins) and poor spatial resolution (typically 10-15mm). These two challenges are linked such that a reduction in voxel size requires lengthening the acquisition time, and that reducing the scan duration requires an increase in voxel size (section 2.2.2.1). Poor spatial resolution is a hindrance to accurate diagnosis of neurological disorders and the scan duration is costly in terms of patient throughput, image quality, time and money.

Faster scan times would help reduce patient movement artefacts which are a major problem in MRSI. Movement artefacts are particularly difficult to correct for when in conjunction with an inhomogeneous field. A reduction in scan duration would be particularly beneficial in

terms of patient comfort, in particular for children who do not tolerate lying still for long periods. Patient throughput could be increased enhancing healthcare efficiency, and MRSI may be more readily incorporated into routine clinical protocols.

Spatial resolution is also of important clinical relevance. MRSI has the potential to indicate important metabolic changes such as tumour infiltration into surrounding healthy tissues. The delineation between tumours which remain focal to the main structure of the lesion and those which have infiltrated into surrounding healthy tissue is paramount. Therefore, higher resolution MRSI would be beneficial for the assessment of all brain tumours.

The data in MRSI is sampled in the frequency domain (section 2.1.2). The under-sampling of data in this domain is one way of reducing MRSI scan duration. However, a reduction in uniformly sampled data normally produces aliasing artifacts (section 2.5.1). A relatively new method of data reconstruction which has potential to overcome this is called Compressed Sensing (CS). CS has been widely investigated in anatomical MRI(Chang and Ji 2010). Scan time is accelerated because it allows the acquisition of fewer, randomly acquired data samples whilst suppressing aliasing artefacts (section 2.5) (Lustig, Donoho et al. 2008; Ge, Bresler et al. 2011; Haldar, Hernando et al. 2011; Xiaowei Tong 2012).

1.1.3 Motivation behind this research

The motivation for this study is to investigate the use of CS in MRSI as a means to reduce scan duration or reduce voxel size, and to determine its effect upon the MRSI image quality, particularly spatial resolution. The effect of CS reconstruction in MRSI (CS-MRSI) and its effect upon spatial resolution are relatively unexplored. To date there is only one quantitative study of spatial resolution which is limited to a single scan speed-up time or acceleration factor of x4 (Heikal, Wachowicz et al. 2013). The investigation of the effect on

spatial resolution with increasing acceleration factor would be extremely beneficial to assess the feasibility of CS to enhance the clinical utility of MRSI.

1.1.4 Aims

The primary aim of this research was to investigate the potential of CS as a method to allow for the reduction in MRSI scan duration, and its effect on the subsequent spatial resolution. The secondary aim was to investigate the use of CS to enhance the spatial resolution of MRSI within a clinically feasible time frame. The final goal was the assessment of the potential application of CS-MRSI in the clinical investigation of OPG.

1.1.5 Objectives

- The first objective was to develop suitable CS reconstruction software applicable to MRSI (CS-MRSI).
- The second objective was to devise a practical technique of providing a measure of relative spatial resolution.
- The third objective was to explore the limits of CS-MRSI by comparison of the spatial resolution of CS-MRSI at different acceleration factors.
- The fourth objective was to compare two different sparse representations (a fundamental requirement of CS reconstruction) of the data at each acceleration factor.
- The final objective was to assess the reliability of CS-MRSI reconstruction for the delineation of tumour margins in Optic Pathway Glioma (OPG).

1.1.6 Road map

The first objective which was to develop CS reconstruction software for MRSI, was completed by the adaptation of existing CS software applicable to conventional proton MR

imaging (section 3). The software was adapted in order to account for the additional chemical shift information provided by MRSI.

The second objective was firstly tackled by means of the development of an imaging test object commonly referred to as a 'phantom' (section 4). The development concluded in a phantom consisting of an uninterrupted, negligibly thin, metabolite edge consisting of two separate agarose gels. This provided means to examine spatial resolution by direct edge response measurements. A digital phantom was also developed (section 6) providing higher resolution MRSI datasets. The digital phantom was developed to include a simulation of an angled, metabolite edge (section 6.3). An investigation of the use of the simulated angled edge as a means to measure the Modulation Transfer Function (MTF) was also pursued in (section 7.2).

For the third objective all reconstructions were compared relative to the non-filtered fully sampled standard reconstructions (FSSR) as available on the scanner. A comparison of the CS-MRSI results to those of the time equivalent Low Resolution Reconstruction (LRR) (section 2.2.2.1) was achieved for all investigations. Initially CS-MRSI and LRR reconstructions were investigated with increasing acceleration factor at standard voxel size by application to retrospectively under-sampled MRSI datasets from the imaging phantom, and from a healthy volunteer acquisition (section 5). Secondly, the digital phantom containing the simulated, angled metabolite edge was implemented for the investigation of CS-MRSI (section 6.3). This provided increased data points for the edge response measurement, and a means of assessment of a smaller voxel size (5mm x 5mm x 5mm) without the need for lengthy scan duration. The comparison of the spatial resolution relative to the non-filtered FSSR resulting from CS-MRSI, and the time equivalent LRR at increasing acceleration was

again undertaken (section 7.1). Comparison with the filtered FSSR was also included for the digital phantom work.

The fourth objective was achieved by the application of CS-MRSI utilising the sparse data transforms of the identity and the wavelet transforms (section 3.3.1). These were compared in Chapter 7 and Chapter 8.

The final objective was initially met by scanning an OPG patient using the BCH standard, clinical protocol at voxel size of (13mm x13mm x13mm) (section 8.2.1). MRSI datasets were reconstructed using CS-MRSI and LRR and compared to the FSSR. This investigation was then extended by two further adaptions of the digital phantom. The first provided a high resolution MRSI simulation of a single, focal OPG lesion (section 8.2.2.1) and the second, an identical lesion exhibiting tumour infiltration into the surrounding healthy tissue. The comparisons of CS-MRSI and LRR relative to the FSSR at increasing acceleration were again undertaken (section 8.2.2.2).

2 Principles of MRSI and Compressed Sensing With Review of Fast MRSI Methods

2.1 Theoretical basis of MRSI

2.1.1 Physical Principles of Magnetic Resonance (MR)

Certain atomic nuclei of the human body have an inherent half integer spin angular momentum. When these nuclei are placed in an external magnetic field B_o, they precess about the applied magnetic field (McRobbie, Moore et al. 2007). In clinical MRI the proton (^1H) is the nucleus of most interest, because of its high natural abundance in the human body and high sensitivity. The resonant frequency of precession is proportional to the applied field strength and given by the Larmor equation

$$\omega_0 = \gamma B_0 \qquad \textbf{Equation 2-1}$$

Where:

ω_0= Larmor frequency (MHz)

γ = Gyromagnetic ratio=42.56MHz/T for Hydrogen (^1H)

B_0 = Applied Magnetic Field (Tesla, T)

This results in an overall net magnetisation M_0 which is in line with the applied magnetic field B_0. Externally applied RF pulses at the Larmor frequency are applied for a duration causing the net magnetisation M_0 to be tipped at an angle relative to Bo into the transverse x-y plane. After the RF is switched off, the magnetisation vector Mo consists of two components, the longitudinal magnetization Mz which is restored back along the vertical axis at a tissue characteristic time T1 (spin-lattice), and the transverse magnetisation Mxy (perpendicular to Bo) which decays along the horizontal axis with a characteristic time T2 (spin-spin relaxation), Figure 2-1 a).

The recovery of the magnetisation Mz(t) at time t after application of the RF is given by equation 2-2.

$$\boldsymbol{Mz(t) = Mz_{eq}\left(1 - e^{-t/T1}\right)} \qquad \textbf{Equation 2-2}$$

Where:

Mz_{eq} = The equilibrium magnetisation along the z-axis.

$Mz(t)$ = The magnetisation along the z-axis at time t.

T1 = The characteristic relaxation time of the tissue.

The magnetisation M_{xy} perpendicular to B_o in the x-y plane induces a signal called a Free Induction decay (FID) detectable by means of the current it induces in a receiver coil, Figure 2-1 b). The magnetisation is given by equation 2-3.

$$\boldsymbol{M_{xy} = M_0\, e^{-t/T2}} \qquad \textbf{Equation 2-3}$$

Where:

In practise this transverse decay is characterised by a faster relaxation time T2* which also includes spin dephasing due to susceptibility and field inhomogeneity effects.

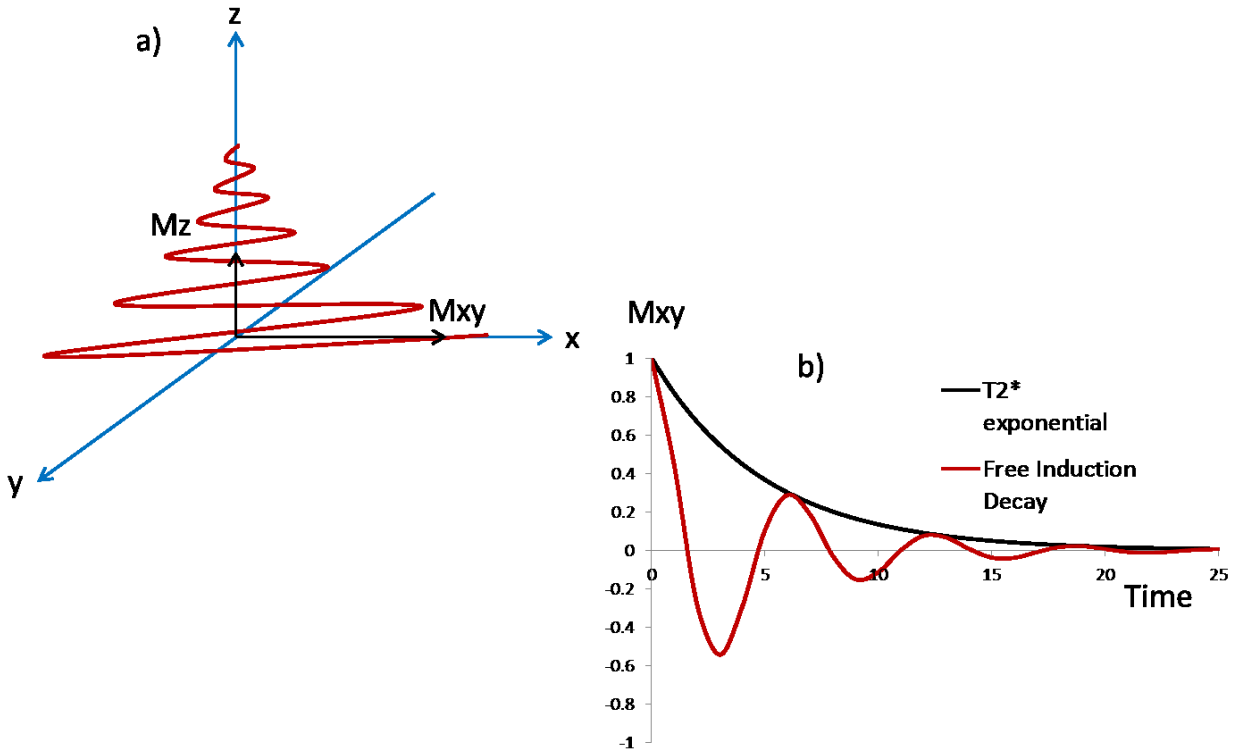

Figure 2-1 - a) The decay of the transverse magnetisation Mxy and the longitudinal magnetisation Mz. b) The Transverse magnetisation Mxy induces a current in a detection coil producing the Free induction decay (FID).

T1 and T2 vary with tissue type. RF pulses are transmitted, and the resulting MR signals are detected by means of RF coils placed over the anatomical area of interest.

2.1.2 MR Image Formation

MR image formation is based on the fact that if a magnetic field is made to vary across a subject, it imposes a spatial variation in resonant precession frequencies across it. This variation with spatial location can therefore be exploited to pin point the location of MR signals. Such spatial variations have to be varied dynamically during imaging. This is achieved with three orthogonal 'gradient coils' which are incorporated into the MRI scanner design. Currents within these coils can be manipulated to achieve gradients for slice selection G_{slice}, frequency encoding $G_{frequency}$, and phase encoding G_{phase}. A typical MRI pulse sequence depicting these gradients along with the RF and the corresponding MR signal are shown in

the gradient echo pulse sequence of Figure 2-2. The gradient amplitude and polarity of $G_{slice\ select}$, $G_{frequency}$ and G_{phase} indicate the gradient power and coil current direction respectively.

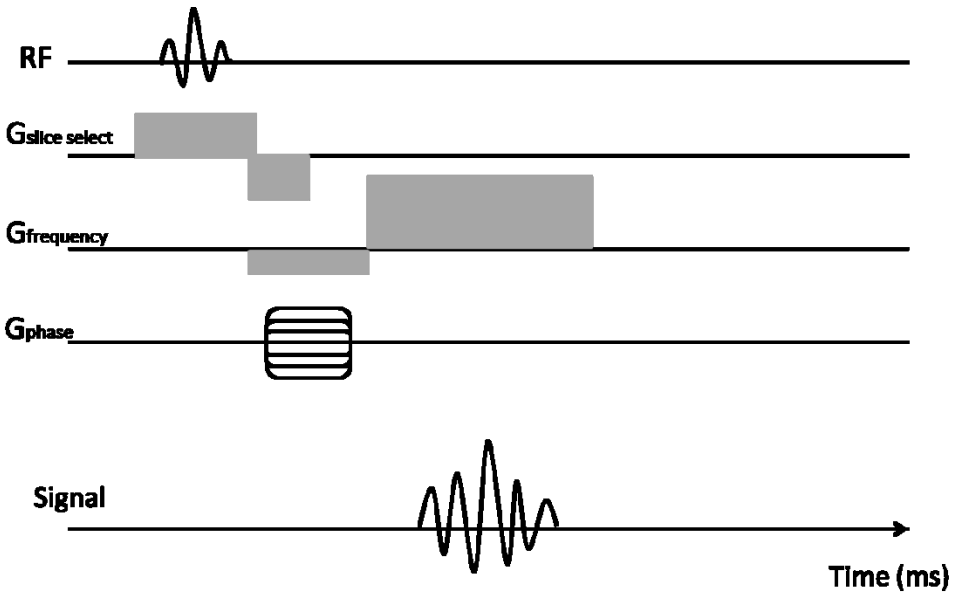

Figure 2-2 – Basic gradient Echo MRI Imaging sequence

The line marked 'RF' indicates the duration of the radio frequency pulse used to tip the net magnetisation M_0. The angle through which the magnetisation is flipped is dictated by the duration and power of this pulse. The RF is usually a sinc pulse and is applied at the same time as the slice select gradient. A truncated sinc pulse is desirable since its Fourier transform is effectively a square wave. The RF pulse has a specific frequency band width (bw) determined by pulse duration, centred around a specific frequency. The pulse acts upon only those nuclei precessing at frequencies within the band. Slice selection therefore restricts the excited nuclei to a single slice from which to form the 2D image. The slice thickness T is given by:

$$T = {bw}/{\gamma G_{slice\ select}} \qquad \textbf{Equation 2-4}$$

Where:

bw = the RF bandwidth

G_{slice} = Magnitude of the slice select gradient

γ = Gyromagnetic ratio=42.56MHz/T for Hydrogen (^1H)

The gradient echo is formed by applying a bipolar frequency-encode gradient (or readout gradient). The negative lobe is designed to dephase the spins, whilst the positive lobe rephases the spins forming an echo. The dephasing stage is designed such that it corresponds to half of the dephasing effect of the frequency encode gradient during data acquisition.

The 2D image is formed by encoding the image signal within the chosen slice. The measurements of the MR signals are recorded in reciprocal space known as 'k-space'. K-space is the Fourier Transform (FT) of real 2D space (x,y). The x and y dimensions of the MR image are encoded by means of the frequency $G_{frequency}$ (or readout gradient), and phase encode gradient G_{phase} respectively. The phase-encode gradient is switched on and off for a duration of time such that the protons precess at a frequency dictated by their position. After the gradient is switched off the spins are left with a net phase shift proportional to their position. The frequency-encode gradient is applied whilst the MR signal is being acquired. The time at which the signal or echo occurs is known at the 'Echo time' and is designated as TE. As a consequence of the frequency encode in the x-direction during this period, the spins will be precessing at a frequency proportional to their spatial location. The frequency and phase-encode gradients work together to traverse k-space. In order for sufficient T1 relaxation to occur to provide useful signal contrast, the sequence is repeated at intervals of time TR (Repetition Time). For each sequence repetition, the phase-encode gradient steps to another line in k-space along which the gradient echo is sampled. To acquire a matrix size of 256x256 this therefore requires 256 repetitions to traverse each line

of k-space. The total acquisition duration is therefore dictated by the number of phase encode steps and the TR.

2.1.3 Principles of Magnetic Resonance Spectroscopy (MRS)

Since the gyromagnetic ratio (γ) is constant for each nuclear species, the Larmor frequency of a particular spin-half nucleus, (ω_0) depends on the external magnetic field (B_0) and the local microenvironment. A chemical shift in the Larmor frequency arises due to the effect of surrounding electrons in a molecule which partially shield the nucleus from the external field. Therefore, the chemical environment dictates the resonant frequency of the molecule. These differences in frequency between different chemical species are used for identification. The frequency shift is measured in Hz but usually expressed in parts per million (ppm) and given by the following equation:

$$\delta = \frac{\mathbf{f_i - f_{ref}}}{\mathbf{2\,\pi\,B_0}}\,\mathbf{10^{\,6}} \qquad \textbf{Equation 2-5}$$

Where:

$\mathbf{f_i}$=Frequency of metabolite (Hz)

$\mathbf{f_{ref}}$=Reference frequency (Hz)

$\mathbf{B_0}$=Main applied external magnetic field (T).

The chemical shift dictates the position on the frequency spectrum of chemically equivalent molecules. This peak may in turn be split due to the individual nuclear spins from neighbouring nuclei within the same molecule. This is known as spin-spin or J-coupling Figure 2-3. In proton MRSI, the resonances of chemically equivalent protons within a molecule may be split by the presence of one (resulting in a doublet) or more (resulting in multiplets) adjacent proton(s). The MRSI spectra reveal information about the chemical content and concentration, while the multiplet patterns indicate chemical structure.

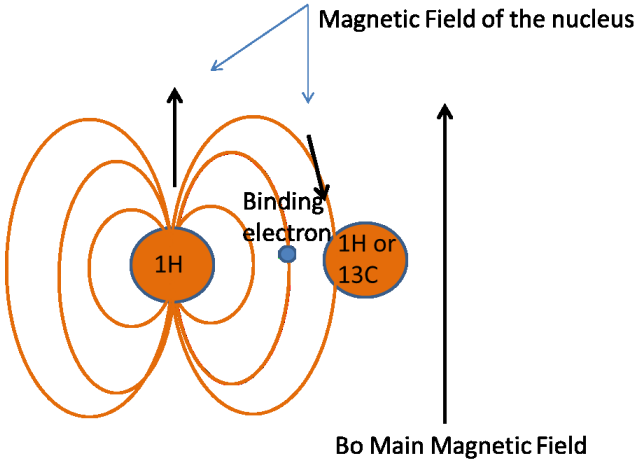

Figure 2-3– The J-coupling between two nuclei

The proton spectrum of the human brain provides information regarding the relative metabolite concentrations. The Prominent neurological features in a healthy human brain spectrum are depicted in Figure 2-4, typical concentrations are around 10mM(Govindaraju, Young et al. 2000). Although not normally of detectable concentration within a healthy brain spectrum, the figure indicates the location of lipids which are prevalent in certain tumour types(Orphanidou-Vlachou, Auer et al. 2013) and may be present in a healthy spectrum from inter-voxel contamination (section 2.3.1).

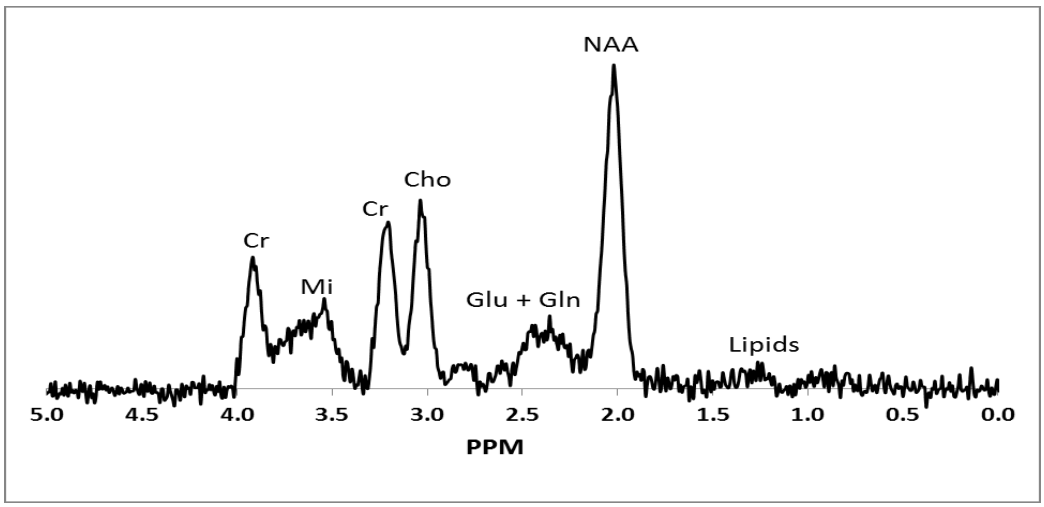

Figure 2-4- Proton spectrum of a healthy human brain (short echo time). Peaks shown are: total Creatine: Glycerophosphocholine (GPC) and Phosphocholine (PCh), NAA: N-acetylaspartate, and Glx: the combined peaks of glutamate (Glu) and glutamine (Gln), Ins: myo-inositol. Cho: choline, and lipid: the broad resonance of lipids and triglycerides.

MRS is becoming a useful tool in the diagnosis and management of neurological diseases in particular brain tumours(Barker 2014). MRS is acquired from a volume or voxel typically around (15mm x15mm x15mm). In Magnetic Resonance Spectroscopic Imaging (MRSI), the data is processed to form a grid of voxels defined as a Volume of Interest (VOI) allowing the spatial distribution of spectra to be viewed.

2.2 Practical considerations of MRSI acquisition

In order to obtain good quality MR spectra in MRSI, there are necessary practical steps. Each presents its own challenges, and each ultimately affects the outcome of the data quality. The general steps are outlined below:

2.2.1 Multi-Voxel Spectroscopy

A typical Point Resolved Spectroscopy (PRESS) MRSI pulse sequence can be seen in Figure 2-5. Unlike conventional MRI image formation (section 2.1.2.), most MRSI techniques use only volume selective (Gz, Gy, Gx) and phase-encoding gradients. The phase-encoding gradients (Gx and Gy) are stepped with every repetition of the whole sequence at the sequence repetition time TR. Frequency-encoding is not used in 2D phase encoded MRSI as it is in MRI, since this would destroy the chemical shift information. It is possible to acquire 3D MRSI with the addition of a third phase-encode gradient, further lengthening scan duration. This study is limited to 2D phase encoded MRSI, however acceleration techniques may also be applicable for 3D phase encoded MRSI. The gradients labelled ‘crusher’ in the figure is explained in (section 2.2.5).

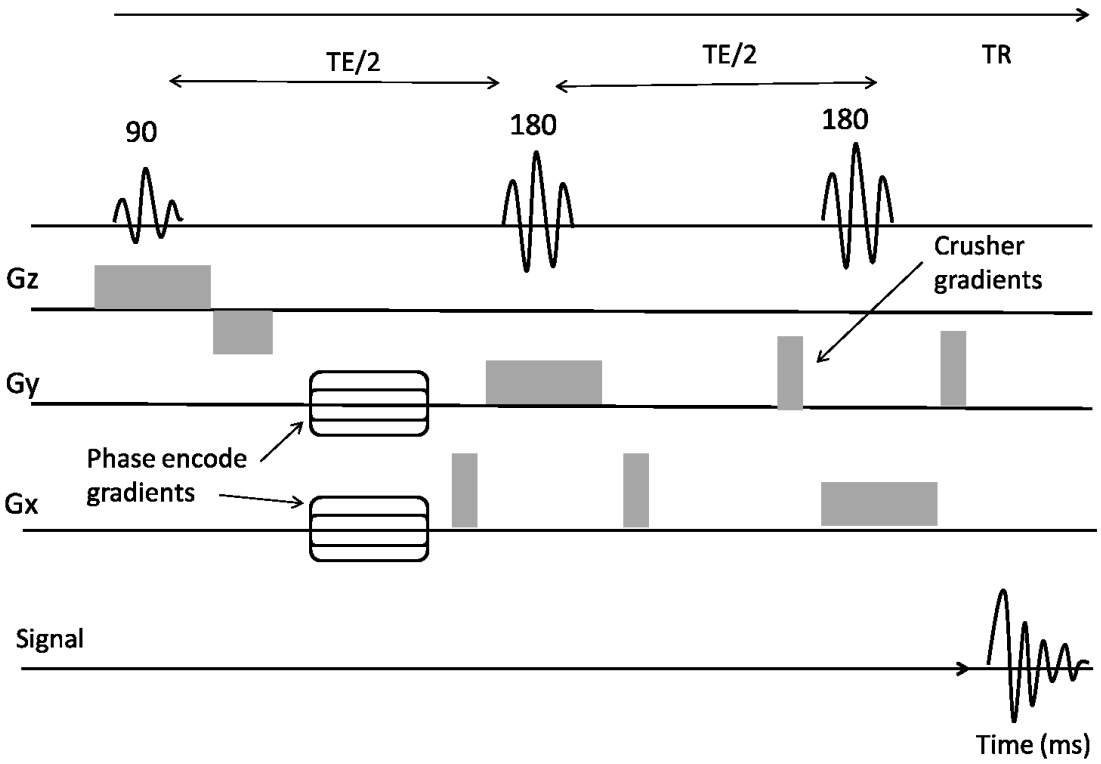

Figure 2-5 The pulse sequence for 2D phase encoded MRSI (PRESS).

2.2.2 Data Acquisition in k-space

The signal in 2D phase encoded MRSI is uniformly sampled in k-space (kx,ky). K-space is the representation of an image in terms of its spatial frequencies. The maximum extent of coverage of k-space is limited due to time constraints. Measurements towards the centre of k-space will contain lower spatial resolution MRSI data while information relating to higher spatial resolution is encoded towards the periphery. For each phase encode step, the FID signal is sampled typically 1024 times, Figure 2-6. The bandwidth of the spectrum is determined by the sampling rate of the time domain signal, typically 1-2kHz. The sampling rate needs to obey the Nyquist sampling criteria (section 2.5.1) in order to provide sufficient bandwidth for all the metabolite chemical shifts of interest, and the number of samples must be sufficient to maintain the resolution between spectral peaks.

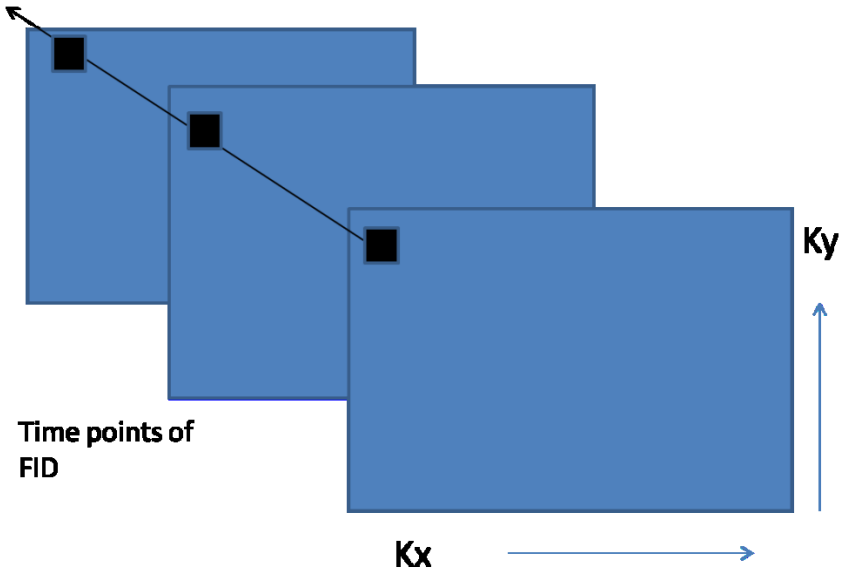

Figure 2-6 Diagram explaining how the spectroscopy data is collected in k space. Each FID is collected at each k-space location. One point in k-space is indicated by the black square on the figure, which has three sampled time points.

A complete spectroscopic image results as the time points of the FID (t) are obtained for each k-space location (kx,ky) which is stepped by phase encoding, every TR time (secs). The time taken to collect each FID is determined by the sampling rate and the desired spectral resolution which is directly proportional to the number of measurements taken at that rate. The time taken to step through k-space is therefore governed by TR and the number of k-space steps. Hence, the maximum extent of coverage of k-space is limited due to time constraints. The acquisition results in a matrix containing values (kx,ky,t).The inverse FT of the two k-space dimensions, along with the 1D FT of the sampled time signal, results in a matrix of frequency spectra at given spatial locations (x,y,f), the MRSI dataset.

2.2.2.1 Acquisition duration and spatial resolution trade-off

The repetition time TR between each k space step (section 2.2.1) must be long enough to avoid saturation effects owing to metabolite T1 relaxation times. TR is typically 2 seconds. A typical FOV of 160mm x 160mm is required in order to cover the brain. If a reduced FOV is

utilised this can lead to aliasing artefacts (section 2.5.1). The total acquisition time TA is given by:

TA =Image matrix size x TR **Equation 2-6**

Utilising a nominal voxel size of 10mm x 10mm x 10mm (matrix size, 16 x 16 = 256 voxels), at a TR of 2 seconds, results in a scan duration of 8.5 minutes. If high spatial resolution and hence reduced voxel size is desired, then more high spatial frequency k-space locations are necessarily recorded, and scan time increased. If required spatial resolution is doubled for the same FOV, then scan duration is quadrupled. If the desire is to reduce scan duration at this same FOV, then this comes at the expense of spatial resolution as k-space is truncated to reduce the number of k-space samples and hence scan time.

A simple method of accelerating MRSI acquisition is to uniformly sample a circular central region of k-space, while setting the signal at the outer edges to zero to maintain the nominal voxel size. This is commonly available by default on clinical MRI scanners. This technique, referred to as applying an elliptical or circular k-space 'mask' or 'shutter' reduces the number of samples required, and hence scan duration, by 25%(Philips 2011) . In practice the sampled area at the centre of k-space can be varied relative to the nominal k-space coverage by applying this standard 25% 'shutter' to MRSI acquisitions of different voxel sizes, and then using scanner options to reconstruct the acquired data to a nominal voxel size.

2.2.3 Shimming

Shimming is required to ensure that the main magnetic field B_o is uniform. Consideration has to be given to the magnetic susceptibility artefact between different tissue boundaries, particularly at air/tissue interfaces (Farahani, Sinha et al. 1990). This results in large inhomogeneities in the main magnetic field experienced by the tissue of interest. This

therefore can lead to discrepancies in the Larmour frequencies of such tissues and hence an incorrect chemical shift between their metabolites. Shimming is employed to even out these differences(Vikhoff-Baaz 1999; Philips 2011). It is achieved via the use of specialised shim coils employed in the scanner design. The currents from these coils produce magnetic fields to counteract the discrepancies to attempt a spatially uniform field. Algorithms are utilised to calculate the required shim coil currents. Current shimming algorithms however are hampered by complex anatomical geometry particularly over areas of stark magnetic susceptibility difference such as the inferior frontal cortex, due to the proximity to the frontal sinuses. It is difficult to optimise the currents to correct for this. A reduction in the apparent T2* of tissue will result and therefore cause spectral broadening and hence a reduction in spectral resolution.

In MRSI the objective is usually to achieve maximum coverage in order to define heterogeneity of disease over large volumes. Large tissue volumes are likely to contain a greater diversity of field inhomogeneity profiles than smaller volumes. Therefore, since it is hard to simultaneously correct for all the field inhomogeneities over larger volumes, shimming is often more of a challenge for MRSI than for single voxel MRS, where a much smaller VOI is usually defined. The shimming is achieved for a volume over which shim currents are optimised to achieve maximum homogeneity. The shim volume is most usually defined over the VOI. A balance needs to be struck between a VOI which optimises the shim and one which allows enough coverage for comparison between disease and normal appearing tissue, and detection of disease infiltration.

2.2.4 Water suppression

The human body is approximately 70% water. Therefore in proton MRSI there is a very high signal from water. The water peak dominates the spectrum rendering the detection of

metabolite peaks a challenge. In order to overcome this, various water suppression techniques may be utilised. The quality of the water suppression depends upon the quality of the shimming. An inhomogeneous field will cause local variations in the Larmor frequency of metabolites and the water peak. The magnetic susceptibility artefact may have severe consequences for adequate water suppression. This is because the unsuppressed water may become sufficiently shifted in Larmor frequency, such that the water suppression bandwidth does not encompass it entirely. A poorly shimmed magnet will therefore have a detrimental effect upon the resultant MR spectral quality often producing unsuppressed water peaks known as residual water. These residual water peaks can often be substantial leading to inter-voxel contamination at distant voxels from residual water ringing artefacts (section 2.3.1).

There are a variety of water suppression techniques available on the Philips 3T scanner (Philips 2011). In this study the Excitation and (CHEmical-Shift Selective) CHESS methods were utilised (Haase, Frahm et al. 1985). The default water suppression method on the Philips 3T scanner is known as the Excitation method. This applies two bandwidth selective RF pulses to produce zero magnetization from water at the beginning of the acquisition. The water magnetization is slightly over flipped by the RF pulses, after which spoiler gradients are applied to destroy the transverse water magnetization, Mxy. Any small residual water peak will return to equilibrium through T1 relaxation. The suppression is optimal when the longitudinal water magnetization Mz passes through zero at the start of the measurement. CHESS consists of the addition of extra RF pulses along each of the three orthogonal axes. These pulses act to minimise the longitudinal magnetization of the water signal at the time of the RF excitation by adjusting the flip angle of the third RF pulse.

2.2.5 Outer Volume Suppression

Signals from outside the desired volume need to be eliminated. These can arise from spurious stimulated echoes outside the VOI due to imperfections in pulse shape. These are removed via the use of crusher gradients which are placed either side of the 180 degree pulses Figure 2-5. An imperfect pulse profile from a volume near the scalp can inadvertently excite subcutaneous fat. Lipid produces a very high MR signal which can bleed into the VOI (section 2.3.1). These spurious signals can be reduced via the use of fat saturation bands placed around the scalp, depicted in blue on Figure 5-3. The saturation bands consist of a 90^{o} RF pulse in combination with a gradient at right angles to the imaging plane to restrict the band to a select region of the FOV. This is applied just prior to imaging such that the longitudinal magnetisation in this region is saturated and unavailable to be excited by the RF pulse.

2.3 Challenges to data quality in MRSI

Achieving good quality MRSI data is not as straight forward as in conventional anatomical MRI. Since the signals from the metabolites are very low in comparison to the water signal, it is essential to obtain good SNR and water suppression as well as achieving high spectral resolution and good quality shimming. Due to the nature of the 2D phase encoding of the MRSI acquisition, low spatial resolution and lengthy scan duration are also considerable challenges to data quality as discussed in (section 2.2.2.1).

The difficulties often encountered in obtaining spectra are outlined below:

2.3.1 Inter-Voxel contamination (Bleed Through)

Inter-voxel contamination or ‘Voxel bleeding’ is a major challenge in MRSI limiting its spatial integrity. Inter-voxel contamination can lead to partial volume effects and possible

misidentification of tissue. This is of particular concern for the delineation of the extent of tumour infiltration into surrounding healthy tissue.

As previously mentioned MRSI data is measured by uniformly stepping through k-space and sampling at each location (kx,ky) (section 2.2.2). If an infinitely small point (dirac delta function) were imaged, its acquisition in k-space would require sampling an infinite 2D plane. In reality, the rectangular image matrix, truncates k-space sampling. The Fourier transform is effectively the representation of a signal as the summation of sin and cosine basis functions of various frequencies. The reduction in the maximum available spatial resolution in k-space, limits the possible higher frequency Fourier basis functions available for the inverse FT to real space (x,y). As a consequence the point signal broadens and it exhibits side lobes referred to as 'Gibbs ringing' (Vikhoff-Baaz, Starck et al. 2001; Kirchner, Fillmer et al. 2015). This transformed signal shape is known as the Point Spread Function (PSF) (Posse, Otazo et al. 2013). A 1D version of the PSF is depicted in Figure 2-7. In MRSI the image is a convolution of the true object and the PSF. The broadening of the main central lobe of the PSF degrades MRSI spatial resolution causing the metabolite signal from one voxel to spread to its adjacent neighbours. The Gibbs ringing causes either an increase or decrease in voxel signal as metabolite information from distant voxels bleeds into them. The spread across voxels is termed 'voxel bleeding or 'inter voxel contamination'. The Gibbs ringing can be particularly problematic if subcutaneous fat is inadvertently excited. If the lipid signal is not sufficiently suppressed by the saturation bands, it can bleed into the voxels of normal healthy tissue (section 2.2.5).

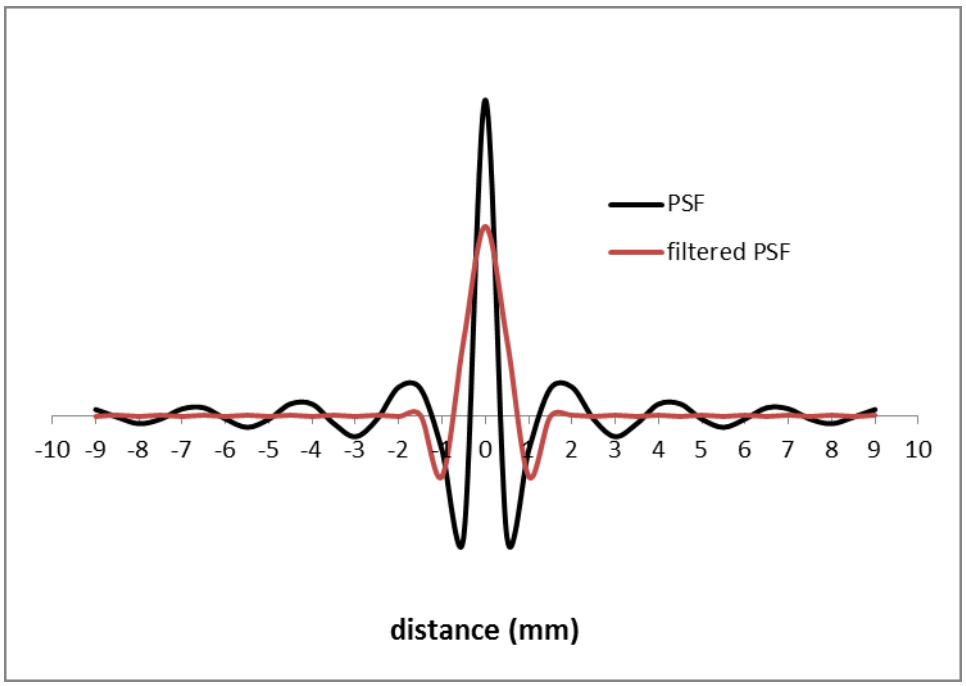

Figure 2-7- A depiction a 1D Point Spread Function (PSF).

A method to reduce the side lobes of the PSF is to apply post acquisition k-space filtration. Filtration consists of the application of variable weighting to the k-space samples, which decreases towards the periphery. The actual filter utilised varies between manufacturers but they achieve a similar result. A typical filter utilised in MRSI is the Hamming filter (Skoch A 2008), given by equation Equation 2-7.

$$H(n) = 0.54 - 0.46\, cos\ {}^{2\pi n}/_{N} \qquad \textbf{Equation 2-7}$$

The result of filtration is a reduction in Gibbs ringing but at the expense of spatial resolution, as it broadens the main central lobe, as depicted in Figure 2-7. It is suggested that the reduction in spatial resolution due to the application of such a filter is around 50% (Barker and Lin 2006). The application of a k-space ringing filter is a standard default in clinical MRSI. Therefore, the actual spatial resolution in clinical MRSI is worse than its nominal voxel size. A significant objective in MRSI research is to find a method of eliminating inter-voxel contamination by reducing Gibbs ringing without loss in spatial resolution (section 6.3.2).

2.3.2 Signal to Noise Ratio (SNR)

The SNR of MRSI is much lower than that of conventional anatomical MRI. This is due to the very low abundance of metabolites relative to that of water in the human brain. The SNR is directly related to the voxel volume. Increasing the voxel volume to enhance SNR will however reduce spatial resolution and vice versa. The SNR can be improved by either increasing the Number of Signal Averages (NSA) or increasing the voxel dimensions. Both of these solutions have associated problems. Increasing NSA increases the already lengthy scan time.

2.3.3 Chemical Shift Displacement

Gradient driven volume selection methods in MRSI such as PRESS (section 2.2.1) utilise frequency encoding to determine the VOI by exciting spins resonating at the Larmor frequency within this volume only. Metabolites however resonate at different frequencies, resulting in different VOI selections for differing metabolites as shown in Figure 2-8.

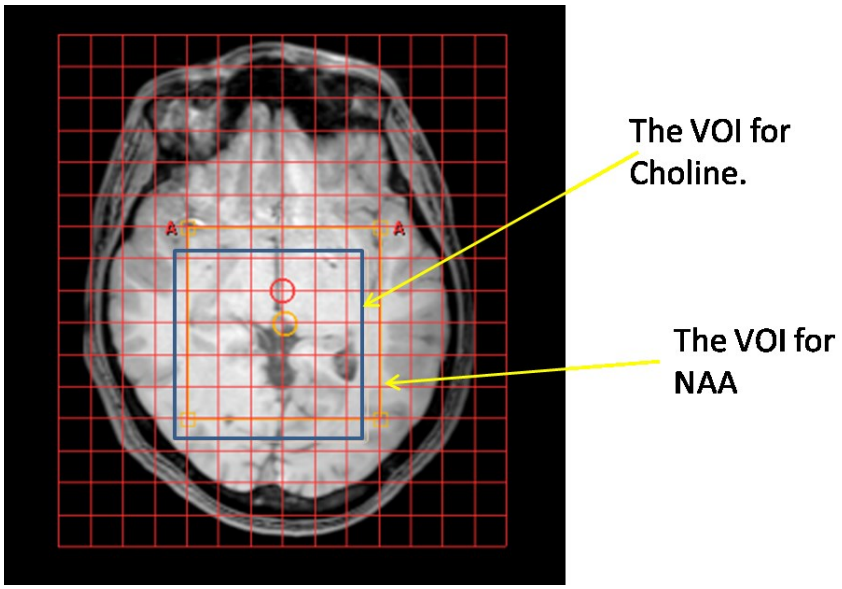

Figure 2-8 - Molecules of Choline experience a different spatial localisation from the 2D gradient selection to that experienced by NAA. This results in a slight shift in the VOI indicated in blue for Choline, and yellow for NAA.

The distance a VOI will be chemically shifted is related to the bandwidth of the excitation from the RF, and the refocusing pulses. At increasing field strength the chemical shift displacement artefact is also enhanced (Lange 2006; Scheenen, Klomp et al. 2008). The inherent chemical shift displacement of PRESS maybe corrected for by using oversized VOI's (half a voxel boundary on Philips 3T) (Edden, Schär et al. 2006). The disadvantage of increasing the VOI size is that it may become too large for whole brain studies, or it may extend into undesirable anatomical locations such as subcutaneous fat.

2.4 Post-processing of MRSI datasets

After the MRSI data has been acquired the FID signals are usually processed offline. A Fourier transform is applied to convert the time domain signal to frequency, producing the NMR spectrum associated with each voxel. The detected FID is complex, comprising of real and imaginary components from the spins in the transverse magnetisation plane section (2.1.1). The real frequency component is conventionally displayed as parts per million (ppm) against signal. There are several post processing steps which are needed in order to enhance the data quality of the resulting spectra and provide quantification of the metabolites present. The main considerations are outlined as follows:

2.4.1 Residual water removal

As mentioned in (section 2.4.1), the water suppression does not always entirely remove the water peak. This can lead to peaks at around 4.7ppm known as residual water. These peaks are often removed in post-processing using an HSVD algorithm (Pijnappela 1992). This is based on the estimation of the water FID and its subsequent removal from the time domain signal. This method is successfully utilised in MRSI post-processing however the residual water can distort the spectrum baseline which can have consequences for quantification of neighbouring metabolite peaks.

2.4.2 Baseline correction

Small baseline distortions can be rectified by a simple shift of the spectrum up or down. This is often achieved by taking the average signal from a stable portion of noise in the spectrum, and subtracting this from the entire spectrum. The correction of the baseline distortion due to severe residual water contamination as mentioned above may be impractical.

2.4.3 Peak phasing

The real component of the complex spectra is normally displayed. The Real data spectra sometimes exhibit a mixture of positive and negative peaks above and below the baseline. This is due to frequency offset errors and pulse sequence delays between excitation and receive. Spectra can be re-phased in either the time or frequency domain after acquisition in order to correct this, or the magnitude data can be displayed although this broadens the peaks.

2.4.4 Apodisation and Line broadening (time domain filtering)

The SNR in MRSI is inversely proportional to the height of the noise intensity of the FID. If noise could be reduced then SNR is improved. This is often achieved by multiplying the time domain FID by an exponential function containing a line broadening term (lb), such as the one below:

$$\boldsymbol{A(t) = e^{-lb\,t}} \quad \textbf{Equation 2-8}$$

It follows from Fourier theory that the more rapid the decay of an exponential the broader will be its Fourier Transform, hence the line broadening term in the above equation. Therefore, the optimum SNR will be achieved when the line broadening term matches the signals own width. Since line width is metabolite dependent, a single line broadening term will not be optimised for every peak, however an average is often utilised.

Apodisation can also be used to improve spectral resolution by enhancing the extremity of the FID. This may however result in a significant decrease in SNR.

2.4.5 Zero Filling

Zero filling is a method to artificially improve the spectral resolution. It really only improves the appearance of the resolution but not the actual spectral resolution. Zero filling consists of the addition of zero valued data points to the end of the FID without adding additional noise. The main advantage of zero filling is that if a metabolite is very closely coupled, zero filling will make its components more distinguishable in the frequency domain.

2.4.6 The quantification of brain metabolite concentration

The relative concentrations of the metabolites within brain tissue are indicators of disease state (section 8.1.1). A major component of post processing is the quantification of these metabolites. The absolute quantification of the concentrations of each metabolite within the human brain is subject to much research. The concentration of an individual metabolite is age, location and disease dependent. There is evidence suggesting differences in metabolite concentrations between grey and white matter (Pouwels and Frahm 1998). In a healthy human brain the MRS detectable concentrations are of the order of 1-10mM.

Methods of absolute quantification of the concentrations of brain metabolites obtained from NMR spectroscopy are available in software packages. Quantification of in-vivo metabolite concentration is not a simple linear relationship between peak height and quantity (Reynolds 2008). There are many automatic systems available aiming to achieve optimum quantification. They utilise a variety of algorithms based on either integration of peak area, peak fitting or basis-set methodologies (Poullet, Sima et al. 2007). Integration methods (typically employed by scanner spectrometer manufacturers) work in the frequency domain on simple spectra by summing the area under the metabolite peak of

interest. This methodology is prone to inaccuracy when quantifying short-TE, MRSI due to the complexity of the spectra of some metabolites (Wilson, Reynolds et al. 2011). Other methods of spectral interpretation attempt to overcome the problems encountered by this integration method by utilising known spectral data as a set of basis functions of the metabolites to provide a mathematical fitting. Non-linear Least Squares fitting is employed in the AQSES (Automated Quantitation of Short Echo time MRS Spectra) system (Poullet, Sima et al. 2007). A method of constrained least squares analysis to obtain (approximately maximum-likelihood) estimates of model parameters such as metabolite concentrations, phases, referencing shift, lineshape, baseline, and uncertainties in the concentrations, is employed in the Linear Combination, LCModel (Provencher 2001). Another recently developed system known as TARQUIN (Totally Automatic Robust QUantitation In Nmr), is based upon a quantum mechanical simulation of spectra in the time domain (Wilson, Reynolds et al. 2011). TARQUIN is a fully automatic system producing reproducible quantification for multi and single voxel spectroscopic data.

2.5 Introduction to Compressed Sensing

The essence of CS is a mathematical concept stating that a signal may be accurately reconstructed from a few randomly distributed measured samples, the number of samples being much less than that normally measured. If the signal is compressible after the application of a specific mathematical transform, the random measurements will produce incoherence artefacts within it. If the signal also has a sparse representation, it will contain a few high energy components described in the transform domain which signify the true signal above the level of noise like incoherence. With the application of a convex, nonlinear reconstruction algorithm, the major high energy components can be extracted and the data reconstructed to its original domain.

According to the Nyquist-Shannon sampling theorem, the sampling rate must be at least twice the highest analogue frequency component of the signal. Failure to follow this theory results in signal aliasing after reconstruction; however CS is a method which has been proven to overcome the Nyquist-Shannon sampling allowing much fewer samples to be collected without such artefacts.

2.5.1 Signal Aliasing in MRSI

Aliasing is the misrepresentation of the frequency components of a signal. Figure 2-9 demonstrates this concept showing that for the signal represented in blue, if it is only sampled at the points shown in black, after reconstruction of these few data points, it will appear as the signal shown in red possessing a very different frequency to that of the original signal.

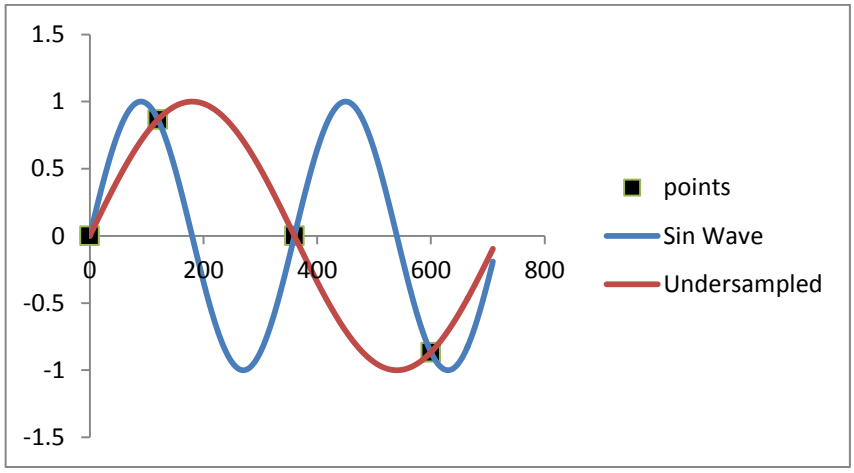

Figure 2-9-An Illustration of 1D signal aliasing. The full signal is represented in blue. The data is sampled at the points shown in black. The resultant representation after under-sampling is the red signal which misrepresents the frequency of the original signal.

The effect of aliasing in MRSI was investigated as a preliminary to this research. In MRSI signal aliasing manifests itself as a misrepresentation of the spatial location of metabolites. This was demonstrated for 2D MRSI in this study by writing MATLAB software to simulate a

reduced Field of View (FOV) scenario. According to the Nyquist-Shannon sampling theorem a bandlimited signal will exhibit aliasing when data is sampled below a rate equal to twice the bandwidth (BW). In MRSI or MRI the bandwidth is in the imaging domain in both x and y directions (FOVx, FOVy). The signal is sampled in k-space at a step size of Δkx and Δky (section 2.2.2), before inverse transformation to the imaging domain. The Nyquist sampling frequency in the x direction is given below:

$$\Delta kx < 1/FOVx \quad \textbf{Equation 2-9}$$

The software read in an MRSI dataset in DICOM format which had a matrix (x,y,f) size of (14 x 12 x 1024). A high signal outside the VOI was added Figure 2-10 a). The MRSI dataset was then Fourier transformed to k-space. A reduced FOV measurement scenario was simulated by uniformly under-sampling only alternate k-space points thus increasing Δk in Equation 2-9 to simulate sampling above the Nyquist rate. The reduced k-space dataset was then inversely Fourier transformed back to real space. The distance between k-space samples and the FOV are inversely related, so this has the effect of reducing the original FOV in real space. The result is demonstrated in Figure 2-10 b). A reduction in the FOV allows a reduction in data sampling and therefore reducing real-time acquisition, however it can be seen that the large signal from outside the VOI can is folded into the VOI as an aliased signal as a result.

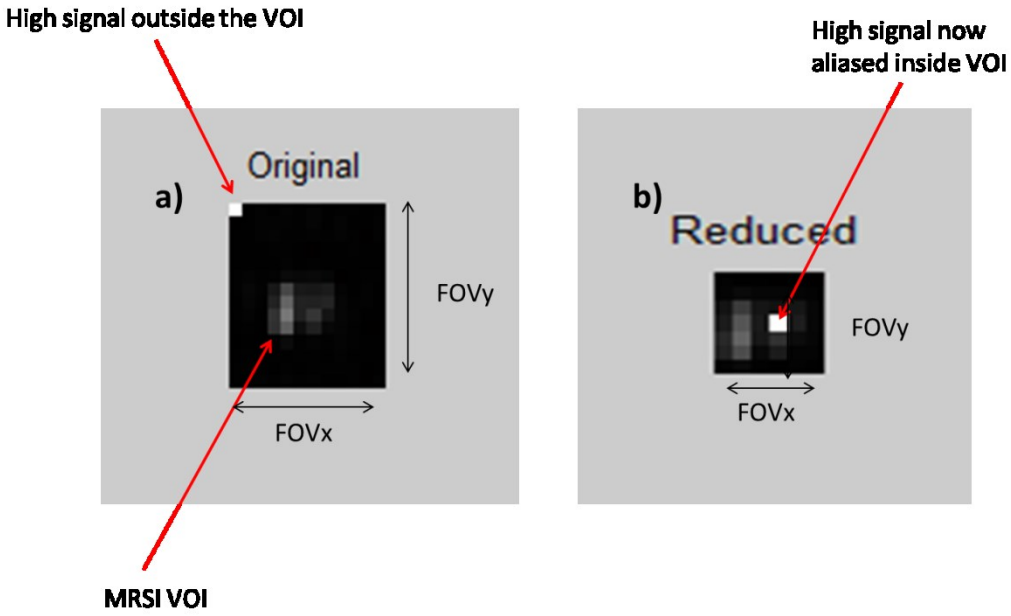

Figure 2-10 – Demonstration of aliasing in MRSI. The original MRSI a) has a voxel with a high signal outside of the VOI. After the size of the k-space steps has been increased, the FOV has reduced b). This process has caused the high signal to alias into the VOI.

This aliasing is often prevalent in MRSI where high outer volume signals such as subcutaneous lipids or residual water are present. The high signal lobes get bled into the region of interest (section 2.3.1). CS is a potential method of reconstructing sub-Nyquist sampled datasets without introducing significant aliasing artifacts whilst maintaining spatial resolution by sampling enough high spatial frequency data samples (Lustig, Donoho et al. 2008).

CS may therefore allow a significant reduction in acquisition time if fewer samples are required without causing signal aliasing. Compressed Sensing should theoretically overcome the Nyquist limitation by meeting the following three requirements:

2.5.2 Signal requires Transform Sparsity

A signal vector which contains a significant amount of information in only a few non-zero components is said to be sparse. A sparse signal contains most of its energy in only a few

measurements, while the rest of the measurements are either zero or negligible. Such a signal may be well represented without a perceptible loss after reconstructing with only these few high energy data components.

A signal has transform sparsity if a transform exists which renders the signal sparse after application of that transformation. This forms the basis of data compression techniques. An example of transform sparsity is the Fourier transform of a sinusoid. In the time domain the signal is continuous, however after transformation, there exists only one frequency component which fully represents the entire signal. MR images are naturally sparse in some transform domain such as wavelets or FREBAS, making them good candidates for compressive sensing techniques(Lustig, Donoho et al. 2008; Ito 2011). MRSI spectra are also naturally sparse in the frequency domain(Bostock, Holland et al. 2012). It has not yet been determined in which domain MRSI data is most sparse, which may be application specific(Geethanath 2012).

2.5.3 Random Sampling is required

The data in MRI and MRSI is collected in k-space (section 2.2.2). In order to reduce the aliasing artifacts (section 2.3.1) introduced by the under-sampling of k-space during CS, the data is collected in a random pattern, not uniformly. The effect of random under-sampling of k-space is to produce noise-like incoherence of the aliasing artifacts in the sparse transform domain (Lustig, Donoho et al. 2008). This can be explained by thinking about an image which is already sparse in the spatial domain. The point spread function (PSF) is a measure of an imaging systems ability to retain the energy of a signal at one single location without leakage away from it. This energy leakage in an MRSI context is referred to as ‘bleed through’ (section 2.3.1). If an image of a single infinitely small point is fully Cartesian sampled in k-space and inverse Fourier transformed back to real space, the PSF will be its identity. If it is

subject to under sampling of any kind random or uniform before inverse transform, the PSF will contain non zero components beyond the single point in all directions. These extra components constitute the energy leakage of the system and usually take the form of a sinc function. In a 2D MRSI imaging scenario, one particular voxel will experience a combination of leakage from all other surrounding voxels. Even if a voxel originally contained zero signals, after under-sampling, it may now contain this unwanted signal. CS therefore endeavors to reduce this leakage by random under-sampling of k-space such that the combination of the leakage is incoherent and spread minimally across the image.

2.5.4 Non-Linear reconstruction technique

Since CS requires the enforcement of transform sparsity together with the need to maintain data consistency with the measured samples, this therefore lends itself to iterative non-linear reconstruction. A nonlinear solution is one which provides the reconstruction of data modelled by a function written as a series of nonlinear equations. The model fitting usually employs an iterative technique based on an initial estimate of the solution. In this case a nonlinear convex optimisation model is required. Such a model is required to minimise the difference between the measured, and current, estimated data whilst simultaneously ensuring the minimisation of the sparse transform coefficients.

2.6 Literature Review of Fast MRSI techniques

Using standard clinical methods, significantly enhancing MRSI spatial resolution would require scanning to be increased beyond a clinically acceptable time frame. Therefore, methods of accelerating MRSI acquisitions, whilst maintaining adequate signal to noise ratio and minimizing the effects of aliasing and lipid contamination are of great potential benefit in MRSI. There has therefore recently been much interest in fast MRSI acquisition techniques (Barker and Lin 2006).

2.6.1 SENSE

One such method for investigation utilises a combination of multiple phased array receiver coils for parallel imaging(Dydak 2001). Reduction in the amount of acquired k-space has been achieved by combining the measured data with the coil sensitivity in parallel imaging. This has been shown to reduce scan time by a factor of 4 (Dydak 2001; Bonekamp, Smith et al. 2010). If the number of phase encoding steps is reduced by a chosen factor R, the resulting images from each component coil possess both aliasing, and a Field of View (FOV) reduced by a factor of 1/R, in the PE directions. In parallel imaging the sensitivity of each coil relates to position in the PE directions. This, in combination with each of the component coil signals, can be utilised to unfold the aliasing and reconstruct the full image. Reconstruction can take place in the image domain for techniques such as SENSitivity Encoding (SENSE), or in the frequency or k-space domain in techniques such as SiMultaneous Acquisition of Spatial Harmonics (SMASH). Parallel imaging is available on the Philips 3T scanner at Birmingham and may be combined with all spectroscopic techniques. A potential pitfall of this technique is the inherent artifact due to the unfolding accuracy of the system, enhancing any spurious lipid signal (Barker and Lin 2006; Zierhut, Ozturk-Isik et al. 2009). Fat suppression bands maybe utilised to overcome this issue. It also requires an additional calibration scan to acquire the coil sensitivities, increasing the overall scan time.

2.6.2 Reduced Field of View (FOV)

A reduction in the Field of View would produce a reduction in the number of phase encoding steps by increasing step size and therefore reducing scan time. A small enough reduction in FOV making significant impact on scan time would fall within the anatomy of the brain. This will cause an inherent aliasing or ‘fold over’ artefact (de Graaf 2007). Efficient signal suppression outside the VOI may compensate for this. Reduced FOV spectroscopy outside

the brain anatomy has been investigated on a 1.5T scanner utilising a rectangular FOV producing scan times of 65% of full FOV imaging(Golay, Gillen et al. 2002). So far, due to insufficient signal suppression this has not been investigated within the brain anatomy.

2.6.3 Turbo Spectroscopic Imaging (TSI)

Turbo spectroscopic Imaging (TSI) reduces the scan time by acquiring multiple echoes after each excitation pulse, effectively gathering multiple sections of k-space at each repetition(Barker and Lin 2006). This technique is available on the Philips 3T and has been utilised in combination with parallel imaging (Dydak 2006). It has also shown good results for the investigation of the coupled spins of Glutamate and Glutamine(Yahya and Fallone 2009) on a Philips 3T. TSI is normally limited to metabolites with longer T2. This is because a long echo train is required as a trade off with spectral resolution limiting the minimum allowable echo time TE. A long echo train length may induce spatial blurring if a significant degree of T2decay has occurred between echoes(de Kok 2007).

2.6.4 Non Cartesian Techniques

In conventional phase encoded MRSI, it is the time taken for the readout gradients to acquire the spectroscopic data which limits the minimum duration. Therefore, attempts have been made to reduce the scan time by acquiring the data in a non-Cartesian fashion. Instead of the stepped, 2D phase encoding of k-space, the readout gradients traverse through k-space in a non-uniform pattern.

Non-Cartesian readout gradients have been utilised in Echo Planar Imaging (EPI), Echo Planar Spectroscopic Imaging (EPSI) or Proton Echo Planar Spectroscopic Imaging (PEPSI). These techniques can dramatically reduce scanning time by the interleaving of an oscillating read out gradient, and Spiral-MRSI which has two oscillating gradients, acquire one or two spatial dimensions in a single shot. This allows the simultaneous encoding of spatial and spectral

information and therefore reducing overall acquisition time. The spatial resolution is determined by the readout gradient duration, and the spectral resolution by the overall time taken for interleaving each readout module. These techniques, although one of the fastest methods of MRSI, can suffer from a reduced SNR relative to conventional MRSI, along with spectral broadening and line drifts occurring due to gradient heating (Barker and Lin 2006; Posse, Otazo et al. 2013). Echo Planar spectroscopic methods offer technical challenges due to the high demands placed on the system for the required rapid gradient switching, and requires a degree of data interpolation in reconstruction potentially hindering accuracy.(Barker and Lin 2006). Spiral MRSI is actually faster than EPSI but data reconstruction can be complex (Posse, Otazo et al. 2013). PEPSI has successfully been utilised in 3D prostate spectroscopy in combination with CS, and has successfully been utilised with SENSE in the brain (Lin 2007; Furuyama 2012). This technique is not currently available at Birmingham.

A technique which claims MRSI data can be obtained in less than a minute by using a burst of low flip angle pulses on a conventional clinical system is also a potential avenue of research(Jakob, Ziegler et al. 1995). An implementation on rat brains of a technique known as Gradient and Spin Echo (GRASE) has shown that scan times are reduced with high resolution(Dreher and Leibfritz 2000). This technique suffered poor SNR, requires high quality gradient switching and achieved using 4.7T only.

2.6.5 Steady State Free precession (SSFP).

Steady state Free precession techniques can also offer a significant decrease in scan time without loss of sensitivity(Dreher, Geppert et al. 2003). They have a short readout time which can however limit the allowable spectral resolution at field strengths of 3T and below.

This technique is particularly susceptible to off resonance effects due to imperfections in shimming and from eddy currents.

2.6.6 Sparse Image based k-space encoding schemes

In the quest for faster imaging and higher spatial resolution, methods have been investigated which utilise prior information about the object being imaged. 'spectral localization by imaging' SLIM is a non-fourier reconstruction technique which aims to improve the effective MRSI spatial resolution(Hu, Levin et al. 1988). This basically uses the known spatial resolution of a corresponding high resolution anatomical MR image to identify areas of homogeneous signal. This is then used to effectively divide the anatomy into metabolite compartments from which spectra can be reconstructed. This technique is limited by the assumption that each compartment is uniform. To provide some inhomogeneity within the compartments a technique known as 'Generalised spectral localization by imaging', GSLIM has been introduced(Zhi-pei and Lauterbur 1991).

2.6.7 Compressed Sensing in MRSI

The natural sparsity of MRSI data in the frequency and spatial dimensions lends itself to the application of CS reconstruction and leads to its potential application for the acceleration or increased coverage of pre-existing MRSI methods. MRSI is an inherently noisy technique due to the low metabolite signal. Reconstructing with CS in MR has been shown to be an inherently de-noising technique (Lustig, Donoho et al. 2007). Application of CS could therefore be advantageous over the other fast MRSI techniques such as EPSI, SENSE and GRASE which can be limited by SNR.

Pre-clinical studies have shown successful application of CS to ^{13}C MRSI (Hu, Lustig et al. 2010; Larson, Hu et al. 2011). Recently a pre-clinical study has demonstrated the feasibility of CS applied to ^{1}H phase encoded MRSI(Cao and Wu 2014). The use of CS reconstruction

from echo-planar J-resolved spectroscopic imaging (EP-JRESI) datasets of the prostate has shown a potential four-fold reduction in scan time (Furuyama 2012). CS has successfully been utilised retrospectively on clinical, Point Resolved Spectroscopy (PRESS) acquisitions (Section 2.2.1), (Geethanath 2010; Geethanath 2012), and has also recently been used in clinical 31P spectroscopic data(Askin, Atis et al. 2012).

2.7 Conclusion

To conclude, 2D phase-encoded MRSI is a proven technique useful in the diagnosis and monitoring of disease but it has many challenges which limit its clinical utility. One of the major limitations to the clinical application of MRSI is long acquisition time which if reduced whilst ensuring Nyquist sampling, results in a corresponding reduction in spatial resolution. Investigation into reducing MRSI acquisition times is a major area of research. Current solutions suffer from poor SNR and possible reconstruction artefacts. CS is a method which allows sub-sampling below the Nyquist sampling limit thus reducing acquisition time, without detriment to image data quality. CS has had successful application in anatomical MRI but could also provide a potential solution to the lengthy scan duration of MRSI.

3 Implementation and development of CS-MRSI Software

3.1 Introduction to CS in MRSI

Conventionally when a signal is under-sampled below the Nyquist limit, reconstruction quality is compromised as a result of aliasing artefacts (section 2.5.1). CS is a reconstruction technique allowing the acceleration of signal measurement beyond the Nyquist limit without detriment to reconstructed quality (Lustig, Donoho et al. 2008). The technique is reliant upon a signal or image having a sparse representation in some transform domain. This means that the object of interest maybe reliably reconstructed from few but important data coefficients from that transform. A sparsifying transform is applied which maps the image content into a vector of sparse coefficients of which the insignificant ones can be omitted. This is akin to image compression where the largest components after transform to the wavelet domain are retained only, in order to facilitate data transfer. The concept of CS is that the signal is compressed during image acquisition instead of afterwards. The aliasing artefacts from the under-sampling are minimised by acquiring the measurements in a random scheme, such that on transform of the measured samples to the sparse domain the aliasing artefacts combine in an incoherent fashion, the first requirement of CS. Acceleration from CS is achieved by reconstructing highly under-sampled data which has a sparse representation, the second requirement of CS. Utilising a mathematical framework, CS ensures data transform sparsity whilst at the same time minimising the differences between measured and reconstructed samples, this is the third requirement of CS.

One of the major limitations to MRSI is its long acquisition time due to its data sampling requirements (section 2.2.2.1). Therefore, the application of CS to MRSI could provide a valuable method of overcoming this. CS has been successfully implemented in MRI (Chartrand 2009). The data in both MRI and MRSI are acquired in k-space (section 2.2.2). The

difference between MRI and MRSI is the addition of the third spectral dimension kt, which in k-space is acquired in a single shot at each k-space location (kx,ky). Random acquisition of k-space locations will render incoherent aliasing in the resultant MRSI image after inverse Fourier transform from k-space back to real space. This satisfies the first CS requirement. The second requirement of CS is that the images under reconstruction have a sparse representation. MRSI has a natural sparsity in the spatial and spectral dimensions. The actual useful data in an MRSI is contained within the selected VOI (section 2.2) which is typically around 20% of the entire FOV. Therefore the MRSI image is itself sparse. CS has also been successfully implemented utilising wavelets as the sparsifying transform to satisfy this requirement (Geethanath and Kodibagkar 2013; Cao and Wu 2014). Under-sampling in the temporal dimension kt would yield further sparsity. However, since the burden on acquisition speed is the phase encoding of k-space and that the sampling scheme required to under-sample the temporal dimension would in future necessitate a complex pulse sequence with rapid gradient switching, there is little to be gained from this. The mathematical optimisation framework needed for the third requirement of CS is readily available for MRI which lends itself to adaptation to MRSI.

The implementation of CS reconstruction code was developed in this study using the Matlab development platform Version (2012b). The software was based on the 2D MRI compressive sensing code available in the SparseMRI package available at (http://wwwmrsrl.stanford.edu/~mlustig/software/). In this research, the code was adapted to reconstruct a standard 3D matrix (x,y,f) of MRSI data. A description of the adaption of CS to the MRSI data reconstruction is outlined below.

3.2 The random under sampling pattern

Although available as a research tool for MRI, to date there is no system to acquire prospective non-uniform data points in k-space in MRSI acquisition. Therefore, all CS data reconstruction was either achieved on retrospective data which had been previously acquired, or by software simulated MRSI datasets.

The 2D random style sampling required for CS in MRSI k-space has to take into account the fact that there is a balance between the high MRI signal of the points at the centre and the high spatial resolution of data at its periphery. This is achieved by implementation of pseudo-random sampling which fully samples the very centre of k-space and then samples points based on a weighted 2D probability density function decreasing towards the periphery. This provides more samples in the centre of k-space than those at the edges (Lustig, Donoho et al. 2007). The 2D fully sampled centre is dependent on the inverse of the acceleration factor, i.e. smaller fully sampled region for higher acceleration factor(Geethanath 2011).

The pseudo-random under-sampling pattern or k-space mask was based upon the software available in SparseMRI software package (http://wwwmrsrl.stanford.edu/~mlustig/software/). This scheme has been successfully utilised in 2D phase encoded, CS-MRSI (Geethanath 2012; Cao and Wu 2014) and so the same methodology was adopted for this study. The only difference between this previous under-sampling scheme and the one in this research was the inclusion of an elliptical shutter design to mimic the standard, default k-space shutter available on most scanners (section 2.2.2.1). Figure 3-1 shows an example of the k-space sampling mask for an acceleration factor of x5 (20% of samples acquired) and at x2 (50% of samples acquired). Each point (kx, ky) shown in white is sampled. Since the data acquired in k-space is in the form of a matrix

(kx ,ky ,kt) (section 2.2.2), the same mask is applied at each time point t in the k-space temporal dimension.

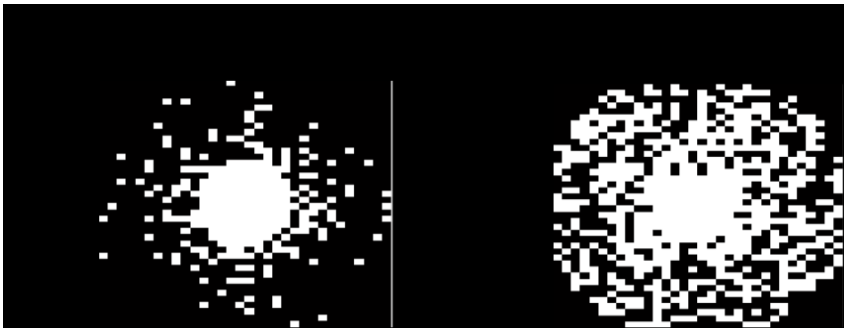

Figure 3-1 - Typical random 2D k-space masks for 20% (x5) sampling a) and 50% (x2) sampling b). Each white square is a sampled location. The overall shape of the sampling is shaped by the k-space shutter.

The ability to acquire real-time under-sampled MRSI datasets in this way is not yet available on the scanner. In order to mimic the random acquisition of such a dataset the following steps were taken:

1) The real-time MRSI data acquired from the scanner after post processing, is in the form of 2D spatial co-ordinates x and y, and an FID of 1024 associated time points t (x,y,t). The number of x and y points depends on the acquired matrix or MRSI grid size.
2) A 1D Fourier transform of the FID time data was achieved to obtain dataset (x,y,f).
3) This dataset (x,y,f) was subject to a 3D Fourier transform to produce data (kx,ky,kt). This replicates the form in which the MRSI data is acquired.
4) A single 2D k-space under-sampling mask as described above was then successively applied to the 3D MRSI data set at each temporal kt point. The (kx,ky) locations not sampled by the mask were zero filled in (kx,ky,kt).

3.3 The sparse representation of MRSI data

The measured data needs to have a domain in which the data is sparsely represented (2.5.2). The particular sparse transform to utilise is an area of much research in the application of CS to MRI (CS-MRI), and is yet unproven. In the application of CS-MRI the sparse domains of the wavelet, Discrete Cosine Transform (DCT) and the identity transforms have been used (Lustig, Donoho et al. 2008; Haifeng, Dong et al. 2009). In previous work on CS-MRSI the wavelet transform has been utilised although this has not been proven as the optimal sparse MRSI domain. The spectra in the MRSI dataset (x,y,f) exhibit sparsity amidst the peaks surrounded by low level noise and for PRESS (section 2.2.1) the data in the image itself is sparse given that the useful data in VOI is much smaller than the whole FOV. It was therefore initially decided to utilise the identity transform. The identity transform is inherently computationally faster and less complex than other sparsifiying transforms. This identity domain was later compared to the wavelet domain.

3.3.1 Wavelets

In this research wavelets were also investigated as a sparse domain representation of the MRSI data. If a signal possesses variation in frequency with time such as sharp spikes or discontinuities, then a Fourier Transform will not appropriately represent the frequencies present. The problem is such that it is not always possible to know the exact time-frequency representation of a signal due to the finite sampling of the signal. The problem results in the exact spectral component at a particular instance of time being undeterminable. What can be determined are the time intervals in which a band of frequencies may exist, a resolution problem. The use of techniques such as the Short Term Fourier Transform (STFT) may be utilised to determine the frequency-time relationship. The STFT segments, or windows the signal into intervals where it is assumed to be stationary, and non-varying in frequency with

time. The window width must be the same as the stationary portion under analysis. The window starts at t=0 and is multiplied by the signal at this location and then Fourier Transformed. The window is then shifted along, the process repeated and the result summed. Unfortunately because of the finite width of the window function, the STFT is limited in its frequency resolution. It does not give the exact frequencies present in the signal, only a band. If a window of infinite length were used to enhance frequency resolution then this is identical to the original Fourier Transform. The use of wavelets is a better approximation than the STFT. Wavelet analysis is achieved in a similar way to the STFT except that the finite window called a wavelet varies in width according to each spectral component, and in that the Fourier Transform for each window is not taken. The wavelet is contracted for low frequency analysis and dilated for high frequency analysis. The degree to which the wavelet contracted or dilated is termed the scale. The initial wavelet used in the analysis is termed the 'Mother Wavelet' and is a prototype for each subsequent wavelet. The choice of mother wavelet can vary dependent upon application. There are different wavelet families such as Daubechies, Coiflets and symmlets which vary according to the number of coefficients and by the level of iteration.

The original signal is represented in terms of wavelet expansion using coefficients in linear combination of each wavelet function. This therefore allows truncation of the wavelet coefficients lending itself to sparse representation. Since this study is examining the ability of CS to reconstruct metabolite edges, a step-like wavelet, the Daubechie 1 (Haar wavelet) was utilised as the mother wavelet for this application.

3.4 Image Reconstruction in CS-MRSI

In CS-MRSI a random k-space sampling pattern is defined 3.2. After acquisition of the random data there will be a sub-sample of measured data. In order to fill in the zeros, the

minimisation of the square error of the measured and the desired datasets via the following objective function are achieved:-

$$\|\boldsymbol{F_u m} - \boldsymbol{y}\|_2 < \boldsymbol{\epsilon} \qquad \textbf{Equation 3-1}$$

Where:

m = The desired reconstruction of the MRSI dataset (x,y,f).

F_u = The Fourier Transform operator of the under-sampling scheme

y = The sampled k-space data.

$\boldsymbol{\epsilon}$ = a parameter to control the reconstruction quality, set to be below the level of expected noise.

This is combined with the L1 norm of the transform sparsity requirement which can be expressed as:-

$$\|\boldsymbol{\Psi m}\|_{\boldsymbol{1}} \qquad \textbf{Equation 3-2}$$

Where:

m = The desired reconstruction of the MRSI dataset (x,y,f).

Ψ = The sparsifying transform.

The L1-norm is used to maintain the sparsity. This is because the L1 norm will favour fewer larger components and hence sparsity, whereas the L2-norm penalises large components, maintaining larger datasets of smaller values. The L-norm is expressed as:

$$\|\boldsymbol{x}\|_{\boldsymbol{p}} = (\textstyle\sum_{\boldsymbol{i=1}}^{\boldsymbol{n}} |\boldsymbol{x_i}|)^{\boldsymbol{1/p}} \qquad \textbf{Equation 3-3}$$

The equations 3.2 and 3.3 are combined to express the problem mathematically as:

$$minimise \ \|\Psi m\|_1$$

$$\boldsymbol{s.t.} \|\boldsymbol{F_u m} - \boldsymbol{y}\|_2 < \boldsymbol{\epsilon} \qquad \textbf{Equation 3-4}$$

It has been shown that it is often useful to extend the problem to also include a term for the Total Variation (Tsaig and Donoho 2006). The finite differences transform may be used as a sparsifying transform. It is referred to as Total Variation, TV(m), and defines the sum of the absolute variation in all dimensions. This transform is defined mathematically for an N point signal x(n), 1≤ n≤ N as:

$$\boldsymbol{TV(x)} = \sum_{\boldsymbol{n=2}}^{\boldsymbol{N}} (\mathbf{x(n)} - \mathbf{x(n-1)}) \qquad \textbf{Equation 3-5}$$

This can also be expressed in matrix form as:

$$\boldsymbol{TV(x)} = \|\boldsymbol{Dx}\|_{\mathbf{1}} \qquad \textbf{Equation 3-6}$$

Where

D= matrix of size (n-1) x n of the form:

$$\begin{pmatrix} -1\ 1\ 0\ 0 & \cdots & 0 \\ \vdots & \ddots & \vdots \\ 0 & \cdots & 0\ 0\ -1\ 1 \end{pmatrix}$$

This means that as well as requiring the imaging dataset to be sparse in the specific transform domain it is also to be sparse in finite differences which provides an effective smoothing of the image. The problem can now be expressed as:

$$minimise \ \|\Psi m\|_1 + \alpha \mathrm{TV(m)}$$

$$s.t. \|F_u m - y\|_2 < \epsilon$$

Where:

α = weight which determines the importance of the TV term over the sparsifying transform

In Lagrangian form this may be expressed as:

$$\|\boldsymbol{F_u m} - \boldsymbol{y}\|_2 + \boldsymbol{\lambda_1}\,\|\boldsymbol{\Psi m}\|_{1+}\boldsymbol{\lambda_2}\ \mathbf{TV(m)} \qquad \textbf{Equation 3-7}$$

Where:

λ_1= Sparsyfying transform weighting factor

λ_2= Weighting factor of TV transform

The weighting factors $\lambda_1$and λ_2 is also a subject of research. They will be application dependent and balanced by the level of expected noise. In this study the values were empirically chosen to be 0.002 and 0.005 respectively with due consideration of (Geethanath 2012; Heikal, Wachowicz et al. 2013).

The above equation is solved using a non-linear iterative reconstruction technique. The iterative technique utilised in this research was conjugate gradient descent, the method already utilised in the sparse MRI package.

4 Phantom development for assessment of spatial resolution in MRSI

4.1 Introduction

Previous research on the application of CS in 2D phase-encoded MRSI (CS-MRSI) is limited and impact upon subsequent image quality relatively unexplored. A standard method to quantify the spatial resolution of MRSI regardless of reconstruction technique has yet to be developed.

To date, only one fully quantitative investigation on the effect of CS-MRSI on spatial resolution has been found. The paper investigated the effect of CS on the spatial resolution of MRSI for one acceleration factor (section 3.2), x4 (Heikal, Wachowicz et al. 2013). Another very recent study examined the use of CS-MRSI on rat brains and on phantom studies at 7T, for acceleration factors up to x7 (Cao and Wu 2014) but was limited to qualitative assessment of spatial resolution.

There is currently no known standard method of assessment of the spatial resolution of MRSI. A major issue in clinical MRSI is inter-voxel contamination from adjacent and distant (Gibbs ringing) voxels (2.3.1). This is a major detriment to accurate spatial resolution since the signal from one voxel may add to or reduce signal in the location of another. Inter-voxel contamination may be exacerbated by under-sampled datasets where aliasing and/or loss of high spatial frequency data may result (section 2.5.1). After MRSI data has been under sampled and reconstructed using CS, methods of assessment of the inter-voxel contamination and spatial resolution are therefore desired. This chapter discusses the process of the development of a methodology to assess these effects.

The impulse response of an imaging system is the PSF (section 2.3.1). The Fourier transform of the PSF indicates which spatial frequencies are being transferred in the imaging system. In a perfect imaging system the impulse response would be a pure Dirac delta function. The Fourier transform of this infinite point source would yield a flat response indicating that all frequencies were equally present.

The measurement of the PSF is complex since to obtain metabolite signal from an infinitely small voxel is impractical. However, the measurement of the signal profile perpendicular to a boundary of negligible width between regions of contrasting signal is technically less challenging. Such a measurement reveals the Edge Response Function (ERF) (Samei, Flynn et al. 1998) . The differential of the ERF reveals the Line Spread Function (LSF). The LSF is effectively the one dimensional representation of the two dimensional PSF(Williams 1991). The Fourier transform of the LSF would therefore reveal the spatial frequencies present in the imaging system.

Possible methodologies in the assessment of the spatial frequencies present in an image are described below.

4.1.1 Measurement of the gradient of the edge response

An indirect evaluation of the spatial resolution of an imaging system can be achieved by analysis of the ERF. From basic imaging theory, the higher the spatial frequencies present in an image the sharper will be the resulting image of an edge(Antoniou 2006). Therefore, the measurement of the maximum gradient of the image of an edge will provide an indirect measure of the spatial resolution of the system.

4.1.1.1 Modelling the ERF

In MRSI an 'edge' would entail a well-defined boundary between regions containing different concentrations of a given metabolite or metabolites. Figure 4-1 shows a simple two-compartment model system containing a bi-directional edge between two different metabolite solutions.

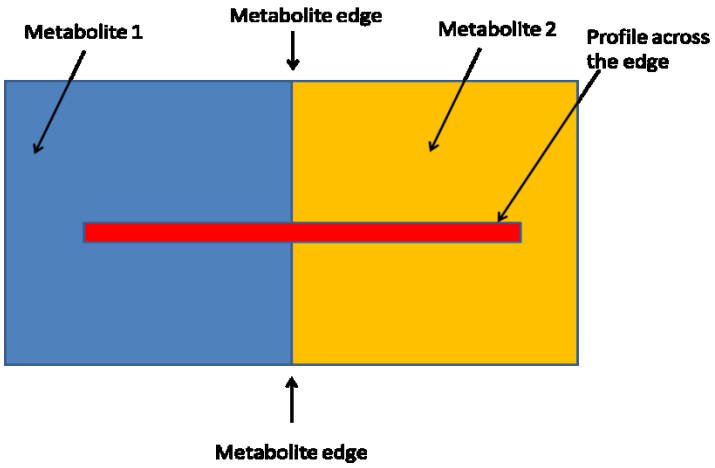

Figure 4-1 - Demonstration of an ideal metabolite edge. Metabolite 1 and metabolite 2 are adjacent to each other and ideally are separated by a negligibly thin, impermeable membrane. The red line is a profile across this edge used to determine the spatial resolution from its slope.

4.1.1.2 Assessment of the ERF

A profile of signal from voxels sampled at right angles to the edge (red line on Figure 4-1), will provide the edge response function. Voxel signal along the profile can be plotted against location. The slope or gradient of the plot will provide a quantitative indication of edge response and therefore an objective measure of spatial resolution.

4.1.2 Measurement of the Modulation Transfer Function (MTF)

The Modulation Transfer Function (MTF) is a widely used technique to describe the modulation of the spatial frequencies present in any imaging system. The MTF is the Fourier transform of the LSF (section 4.1). It has been used to evaluate a variety of medical imaging

systems techniques including x-ray, CT and MRI (Judy 1976; Fujita, Tsai et al. 1992; Steckner, Drost et al. 1994). It measures how faithfully the imaging system reproduces the details present in the object under investigation. The normalised MTF is a function of spatial frequency. The spatial frequency is conventionally expressed in units of line pairs per mm (lp/mm). One line pair is defined as one black line and one white line of equal width and in the same orientation. The value of lp/mm at 50% and 10% of the maximum MTF are often used as indicators to quantify the maximum spatial resolution.

The development of a phantom with a suitable metabolite edge was undertaken in the following sections:

4.2 The Localisation Phantom.

This pre-existing phantom was designed and developed for multicentre EU project (eTUMOUR) primarily for validating localisation of single voxel spectroscopy (Leach, Collins et al. 1995). The phantom contains metabolites Creatine (Cr) and Lactate (Lac) in a central perspex cube of wall thickness 3mm, and Acetate (Ac) in the remaining portion of the perspex cylinder Figure 4-2. This phantom therefore contains a metabolite spatial variation across the outer cylinder (containing the acetate) and the central cube (containing the Creatine and Lactate). Initially it was hoped that an acquisition and subsequent voxel profile plot across this region may indicate the required metabolite edge response.

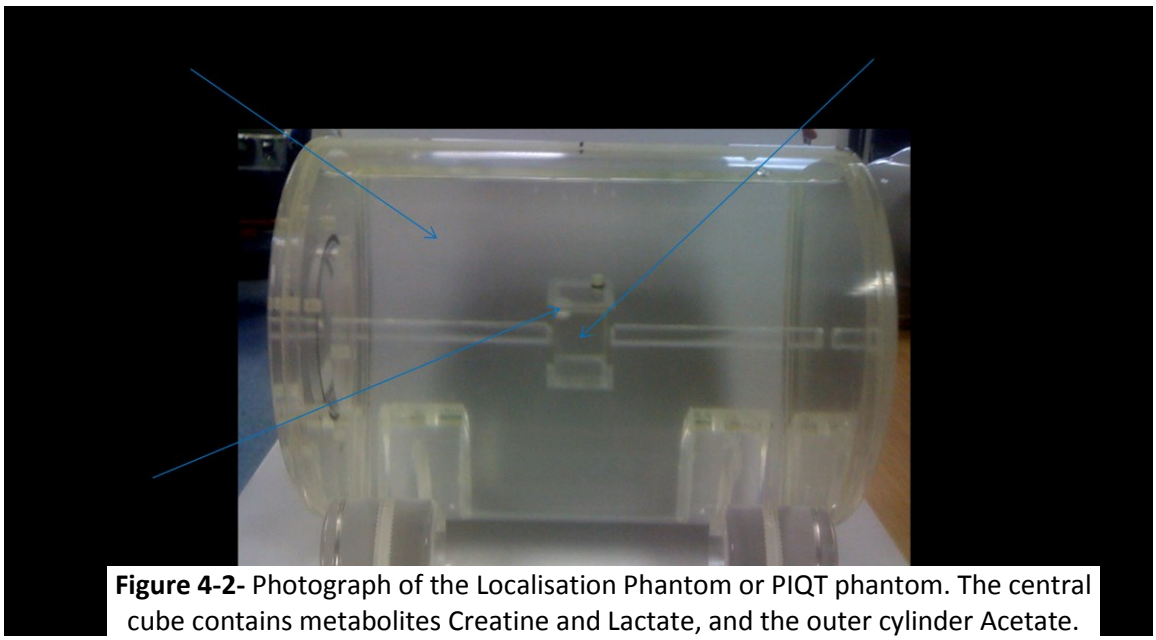

Figure 4-2- Photograph of the Localisation Phantom or PIQT phantom. The central cube contains metabolites Creatine and Lactate, and the outer cylinder Acetate.

4.2.1 Method

The phantom data was acquired with parameters listed in Table 1.

Scanner	Philips 3T TX Achieva
Coil	8-channel Receive Head coil
TE(ms)	35
TR(ms)	2000
Bandwidth	2000
NSA	1
Ringing filter	OFF
Sampled spectral points	1024

Table 1 Acquisition parameters

A Spin Echo spectroscopic sequence was utilised with an initial voxel dimension of (10mm x 10mm x10mm), Figure 4-3. An automatic shim volume was utilised. The Field of View (FOV) encompassed the whole test-object radius. Water suppression was excitation method.

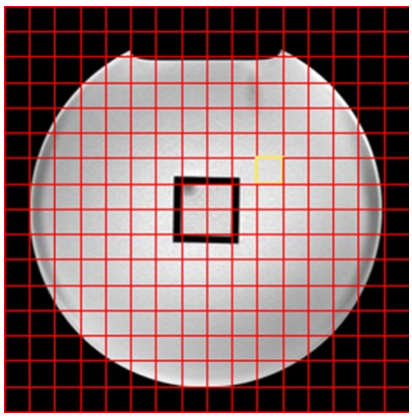

Figure 4-3 -An axial MRI image of the localisation phantom and the MRSI grid (aligned to the central cube) for the 10x10x10mm voxels. The yellow square indicates a single voxel. The red grid is the Field of View (FOV). The black square at the centre is the Perspex cube containing the Creatine and Lactate metabolites. Four voxels were chosen which were the furthest away from the air bubble which can be seen in the top left hand corner.

The spectra were displayed using scanner software Figure 4-4. The figure indicates the peaks from the four voxels in the central perspex cube at a voxel dimension of (10mm x 10mm x 10mm).

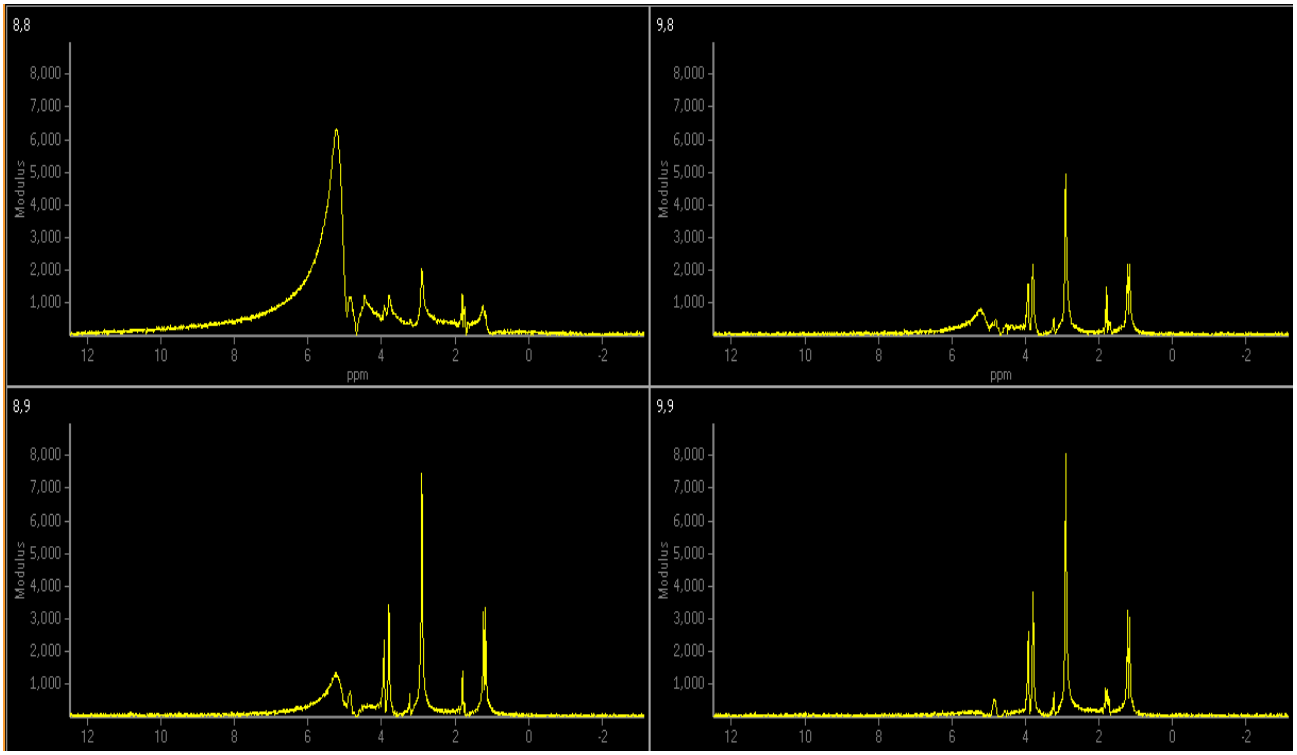

Figure 4-4 The individual spectra (magnitudes) for the 10mmx10mmx10mm are taken from within the central Perspex cube containing Creatine and Lactate.

Figure 4-4 indicates that the main Creatine peak at 3ppm, on the top left hand spectrum is relatively lower than on the other spectra. This may be due to the presence of the air bubble. The spectra on Figure 4-4 also indicate small peaks at around 2ppm, indicating that the acetate peak is contaminating through into all these voxels. There is a large broad peak at greater than 4ppm in the top left voxel corresponding to the location of the air bubble. This is the residual water peak, which is high and broad, indicating poor shimming in this area. The air bubble is creating a magnetic susceptibility artefact distorting the main magnetic field (section 2.2.3).

4.2.3 Discussion and conclusions

The localization phantom was a good starting point but the spectra Figure 4-4 indicate reasons why it is not an ideal test object for further spatial resolution assessment in MRSI. The air bubble formed within the central cube is causing a magnetic susceptibility artefact in this area as well as a reduction in metabolite concentration. The central cube has a Perspex thickness of (3mm), not a negligibly thin edge. If a phantom could be produced that had a perfect edge, with a boundary of negligible thickness, it would enhance the accuracy in the assessment of spatial resolution and so it was decided not to re-scan the localization phantom after attempting to remove the air bubble.

4.3 Development of an Imaging Phantom to assess the ERF

It was therefore decided to develop a phantom which addressed the problems of the localization phantom. Desirable features for this phantom would include a negligibly thin barrier between compartments containing different metabolite concentrations and uniformity of concentration within each compartment. The edge also needs to be flat and impermeable to metabolite penetration. The following sections describe the development of such a phantom.

4.4 Prototype metabolite edge phantom

4.4.1 Method - construction

This phantom consisted of a perspex box filled with tap water, containing a smaller perspex cup submerged at one end of it, Figure 4-5. The perspex cup contained a Creatine mixture. The challenge of how to manufacture a suitable metabolite edge was met by using a piece of latex stretched over the end of the cup. The latex would prevent penetration of one metabolite to the other, the tension in the glove would keep the glove flat and the latext when stretched would be very thin. The piece of latex was stretched and sealed around the open end of the cup with a strong elastic band. The Creatine mixture was a common form available from health food shops. It was mixed with tap water to produce an approximate concentration of 10mM. The cup was placed inside the larger container and maintained in position by means of an elastic band to keep it stable. A T1-weighted MRI, coronal image of the phantom can be seen in Figure 4-6.

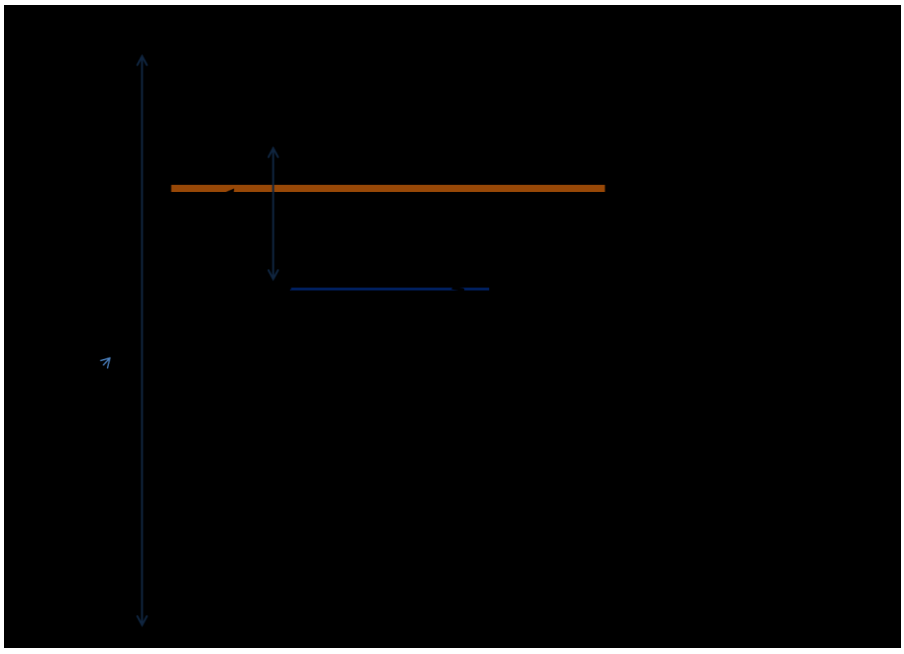

Figure 4-5-The prototype metabolite edge phantom schematic (Plan view). A Perspex cup containing Creatine was placed inside another larger Perspex sandwich box containing tap water.

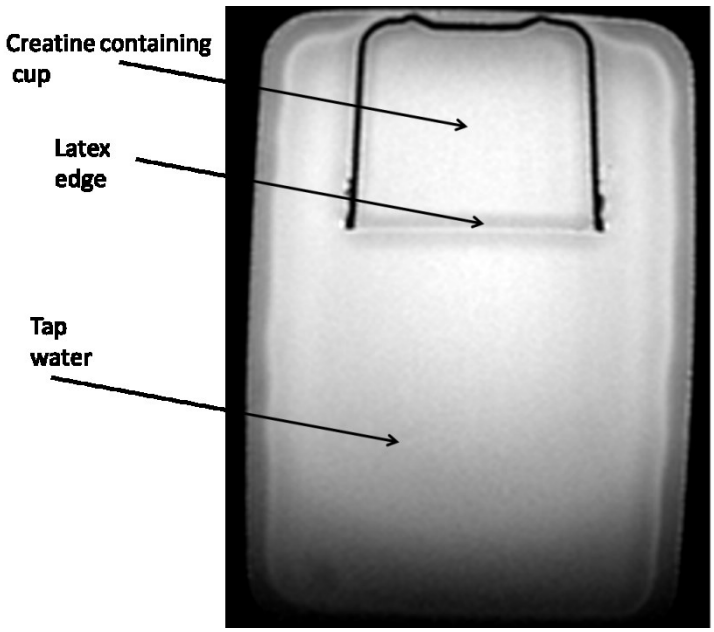

Figure 4-6-A coronal T1-weighted MRI of the second metabolite Edge phantom. A Perspex cup containing a Creatine solution was submerged under water inside another larger perspex box. A latex glove was placed over the end of the Creatine containing cup to seal it.

4.4.2 Method – data acquisition

The phantom was not water tight at the top so it was placed in the coil such that its longest axis was parallel to the scanner's central axis, perpendicular to Bo. The phantom data was acquired according to Table 1. Initially a single ($15mm^3$) voxel PRESS acquisition was obtained from within the cup Figure 4-7 a). This was acquired in order to investigate if the peaks of Creatine were visible and as expected.

The phantom was then imaged again using a spin echo MRSI sequence. Spin echo was utilised to avoid any chemical shift displacement artifact. The phantom was imaged in the sagittal plane to ensure the MRSI slab was across the metabolite edge and that it was central in the cup. The MRSI was acquired again according to Table 1, and voxel size of (10mm x 10mm x 10mm). The matrix size was of 22x10, Figure 4-7 b).

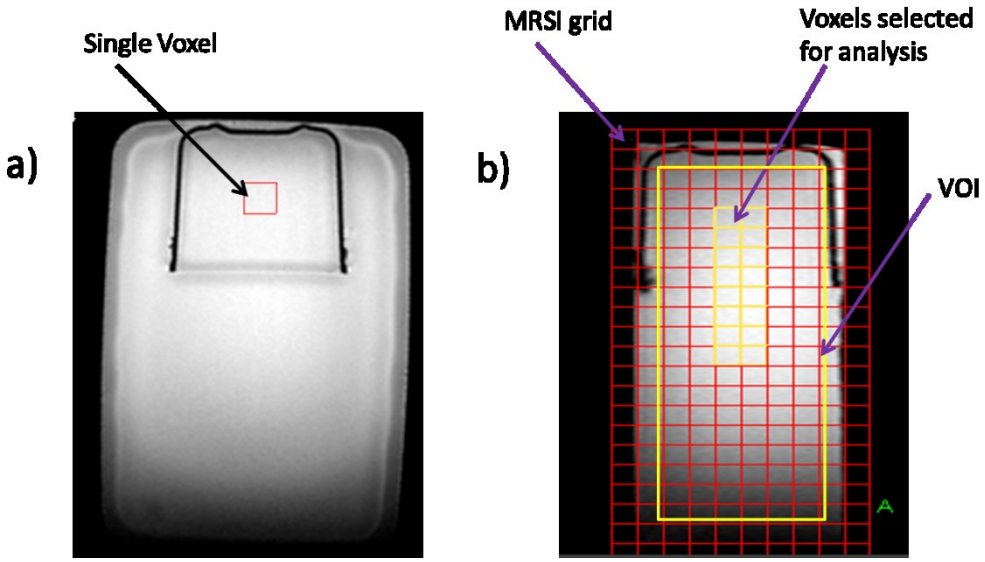

Figure 4-7-The single voxel acquisition planning a) and the MRSI planning b).The yellow voxels indicate those selected across the metabolite edge.

4.4.3 Results

Figure 4-8 depicts the spectrum displayed using scanner software of the single voxel acquisition taken from within the inner cup. This shows peaks at 3ppm and 3.9ppm, the expected peaks of Creatine. The smaller peak at >4ppm are the suppressed, residual water peaks.

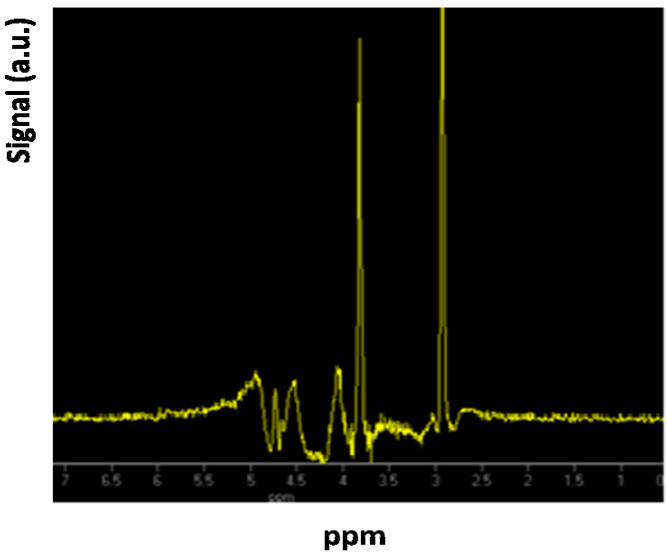

Figure 4-8-The single MRS voxel spectrum indicating the peaks of Creatine and residual water at >4ppm.

Figure 4-9 shows the spectra from the yellow voxels depicted on Figure 4-7 b). The top four rows are those voxels within the Creatine containing cup, and the bottom four are those within the water area. Voxel rows 2, 3 and 4 appear to contain the Creatine peaks along with the residual water at >4ppm. It can be seen that the height of the Creatine peak reduces as the voxel location is moved to the far end of the cup away from the latex. The MRSI signal is dropping off towards the edges of the phantom due to susceptibility artifacts at the air-phantom interface, indicated by the increasing width of the residual water peak signal. It can also be seen that there are small peaks on the other side of the latex metabolite barrier, indicating a degree of inter-voxel contamination from the inherent point spread function in this low resolution (10x10x10mm) MRSI.

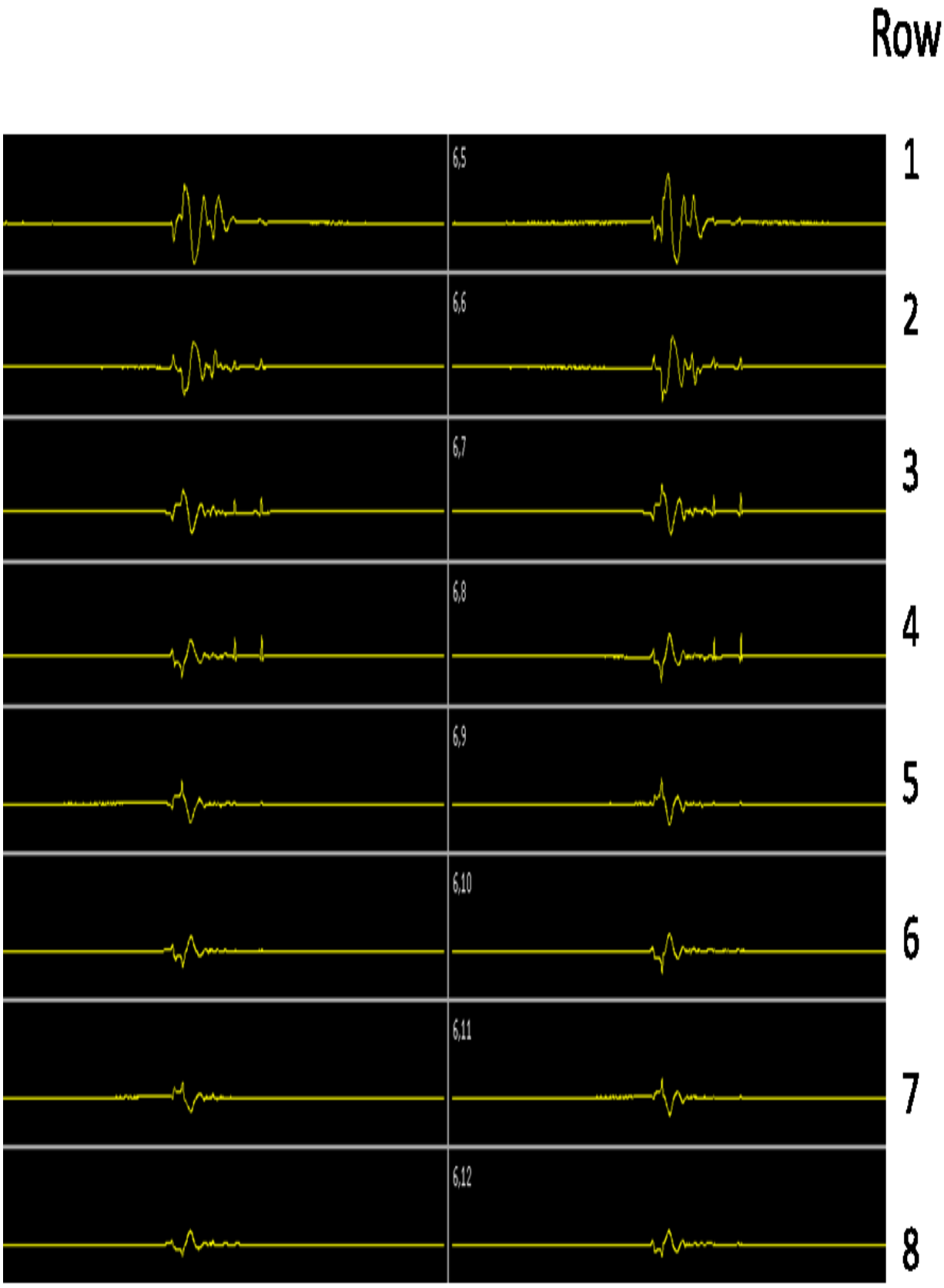

Figure 4-9-The spectra obtained from the MRSI voxels from the second metabolite edge 'cup' phantom. All graphs plotted on the same scale.

4.4.4 Discussion and conclusions

This phantom was an improvement on the localisation phantom since it contained a thin barrier between the metabolite containing area and the water region. The expected metabolite peaks can be seen to be prevalent on the expected side of the latex partition Figure 4-9. It was concluded that there were two main issues with this phantom. The reduction in the signal intensity of the Creatine as the voxels become closer to the end of the Creatine cup indicate that shimming over the volume of the cup is a practical challenge. If a vessel of larger homogeneous volume were utilised for the Creatine this may help overcome this limitation. Secondly, the material from which this phantom is constructed is tap water with the addition of Creatine, not representative of human brain tissue.

4.5 The two-compartment gel metabolite edge phantom

To produce a phantom which has an negligibly thin metabolite edge, has dimensions enough to aid magnetic field uniformity, and constructed of a uniform material similar to human brain tissue, an agarose gel two-compartment phantom was developed. This will aid in the assessment of the resolution of acquired MRSI data sets and any subsequent reconstruction. The use of agarose gel has previously been employed in MRI phantom work(Yoshimura, Kato et al. 2003). The phantom contained water and agarose at 1% weight per volume which has a T2 of the order of bulk water in brain tissue at 3T (Child and Pryce 1972; Träber, Block et al. 2004). Once set, the gel will keep its shape and so can be designed as an edge.

4.5.1 Method - construction

The phantom consisted of two halves each of 1 litre volume of 1% agarose gel and distilled water. Agarose was dissolved in a flask placed in a microwave at maximum power for 8minutes. The gel was then covered with foil and placed on a magnetic stirrer to cool. Metabolites, Creatine (10mM) and NAA (10mM) were added to each flask of agarose at

37^{o}C. One gel was poured into a Perspex container via a glass funnel, left to set, then the other gel added. The gels were separated by cling film to prevent any possible metabolite diffusion between the gels Figure 4-10. The cling film was smoothed by hand prior to the addition of the second gel to remove any air bubbles.

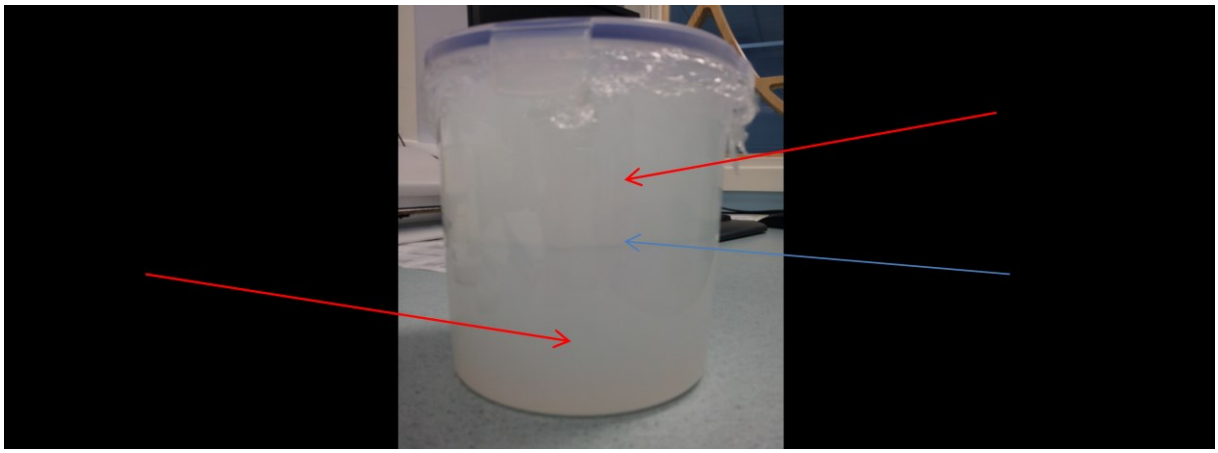

Figure 4-10 The two-compartment gel edge response phantom

4.5.2 Method - MRSI Acquisition

Scanning of the two-compartment gel edge phantom was achieved the day after construction in order to eliminate any possible degradation of the test object over time. The phantom data was acquired according to Table 1. Coronal, Spin Echo spectroscopic MRSI scans were acquired with voxel size (10mm x 10mm x 10mm). The FOV encompassed the whole test-object radius. Square, water suppressing, saturation bands were used to define the VOI to avoid any magnetic susceptibility artifacts due to the indentations in the gel at the interfaces on the far right and left edges Figure 4-11. The water suppression method was the default excitation (section 2.2.4). In order to achieve an absolute quantification of

metabolite concentration, a separate MRSI was also acquired with the same parameters except the water data was unsuppressed.

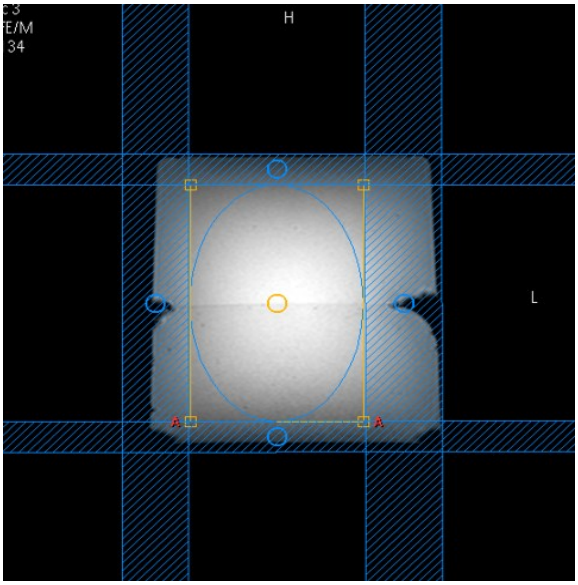

Figure 4-11-The MRSI planning of the two-compartment gel edge response phantom. The VOI is defined with the square water saturation bands in blue.

4.5.3 Method - data processing

A Matlab program version 7.10.0(2010a) was written to reconstruct spectroscopic data and produce plots of the integral of the metabolite peaks as a function of distance across the image. A flow diagram of the program can be seen Figure 4-12. The program reads in the spectroscopy DICOM file. Spectroscopy data from within the file is in a format of a vector of alternating real and imaginary numbers corresponding to the Free Induction decay (FID) (section 2.1.1). Each FID contains 1024 sampled time points. The Matlab software converts this 1D DICOM format to a 3D matrix containing an FID signal within each voxel location (x, y, t). The 1D time data is Fourier Transformed in the third dimension to produce spectroscopic data (x, y, f). The magnitude of the spectra is calculated to eliminate the need for phasing (section 2.4.3). A baseline correction was implemented by calculation of an average of the absolute signal from 8-12ppm of each spectrum and subtracting. The Creatine and NAA

peaks were integrated over the ranges 2.83-2.93ppm and 1.8-2.0ppm respectively for each voxel along a user chosen profile.

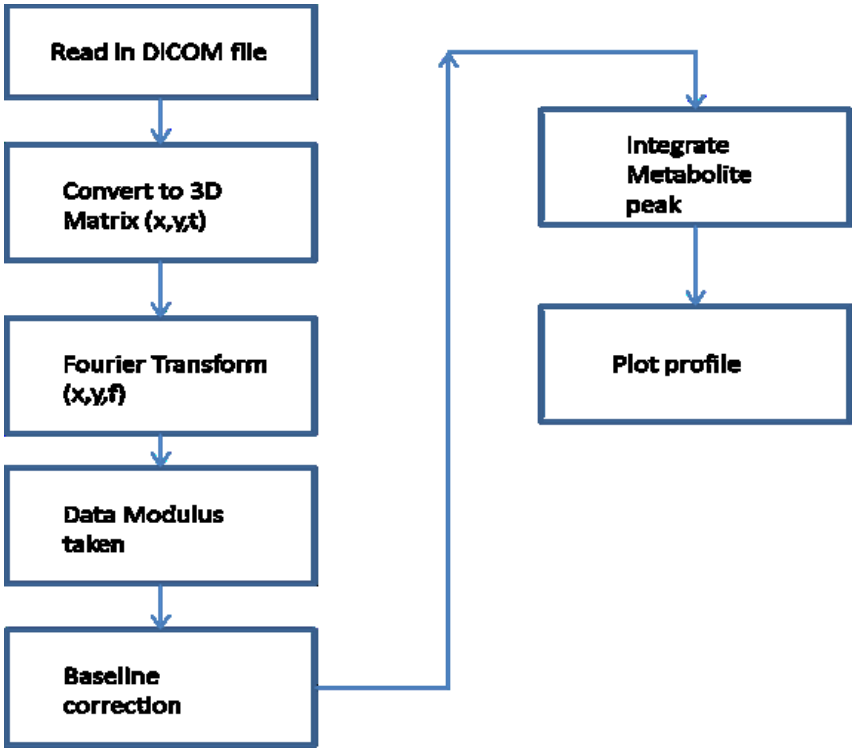

Figure 4-12 Flow diagram of Matlab program to produce profile plot

Metabolite signals were normalised to the unsuppressed water MRSI data to account for B1 field inhomogeneity. The plots are normalised to the signal maximum.

Line broadening (5Hz) was added (section 2.4.4) to aid quantification by improving the SNR. The real peaks were then integrated to produce the profile seen in Figure 4-15 c).

4.5.4 Method – metabolite uniformity analysis

To assess uniformity of metabolite concentration of the gels an experiment using single voxels placed around the phantom was carried out. Single voxel PRESS measurements were acquired according to Table 1. Water suppression was set to excitation and then also to CHESS for comparison. NSA=32. Another MRS acquisition was also acquired with

unsuppressed water to be utilised in absolute concentration calculation. Measurements were taken at locations indicated on Figure 4-13. The concentration of metabolite within the single voxel was calculated using TARQUIN software. The calculation employed a value of 35880mM which is the water concentration of white matter, and a value of 0.7, the approximate ratio of exponential decay factors for average metabolite and white matter water T2, for short echo MRSI(Wilson 2011) .

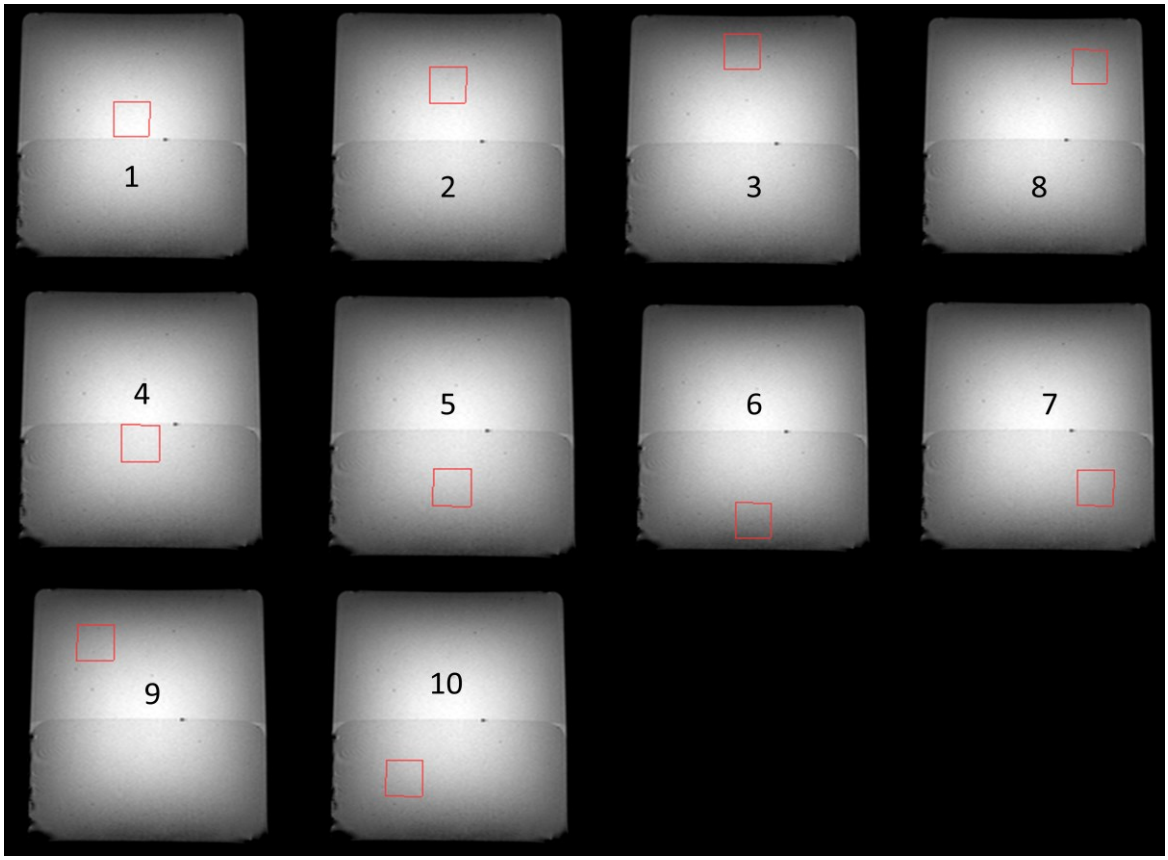

Figure 4-13 Single voxel locations indicating the concentration measurement locations within the two-compartment edge response phantom. The top half of the phantom is Creatine and the bottom half NAA.

4.5.5 Results and discussion

The results of the single voxel concentration measurements can be seen in Table 2.

Single Voxel Position as shown in Figure 4.13	Metabolite Concentration (mM) (CHESS)	Metabolite Concentration (mM) (Excitation)
1 (Cr)	9.9 ± 0.1	10.4 ± 0.1
2 (Cr)	res. Water	8.2 ± 0.1
3 (Cr)	9.7 ± 0.1	11.7 ± 0.1
8 (Cr)	6.2 ± 0.1	11.9 ± 0.1
9 (Cr)	8.8 ± 0.1	res. Water
4 (NAA)	11.0 ± 0.1	11.3 ± 0.1
5 (NAA)	10.7 ± 0.1	10.3 ± 0.08
6 (NAA)	10.1 ± 0.1	10.2 ± 0.1
7 (NAA)	10.4 ± 0.3	11.7 ± 0.7
10 (NAA)	11.2 ± 0.3	10.6 ± 0.2
Mean	10.2	10.7
Standard Dev.	0.8	1.1

Table 2 Concentration measurements from MRS of two-compartment gel phantom (10mM for each metabolite). The standard deviations as indicated in the brackets are estimates of the fitting error produced by TARQUIN.

Table 2 shows the concentrations calculated using the TARQUIN software. The table shows values for acquisitions using both the excitation, and CHESS water suppression methods. The fitting of the Creatine was slightly impaired by the presence of residual water at positions 2 and 8 for the CHESS method, and at 9 for the Excitation method.

The concentration of Creatine in voxel 4 was noted as being 0mM. This indicated that no diffusion of Creatine had occurred into the NAA-half of the phantom at this time. The single voxel spectroscopy at the location of voxel 1 was additionally acquired with a correction for chemical shift displacement for Creatine. This was achieved in order to prevent the voxel being shifted into the NAA area and exciting it. The concentration of NAA in this voxel was also 0mM indicating no diffusion of NAA had occurred into the Creatine-half of the phantom

at this time. The MRSI spectra as displayed using the scanner software of the two-compartment gel edge phantom can be seen Figure 4-14.

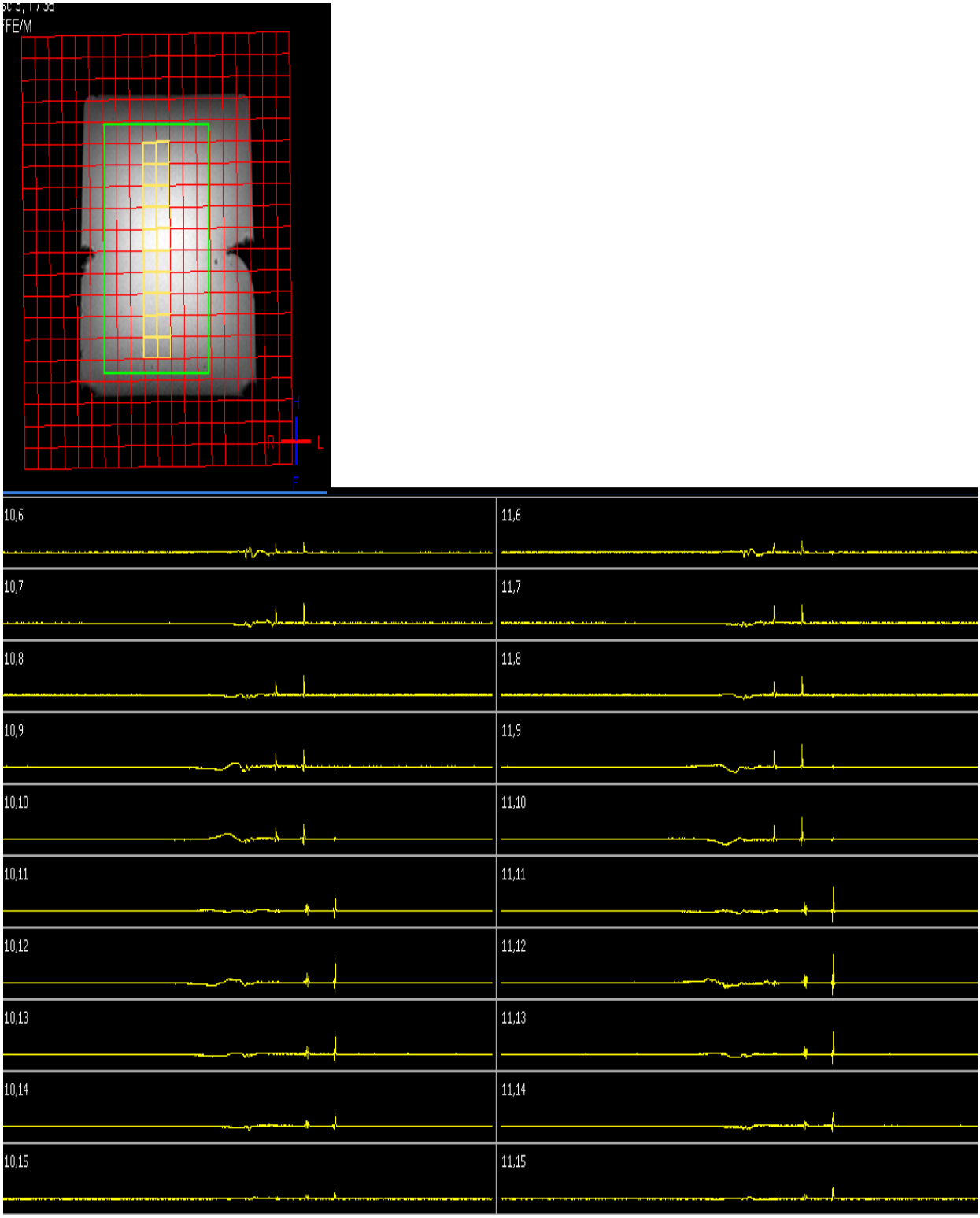

Figure 4-14 The MRSI of the two-compartment gel edge phantom. The Spectra as depicted on the scanner for the voxels shown in yellow. All graphs are plotted on the same scale.

On examination of the spectra in this figure the MRSI acquisition of the edge phantom indicates that there is a substantial aspartate peak which is close to the main Creatine peak. This renders quantification of the Creatine peak problematic using the integration method. The profile of the 10x10x10mm voxel size can be seen Figure 4-15 a), b) and c). The dip towards the far edge of the NAA region Figure 4-15 a) is due to B1 drop off towards the front of the head coil. Therefore the data were normalized to the unsuppressed water peak Figure 4-15 b). The addition of line broadening of the spectra (5Hz) was used to improve the quantification of the real data by reducing the noise(section 2.4.4), Figure 4-15 c).

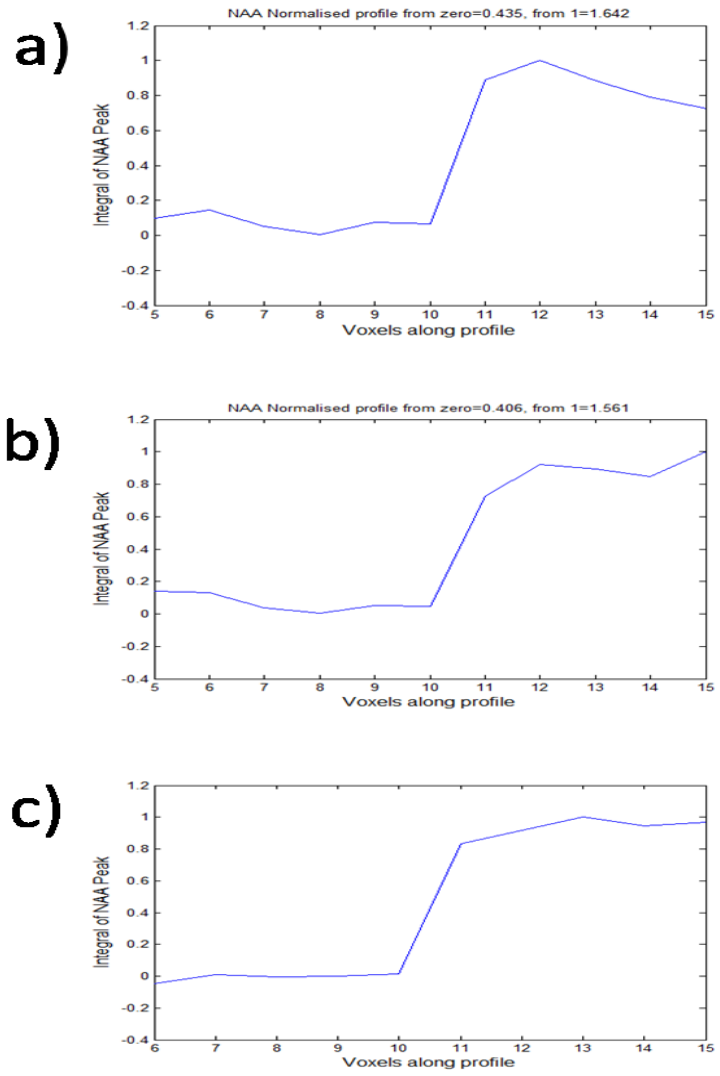

Figure 4-15 The NAA profile across the metabolite edge phantom a) with normalisation to the unsuppressed water b) and with the addition of line broadening c).

4.6 Conclusions

The metabolite concentrations in Table 2 suggest that the two-compartment phantom is uniform within 10% using either water suppression method. The uniformity of the edge profile was improved along the centre of the phantom by normalising the data to the unsuppressed water data and by the application of line broadening to the post processing. There also appears to be no penetration of the barrier between the two metabolites at the time of acquisition. It was decided to integrate the NAA peak only in analysis to avoid any residual water affecting the baseline near the Creatine peak, and any overlap with the NAA aspartate peak. It was therefore concluded that this phantom could be utilised in the investigation of the effect of CS-MRSI on the spatial integrity of MRSI.

5 Investigation of spatial resolution in CS-MRSI with increasing acceleration factor

This chapter investigates the possible negative effects on the spatial resolution of MRSI introduced by CS-MRSI, as the acceleration factor is increased. The two-compartment gel edge imaging phantom from (section 4.5) was utilised. The rationale for using this phantom was explained in section 4.1. The metabolite edge created by the two-compartment phantom allowed for the assessment of inter-voxel contamination across it (section 2.3.1). The datasets acquired from section (4.5.2) were utilised. The gradient of the profile of metabolite concentrations in each voxel across the metabolite edge provided a method of quantification of spatial resolution relative to that of the Fully Sampled Standard reconstruction (FSSR) MRSI dataset at each acceleration factor.

To provide a method of assessment of spatial resolution in a realistic clinical scenario an in-vivo acquisition was also undertaken.

5.1 Application of CS-MRSI to two-compartment gel phantom

5.1.1 Method

The MRSI dataset acquired (section 4.5.2) was retrospectively under-sampled and reconstructed. The datasets were under-sampled using acceleration factors of x2, x2.5 x3.3 x5 and x10. A set of 5 k-space masks (section 3.2) were generated for each individual acceleration factor. The same masks were utilised on the in-vivo and the phantom datasets for each acceleration factor. Each set of 5 masks had the same value of acceleration factor, sampling density, and the central fully sampled area with random sampling to allow assessment of inherent variability of the technique. The Software for CS reconstruction was developed in house using MATLAB (Version 2012b) (section 3).

In this study, the variable shutter technique (section 2.2.2.1) was also applied to retrospective datasets by using zero padding at the edges of k-space to vary the uniformly circularly, sampled centre. For the purposes of this research this was termed the low resolution reconstruction (LRR).

For each MRSI reconstruction, a profile along the centre of the phantom perpendicular to the metabolite edge boundary was defined Figure 5-1 a). This central profile was used since the results of the uniformity measurement (section 4.5.4) indicated that this was where the phantom was most uniform. The normalized NAA intensity for each voxel was calculated and plotted Figure 5-1 (c-g). The maximum gradient of each plot of the profile perpendicular to the NAA metabolite edge was calculated. The mean and standard deviation of each gradient from five separate masks each of the same acceleration factor were calculated and plotted Figure 5-1 b). For all CS-MRSI reconstructed datasets the calculated gradients were plotted on the same graph as those calculated for the fully sampled standard reconstruction (FSSR), against acceleration factor. In order to assess the success of CS in maintaining spatial resolution, each CS-MRSI reconstruction and the resulting gradient of the edge was also plotted for the (LRR) against acceleration factor. The theoretical value for the spatial resolution for the LRR was also calculated as an additional means to assess the validity of the technique, blue triangles on Figure 5-1 b). This was based upon the expected relative resolution for a given LRR radius in k-space. For example at an LRR equivalent to x5 acceleration factor, the resultant radius of the circle it defines in k-space is half the length of the radius of that for an acceleration factor of x1. Therefore half the spatial resolution is expected and plotted against a factor of x5.

5.1.2 Results and discussion

Figure 5-1 b) is a plot of the maximum gradient perpendicular to the metabolite edge against acceleration factor.

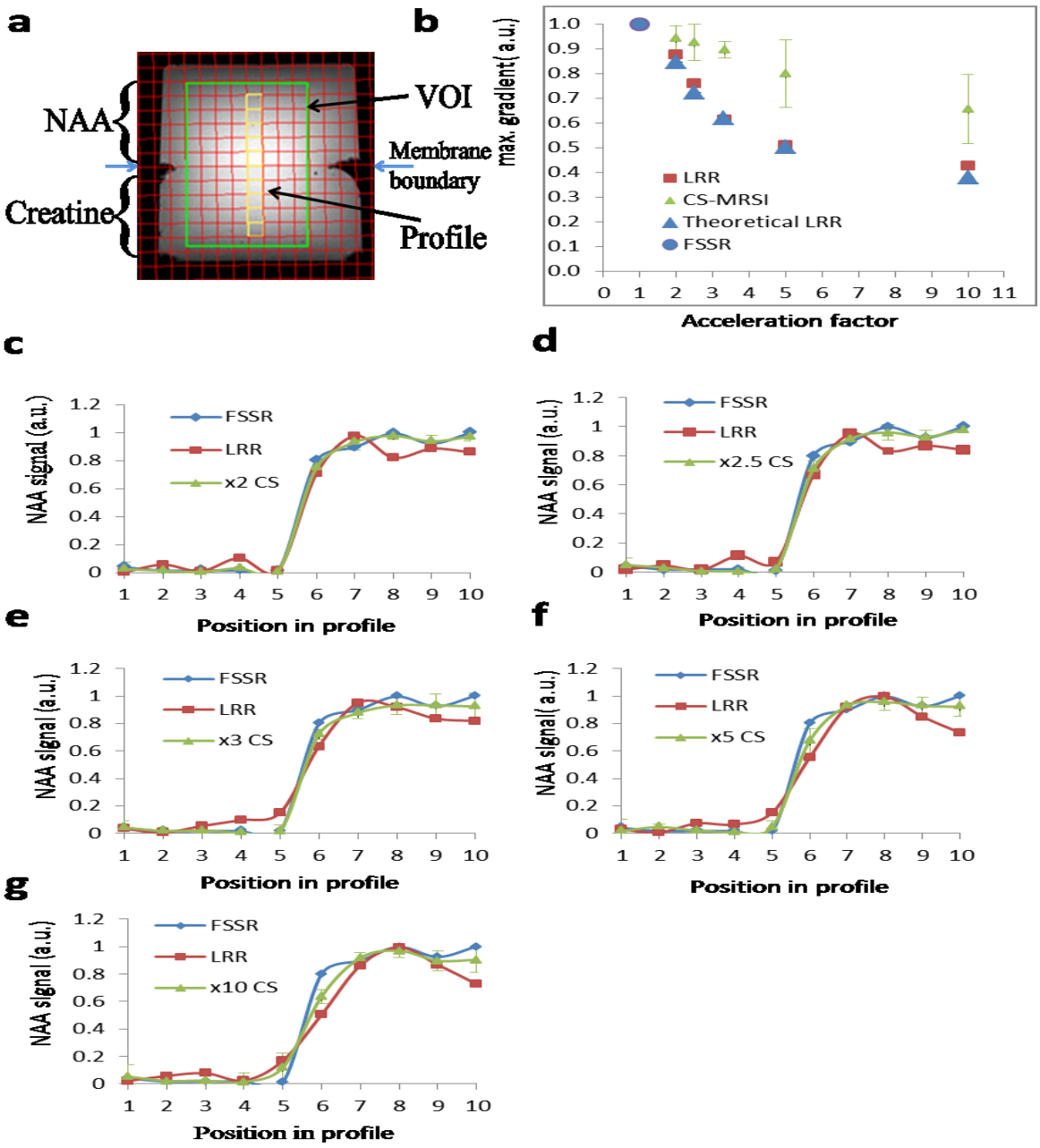

Figure 5-1- a) The MRSI planning of the phantom (yellow line indicates the profile from which data was analysed) b) The average maximum gradient of each CS reconstruction of the phantom at each acceleration factor, for the LRR time equivalent (red) and the CS-MRSI (green) reconstructed datasets. The FSSR is shown as a blue circle. The theoretically calculated LRR is shown as blue triangles, c)-g) The Plots of the profile perpendicular to the metabolite boundary edge for NAA at each acceleration factor. Each plot shows the profile for the fully sampled dataset (blue), the CS-MRSI reconstruction (green) and it's LRR, time equivalent, uniformly sampled reconstruction (red). (The lines joining the plotted points are for display purposes only).

Figure 5-1 b) shows that the resolution is halved at an acceleration of x5 for both the LRR reconstructions and the theoretical equivalent (blue triangles). This is because the sampled k-space for LRR at this acceleration factor is equivalent to a circle with a radius of length 50% of the fully sampled k-space maximum. The theoretical values on this figure are in general good agreement with the measured LRR indicating the reliability of this phantom methodology as an implied in-direct measure of resolution. There is variation between the LRR and the theoretical value of a maximum of 5% at an acceleration of x10. The variation may be due to the assumption that the theoretical k-space sampling area of the LRR is a perfect circle.

The measurement of the gradient perpendicular to the metabolite boundary is an indicator of the relative spatial resolution of the imaging system (section 4.1) and is directly related to the adjacent inter-voxel contamination (2.3.1). It can also be seen in Figure 5-1 b) that relative spatial resolution degrades with increasing acceleration factor for all reconstructions. The figure indicates that the rate of degradation is much lower in the CS-MRSI than the LRR and that the CS-MRSI spatial resolution is consistently higher than the equivalent LRR. The spatial resolution from the CS-MRSI appears to remain constant up to an acceleration of x3.3 then drops off at x5 and x10 with much larger standard deviation. The results appear to indicate that in this phantom scenario utilising the identity transform with the chosen CS weighting factors (section 3.4) that CS-MRSI reliably maintains the spatial resolution to 87% (± 3%) of the resolution of the FSSR with approximately 70% time saving (x3.3 acceleration). The figure implies that there may be potential to further reduce scan time by a factor of x5 and even x10, which maintain spatial resolution to 78%(± 14%) and 64%(± 14%) of FSSR respectively but these factors exhibit with much higher variation. This is compared with a relative resolution measurement of 50% and 41% with LRR for the equivalent scan time reductions. This can be attributed to the fact that the CS-MRSI samples

and estimates more of the higher spatial frequency data points which are then utilised in the CS reconstruction, whereas LRR are effectively low pass filters. These results are consistent with previous work showing that CS-MRSI does not produce a significant loss in in-vivo metabolite information (RMSE<0.05) for acceleration factors up to x5 (Furuyama 2012; Geethanath 2012).

Figure 5-1 (c-g) shows each individual plot of the profile perpendicular to the metabolite boundary for the both reconstructions along with that of the FSSR and the LRR. The figure indicates that up to an acceleration factor of x5, the CS-MRSI profiles show a very similar edge response to the FSSR as indicated on Figure 5-1 b). Gibbs ringing at an interface is a common problem in MRSI (section 2.3.1), causing inter-voxel contamination at a distance. Figure 5-1 (c-g) shows a reduction in Gibbs ringing for the CS-MRSI reconstructions perpendicular to the phantom's metabolite interface when compared to LRR. The effect of the variable density, random under sampling pattern utilised in the CS-MRSI (section 3.2) may aid in the reduction of the ringing artefact due to the incoherence in the resultant under sampling artefacts(Lustig, Donoho et al. 2008).

A brain tumour may be focal in which it has a well-defined border between the diseased and healthy tissue, or it may have an ill-defined border where it has infiltrated into the surrounding healthy area. It is very important to be able to distinguish between these two disease states. Therefore, minimising inter-voxel contamination from adjacent and distant voxels is paramount for correct tumour boundary definition. The phantom results from the measurement of the maximum gradient of the metabolite edge Figure 5-1 b) imply that CS-MRSI is able to retain the definition of the boundary edge possibly as well as 78%(± 14%) at an acceleration factor of x5. The results of Figure 5-1 c-g) also imply that the inter-voxel contamination at a distance is reduced by the implementation of CS-MRSI at all acceleration

factors. Therefore it would appear that increasing the acceleration factor with CS-MRSI in this scenario will more accurately aid in determining if a tumour has infiltrated into healthy tissue or not.

5.2 Application of CS-MRSI to in-vivo MRSI

An attempt to investigate the effect of CS-MRSI on the MRSI spatial resolution in a realistic scenario was undertaken. The healthy human brain exhibits low spatial variation in metabolite signal. Ventricular CSF is a possible area of high metabolite signal contrast; however the ventricles have a complex geometry with irregular boundaries. Coupled with the inherent low resolution of MRSI it makes the assessment of in-vivo MRSI spatial resolution complex. In order to achieve a metabolite spatial variation an artificially suppressed region was introduced during acquisition.

5.2.1 Method

The volunteer data was acquired according to Table 1 except for a TE of 144 ms. A 2D MRSI spin-echo acquisition with a voxel size 10mm x 10mm x10mm,FOV 200mm x 200mm, 20x20 matrix was also implemented. An axial slice through the centrum semiovale was scanned in the volunteer. In order to allow for a more accurate metabolite quantification and assignment, a longer TE was used in order to reduce any potential overlap of shorter T2 metabolite signals with the NAA peak.

A succession of outer-volume, fat saturation bands were applied around the edge of the scalp in order to reduce lipid contamination (section 2.2.5). In order to provide an area artificially subject to metabolite suppression, the MRSI data was acquired with the addition of two overlapping, 20mm wide, one water and one fat saturating bands applied sagitally through the centre of the two brain hemispheres as shown in Figure 5-2.

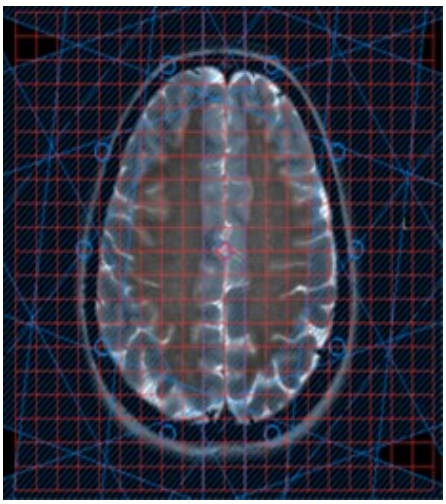

Figure 5-2 The MRSI planning for the volunteer acquisition. The application of the outer, circular lipid suppression bands can be seen in blue, and the central blue metabolite suppression band down the centre of the brain is also shown.

The elliptical k-space shutter on the Philips 3T scanner is routinely applied in the clinic and so was utilised during the acquisitions (section 2.2.2.1). Prior to reconstruction the datasets were subject to the removal of residual water via the HSVD algorithm(Pijnappela 1992).

The in-vivo MRSI dataset was under-sampled and reconstructed in the same way as the phantom dataset, utilising exactly the same k-space masks (section 5.1.1).

Each in-vivo reconstruction was processed in TARQUIN (section 2.4.6) to provide metabolite quantification. The quantification was achieved within a specified volume of interest (VOI) of 6x6 voxels chosen to be at least 1cm away from the outer volume lipid saturation bands in order to prevent any possible interference from them, indicated as the red box on Figure 5-3.

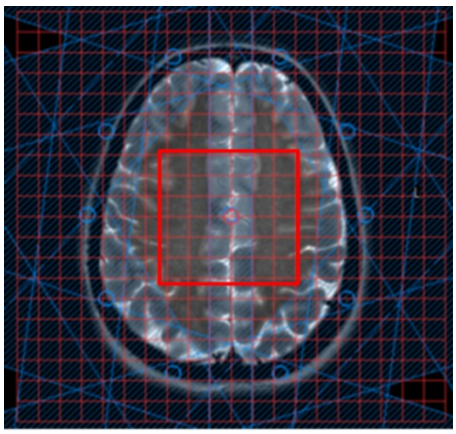

Figure 5-3 The VOI in red utilised for the contrast measurement. The blue are fat saturation bands to eliminate lipid bleed through.

A profile through the centre of the VOI from the high signal area through the suppressed region to the high signal area on the other side was plotted for NAA, Choline and Creatine against voxel location, shown in yellow on Figure 5-4 a). Each metabolite profile was normalised to the maximum value.

The mean contrast (mnC) from each of the five masks was calculated between the unsuppressed metabolite region (24 voxels), and the metabolite signal suppressed area (12 voxels) from the VOI on Figure 5-3, according to the equation:

$$mnC = (Sn-Ss)/(Sn+Ss) \qquad \textbf{Equation 5-1}$$

Where:

Sn=Quantified signal from unsuppressed brain area.

Ss=Quantified signal from metabolite suppressed brain area.

A normalised root mean square error (nRMSE) was calculated between the FSSR dataset and each reconstruction. The average for each of the five masks at each acceleration factor was calculated and compared to that calculated for the time equivalent, uniformly sampled LRR.

5.2.2 Results and Discussion

Figure 5-4 b) shows typical reconstructed NAA profiles from the area in yellow on Figure 5-4 a), through the metabolite suppressed region for the LRR reconstructions and the FSSR dataset.

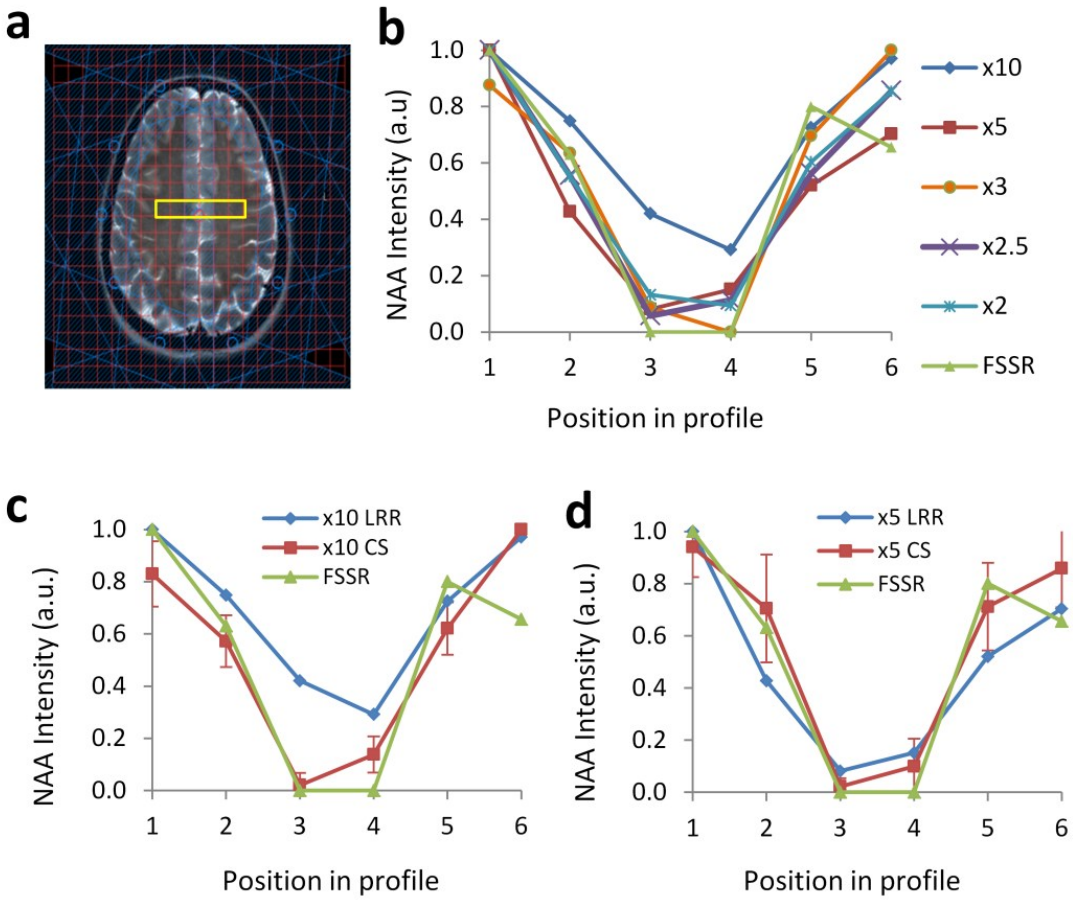

Figure 5-4 -Typical profiles for NAA perpendicular to the boundary between normal brain and the metabolite suppressed area. The profiles shown are taken from the yellow voxels depicted in a). The profiles from the reconstructions of the equivalent time, LRR, uniformly sampled data and the fully sampled dataset are depicted in b). The LRR, time equivalent, uniformly sampled (blue); the full dataset (green), and the CS-MRSI (red) reconstructed profiles for x5 and x10 acceleration factors are depicted in c) and d) respectively. (The lines joining the plotted points are for display purposes only).

Figure 5-4 c) and d) show a typical NAA profile for the CS-MRSI reconstruction of the yellow profile, along with its equivalent LRR reconstruction, and that of the FSSR for acceleration factors of x5 and x10 respectively. There was no significant difference in the profile plots for Choline and Creatine relative to NAA. Figure 5-4 b) indicates that the LRR reconstructions produce a reliable edge response relative to the FSSR up to an acceleration factor of x5, but that the CS reconstruction Figure 5-4 c) is closer than the LRR to the FSSR dataset even at an acceleration of x10, within error. This also indicates that there is less adjacent voxel contamination from the CS-MRSI than that from the LRR at x10 acceleration factor only. This appears to be a different result to that found with the phantom Figure 5-1. It can also be seen that the value of the FSSR at profile position 6 is 60% less than at position 1. This could be due to chemical shift displacement artifact (section 2.3.3).

Figure 5-5 a) is a plot of the mean contrast (mnC) at each acceleration factor after quantification with TARQUIN, between the areas of non-suppressed, healthy brain and the metabolite suppressed region, against acceleration factor for the CS-MRSI reconstruction and its uniformly sampled time equivalent LRR. The mean contrast should give an indication of the amount of inter-voxel contamination as a result of reconstruction. The figure indicates that the mean contrast is equivalent to the FSSR for both the LRR, time equivalent reconstructions, and the CS-MRSI, for acceleration factors up to x3.3 after which there is a significant degradation in mean contrast. The CS-MRSI contrast is significantly closer to that of the FSSR than that of the LRR at x5 and x10 acceleration factors.

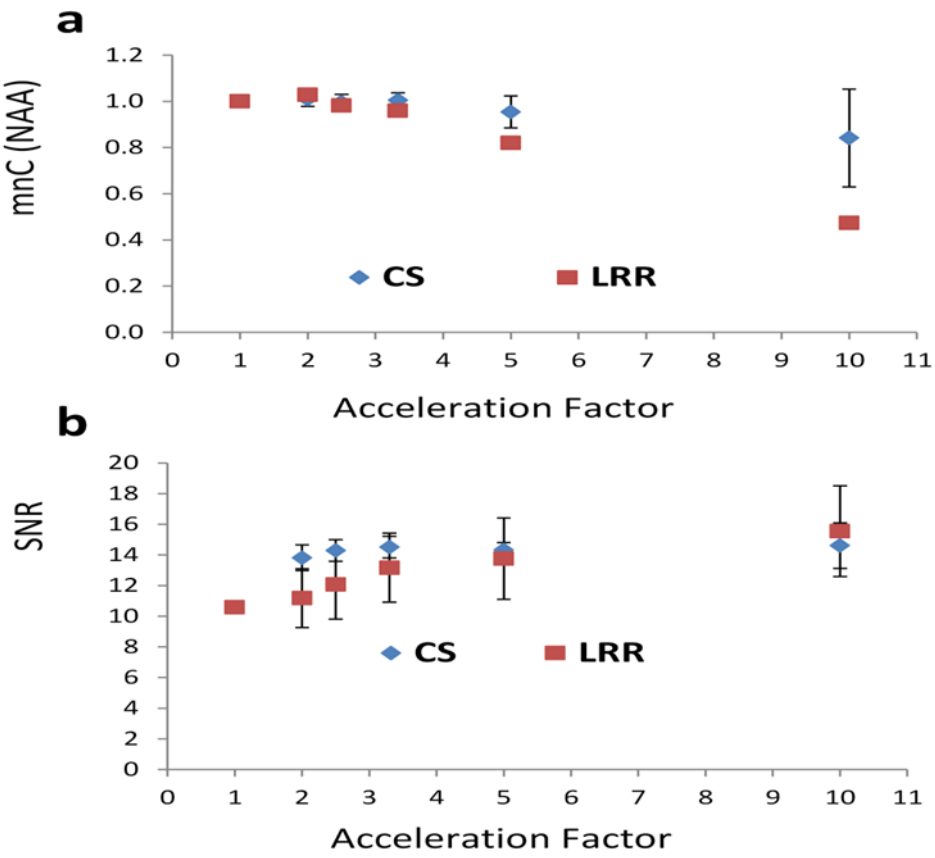

Figure 5-5 Mean, normalised contrast from within and outside the metabolite supressed area for NAA against acceleration factor a). The signal to noise ratio (SNR) from the unsuppressed area, against acceleration factor b). The graphs shows results for the LRR, (red) and those reconstructed using compressed sensing (blue).

The results from both figures imply that the in-vivo experiment is less sensitive to changes in spatial-resolution at low acceleration factors than the phantom experiment due to the imperfect profile of the suppression band and the resulting low spatial frequency variation produced by the suppression band. The discrepancy between the experiments may also be due to k-space filters applied to the raw data prior to reconstruction. The contrast is not much reduced for the LRR above x10 acceleration, Figure 5-4 b), making detection of improvements with CS-MRSI at low acceleration more difficult. This is reflected in the mean contrast results of Figure 5-5 a) which indicates contrast is equivalent for FSSR, LRR and the CS-MRSI, for acceleration factors up to x3.3. The contrast then reduces for both LRR and CS-

MRSI reconstructions at x5 acceleration. In this in-vivo scenario the saturated region was equivalent to two voxels in thickness (50% reduction in nominal spatial resolution). This has implication for the use of CS-MRSI when applied to a clinical scenario where the lesion of interest is large relative to the voxel size. In such cases, this study implies 95% of the contrast of the FSSR may be retained for a reduction in scan time of 80% when using CS-MRSI, Figure 5-5 a). The mean contrast results after reconstruction for Choline and Creatine indicated the same pattern as the NAA.

Figure 5-5 b) shows the maximum signal to noise ratio (SNR) from the unsuppressed region against acceleration factor. This is calculated by the TARQUIN software and defined as the ratio between the maximum in the spectrum minus baseline divided by 2xRMS of the spectral noise level. The SNR of the FSSR is indicated at acceleration factor of 1. The SNR in all cases is higher than that of the FSSR, and the SNR of the CS-MRSI is higher than that of the LRR up to x10 acceleration factor.

Figure 5-6 shows Bland Altman plots for each metabolite quantified via TARQUIN, at each acceleration factor, for LRR and CS-MRSI reconstructions. The plots clearly indicate two groups of points for each metabolite, one inside and one outside the metabolite suppressed region. The standard deviation in the difference indicated by the dotted blue line on the figure gives an indication of the inter-voxel contamination which is larger for the LRR compared to the CS-MRSI at all acceleration factors. At an acceleration of x10 the CS-MRSI has a mean around zero unlike that of the LRR which is below zero indicating bleed-through in agreement with the result of Figure 5-4 c).

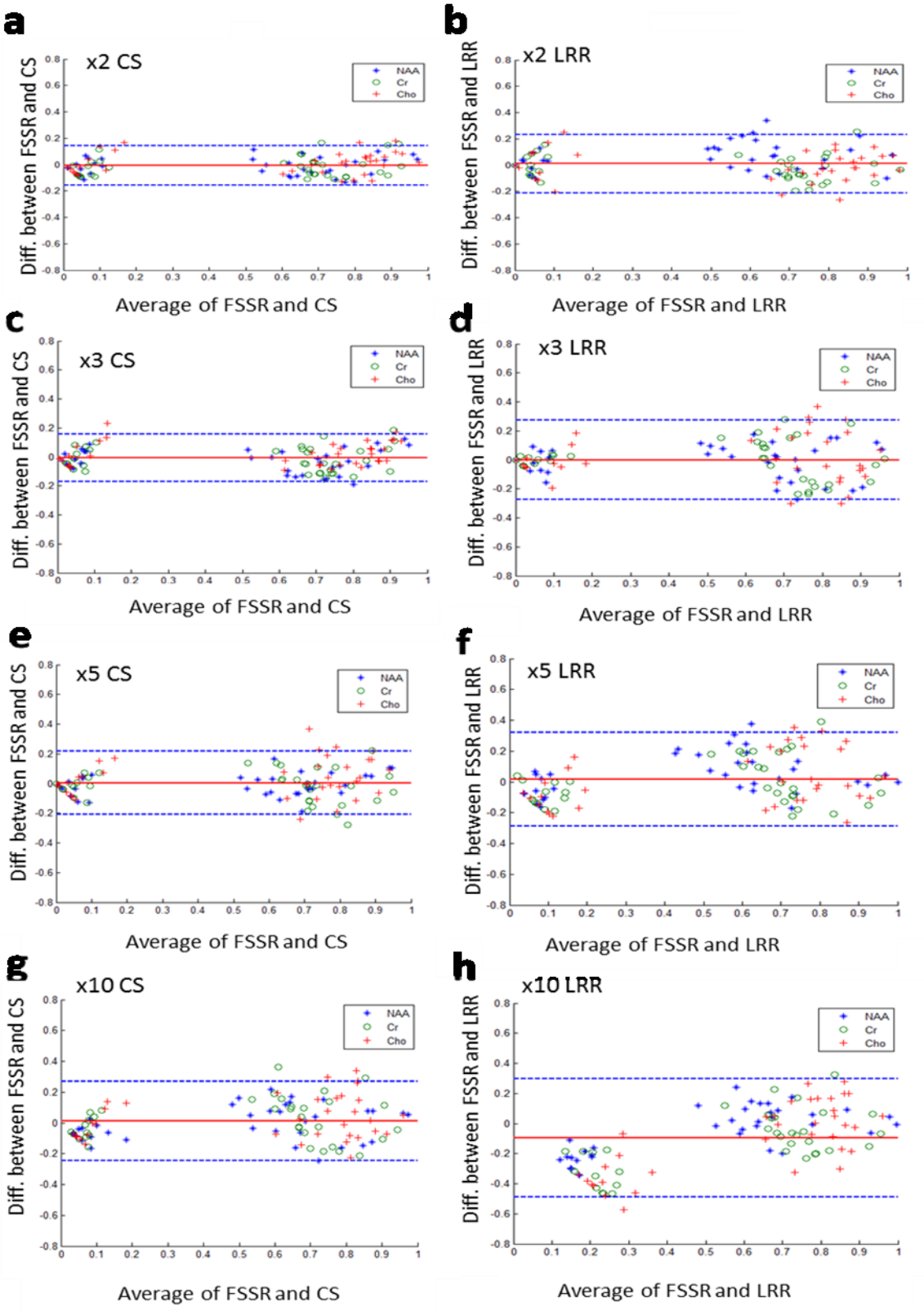

Figure 5-6 Bland Altman plots for voxels located within the area indicated in red are shown for the volunteer study which contained a central area of saturated metabolites. Plots for NAA, Creatine and Choline metabolites for comparison of the fully sampled dataset with the LRR time equivalent reconstructions, and the CS-MRSI reconstructions at x2, x3, x5 and x10 acceleration factors are depicted.

Figure 5-7 shows typical spectra from the region indicated in red on the figure. This demonstrates the large voxel bleed through from the LRR, x10 time equivalent reconstruction compared to that of the CS-MRSI reconstruction. The spectra appear smoother for both the CS-MRSI and the LRR with increasing acceleration factor, which may explain why the SNR is higher for both than that of the FSSR in Figure 5-5 b). The smoothing of the spectra with increasing acceleration factor was also noted by (Geethanath 2012) and potentially attributed to the contribution of the Total Variation (TV) term in the CS reconstruction. There appears to be some inter-voxel contamination at 2ppm within the saturated region for the FSSR Figure 5-7 b). This may possibly indicate that CS-MRSI has limitations in reproducing low signals as it is not present on the CS-MRSI spectra or more likely it could be inter-voxel contamination which is present in the non-filtered FSSR. There is however some baseline distortion at this location which could indicate that the TARQUIN software was producing a phase distortion.

Results indicate that in both scenarios reconstruction with CS-MRSI maintains a higher spatial resolution than that of the LRR as acceleration factor is increased. A recent study has explored the effect of CS-MRSI reconstruction on the Modulation Transfer Function (MTF) of retrospective phantom data(Heikal, Wachowicz et al. 2013). It compared the MTF after reconstruction with that of the FSSR, and with a time equivalent, LRR at an acceleration factor of x4. It determined that for x4 acceleration the CS-MRSI reconstruction was able to maintain greater spatial frequencies than the LRR at 0.1MTF, with an average loss in spatial resolution of 32.4% (1.25 lp/cm), compared to 48.6% (0.95 lp/cm) for LRR. In this study examination of the graph in Figure 5-1 b) shows a resolution loss due to CS reconstruction at an acceleration factor of x4 is near 20% and for LRR 45% which is comparable to the previous work. Although the Modulation Transfer Function (MTF) has not been explicitly calculated, a method to assess the voxel bleed through is of specific clinical relevance.

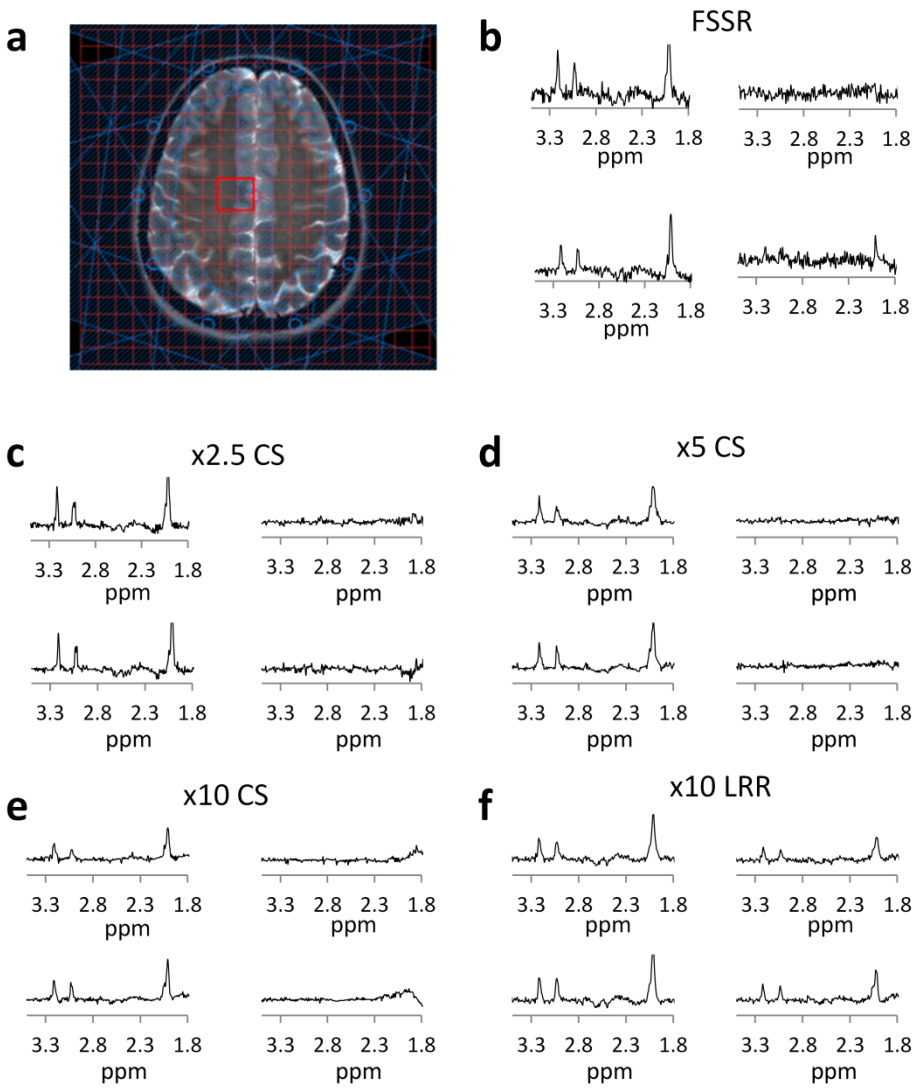

Figure 5-7 Spectra from each voxel from the region indicated in red a) for the FSSR b) , x2.5 c) , x5 d) and x10 e). The spectra for the time equivalent LRR reconstructions are also shown for a time equivalent factor of x10 f). All graphs plotted at the same scale (a.u).

5.3 Conclusion

This chapter demonstrates a practical methodology to assess MRSI spatial integrity after retrospective reconstruction of both phantom and in-vivo datasets. This allowed investigation into the limits of scan time reduction using CS. Spatial resolution in MRSI is linked to inter-voxel contamination (section 2.3.1). Reduction of inter-voxel contamination is of paramount importance in correctly distinguishing between focal tumours and those which have infiltrated into healthy tissue. The phantom provided a practical means to assess

adjacent voxel contamination by means of the maximum gradient of the perpendicular metabolite edge. The phantom also provided a means of assessment of distant inter-voxel contamination by assessment of the Gibbs ringing at the edge.

The two-compartment gel edge phantom indicates good agreement with the theoretical values Figure 5-1 b) implying that the phantom methodology for measuring the spatial resolution is valid and directly proportional to the Edge Spread function (ERF). It also shows that there is a reduction in spatial resolution with increasing acceleration factor as expected. This figure demonstrates that the spatial resolution of CS-MRSI is consistently above that of the LRR however, and is maintained at 87% (± 3%) of the resolution of the FSSR with approximately 70% time saving (x3.3 acceleration), Figure 5-1 b). This implies that inter-voxel contamination of the adjacent voxels is reduced in CS-MRSI. The results of Figure 5-1 c-g) indicate reduced ringing artefact from CS-MRSI as compared to the LRR. This implies less inter-voxel contamination from distant voxels.

The assessment of the in-vivo contrast provided a means of assessment of the inter-voxel contamination in a more realistic clinical scenario. The results indicated that the contrast remains consistent up to a factor of x3.3 but degrades with increasing acceleration factor after this; Figure 5-5 a). The in-vivo methodology appears to only be sensitive to losses in spatial resolution of more than 50%.

The signal to noise ratios indicated on Figure 5-5 b) show that the CS-MRSI maintains a consistent SNR above that of the FSSR at all acceleration factors, and an SNR higher than the LRR up to a factor of x10. The LRR has a higher SNR at x10 acceleration factor but Figure 5-7 f) indicates that there is more inter-voxel contamination into the unsaturated region at this factor. The consistency in the SNR for the CS-MRSI is a reflection of the smoothing property of compressed sensing (Lustig, Donoho et al. 2007; Geethanath 2012).

The Bland Altman plots for the in-vivo dataset Figure 5-6 show that the CS-MRSI has a consistently reduced standard deviation as compared to the equivalent LRR. Some of the plotted points for Choline are above the level of one standard deviation for CS-MRSI at acceleration factors of x5 and x10. This may have implication for the use of CS-MRSI for the investigation of metabolites with lower concentrations such as my-inositol. This reduction in perceived concentration may be as a result of the applied weighting of the TV transform which warrants further investigation.

The reduction in inter-voxel contamination (section 2.3.1) as a result of CS-MRSI for the in-vivo datasets as compared to LRR at x10 acceleration is visible on the typical spectra obtained from the region highlighted in red on Figure 5-7.

In this work, both phantom and in-vivo results indicate an increase in standard deviation for repeated reconstructions as acceleration is increased beyond x3.3. This is likely to be due to the very high under-sampling requirement at these acceleration factors and the resulting lack of true measured data (Barker and Ernst 2013). The maximum gradient measurements were also only based on two data points in the edge response profile. The performance and reliability of CS-MRSI at higher acceleration factors is therefore likely to be improved for higher spatial resolution datasets with larger matrix sizes.

6 Development of digital phantoms for simulating high-resolution CS-MRSI

The objective of this chapter was to provide a means to produce datasets which overcome the high sampling requirements at high acceleration factors (section 5.3), to provide a more realistic scenario, better statistics and to overcome the problems incurred during real-time MRSI acquisition. The measured ERF in the previous chapter only contained 2 data points, therefore increasing this will aid in the accuracy of the assessment.

The objective can most easily be achieved by creating software simulated, higher MRSI matrix size datasets (digital phantom). A typical MRSI scan takes between 5-10 minutes to acquire. Given that a patient will undergo several MRI scans during one appointment; this is prohibitive in terms of time and cost. Even with an adult volunteer there is still potential for movement artefacts in that time frame. The creation of software simulations of MRSI data can also be designed to provide datasets at a desired resolution, and permit controlled analysis of the effects of different reconstruction techniques in MRSI under very controlled conditions. Such conditions would include magnetic field strength, SNR, lipid contamination, and the addition of features in the MRSI dataset such as tumour spectra and anatomical features of particular shape and dimension. Software simulated MRSI data is not subject to the challenges often encountered during acquisition (section 2.3). An MRSI software simulation system was therefore developed in Matlab version 2012b.

6.1 Design and development of a digital brain metabolite phantom

6.1.1 Anatomical template

A 2D axial, T1-weighted, anatomical MRI image from a 1.5T scanner was utilised in the simulation phantom as a template for the anatomy. The image had a 256mmx208mm FOV,

with a pixel size of 1mm x 1mm and slice width of 5mm. A 1.5T image rather than 3T image was used since the greyscale levels are more consistent across the image at this field strength being less subject to field inhomogeneity. Initially a python script was written to remove the outer background of the image to crop the 2D image FOV to 200x160mm Figure 6-1.

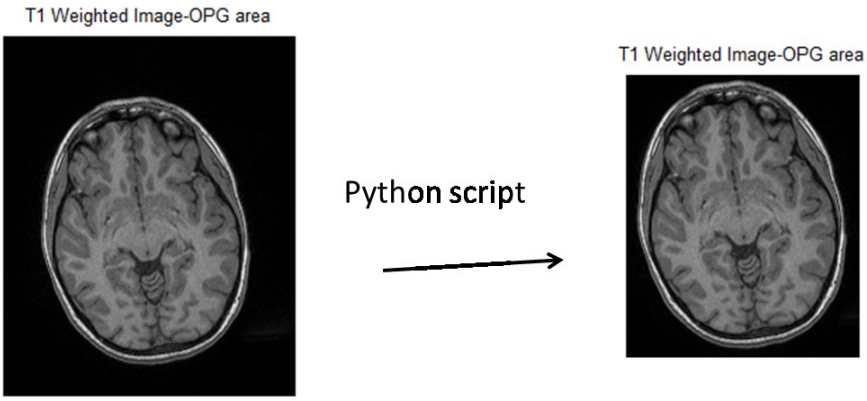

Figure 6-1 -Reduction in the Field of View of the anatomical 1.5T MRI image

The croppped MRI image was then read into the Matlab program where it was segmented by thresholding greyscale level to reveal the different anatomical structures of white matter, grey matter and Cerebral Spinal Fluid (CSF). These can be seen Figure 6-2. Other techniques such as the use of an Atlas can also be utilised to achieve this but the figure indicates that this method was adequate for this purpose.

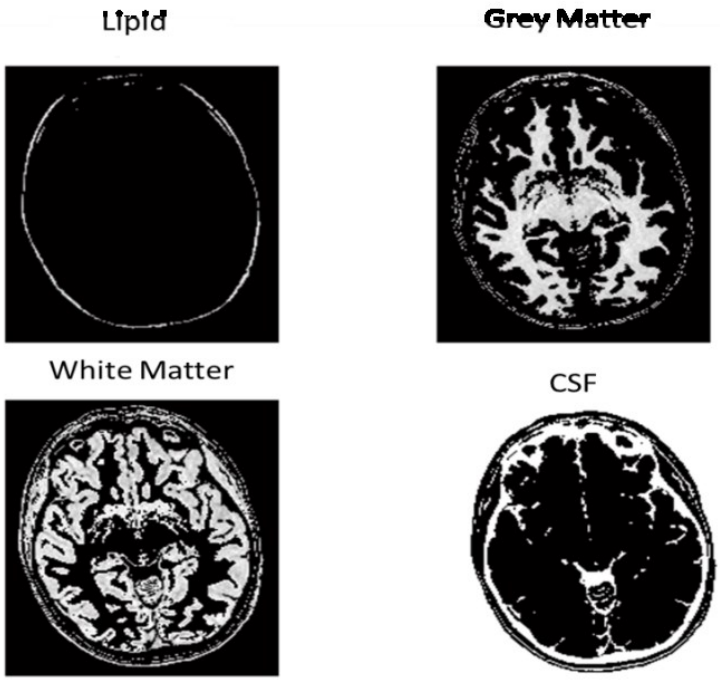

Figure 6-2 Images of the segmented anatomical MRI. The white pixels indicate the different anatomical structures within the brain of grey matter, white matter, lipid and CSF.

6.1.2 Spectral composition

The spectra used in the simulations were from the basis sets previously developed for TARQUIN (section 2.4.6). Basis sets are model spectra of the metabolites present in a healthy human brain based on work by (Govindaraju, Young et al. 2000; Wilson, Reynolds et al. 2011). A basis set consists of a series of complex numbers, each set represents a spectrum appropriate for a particular field strength and echo time(Wilson, Reynolds et al. 2011). The basis sets are utilised in TARQUIN for comparison with the NMR spectra obtained from each voxel in clinical MRSI. TARQUIN then automatically quantifies the metabolites detected within each of the voxels.

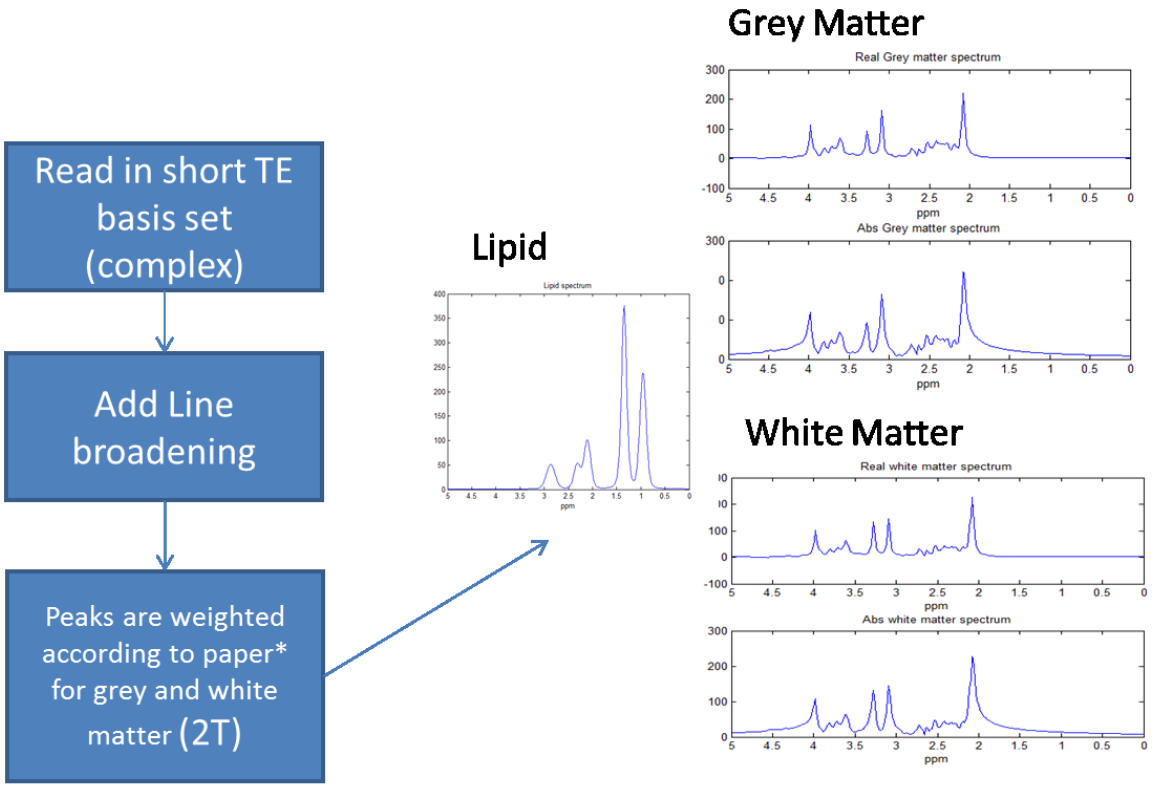

*Petra J. W. Pouwels, Tens Frahm, MRM 3953-60 (1998)'Regional Metabolite Concentrations in Human Brain as Determined by Quantitative Localized Proton MRS'

Figure 6-3 The outline of the process for the creation of the simulated MRSI data. Grey and white matter are assigned concentrations according with (Pouwels and Frahm 1998).

For the simulations, each metabolite peak from the appropriate TARQUIN basis set was weighted according to the expected concentration for its anatomical location. The assignment of the peak weightings for grey and white matter spectra were based upon the concentrations given in (Pouwels and Frahm 1998). CSF produces negligible metabolite NMR signal so was therefore assigned either zero or a user defined noise level. The process is outlined in Figure 6-3.

Line broadening was applied to each voxel's FID by multiplying it with a mixture of a time domain Lorentzian and Gaussian (Voigt profile) damping functions, Equation 6-1. The Lorentzian damping is required to account for small changes in the T2 value, shimming and in the chemical environment of the resonant molecules. The Gaussian term is included in

TARQUIN to provide modelling of imperfect shimming and susceptibility variations which lead to T2* effects (Wilson, Reynolds et al. 2011).The values of α and β in the equation are given by TARQUIN after quantification of MRSI data. The values utilised in the simulations were based on average values obtained after examination of existing 3T MRSI datasets. These were values of α=1.5 and β=500.

$$\mathbf{B(t) = b(t)e^{-\alpha t}.\, e^{(-\beta t^2)}} \qquad \textbf{Equation 6-1}$$

Where:

α= Lorentzian damping constant

β= Gaussian damping constant

b(t)= metabolite FID from basis set.

B(t) = metabolite FID subjected to line broadening

t= time

The pixel greyscale determines if it is white matter, grey matter, CSF or lipid. Each pixel from the cropped FOV image Figure 6-1 was assigned an appropriate NMR spectrum which is dependent upon the pixel's greyscale level. Random Gaussian noise was added to each spectrum. This was achieved using a Matlab function to produce random values drawn from the standard normal distribution, and then scaled to the desired SNR.

6.1.3 Digital brain metabolite phantom construction

The software simulation produces an MRSI dataset of (x,y,f) where x and y are the pixel or voxel location, and f is the frequency spectrum. After application of the MRSI spectral data to each pixel (section 6.1.2), at this stage, the dataset has a voxel size of 1mm x1mm x5mm. This is currently not a realistic spatial resolution for MRSI. The simulated MRSI dataset is

altered to a more realistic voxel size by applying a 3D Fourier transform of the dataset into k-space (section 2.2.2), and truncating the maximum 2D k-space (kx_{max}, ky_{max}) dimension down to the required maximum spatial frequency to produce the desired voxel dimension Figure 6-4. After inverse 3D Fourier transform back to real space, the reduction in maximum spatial frequency (kx_{max}, ky_{max}) produces a corresponding increase in voxel size. This has the effect of simulating the appropriate mix of grey and white matter spectra according to inter-voxel contamination (section 2.3.1) at this spatial resolution.

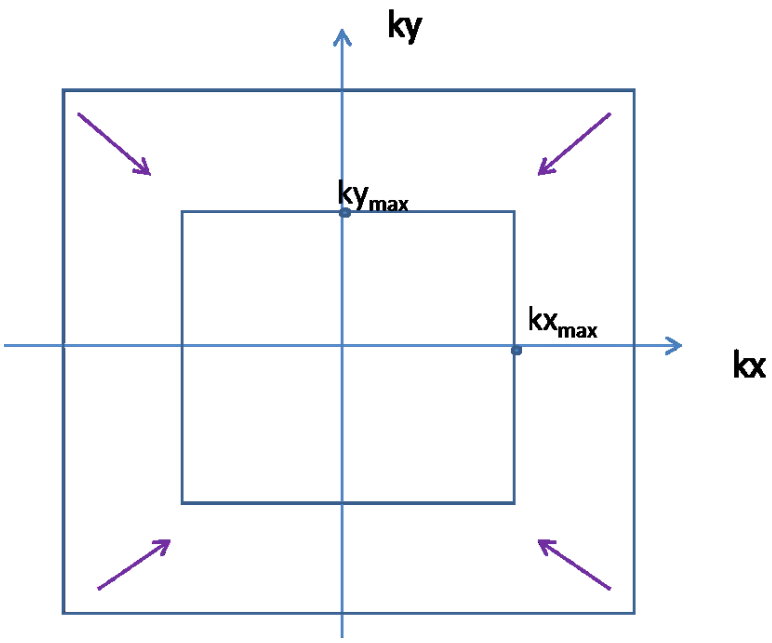

Figure 6-4 Diagram of how the voxel size is adjusted by reducing the k-space dimensions.

The effect of the reduction in voxel size can be seen in Figure 6-5. The images to the right of this figure are the absolute sum of the metabolite data in f, which shows the total effective NMR signal. This gives a representation of the effect of the change in voxel dimension. As expected the image becomes less resolved and the spectra on the left of this diagram are smoother. This is because part of the higher frequency data present at the edge of k-space

has been removed by the k-space reduction process, which effectively acts as a low pass filter.

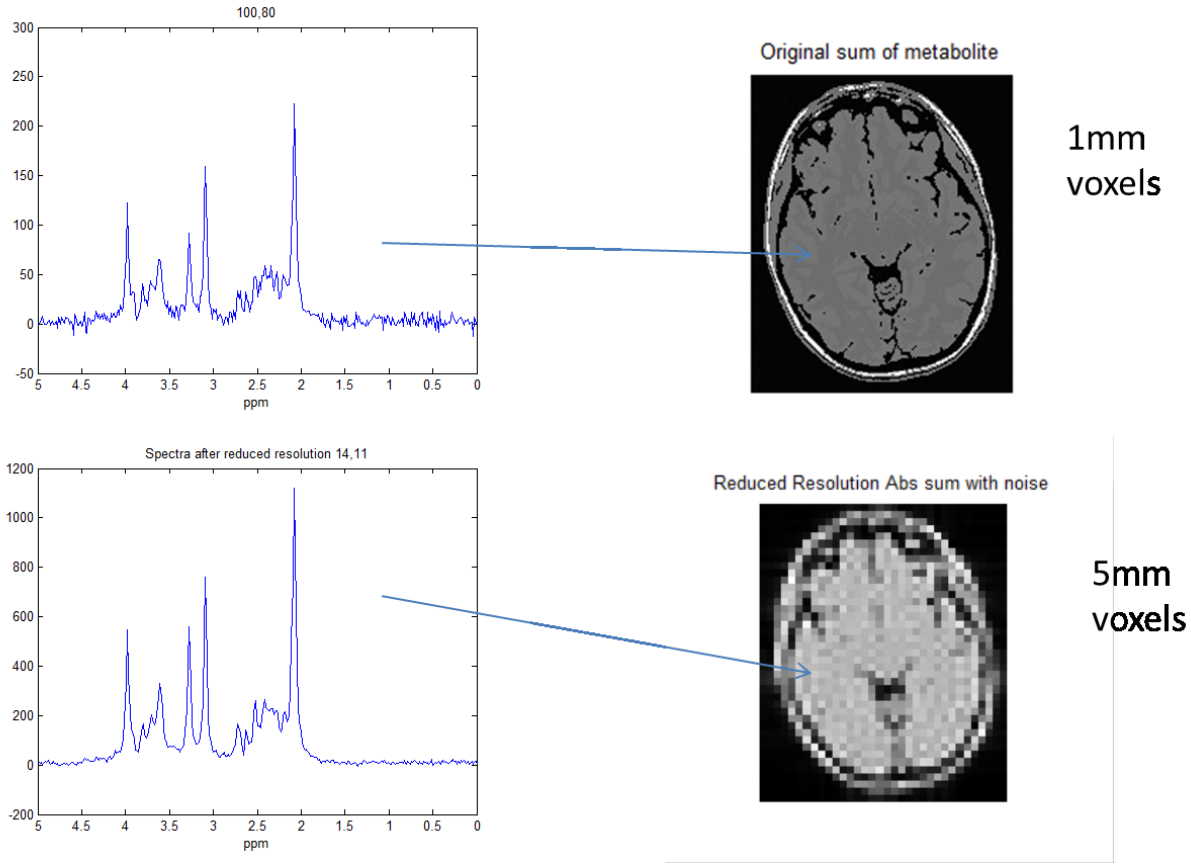

Figure 6-5 Diagram showing the effect of the increase in voxel size produced by the reduction of k-space dimensions. The spectra become less noisy and the image of the sum of the metabolite data becomes less resolved.

6.2 Validation of the digital phantom methodology

6.2.1 Method

In order to ensure that the simulation process produced as realistic an MRSI dataset as possible a simulation of the MRSI profile of the metabolite edge phantom (section 4.5) was created. This simulation could then be compared to that of the profile obtained from the phantom acquisition. Despite efforts to be realistically relevant, it is extremely difficult to manufacture a physical imaging phantom with the same spin environment as human brain

tissue. A physical phantom is subject to different temperature, pH, T2 and water and metabolite concentrations to that of healthy brain tissue. Since the physical phantom spectra are non-identical to healthy brain spectra the basis set NAA peaks for the brain were not implemented in the digital simulation of the two gel metabolite edge phantom. Instead an artificially derived NAA peak was created mathematically by approximating a Lorenzian FID and multiplying this by a Gaussian, as in Equation 6-1, to provide NAA frequency spectrum peaks that matched those of the phantom.

The FID was then subject to a 1D Fourier transform to produce an NMR peak in the frequency domain shown Figure 6-6 a). Random Gaussian noise was added to the spectrum using the technique described in section 6.1.2, at an equivalent SNR to the two-compartment gel edge phantom. The same profile across the metabolite edge in both the simulated and the two-compartment gel edge phantom was taken as shown in Figure 5-1 a). The simulated and original phantom peaks are displayed perpendicular to the edge profile in Figure 6-6.

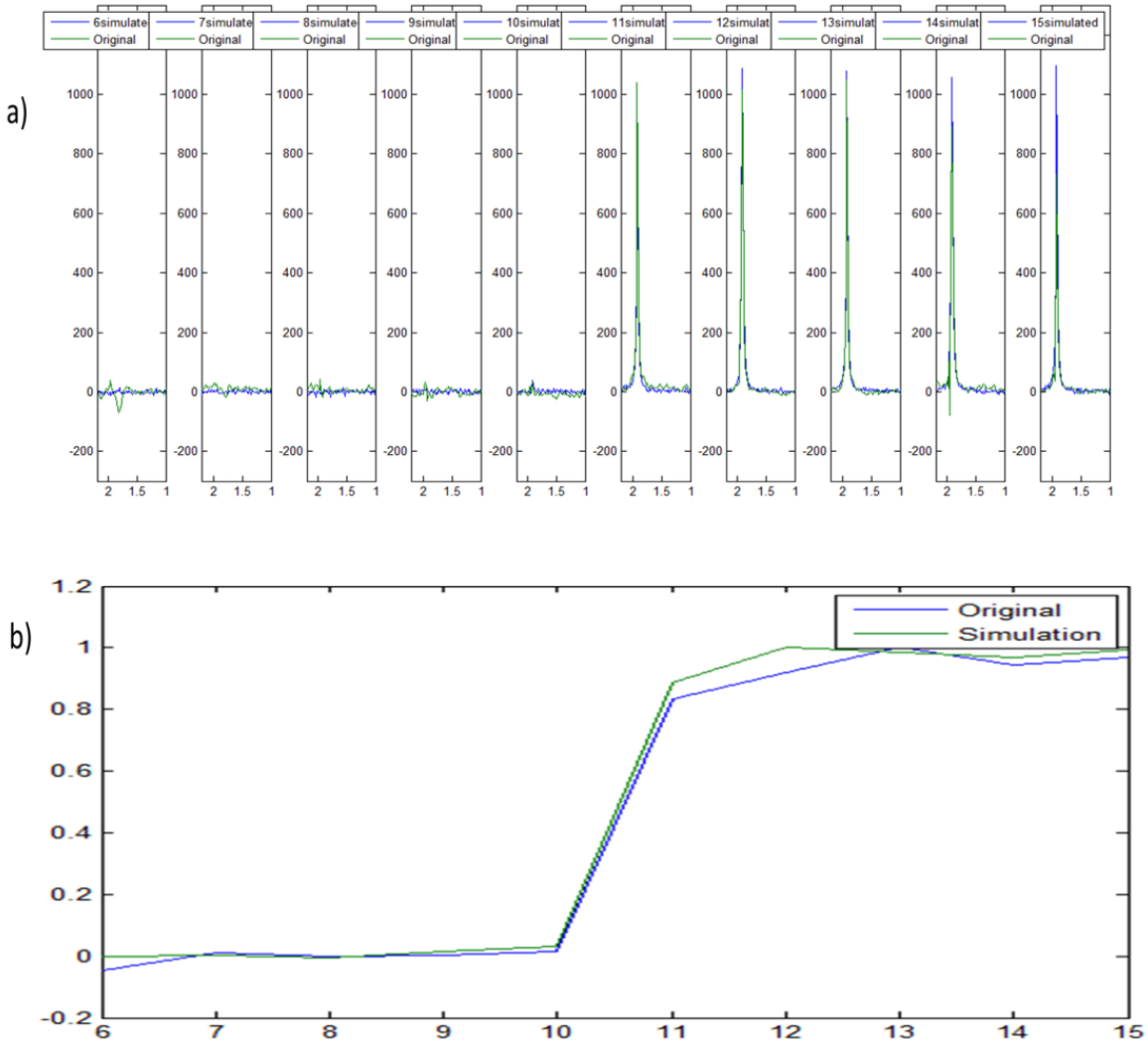

Figure 6-6 Diagram indicating the original edge phantom peaks and the simulated peaks a) perpendicular to the metabolite profile edge b)

The initial simulation consisted of a matrix size of 200x200 and a voxel size of 1mm x1mm x1mm. The acquired edge phantom voxel size was 10mm x10mm x10mm with a FOV of 200 x 200mm. Therefore, the original acquired matrix size of the phantom was 20x20. The simulated dataset was reduced to a 20x20 matrix size to match the phantom, and therefore a 10mm x10mm x10mm voxel size via the technique discussed in (section 6.1.3). This increased the voxel dimension and reduced the matrix size for the same FOV, Figure 6-7.

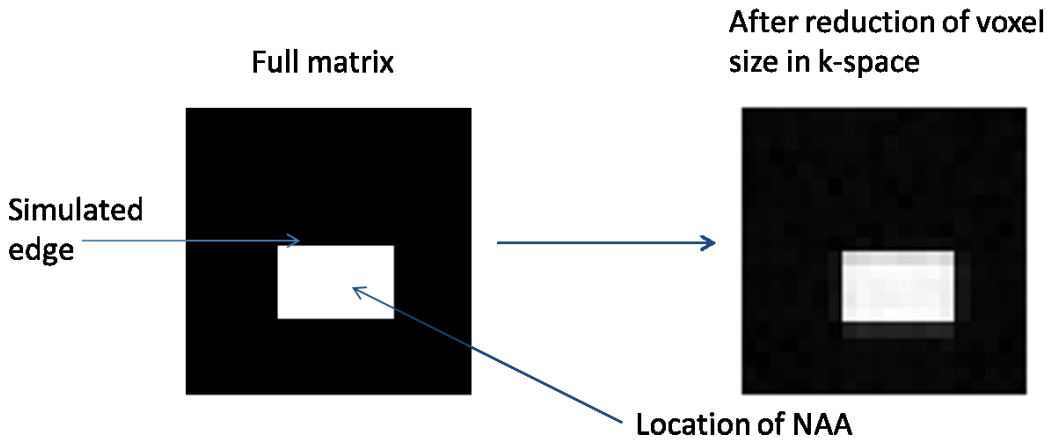

Figure 6-7 The full 200x200 matrix size simulation reduced down to a 20x20 matrix size, equivalent to the acquired edge phantom matrix size.

The edge phantom and simulated phantom data were subject to the same post processing as described in section 4.5.3. The simulated dataset did not contain an unsuppressed water peak so normalisation to this was not necessary.

6.2.2 Results and discussion

The resultant profiles of the integrated NAA peak perpendicular to the original edge phantom and the simulated edge can be seen in Figure 6-8. The profile perpendicular to the edge for both full datasets can be seen in Figure 6-8 a) and for an LRR reconstruction of 50% of the data samples in Figure 6-8 b). The nRMSE between the simulated and the original profile for the full dataset was 4%, and for the LRR reconstructed datasets was 3.87%.

The main difference between the two-gel edge phantom and the simulation was that the NAA spectra from the two-compartment gel edge phantom were created artificially in the digital phantom as discussed (section 6.2). The phantom is also subject to field inhomogeneity and potential baseline distortion from residual water. Despite these differences the resulting nRMSE above gives confidence in the methodology of the simulation technique.

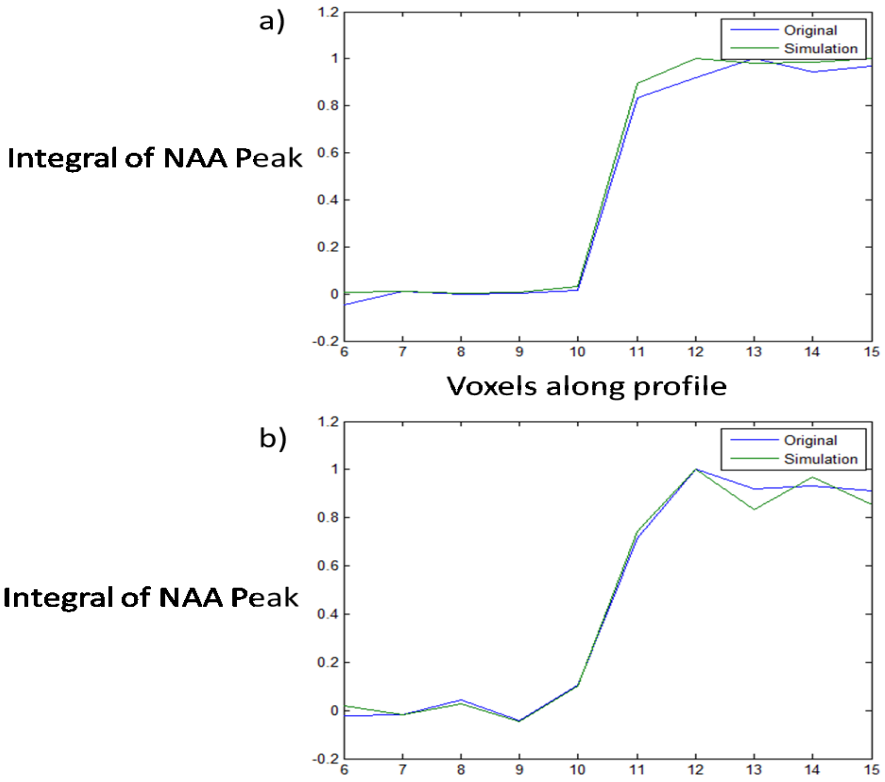

Figure 6-8 Profiles perpendicular to the original two-compartment metabolite edge phantom and the simulated edge phantom for the full data set a) and an LRR reconstruction of 50% of the data samples b).

6.3 Simulations for improved measurement of the edge response in CS-MRSI

In order to produce a quantitative measure of the effect of CS on the MRSI spatial resolution, the two-compartment metabolite edge phantom can be used (section 4.1.1.) to investigate the ERF. When using this phantom for the spatial resolution investigation it was found that the standard deviation of the mean at higher acceleration factors (x5 and x10) was increased relative to factors below these (section 5.3). The two-compartment metabolite phantom methodology only provided an edge gradient containing 2 data points which may confound this result. The measurement of a profile across an angled edge is a well-established technique which provides a more highly sampled ERF than that from a perpendicular profile (Judy 1976). The measurement of an angled edge on a real-time acquired phantom presents

practical challenges. The digital phantom simulation was therefore adapted to provide a metabolite angled edge. The digital phantom permits investigation of the effect of CS on the MRSI spatial resolution as acceleration factor is increased. The digital phantom contained 2D phase encoded MRSI simulated datasets containing high matrix size, and reduced voxel dimensions, without the need for lengthy real-time acquisition.

6.3.1 Method

An edge was defined as the line between those pixels containing 100% metabolite signal and those containing 20% metabolite signal. A line was drawn at an angle of 11^{o} Figure 6-9. The voxels to the left of the line contained 100% metabolite concentration and those to the right of the line 20% of the metabolite concentration.

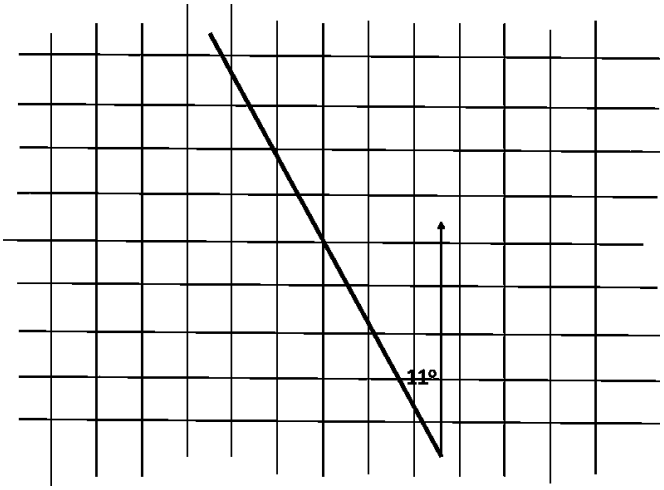

Figure 6-9 Schematic of the simulated edge

An angled edge was chosen because this effectively allows more data points to be measured along the edge response function. This is a technique widely used in medical physics applications to measure the resolution of a medical imaging device (Judy 1976). It can be seen in Figure 6-10 that pixels 1 and 2 have a relative distance dx from the angled edge. The distance dx is given by:

$$dx = p \sin 11^{o} \qquad \textbf{Equation 6-2}$$

Where:

p=pixel spacing

Figure 6-10 Diagram demonstrating the relative distance dx, of pixel 1 and pixel 2 from the angled edge.

The equivalent pixel thickness of the angled line is unknown. Therefore the edge's width was defined by calculating the proportion of the area of the pixel to the left of the dashed line Figure 6-11. This area is therefore directly related to the percentage of metabolite concentration to assign to that pixel. The area was calculated as follows. The pixels cut by the line were divided into rectangles and/or triangles as can be seen on the figure. Each

shape's area was calculated and compared to the area of a full pixel to determine the proportion of area to the left of the line. A Matlab program was written to calculate this.

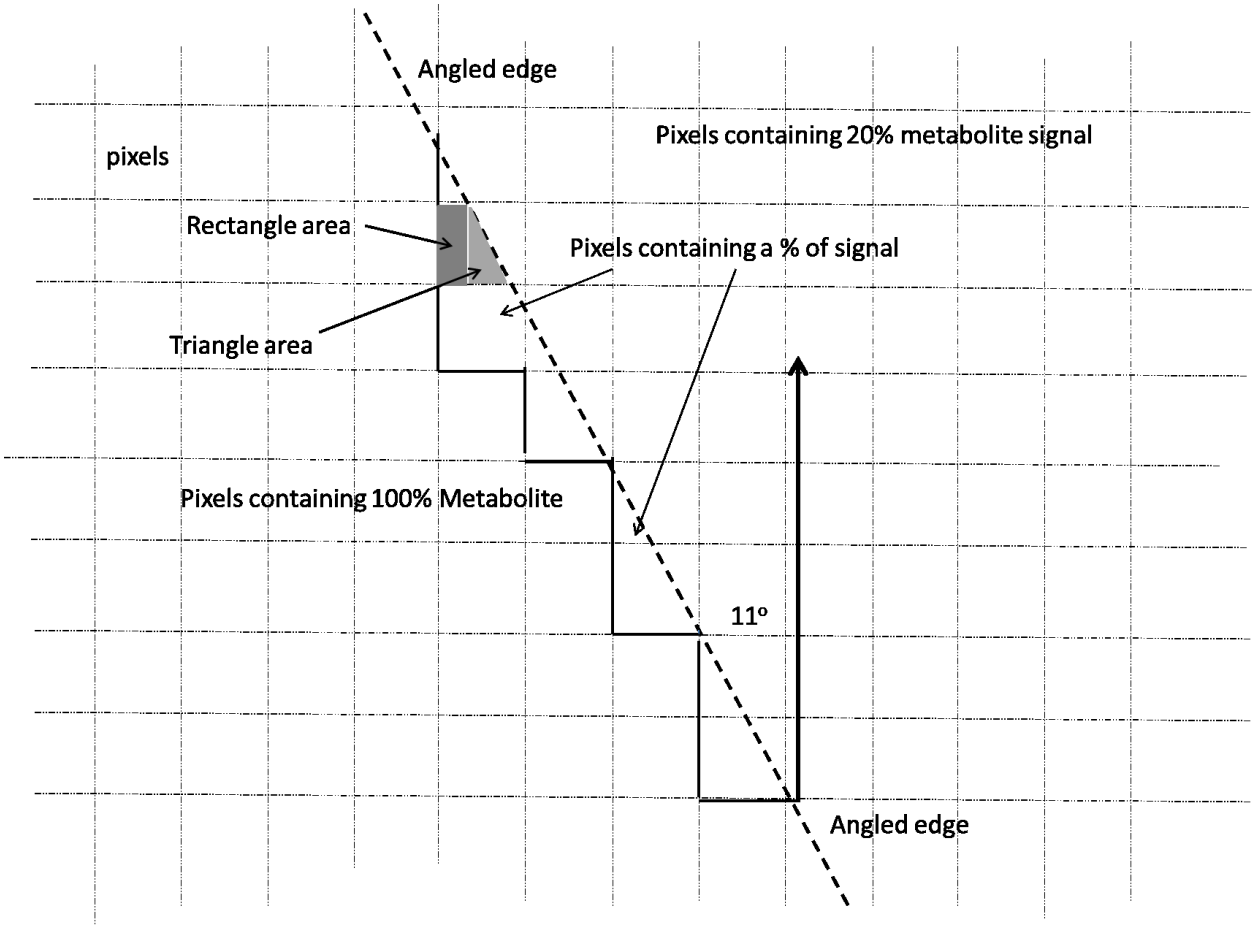

Figure 6-11-Diagram illustrating how the pixel edge thickness was defined. The pixels cut by the line were divided into rectangles and triangles, the area of such pixels then calculated, and the proportion used to calculate the percentage of metabolite contained to the left of the line.

A spectrum from the TARQUIN basis set was assigned to each pixel. At this stage the pixel or voxel size is 1mm x 1mm and depth of 5mm. The basis set was appropriate to the chosen field strength. The complete pixels to the left of the line Figure 6-11 were assigned 100% of the signal and those to the right were assigned 20%. The lower concentration value was utilised in order to be able to investigate negative concentration levels created by Gibbs ringing at the edge (section 2.3.1). The other 0^{o} edges and the remaining 90^{o} edge of the phantom were graduated so that there was a gradual fall-off in metabolite signal from 100-

20% in steps of 20%. The reason for this was to prevent any potential aliasing artefact from a high contrast area. The phantom voxel or pixel size was then increased to 5mm x 5mm x5mm using the method described in (section 6.1.3). The simulated edge phantom at this voxel size is depicted in Figure 6-12.

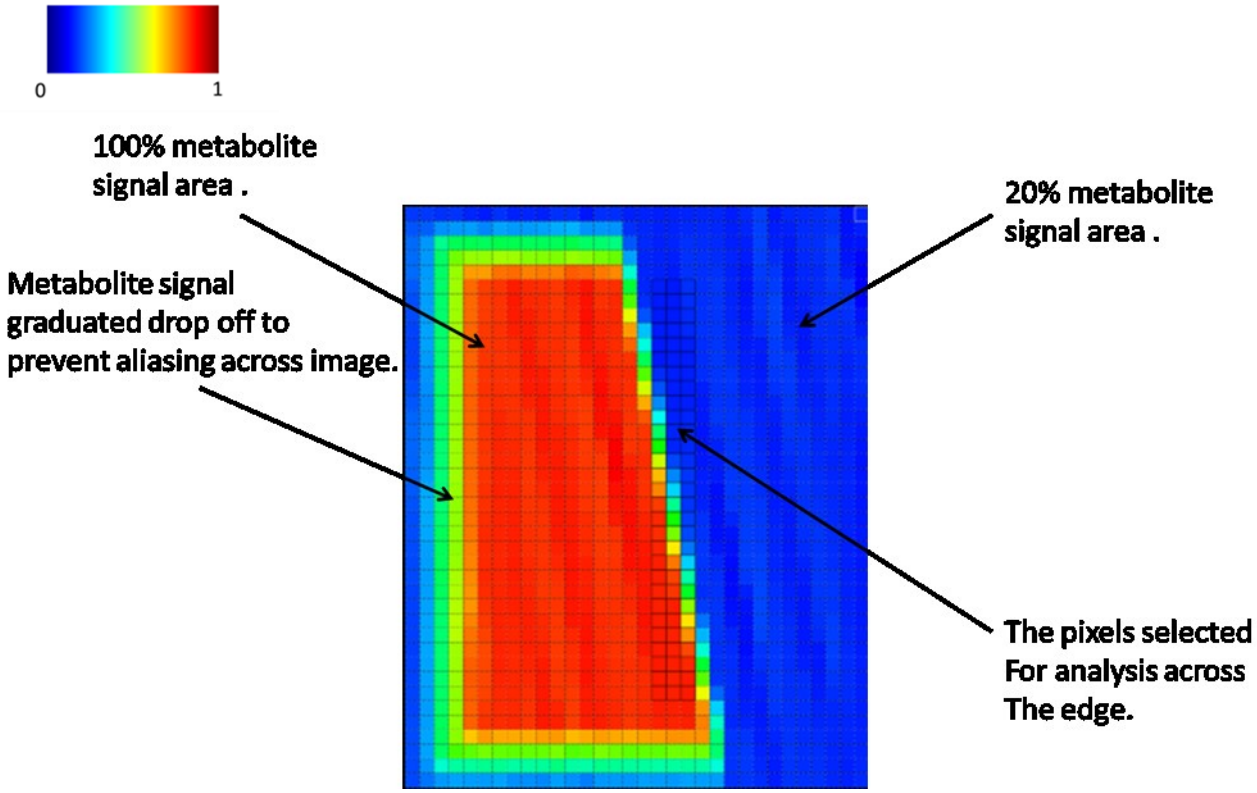

Figure 6-12 Simulated metabolite edge phantom at a voxel size of 5x5x5mm. Voxels highlighted in black across the edge were chosen for quantification.

The area of highlighted voxels across the edge depicted in Figure 6-12 were chosen for quantification by TARQUIN. TARQUIN provides a value of a metabolite's concentration for each of the voxels shown. The output from TARQUIN is in the form of an excel spreadsheet. All profile distances were calculated using the formulae of Equation 6-2.

The digital metabolite edge phantom was created with a fully sampled dataset subject to an elliptical k-space shutter (section 2.2.2). Two FSSR datasets were compared, one with, and

one without added k-space filtration. A standard hamming filter was applied to one of the datasets (section 2.3.1). It is expected that the filtered (smoothed) version should exhibit less inter-voxel contamination at a distance than the non-filtered version but at the cost of adjacent inter-voxel contamination and high spatial frequency (section 2.3.1).

6.3.2 Results and discussion

A plot of the NAA profiles of the fully sampled non-filtered and filtered datasets are depicted Figure 6-13. It can be seen that as expected the non-filtered profile has a sharper edge gradient than that of the filtered profile. This indicates that it exhibits higher spatial frequency content, however it suffers from the Gibbs ringing (section 2.3.1) not present on the filtered version.

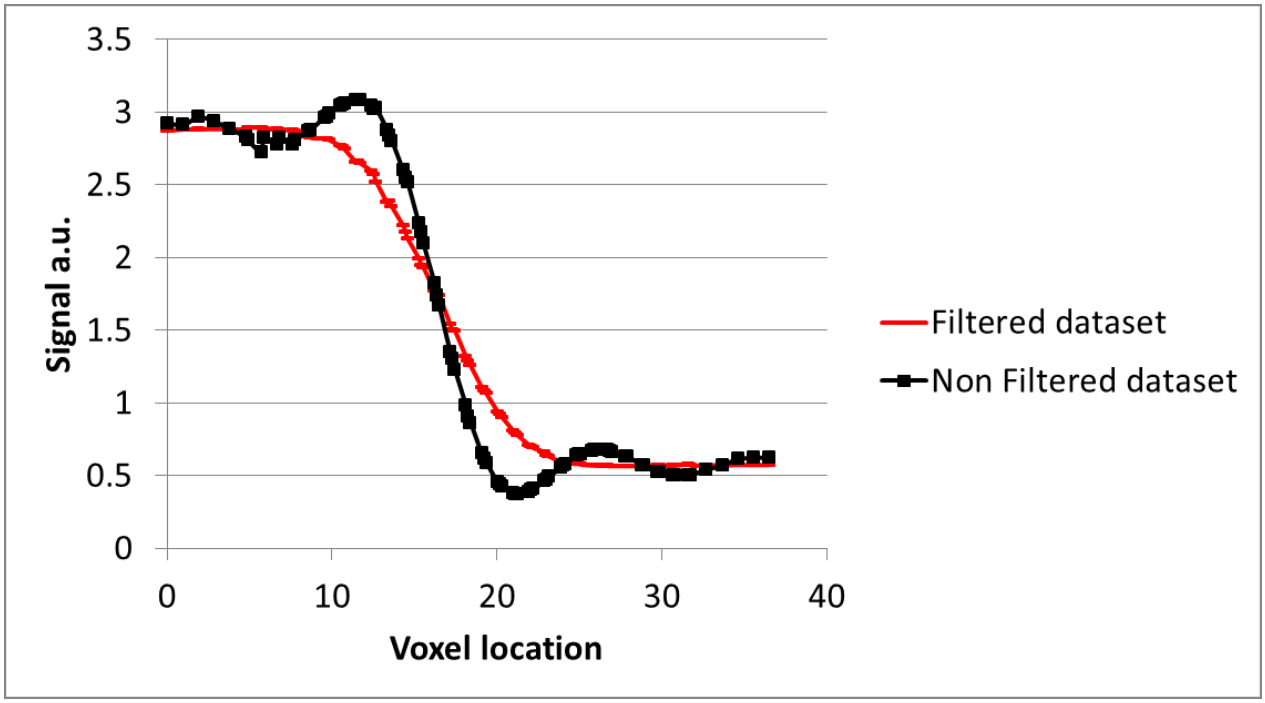

Figure 6-13- NAA profiles across the simulated metabolite edge phantom for the FSSR filtered and non-filtered datasets.

6.4 Conclusion

The use of software simulated 2D phase encoded MRSI is of great benefit to this investigation since it allows the reconstruction of high spatial resolution, high matrix size MRSI datasets without lengthy acquisition duration. The simulations are also not subject to the potential artifacts which pose a challenge when MRSI data is acquired in real-time (section 2.3). The validation of the simulation technique by its application to the simulation of the two-compartment gel edge phantom MRSI indicated that the software simulation produced an edge response within 4% of that of the two-compartment gel edge phantom real-time acquisition dataset.

The application of the software simulation of an angled metabolite edge was created and NAA profiles across the edge were measured to provide the ERF. The non-filtered MRSI dataset exhibited a steeper edge response implying higher spatial resolution and prominent Gibbs ringing Figure 6-13. The Filtered dataset exhibited no Gibbs ringing but was of lower spatial resolution having a slope of lower gradient. This was as expected (section 2.3.1).

As well as the effect of CS-MRSI on adjacent inter-voxel contamination provided by examination of the maximum gradient of the ERF, the non-filtered angled edge simulated dataset also permits investigation of inter-voxel contamination by examination of the Gibbs ringing after CS-MRSI reconstruction with increasing acceleration factor. The non-filtered angled edge MRSI dataset was therefore suitable for high matrix retrospective MRSI reconstruction.

7 Simulations of the effect of CS on MRSI at High Spatial Resolution

The methodology outlined in (section 4.1.1) to provide a means of quantifying the relative spatial resolution in MRSI was successfully applied to a two-compartment gel imaging phantom in Chapter 5. The chapter described measurement of the maximum gradient of a profile perpendicular to a boundary between areas of low and high metabolite concentration. One of the results from this chapter showed a high standard deviation (section 5.1.2) at low sampling values (x5 and x10 acceleration factors). This may be due to the fact that the gradient calculation was based upon the measurement of two data points only, limiting the statistics. The number of data points was governed by the MRSI matrix size used in the previous analysis of (20 x 20). Also, the unrealistically sparse spectrum produced by the two-compartment gel phantom may also affect the results of CS-MRSI. CS may produce more consistent results at higher acceleration factors when applied to MRSI at higher spatial resolution (larger matrix size for the equivalent FOV).

Real-time acquisition of MRSI at this higher resolution is currently prohibited by scan time, so the application of the simulated digital edge phantom as described in section 6.3 was utilised to further investigate the effect of CS-MRSI on the relative spatial resolution. This would allow investigation of any potential smoothing, blurring, inter-voxel contamination and/or aliasing as a result of this technique. Smoothing may occur due to the fact that the k-space mask (section 3.2) has fewer data points at the outer edges which may reduce noise. Smoothing may result however at the expense of spatial resolution (adjacent inter-voxel contamination). Aliasing (inter-voxel contamination at a distance) may be an issue due to the fact that the data is under-sampled (section 2.5.1). The data is randomly under-sampled in k-space so theoretically the artifacts should destructively interfere(Lustig, Donoho et al. 2008).

Spatial resolution in medical imaging systems is often quantified by means of the Modulation Transfer function (MTF) (section 4.1.2) a methodology for its measurement was also investigated using the same simulated digital edge phantom.

7.1 Gradient of the Edge Response Measurement

7.1.1 Method

The simulated metabolite edge digital phantom described in section 6.3 was utilised in this analysis. In summary this contained a sharp 11^0 angled metabolite edge. The angle was relative to the perpendicular of MRSI matrix. The relative concentration of the metabolites was 1:5 on either side of the edge. The dataset had a FOV of 200mm x 160mm with a matrix size (40 x 32).The non-filtered MRSI (FSSR) dataset was subject to reconstruction by CS at acceleration factors of x2, x3.3, x4, x5 and x10. This was achieved on a simulated software phantom created using TARQUIN basis sets for 3T MRSI section 6.3. The experiments were achieved with and without noise. Random, Gaussian noise was added to the noise-free simulation to give an SNR of 10 which is a realistic clinical value. Reconstruction was also achieved with and without noise for the time equivalent, uniformly sampled low resolution (LRR) datasets.

The compressed sensing was implemented as described in Chapter 3. The CS reconstruction was achieved using the Identity and also the wavelet transforms. The Daubechie wavelet 1 was utilised with level 2. This wavelet is also known as the Haar wavelet and looks like a step function, therefore appropriate for this application. Level 2 has been successfully implemented in other studies(Geethanath and Kodibagkar 2013). The CS reconstruction was achieved by under-sampling the non-filtered FSSR dataset with three different k-space

masks for each acceleration factor. This resulted in three CS reconstructions for each factor. Every reconstruction was then quantified using the TARQUIN software to provide a measure of the relative concentrations of each metabolite.

TARQUIN provides the quantified output of the metabolites within a metabolite spectrum in a csv file which can be read into an Excel spreadsheet. Profile plots from the TARQUIN output from across the simulated metabolite boundary were calculated (Section 6.3.1). This was achieved for NAA which has the largest peak in the spectrum, and for Choline to compare the results with another metabolite of lower peak height in a healthy human brain. Three profiles were created for each acceleration factor, and a maximum gradient of the NAA calculated for each. The gradient was calculated using linear regression on 9 points either side of the centre of the slope. The square of the Pearson product moment correlation (R^2) for the NAA noise free slopes averaged at 99%. The lowest value was 97%. The NAA with SNR10 had an average R^2 of 90%, with the lowest value being 85%. For Choline the noise free linear regression had an average R^2 of 97%, with a minimum of 93%. The Choline in the presence of noise SNR 10 had an R^2 of 75%, with the lowest value of 71%. The presence of noise makes it harder to fit the straight line but with a minimum of 71% for all fitting, this is still a good fit.

A mean and standard deviation of the maximum gradient of the three masks were plotted for each acceleration factor along with the FSSR (filtered), FSSR (non-filtered) and the LRR for each acceleration factor. The results for the gradient of the slope were normalised to that of the non-filtered value to provide a relative spatial resolution measurement.

7.1.2 Results

Typical examples of the profiles across the simulated metabolite edge for NAA can be seen Figure 7-1. These plots show the profile for the FSSR (filtered and non-filtered datasets), the

LRR, the CS-MRI (Identity) and the CS-MRSI (wavelet) for each acceleration factor x2, x3.3, x4, x5 and x10 a) to e).

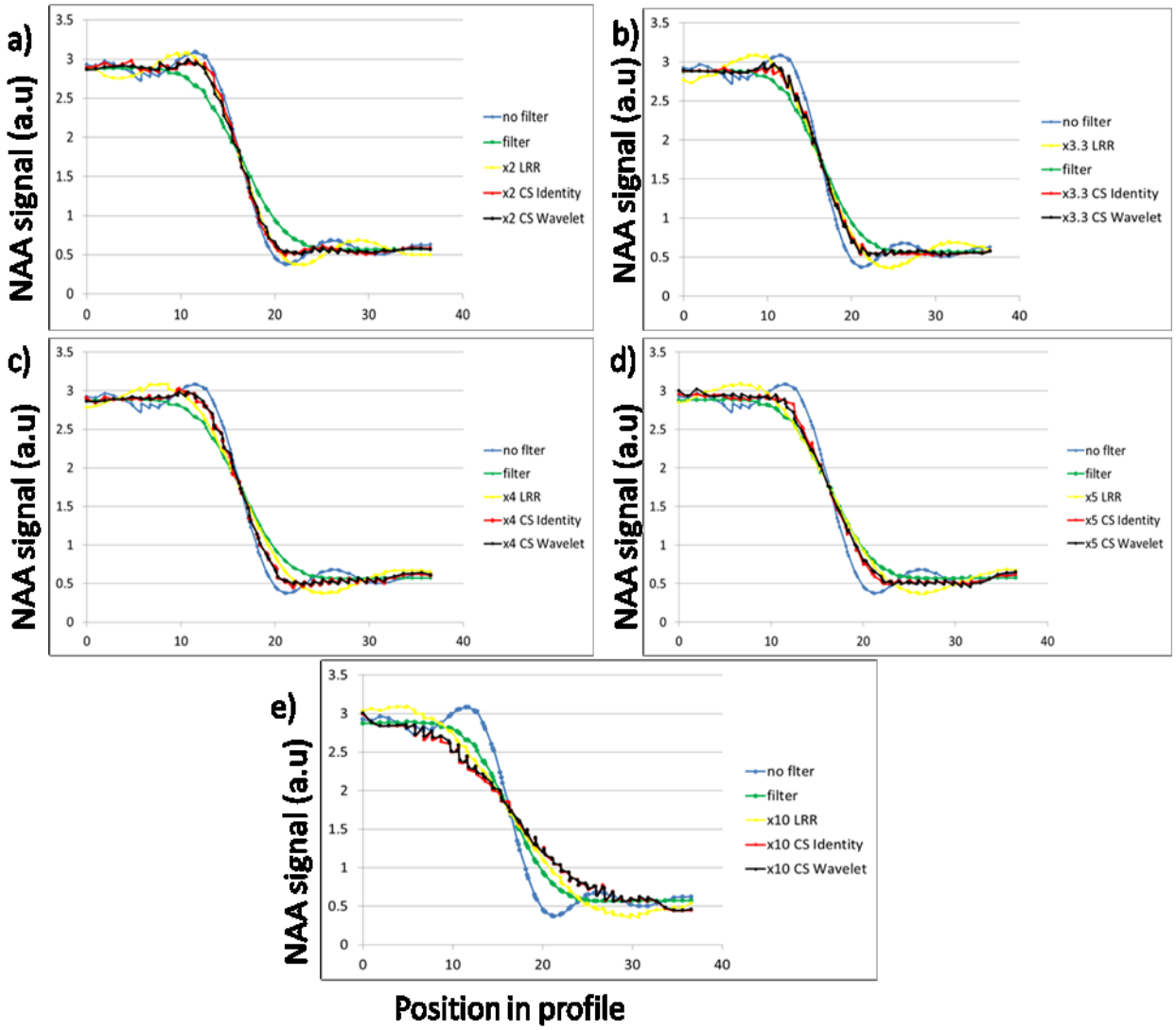

Figure 7-1 Plots of the NAA profiles across the simulated NAA edge (3T) at acceleration factors of a) x2, b) x3.3, c) x4, d)x5 and e) x10. Each plot shows the non-filtered FSSR, the filtered FSSR, CS-MRSI(identity) , CS-MRSI(wavelet), and the LRR.

It can be seen that the Gibbs ringing prevalent in the non-filtered FSSR is clearly removed with the CS-MRSI up to a factor of x5. The plots also clearly indicate that the CS-MRSI maintains the slope (and hence spatial resolution) better than that of the LRR up to a factor of x5. This is reflected in the plots of the maximum gradient across the simulated metabolite

edge calculated for CS-MRSI Figure 7-2. The plot using the CS-MRSI(Identity) can be seen in Figure 7-2 a) and CS-MRSI(wavelet) b).

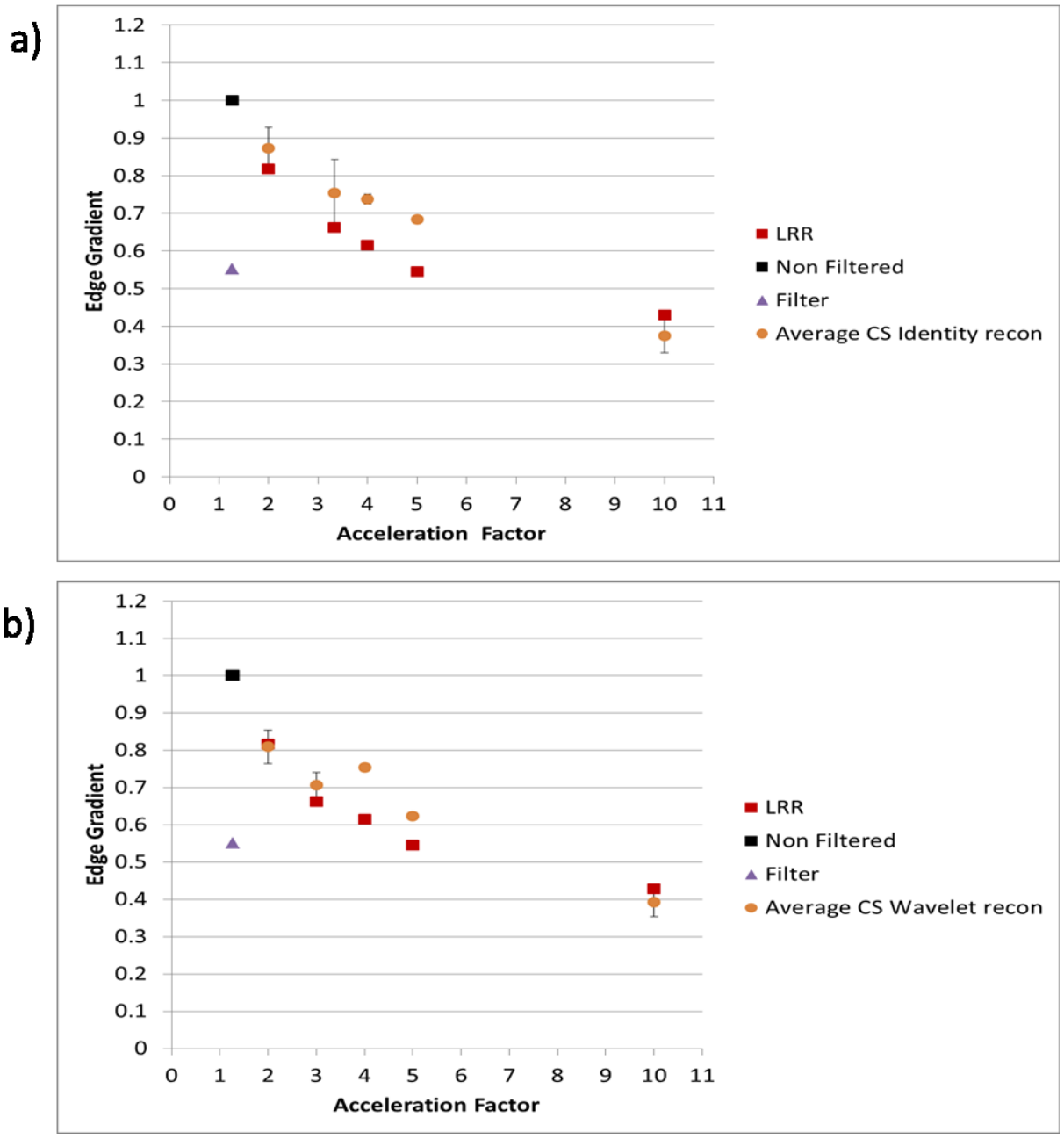

Figure 7-2 Plot of the maximum gradient of the slope of the simulated NAA edge (3T) against acceleration factor (no noise). The CS-MRSI(identity) a) and the CS-MRSI(wavelet) b).

Examples of the profiles across the simulated metabolite edge with SNR 10 for NAA can be seen Figure 7-3 . These plots show the profile for the filtered FSSR and non-filtered FSSR datasets, the LRR, the CS-MRSI(identity) and the CS-MRSI(wavelet) for each acceleration factor x2, x3.3, x4, x5 and x10 a) to e). Although it is harder to define the edge at this SNR

the figure still indicates that the CS reconstruction provides an edge closer to the FSSR up to a factor of x5. Figure 7-4 depicting the gradient of the metabolite edge at each acceleration factor also reflects this result. The figures of the average gradients of the metabolite edges with and without noise would appear to indicate that the identity transform provides a better reproduction of the FSSR than the wavelet transform. This is shown in the result for x5 acceleration factor. In the noise free scenario the identity provides an average gradient of 68 ± 0.3% of the FSSR gradient, and the wavelet, 62% ± 0.8% of the FSSR gradient. In the scenario encompassing an SNR of 10, the identity provides 68% ± 5% to that of the FSSR, and the wavelet 58% ± 0.2% of the FSSR gradient. Both the compressed sensing reconstructions result in significantly higher gradients as compared to the equivalent LRR up to a factor of x5 which are 54% (no noise) and 44%(SNR10) at this factor. At x10 there is no gain provided by reconstruction with compressed sensing.

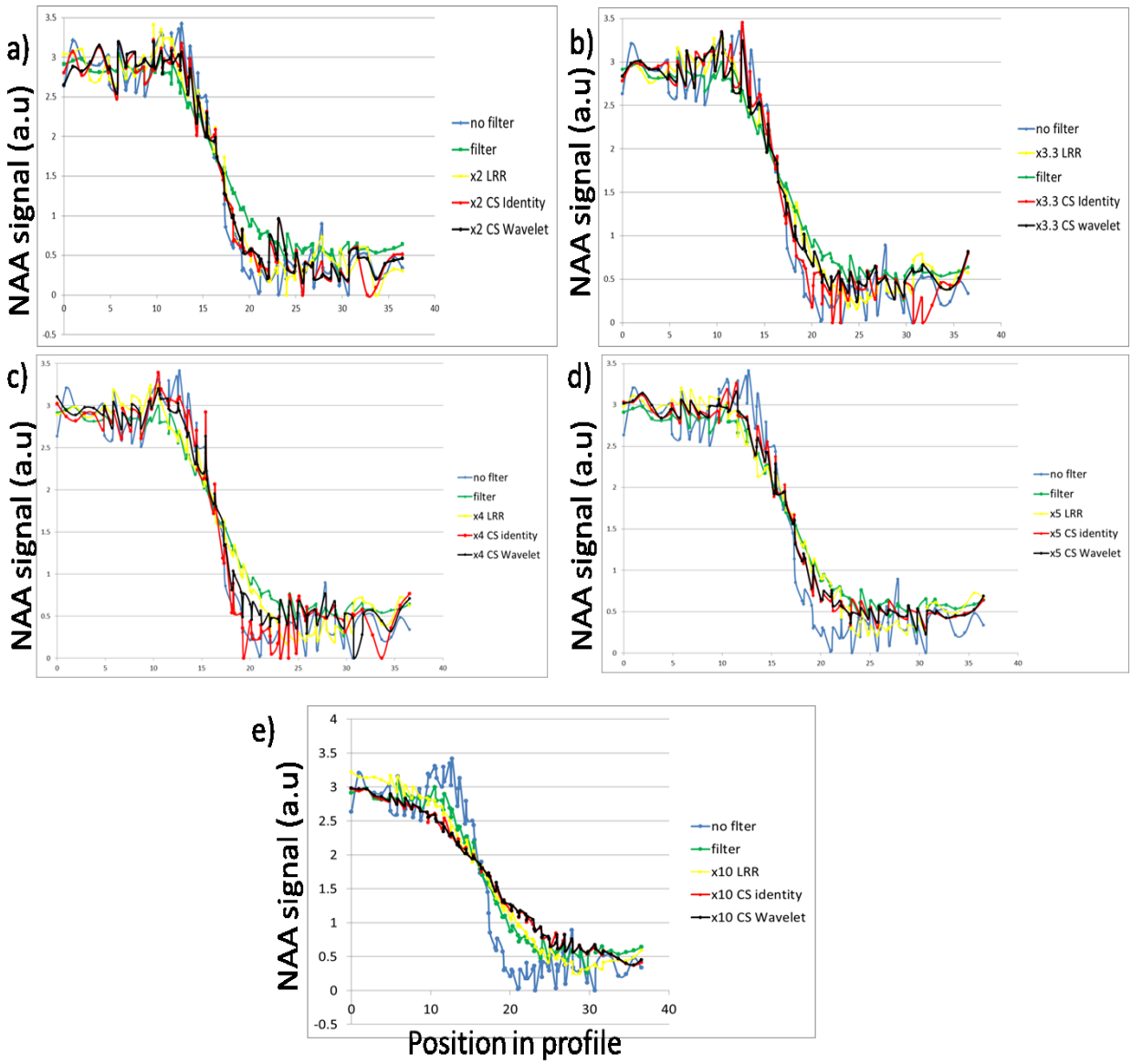

Figure 7-3 Plots of the NAA profiles across the simulated NAA edge (3T) with SNR of 10, at acceleration factors of a) x2, b) x3.3, c) x4, d)x5 and e) x10. Each plot shows the non-filtered FSSR, the filtered FSSR, the CS-MRS (Identity) and CS-MRSI(wavelet), and the LRR.

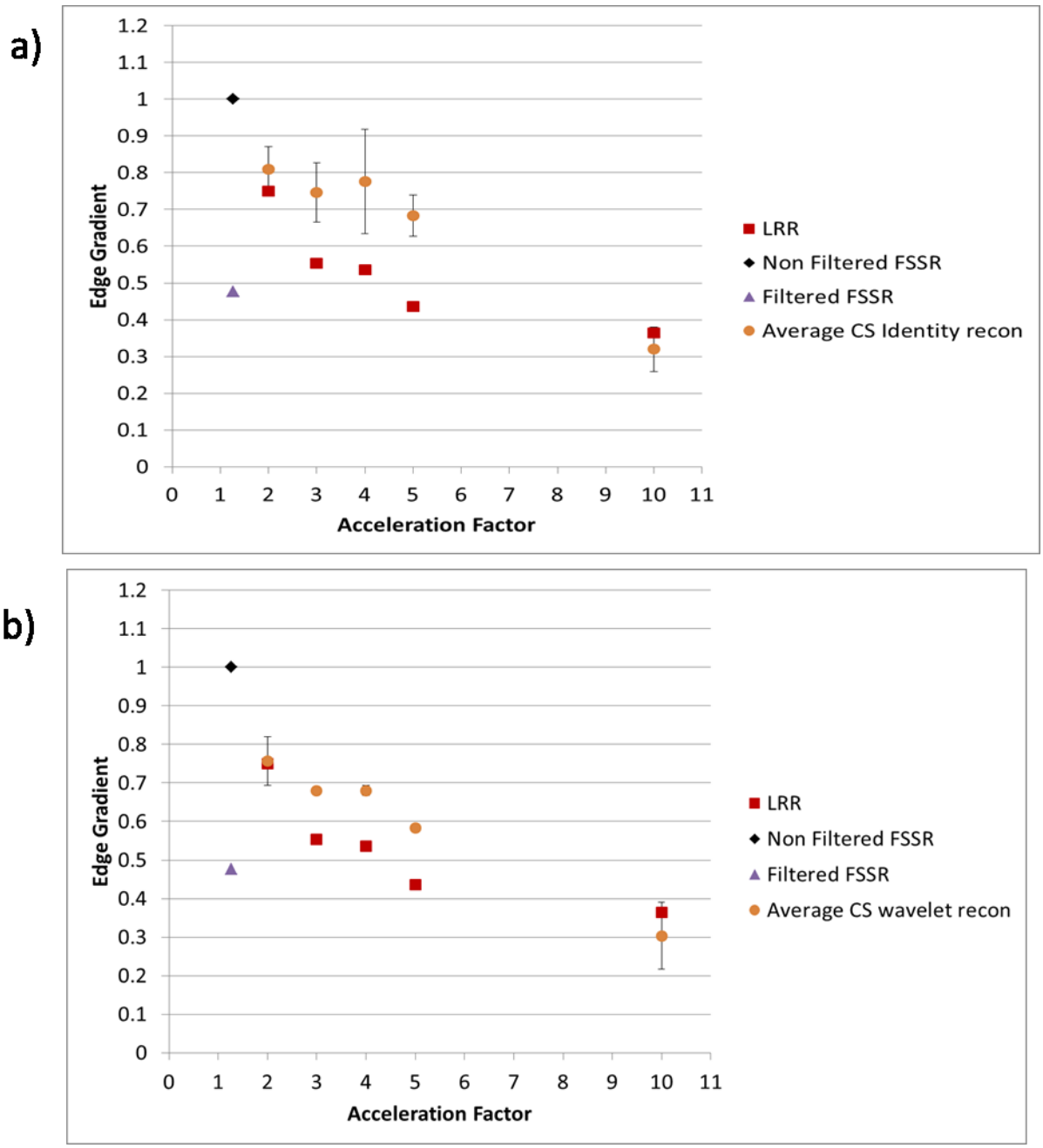

Figure 7-4 Plot of the maximum gradient of the slope of the simulated NAA edge (3T) with SNR 10, against acceleration factor. The CS-MRSI(identity) a) and the CS-MRSI(wavelet) b).

The maximum average, gradient plots for the Choline profiles without noise can be seen Figure 7-5 and with SNR of 10 Figure 7-6. These again reflect the results of the NAA profiles in that the CS reconstruction provides a superior gradient of the edge compared to the LRR at the equivalent acceleration factor up to x5, and there is no benefit at a factor of x10.

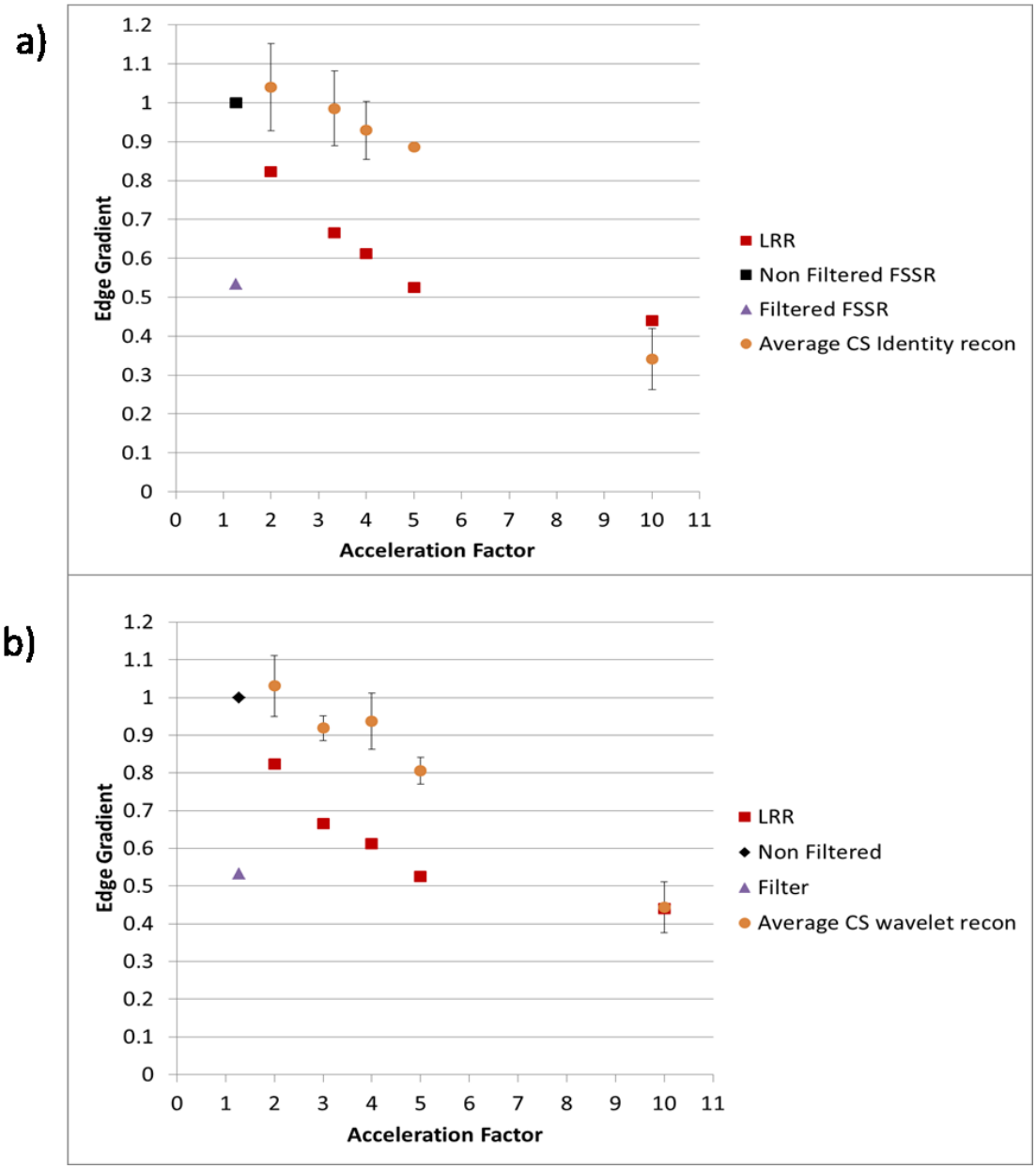

Figure 7-5 Plot of the maximum gradient of the slope of the simulated Choline edge (3T) with no noise, against acceleration factor. The CS-MRSI(identity) a) and the CS-MRSI(wavelet) b).

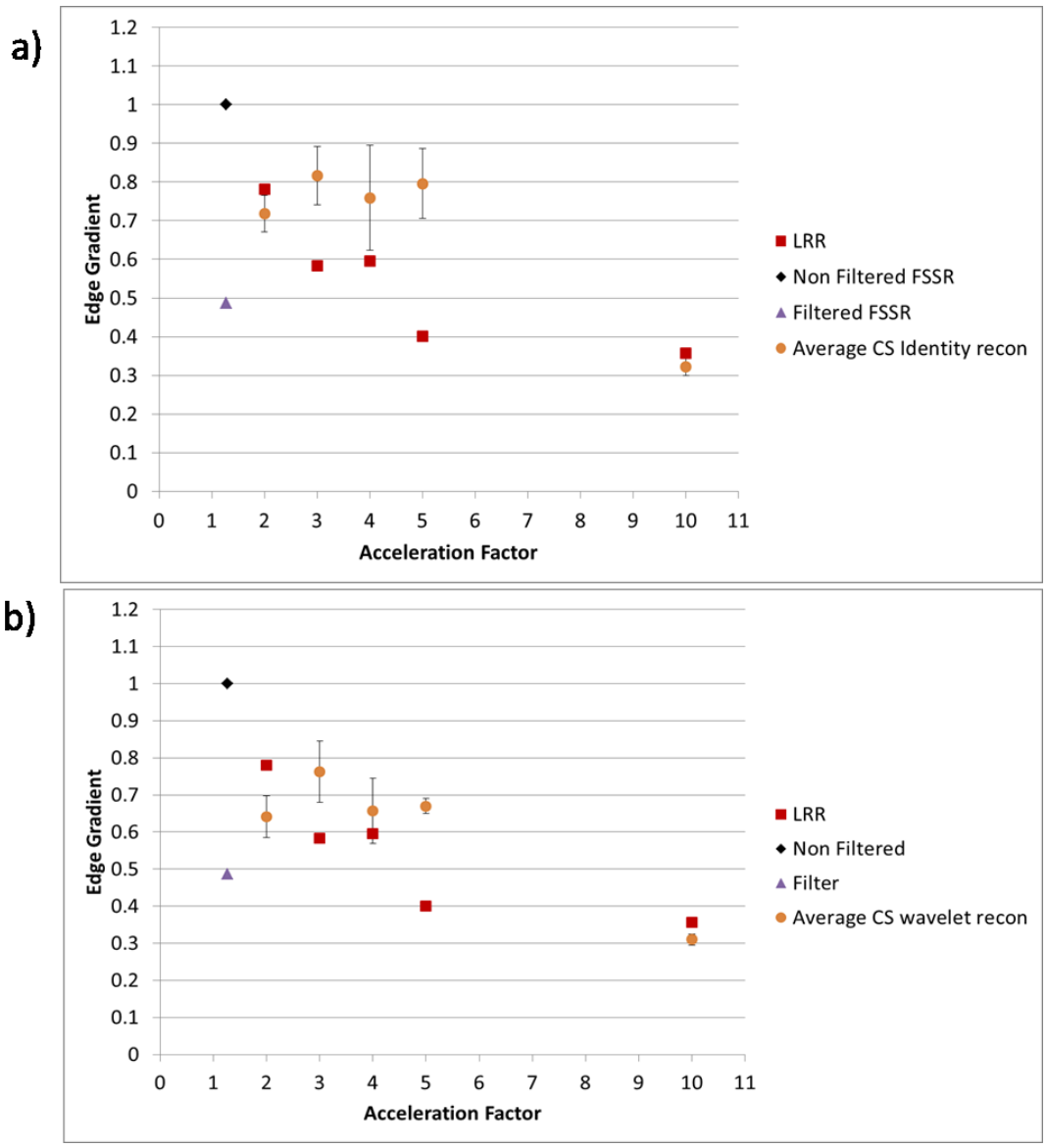

Figure 7-6 Plot of the maximum gradient of the slope of the simulated Choline edge (3T) with SNR10, against acceleration factor. The CS-MRSI(identity) a) and the CS-MRSI(wavelet) b).

7.1.3 Discussion

The application of the simulated, angled metabolite edge provided a successful means to measure relative spatial resolution using higher data samples across it. Results suggest that there is a benefit to utilising CS-MRSI as a reconstruction technique to maintain spatial resolution whilst also minimising Gibbs ringing for accelerated MRSI up to a factor of x5.

Adjacent inter-voxel contamination will hinder the accurate delineation of tumour borders with healthy tissue. Up to an acceleration factor of x5 Figure 7-1 d) indicates that the gradient of the edge appears to be maintained close to that of the non-filtered FSSR, implying that there is little introduction of adjacent voxel contamination at this acceleration factor. The figure also indicates that the CS-MRSI when using either sparse transform, appears to improve the inter-voxel contamination at a distance (Gibbs ringing) compared to the non-filtered FSSR at all acceleration factors. The variable k-space mask samples to the outer edges of k-space (3.2) which is why the spatial resolution is maintained, but also due to the variable density towards the outer edges, the mask has a filtering effect reducing the ringing. These results suggest MRSI real-time acquisition could be potentially five times quicker using CS-MRSI whilst maintaining tumour boundary definition. The CS profiles also show a slight ripple artefact along its length. This is most likely due to the noise-like incoherence artefacts due to the random under-sampling (section 2.5.3).

Figure 7-2 shows the maximum gradient across the NAA edge in a noise free environment. This figure serves to demonstrate that the spatial resolution degrades with increasing acceleration factor and that the CS-MRSI reconstructions are above those of the LRR up to a factor of x5. CS-MRSI(identity) appears to retain 68% ± 0.2% of the spatial resolution as compared to the non-filtered FSSR at an acceleration factor of x5, and 62% ± 0.01% for the CS-MRSI(wavelet). This is compared to 54% for the LRR at this factor. It can also be seen that at an acceleration factor of x10 the spatial resolution drops to around 40% and that there is no advantage of CS-MRSI over the LRR at this factor for both Identity and wavelet reconstructions.

Figure 7-3 indicates the equivalent NAA profiles of Figure 7-1 except that noise was added to the spectra to provide an SNR of 10. This is a more realistic scenario. The plots also indicate

that the inter-voxel contamination at a distance (Gibbs ringing) is reduced when CS-MRSI is utilised, although this is not as obvious as it is in the noise-free environment. Figure 7-4 indicates that at acceleration factor of x5 the spatial resolution for NAA is retained to an average of 68% ± 5% for CS-MRSI (Identity), CS-MRSI (wavelet) 58% ± 0.2% and 44% LRR. This is similar in trend to that of the noise-free scenario in which the adjacent inter-voxel contamination is again less than that of the LRR at x5 acceleration factor when employing CS-MRSI. The advantage of CS-MRSI over the LRR at an acceleration factor up to x5 is also reflected in the maximum average gradient results for choline both with and without noise, Figure 7-5 and Figure 7-6. Again there is an advantage of CS-MRSI up to x5 acceleration factor but not at x10 over the LRR. The noise free results for Choline Figure 7-5, indicate that the CS-MRSI (Identity) at x5 acceleration provides a maximum average gradient of 89% ± 0.6% of that of the non-filtered FSSR, for CS-MRSI (wavelets) 80% ± 6% and 52% for LRR. When a realistic level of noise is added to produce an SNR of 10, the values for the relative spatial resolution for Choline were CS-MRSI (identity) 80% ± 7%, CS-MRSI (wavelets) 67% ± 1.6%, and 40% for the LRR. A recent study also found that CS-MRSI produced a significant degradation in results at an acceleration factor of x10 compared to those at x5 (Geethanath 2012).

The spatial resolution results appear to be significantly better for the Choline metabolite than for the NAA both with and without noise. This could be related to the chosen CS weighting factors in particular the TV weighting which may favour spectral peaks of different signal height or possibly that the TARQUIN peak fitting is more suitable for Choline than NAA at short echo times.

The results for both NAA and Choline also imply that CS-MRSI utilising the identity transform provide an advantage over the wavelet transform in terms of spatial resolution at x5

acceleration factor. The use of wavelets may have a filtering effect upon the image or the performance of the CS-MRSI(wavelet) could be related to the chosen mother wavelet which warrants further investigation.

Results from the angled edge simulation agree with those of the real-time acquired two-compartment gel edge phantom (section 5.2.2) in that the spatial resolution provided by the CS-MRSI reconstructions are higher than those utilising LRR up to an acceleration factor of x5, and that the spatial resolution reduces with increasing acceleration factor. The spatial resolutions at factors of x5 and x10 had high standard deviations for the two-compartment gel edge phantom and both appeared above the LRR. The simulated angled edge spatial resolution measurement was not above the LRR using CS-MRSI at x10. The voxels measured in the gel phantom scenario were four times the area of those utilised in the simulation, which limited the number of edge samples to two. The major difference between the two scenarios is that the number of sampled data points used in the calculation of the gradient across the digital phantom angled edge was 9 times that of the two-compartment gel edge, ensuring better statistical accuracy. The quantification method in both scenarios was also different. The gel phantom was quantified by summing up the area under the metabolite peaks whereas the simulations were quantified using TARQUIN (Wilson, Reynolds et al. 2011). However despite the differences in the two, the results still agree that there may be an advantage in using CS-MRSI up to an acceleration factor as high as x5, particularly when compared to the LRR.

It is interesting to note that the filtered FSSR results in all scenarios produce a maximum edge gradient (spatial resolution) from the simulated angled edge which is 45-50% below that of the non-filtered FSSR. This is in agreement with the suggestion that the application of certain MRSI k-space filters can double the voxel size (Barker and Lin 2006). The advantage

of using the filter is that it reduces the side lobes of the PSF (section 2.3.1) and therefore inter-voxel contamination particularly from distant voxels. The results of this study suggest that the CS-MRSI also reduces these side lobes and reconstructs with consistently higher spatial resolution than the filtered FSSR. The ringing filter is currently implemented in all 2D phase encoded clinical MRSI acquisitions. Therefore, CS-MRSI could potentially be utilised in the clinic in place of the filter to reduce the side lobes of the PSF with the added advantage of increased spatial resolution, whilst at the same time accelerating MRSI acquisition by up to 80%!

7.2 MTF Measurement

The modulation Transfer Function (MTF) is an established technique for examining the spatial frequencies present in an imaging system (Section 4.1.2). The MTF is therefore a useful measure for the examination of the spatial frequencies present in MRSI after it has been reconstructed using compressed sensing. The software simulation of an angled metabolite edge from (Section 6.3) provides a way of establishing the edge response of these reconstructions. This can then be differentiated and a 1D Fourier transformed applied to reveal the modulation of the spatial frequencies of the reconstruction. This research examined the feasibility of this technique in its application to the metabolite edge simulations. The Filtered and non-filtered FSSR datasets were initially examined. Datasets reconstructed with CS were compared to those of the uniformly sampled LRR reconstructions at each acceleration factor. Reconstruction was then repeated utilising the wavelet transform as the sparsifying transform (Section 3.3.1) and compared with the use of the identity transform.

The addition of noise providing an SNR of 10 and its effect upon the MTF calculation was also investigated on the filtered and unfiltered FSSR datasets.

7.2.1 Method

The simulated metabolite edge phantom described in section 6.3 was utilised in this analysis. Initially the noise free version was investigated. The non-filtered MRSI (FSSR) dataset was subject to reconstruction by CS at acceleration factors of x2, x3.3, x4, x5 and x10 for both the identity transform, CS-MRSI(identity) and the wavelet, CS-MRSI(wavelet) sparse transforms. The LRR reconstructions at each equivalent acceleration factor were also examined along with the filtered and non-filtered FSSR. The reconstructions for each dataset from section 7.1 were utilised.

A Matlab program was written in order to calculate the MTF for each reconstructed dataset. The edge responses which are the profile plots calculated from the TARQUIN output across the simulated metabolite angled boundary were calculated according to section 6.3.1. The edge responses for NAA, at each acceleration factor without noise can be seen Figure 7-1. The program initially reads in the edge response. The calculation is based upon the Fourier transform of the Line Spread Function (LSF). The LSF is calculated by finding the approximate derivative of the edge profile using the Matlab function ‘diff ‘implemented as diff(X)/diff(Y). It can be seen on seen Figure 7-1 that the edge responses are not are not perfectly smooth which introduces gradient anomalies within the profiles. This is due to approximation errors, and small errors in the TARQUIN quantification process. The edge profiles were therefore subject to mathematical smoothing. The smoothing was achieved using a 7 span averaging filter in Matlab. Figure 7-7 shows the smoothing of the non-filtered and filtered FSSR datasets. The smoothing does not detract from the gradient of the slope which is the fundamental indicator of the spatial frequency response.

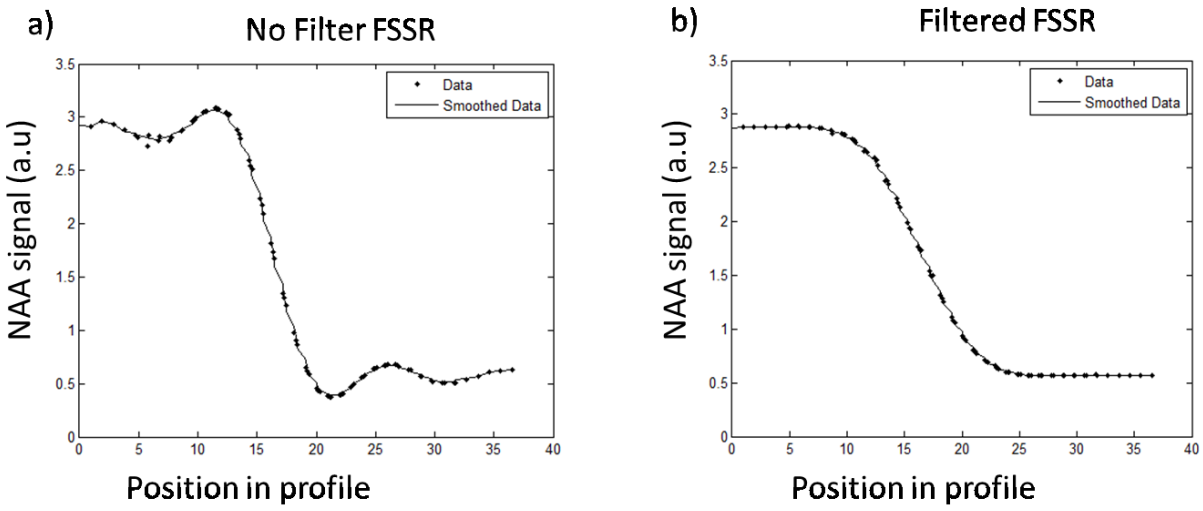

Figure 7-7 The edge response profiles across the metabolite edges for the non-filtered a) and the filtered b) MRSI datasets with smoothing.

Once the data is smoothed the LSF is calculated as above. This is then 1D Fourier transformed to produce the MTF. Each MTF is normalised. Figure 7-8 shows the difference in the MTF calculation between the smoothed and the unsmoothed profiles. If no smoothing is utilised it introduces high frequency noise to the profile and thus distorts the MTF.

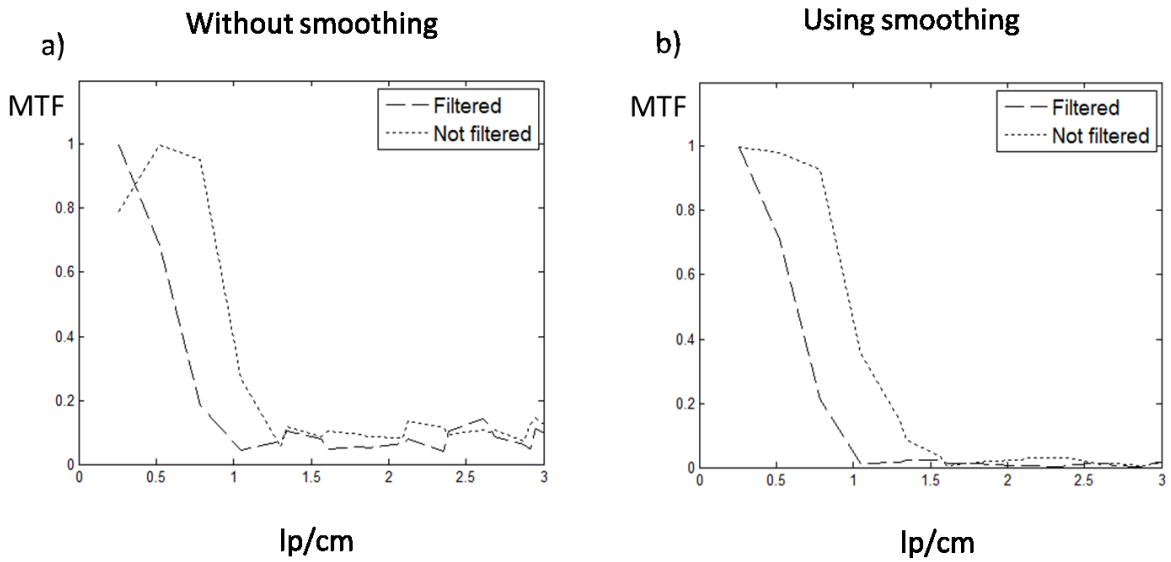

Figure 7-8 The MTF calculated for the non-filtered and filtered FSSR without smoothing a) and with smoothing b).

The MTF50 (section 4.1.2) was calculated using a linear interpolation of the MTF curve to find the spatial frequency response at an MTF of 50%. Although an arbitrary cut-off this is a common indicator of the spatial frequency response.

The CS-MRSI reconstructed edge response profiles were processed utilising the MTF program to determine the effect on the spatial frequency response in a noise free scenario. The reconstructions for each dataset from section 7.1 were utilised. Each reconstructed edge response was subject to smoothing in the same way as the filtered and non-filtered FSSR.

7.2.2 Results

The ERF can be seen on the left hand side of Figure 7-9 a-e) for each acceleration factor x2, x3.3, x4, x5 and x10. The equivalent LRR edge response can be seen to the right hand side of each CS-MRSI edge profile.

The smoothing does not appear to alter the profile in a way which greatly reshapes the overall profile and the gradient of slope of the edge is maintained. It can be seen that the profile becomes less like a step function and more rounded at the edges at an acceleration factor of x10.

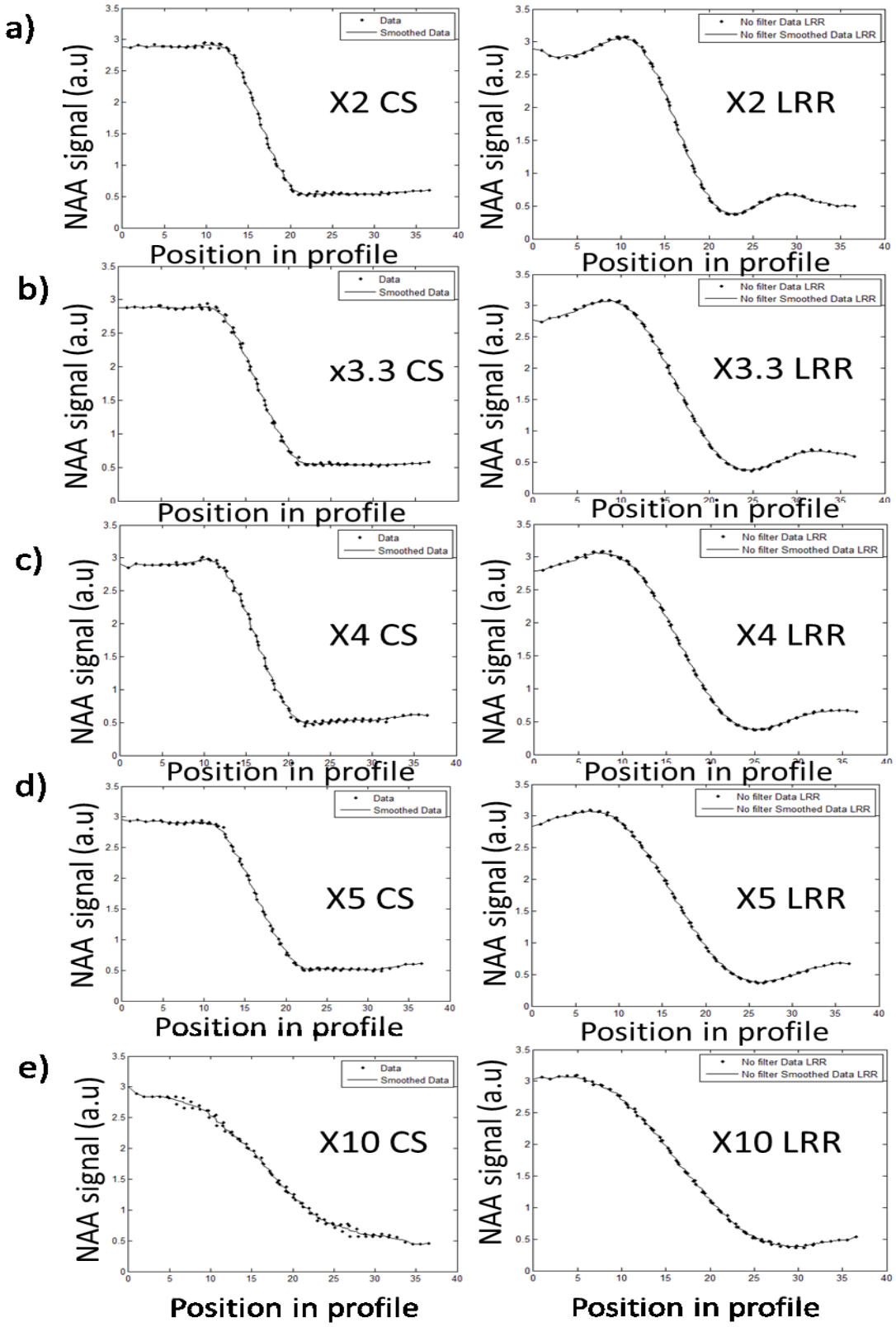

Figure 7-9 The NAA edge responses indicating unsmoothed data points and the smoothed approximations at each acceleration factor a-e). The compressed sensing reconstructions are indicated on the left and the equivalent LRR on the right.

The plots of the MTF at each acceleration factor can be observed Figure 7-10 for the CS-MRSI(identity) and Figure 7-11 for the CS-MRSI(wavelet). The calculated MTF50 can be seen in Table 3. The MTF50 calculation and the plots all indicate that the CS reconstruction provides a superior spatial resolution up to a factor of x5 after which it starts to degrade. This is also reflected in the shape of the edge response profiles Figure 7-9.

Acceleration Factor	**Spatial frequency at 50% of the maximum modulation (MTF50) (lp/mm)**				
	LRR	**CS (identity)**		**CS (wavelet)**	
		Mean	**std**	**Mean**	**std**
1 (no filter)	0.98	-	-	-	-
1 (filtered)	0.63	-	-	-	-
2	0.86	0.89	0.03	0.83	0.04
3.33	0.7	0.77	0.07	0.75	0.08
4	0.67	0.77	0.05	0.8	0.07
5	0.63	0.73	0.01	0.67	0.02
10	0.52	0.5	0.04	0.5	0.04

Table 3 The MTF50 calculated at each acceleration factor (no noise) for each reconstruction. The MTF50 for the non-filtered FSSR and the filtered FSSR datasets are shown as LRR with acceleration factor of 1.

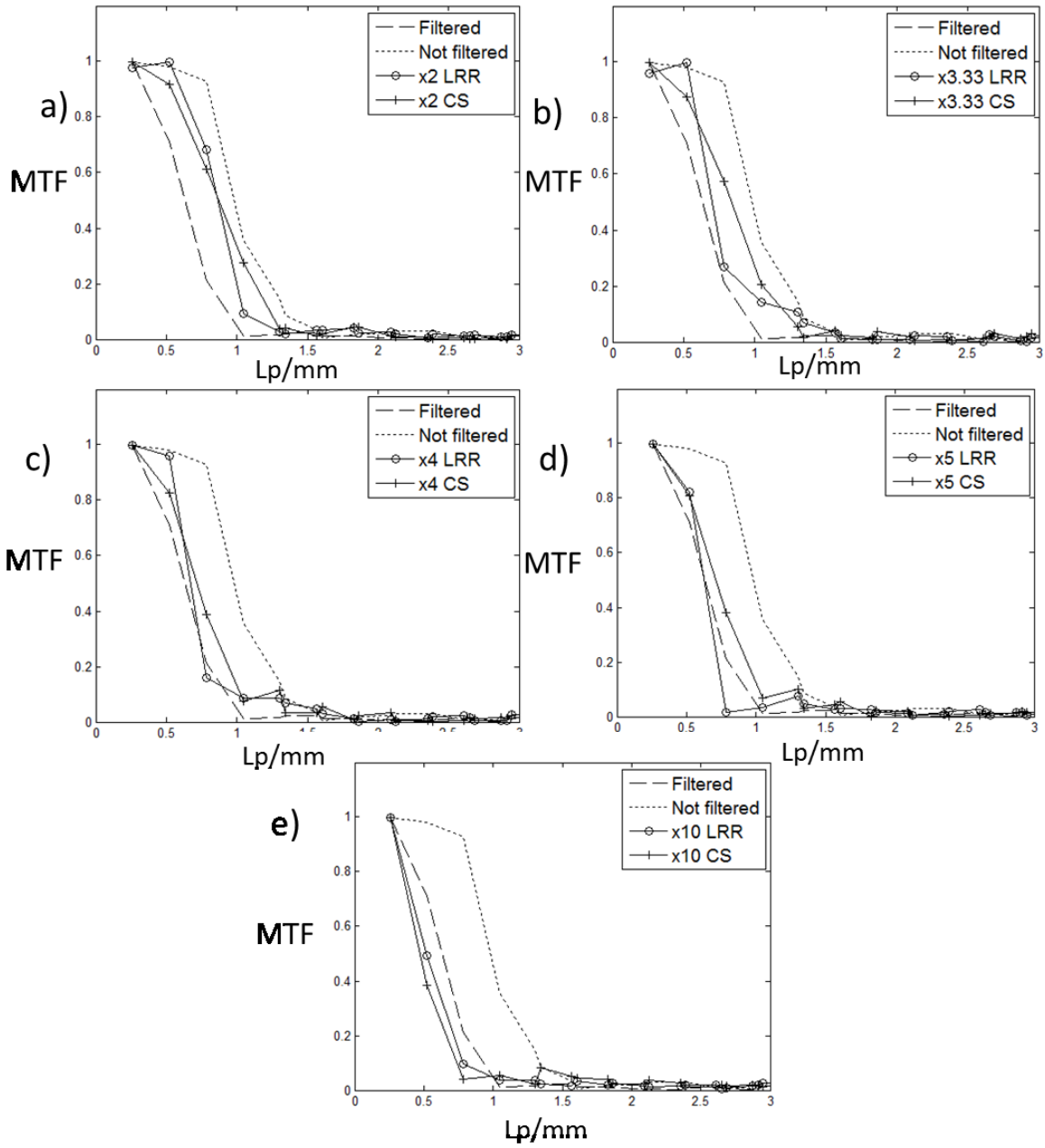

Figure 7-10 MTF curves for CS-MRSI (identity) and LRR at the acceleration factors x2, x3.3 ,x4, x5 and x10.(no noise)

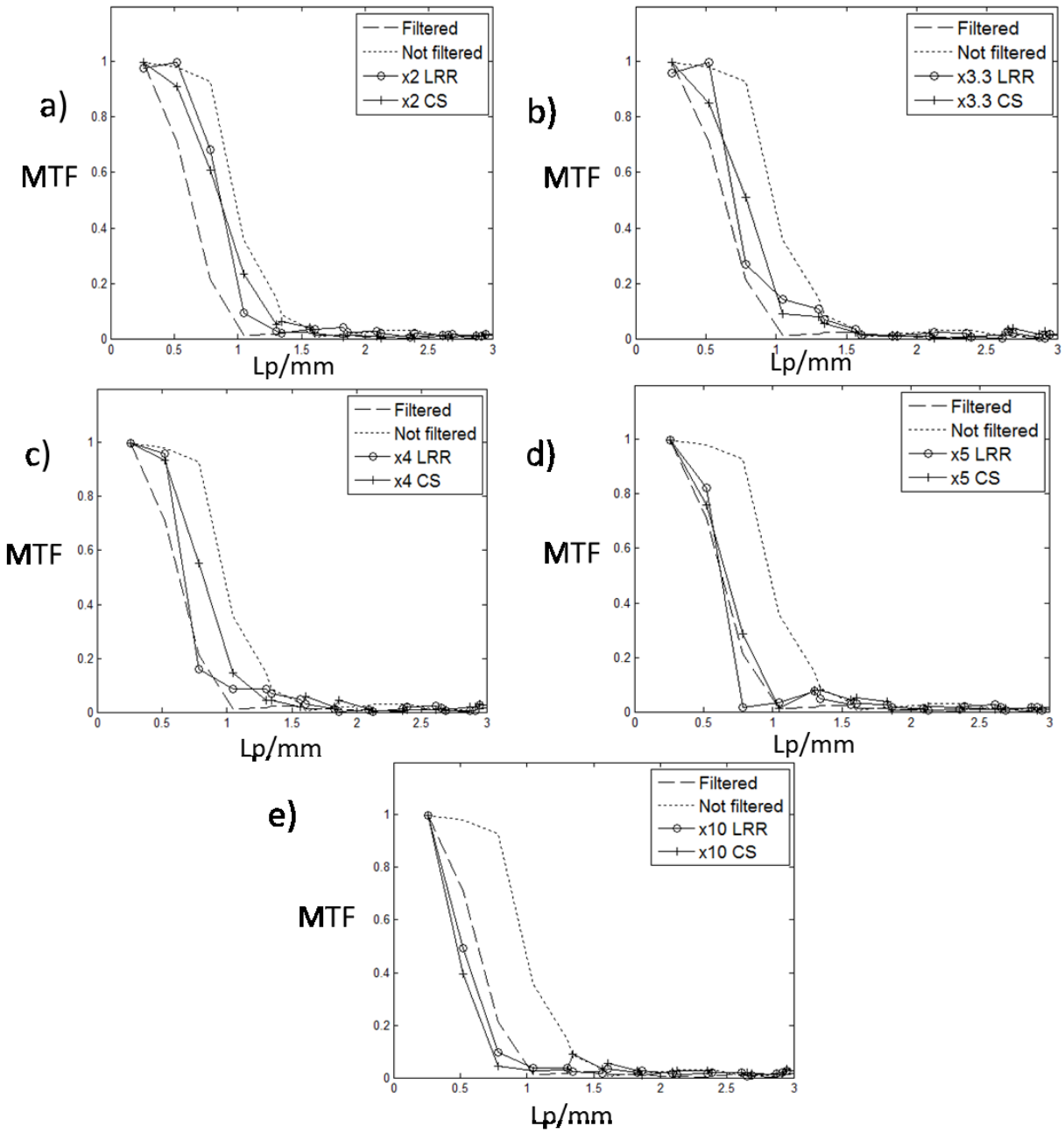

Figure 7-11 MTF curves for CS-MRSI (wavelet) and LRR at the acceleration factors x2, x3.3 ,x4, x5 and x10.(no noise)

In a realistic, clinical MRSI the SNR is around 10. This level of noise was added to the filtered and non-filtered FSSR datasets. The NAA profile across the metabolite edge can be seen Figure 7-12 a). The corresponding MTF curve can be seen in Figure 7-12 c).

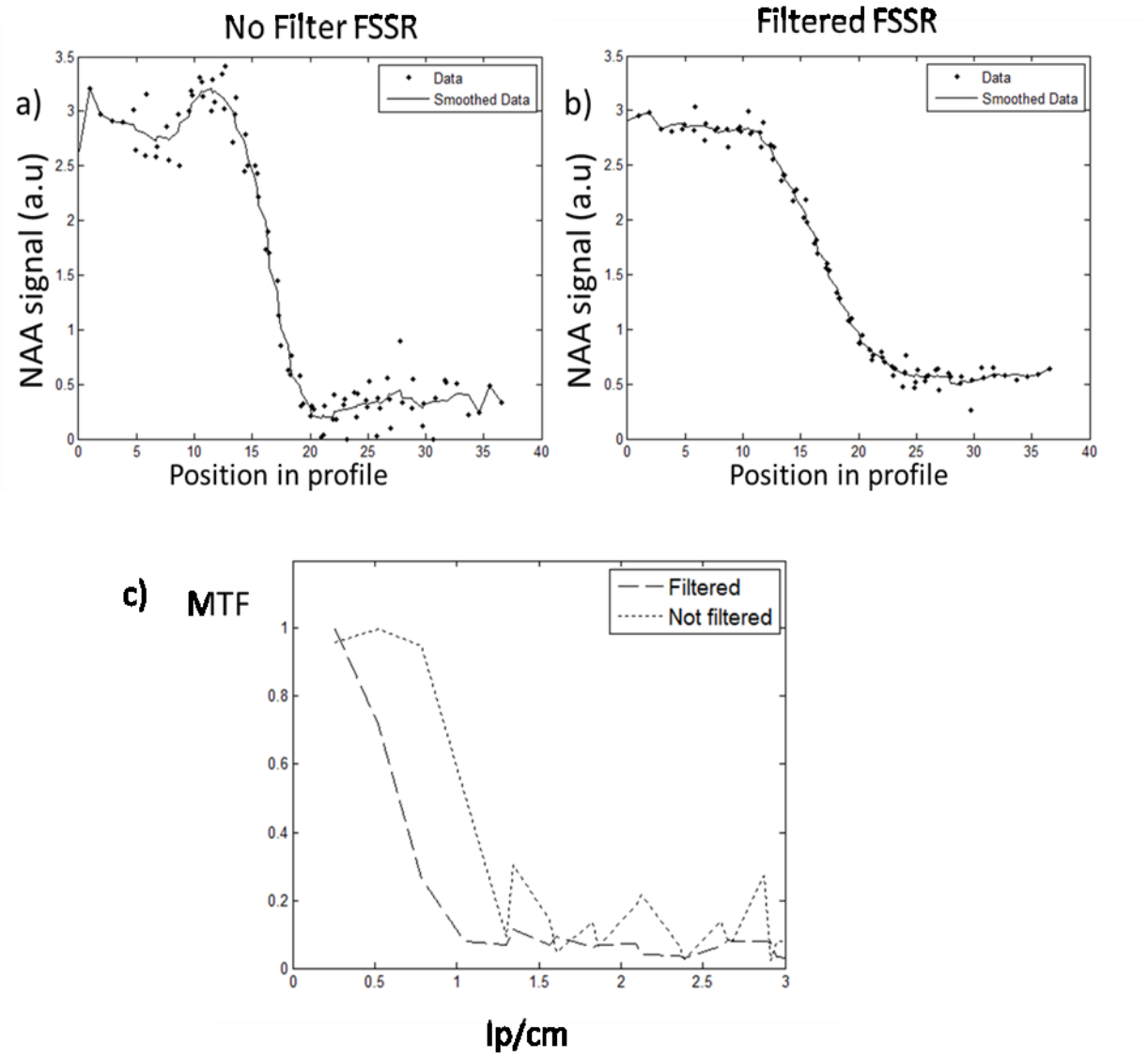

Figure 7-12 The Edge response profile with the solid line indicating the smoothing for the non-filtered FSSR a) and filtered FSSR b). The calculated MTF curves for both FSSRs are shown in c).

7.2.3 Discussion

Figure 7-8 shows the MTF calculated with b) and without a) smoothing applied to the NAA profile edge responses of the FSSR with and without filtering in a noise free scenario. The main difference between the two MTF's is that the smoothed profiles do not exhibit the high frequency noise present in the unsmoothed dataset profiles. The MTF50 (Table 3) was calculated via linear interpolation was found to be 0.98 lp/cm for the non-filtered FSSR and

0.63 lp/cm for the filtered FSSR. The voxel dimension in the x-y plane is 5mm x 5mm, therefore one line pair would be 1cm. The value of 0.98 lp/cm for the non-filtered FSSR MTF is therefore in close agreement with this providing validity of the technique. It can also be seen that the non-filtered MTF is zero at approximately 1.7 lp/cm. Since the data acquisition FOV is rectangular and not circular the diagonal extent of k-space is around 40% larger. This would correspond to a limiting resolution corresponding to a 3mm voxel size (~1.66 lp/cm). In the case of the non-filtered dataset the MTF appears constant up until 1 lp/cm. This is expected since k-space is not amplitude modulated as it is for the filtered version. The MTF then rapidly falls away as frequency is increased, between 1-1.66 lp/cm until the resolution limitation. The MTF falls to zero for the filtered FSSR at around 1 lp/cm which is the limit of resolution. The non-filtered MTF is always higher than that for the filtered dataset which is not unexpected as the non-filtered FSSR contains higher spatial frequencies.

The results from Table 3 indicate that the CS-MRSI(identity) provides up to 73% of the resolution of that of the non-filtered FSSR dataset at x5 acceleration factor. The corresponding LRR provided 63% spatial resolution at this acceleration factor. This is compared to the average gradient (section 7.1.2) which gave a gradient of 68 ± 0.2% of the non-filtered FSSR gradient at this acceleration factor. The MTF50 values agree with the results of the angled edge gradient evaluation in that the spatial resolution is greater when using CS-MRSI up to an acceleration factor of x5. The CS-MRSI degrades at x10 acceleration factor where the LRR reconstruction is slightly better. This is in agreement with the ERF results of (section 7.1.2). Values between x5 and x10 have not been examined so the exact limit of CS-MRSI is yet to be determined. The filtered FSSR dataset has a reduced spatial resolution with an MTF50 of 63%, compared to the non-filtered FSSR dataset, and to CS-MRSI up to an acceleration factor of x5. The LRR reconstruction appears to modulate the lower spatial frequencies better than the CS-MRSI for acceleration factors up to x5 after

which the CS-MRSI appears to modulate the higher spatial frequencies. This is in agreement with the result of (Heikal, Wachowicz et al. 2013) which examined CS-MRSI at an acceleration factor of x4 only. At an acceleration factor of x10 the LRR appears to degrade less than the CS-MRSI again in agreement with the gradient results of the previous section. This result indicates that the use of CS-MRSI is beneficial compared to the LRR reconstruction up to an acceleration factor of x5. The wavelet results again also reflect the results from 7.1.2. The average MTF50 calculations are consistently higher than those of the average gradient calculations; however the results are consistent with the identity transform results in that CS-MRSI appears beneficial up to an acceleration factor of x5.

Even though all the edge response profiles are subject to smoothing, the results of Figure 7-10 and Figure 7-11 indicate that there is still a degree of high frequency noise present on the MTF curves after 1 lp/cm. This also means that examination of a different standard MTF the MTF10 is complicated by the presence of this noise and would therefore be unreliable in this circumstance.

Figure 7-12 depicts the NAA ERF's a) and b) and corresponding MTF curve c) in the presence of noise (SNR10). This figure demonstrates a difficulty with the MTF calculation. The non-filtered dataset can be seen to contain a substantial amount of noise. The edge response is therefore not so easily modelled. This is not so prevalent in the filtered FSSR dataset, Figure 7-12 b) which inherently reduces the level of noise by reducing the outer edges of k-space at the cost of spatial resolution. The MTF in this scenario Figure 7-12 c) indicates again that even with the addition of data smoothing, the non-filtered FSSR dataset is too noisy to give an accurate MTF particularly at higher spatial frequencies. It was therefore decided not to utilise this technique for the CS reconstruction of datasets with added noise.

7.3 Conclusion

The use of the digital phantom containing an angled metabolite edge successfully provided further means to assess the relationship between the MRSI spatial resolution with increasing acceleration factor, providing an increased number of data points in the measurement of the edge response.

It is of paramount importance for an imaging system to discriminate between focal and those tumours which have infiltrated into the surrounding healthy tissue. The definition of the edge of a tumour is hampered by inter-voxel contamination both from adjacent and distant voxels (section 2.3.1). If a tumour is focal and the employed MRSI reconstruction introduces inter-voxel contamination into the surrounding healthy tissue then misdiagnosis may occur, possibly resulting in the removal of healthy tissue. If the LRR technique is employed to accelerate the MRSI acquisition by 80%, results indicate an increase in adjacent voxel contamination of 54%, whereas CS-MRSI (identity) only increases it by 32% without introduction of distant voxel contamination.

The gradient of the edge is related to inter-voxel contamination from adjacent voxels (section 2.3.1). The results imply that employment of CS-MRSI maintained the MRSI spatial resolution up to 24% above the LRR for NAA and 37% above for Choline, in both noisy and noise-free environments up to an acceleration factor of x5. There appears no benefit of CS-MRSI over the LRR at x10 acceleration factor. The CS-MRSI(identity) maintained spatial resolution up to 68% ± 5% of that of the FSSR at x5 acceleration factor in both noisy and noise free environments. The CS-MRSI wavelet reconstruction had a lower value of spatial resolution at all factors when compared to the CS-MRSI using the identity transform.

Gibbs ringing inherent in the non-filtered FSSR contributing to voxel contamination (section 2.3.1) appears reduced in the plotted profiles of a noise-free scenario for the CS-MRSI up to

x5 acceleration factor. The introduction of noise (SNR10) hampered the assessment of Gibbs ringing but it can be seen on the corresponding plots that again this is reduced up to a factor of x5 for CS-MRSI reconstructions.

The MTF calculated from the ERF in a noise free environment confirmed the same trend as the gradient calculations; however the MTF methodology did not provide a reliable method of MTF calculation once noise was added to the simulation.

The results of this study suggest that CS-MRSI could have a potential advantage in the clinic in place of the standard ringing filter currently used in all MRSI acquisitions. The filter reduces the side lobes of the PSF reducing inter-voxel contamination. Similarly, the CS-MRSI appears to also reduces this ringing but with the added advantage of increased spatial resolution, whilst at the same time accelerating MRSI acquisition by up to 80%!

8 Application of CS-MRSI to Optic Pathway Glioma (OPG)

This chapter examines the effect of CS-MRSI reconstruction on clinical MRSI datasets. The effect of CS-MRSI on image integrity and on inter-voxel contamination was investigated with increasing acceleration factor. Inter-voxel contamination in MRSI presents challenges to the correct delineation of tumour boundaries between healthy and diseased tissue. A tumour type for which correct boundary definition is beneficial is called Optic Pathway Glioma (OPG). OPG is a low grade brain tumour which due to its proximity to the optic nerve presents great challenges in diagnosis and management.

The effect of CS-MRSI on a retrospective real-time OPG MRSI dataset was investigated along with its application to two digital phantom MRSI datasets developed in Chapter 6. Two digital phantoms were created one with a focal OPG tumour, and one with the same tumour but with the addition of tumour infiltration into healthy tissue.

8.1 Introduction to Peadiatric Brain tumours

Brain tumours are the most frequent form of solid cancer in children and exhibit a diversity of histopathological subtypes and grades(Walter and Hilden 2004). A paediatric brain tumor is defined as a mass (neoplasm) of tissue resulting from abnormal proliferation or cell division in the brains of patients who are children or young people. Figure 8-1 indicates an approximate summary of the incidence pediatric brain tumours in children (Pizzo, Poplack et al. 2006).

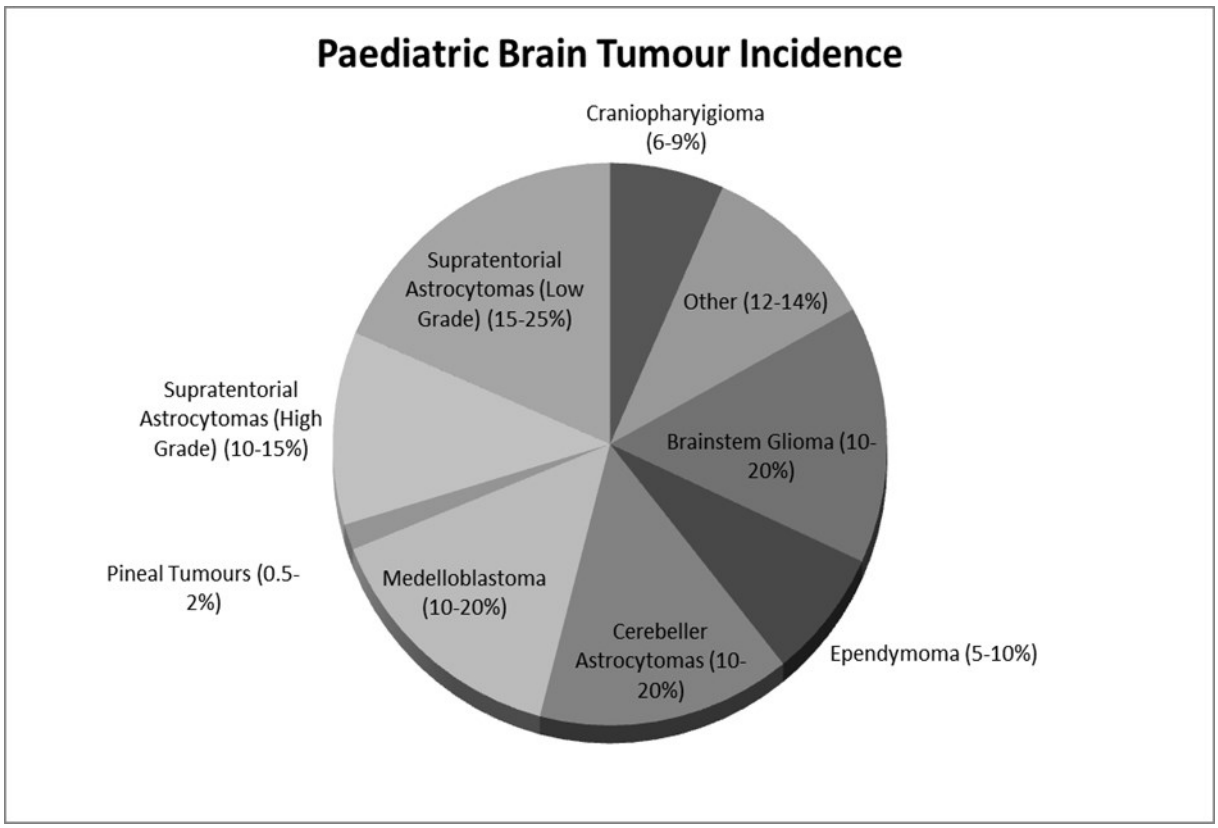

Figure 8-1 Approximate Incidence of paediatric brain tumours (Pizzo, Poplack et al. 2006)

The gold standard in diagnosis is a biopsy allowing classification via histopathology; however this is often hindered by anatomical location or predictability of pathology. Children unable to have surgery are classified via relevant clinical information. Medical imaging is an important part of this.

Paediatric brain tumour classification is defined according to cell type and graded according to histopathology, and from criteria related to growth and aggressiveness such as mitosis and necrosis, as outlined in the 2007 WHO Classification of Tumours of the Central Nervous system (Louis, Ohgaki et al. 2007). Table 4 shows a brief summary of common Central Nervous System (CNS) pediatric brain tumours, their grade and classifications.

Type	SubType	Grade	Location	Diagnosis
Primitive Neuroectodermal Tumours (PNETs)	**Medulloblastoma**	IV	Cerebellum	Histopathology
	Craniopharyigioma	I	Pituitary Gland	
	Pineoblastoma	IV	Pineal gland	
Glial Tumours (Glioma)	**Ependymomas**	II-III	peri-ventricular	
	Astrocytomas			
	Pilocytic	I	Supratentorial/Cerebellum	
	Diffuse	II	Supratentorial/Cerebellum	
	Anaplastic	III	Supratentorial/Cerebellum	
	Glioblastoma Multiforme	IV	Supratentorial/Cerebellum	
	BrainStem Glioma		Brainstem	Radiology
	Diffuse Pontine Glioma (DIPG)	Mixed		
	Optic Pathway Glioma	Low	Supratentorial	

Table 4 Common Peadiatric brain tumours

A range of treatments are available which are tailored dependent upon factors such as tumor subtype, patient age, location and stage of disease. It is often difficult to predict when clinical intervention is necessary in each case or the best course of action to take in the management of the disease. In recent years paediatric brain tumours have exhibited slow improvements in outcome compared to other forms of childhood cancer such as leukaemia, and remain clinically challenging (Pollack and Jakacki 2011). MRI is an invaluable aid in the diagnosis and long term monitoring of this disease and functional imaging methods such as spectroscopy are increasingly being used to add information to this.

8.1.1 Relevance of MRSI

Brain tumours are generally metabolically inhomogeneous, for example the necrotic core of a lesion may have a very different spectral identification to an actively growing tumor edge, and likewise odema surrounding a tumour may also have a very different spectrum from its invasion into neighboring tissue. Therefore, high resolution multi-voxel spectroscopy MRSI is extremely desirable (Lazareff, Bockhorst et al. 1998; Horská and Barker 2010; Stadlbauer, Hammen et al. 2012). MRSI provides an assessment of the spatial distribution of brain metabolites. Individual spectra can be visually assessed at each voxel location or the metabolites can be quantified using available software mentioned in (Section 2.4.6). The

quantified metabolites are often displayed as a metabolite map across the anatomical images. The quantified metabolites or their ratio can be visualized on such maps providing the clinician with an insight into the extent of pathology. An example MRSI can be seen in Figure 8-2. This figure shows metabolite maps as depicted on MR scanner software. The maps show brain metabolites NAA and Cho a), NAA and lipids b) and again NAA and Cho c). The spectrum below each map is from the voxel indicated in green on the figure. The green voxel is located within a region indicated as tumour on the anatomical MRI in a). The green voxel is located outside of the tumour in relatively normal healthy tissue in b), and in c) it is located outside the tumour in an area depicted as having a reduced level of NAA relative to Choline, possibly indicating tumour infiltration. This last voxel in c) appears normal on the anatomical MRI image. Defining the extent of infiltration into the surrounding healthy tissue is of paramount importance in the management of OPG.

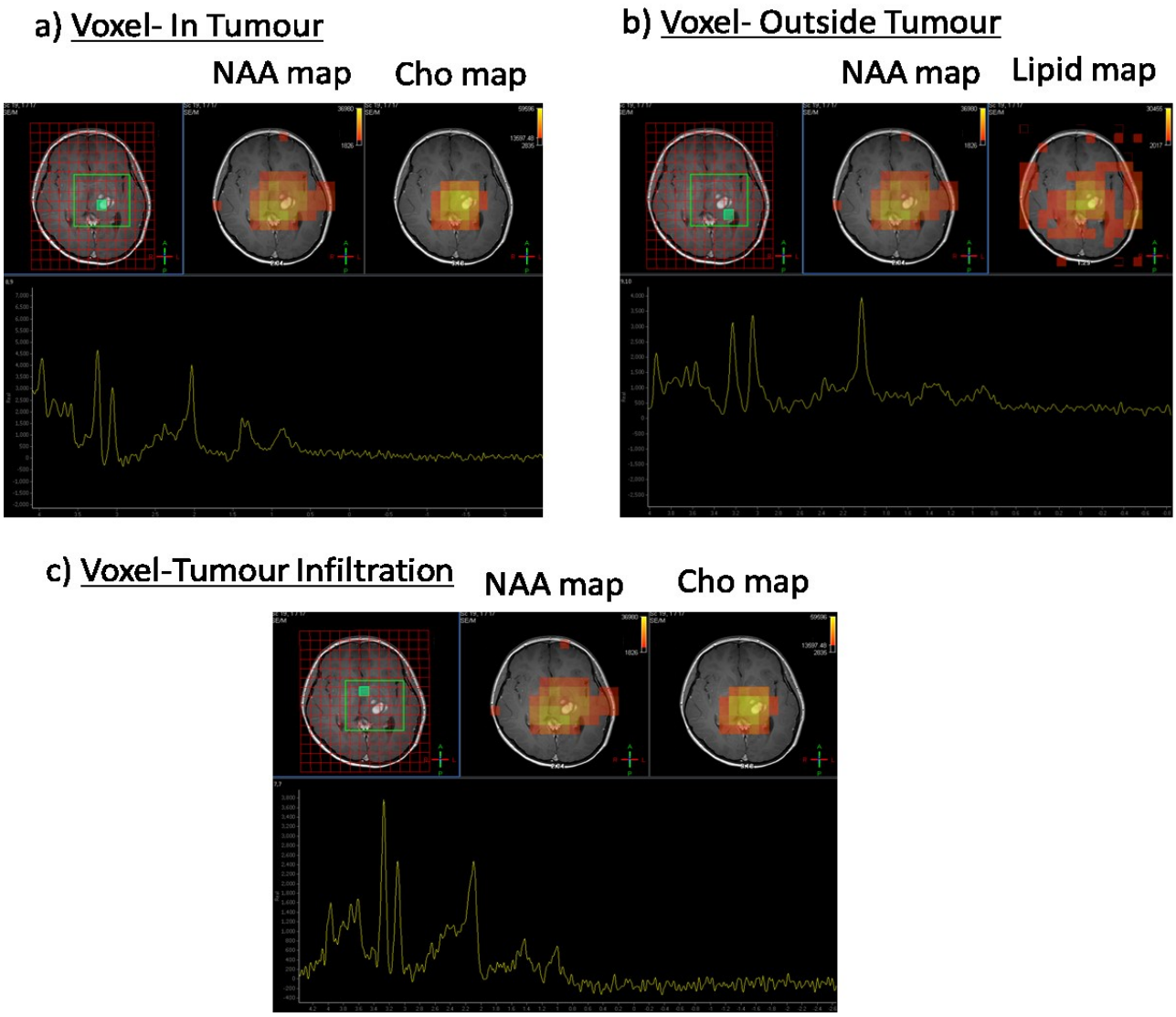

Figure 8-2 MRSI of patient with Optic pathway Glioma. The voxel in a) is taken from an area shown from MRI to be within the tumour, b) is outside of this region and c) is also outside the region but shows pathology not observed on the MRI**.**

8.1.2 Optic Pathway Gliomas (OPG)

The majority of gliomas are low grade tending to be located in the posterior fossa and diencephalic region of the brain. The low grade gliomas are an extremely diverse group in terms of histopathology, age at occurrence and anatomical location. One type of glioma located around the optic pathway which is particularly difficult to manage is the Optic Pathway glioma (OPG) (Hoffman, Humphreys et al. 1993).

A genetic condition known as Neurofibromatosis Type 1 (NF1) predisposes children to OPG (Steen, Taylor et al. 2001). A patient with NF1 exhibits enhancing lesions on MRI termed

Neurofibromatosis Bright Objects (NBO). These are benign lesions, healing or regressing over time. These patients are often rendered with learning difficulties. The difference between NF1 and non NF1 OPG is currently not well understood being undetectable with anatomical MRI. A recent study revealed differences in the MRS spectra obtained between these two patient groups (Orphanidou-Vlachou, Auer et al. 2013). There has also been recent interest in the use of 31-P MRS in the evaluation of choline levels in OPG (Novak, Wilson et al.). The grading of OPG is a challenge. For those that are biopsied the majority of OPGs are histopathologically characterised as Pilocytic Astrocytoma (PA). A biopsy is often not possible however in OPG since it is complicated and risky due to the proximity to the Optic pathway. A biopsy also only samples a small portion of the tumour and may not be indicative of the overall pathology. Some OPG are more aggressive than others. Due its often diffuse and inhomogeneous nature, OPG is not necessarily restricted to a single lesion. Determination of the extent of tumour infiltration into surrounding healthy tissue is of primary importance in the clinical diagnosis and management of OPG and all brain tumours.

8.2 Investigation of CS-MRSI for Characterisation of OPG

The application of CS-MRSI in OPG was investigated in three scenarios. The first was a retrospective investigation of CS-MRSI using real-time OPG patient data acquired on a 3T scanner at standard voxel size. This revealed a potential advantage for CS-MRSI compared to the equivalent LRR reconstructions for some acceleration factors, but was hampered by the low resolution, low data sample size and poor spectral baseline (section 2.2.4 and 2.4.1). It was therefore decided to investigate the application of CS-MRSI to OPG using the digital phantom developed in Chapter 6. The phantom was of a simulated OPG MRSI dataset containing a higher matrix size (40x32). This first simulation was designed to mimic a glioma

with a clearly defined metabolite edge. The second simulation, incorporated tumour infiltration into the healthy surrounding tissue.

8.2.1 Retrospective application of CS-MRSI to in-vivo OPG dataset

8.2.1.1 Method

An OPG patient was scanned on the Philips 3T Achieva scanner using standard clinical protocol with and without the application of the default ringing filter. The data was collected and subsequently under-sampled and reconstructed using CS and LRR. Each reconstruction was quantified using the TARQUIN software and the normalised metabolite outputs examined on Bland-Altman plots.

A non-NF1 OPG patient was subject to two MRSI acquisitions on the Philips 3T scanner. A non-NF1 patient was chosen for the investigation since the lesions tend to be less diffuse. Standard clinical protocol was followed for the first scan. This consists of a PRESS acquisition, short echo TE=35ms, TR=2000ms, 1024 data points collected. The FOV was (195mm x 165mm), voxel size (13mm x 13mm x 13mm), matrix size 15x13. The planning of the MRSI can be seen in Figure 8-3.

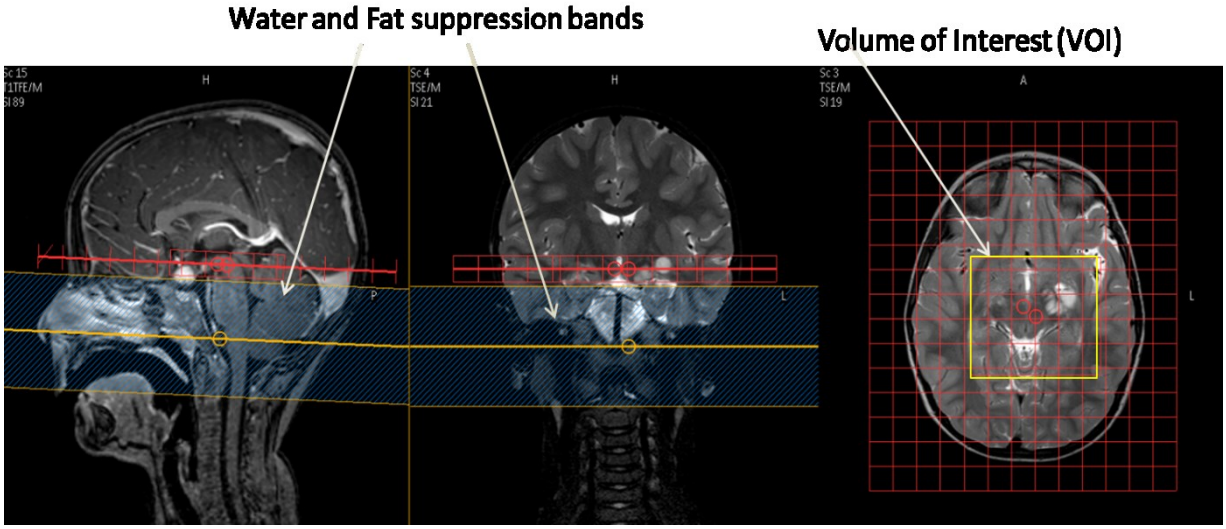

Figure 8-3- The PRESS MRSI planning of the OPG patient

The red line in the figure indicates the MRSI slab. The optic pathway is low down in the brain so a water and a fat suppression band Section(2.2.5) was added to the scan in order to prevent any air-tissue susceptibility artefacts from the nasal sinus's. The VOI shown in yellow on Figure 8-3 consists of 4x4 whole voxels surrounded by a half voxel margin to reduce any chemical shift artefact (Section 2.3.3). The first scan was acquired with the k-space shutter and application of the ringing filter as required in clinical protocol. The second scan was acquired in exactly the same way except the ringing filter was removed. This second acquisition was required because section 7.1.3 showed that the addition of filtering may reduce the metabolite spatial resolution. This section also indicated that the CS reconstruction appeared to reduce the inter-voxel contamination (2.3.1) from distant voxels (Gibbs ringing artefact), whilst maintaining the spatial resolution which is hampered by adjacent voxel contamination. Residual water removal was achieved prior to reconstruction by implementation of the HSVD algorithm ((Pijnappela 1992). The non-filtered MRSI (FSSR) dataset was subject to reconstruction by CS at acceleration factors of x2, x3.3, x4, x5 and x10 using both CS-MRSI(identity) and CS-MRSI(wavelet). The LRR was also reconstructed for each equivalent acceleration factor for comparison. The metabolites were then quantified using the TARQUIN software (section 2.4.6) and metabolite maps displayed for NAA, Creatine and Choline. Bland-Altman statistics were also calculated and plotted for each reconstruction.

8.2.1.2 Results and Discussion

The metabolite maps for NAA, Cr and Cho after reconstruction using CS-MRSI utilising the Identity as the sparse domain, utilising wavelets as the sparse domain, and the equivalent LRR, can be seen in respectively in Figure 8-4, Figure 8-5 and Figure 8-6. Each figure shows the map for the FSSR with and without filtration.

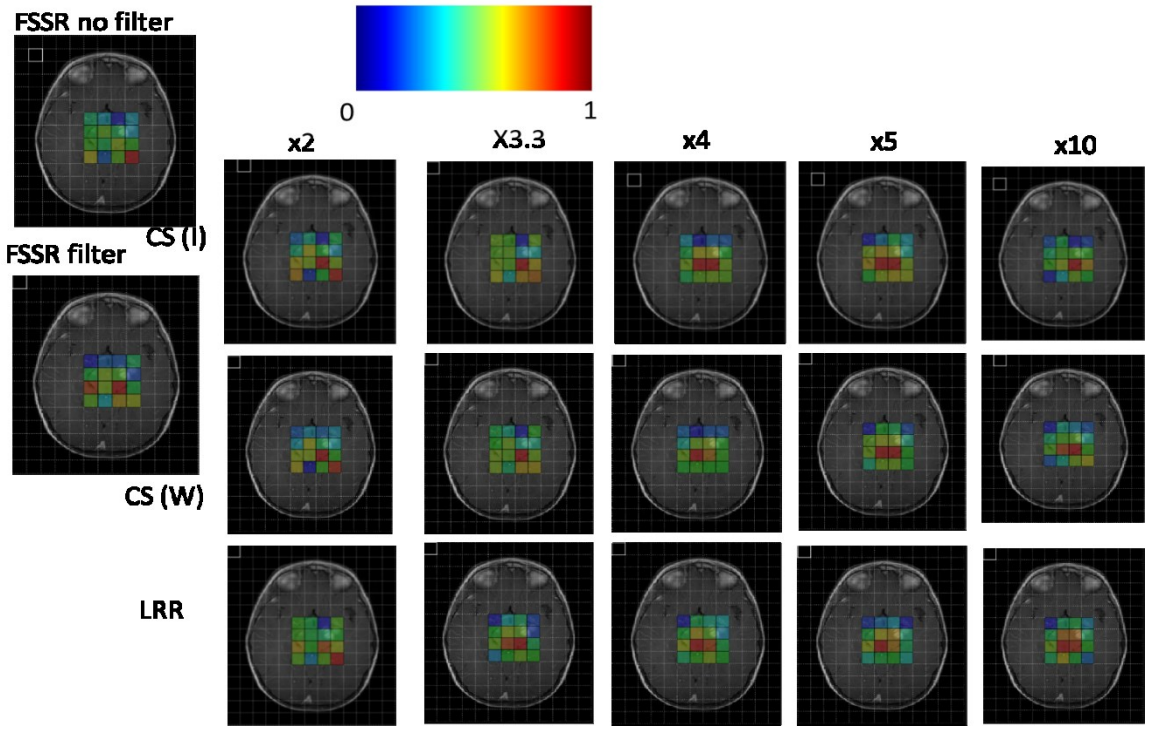

Figure 8-4 – NAA Metabolite maps for the OPG patient MRSI dataset utilising CS-MRSI(identity) and CS-MRSI(wavelets) and the LRR reconstructions as compared to the FSSR with and without filtering. The colour maps are normalised to the highest pixel value.

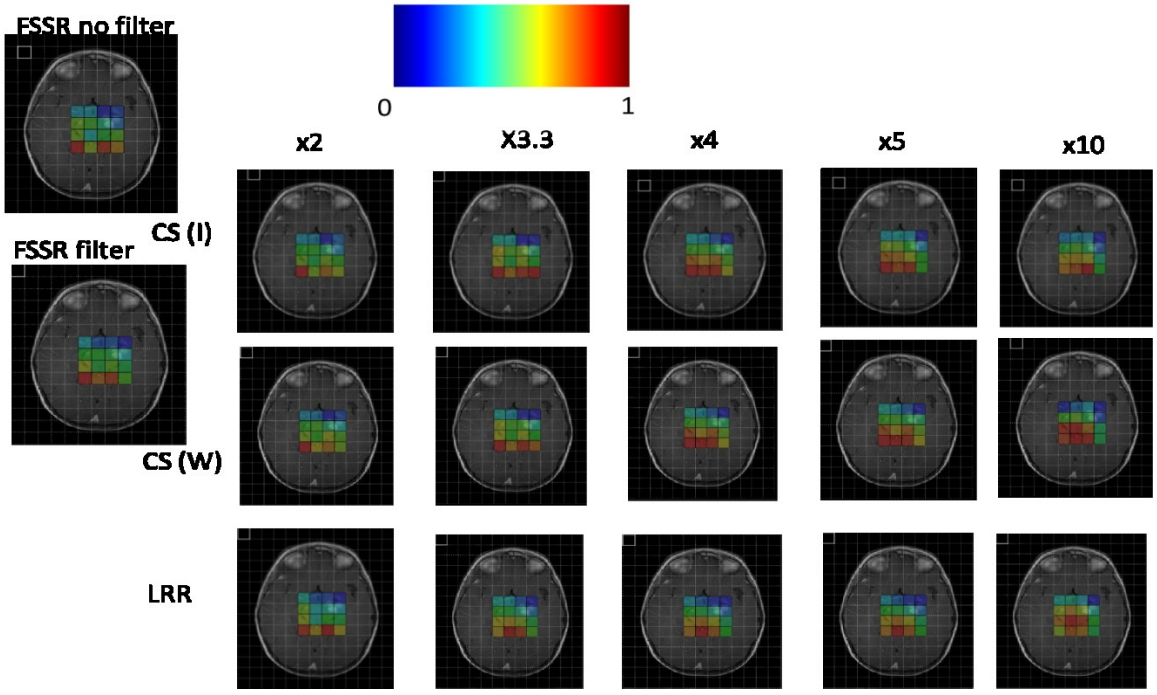

Figure 8-5 - Creatine Metabolite maps for the OPG patient MRSI dataset utilising CS-MRSI(identity) and CS-MRSI(wavelets) and the LRR reconstructions as compared to the FSSR with and without filtering. The colour maps are normalised to the highest pixel value.

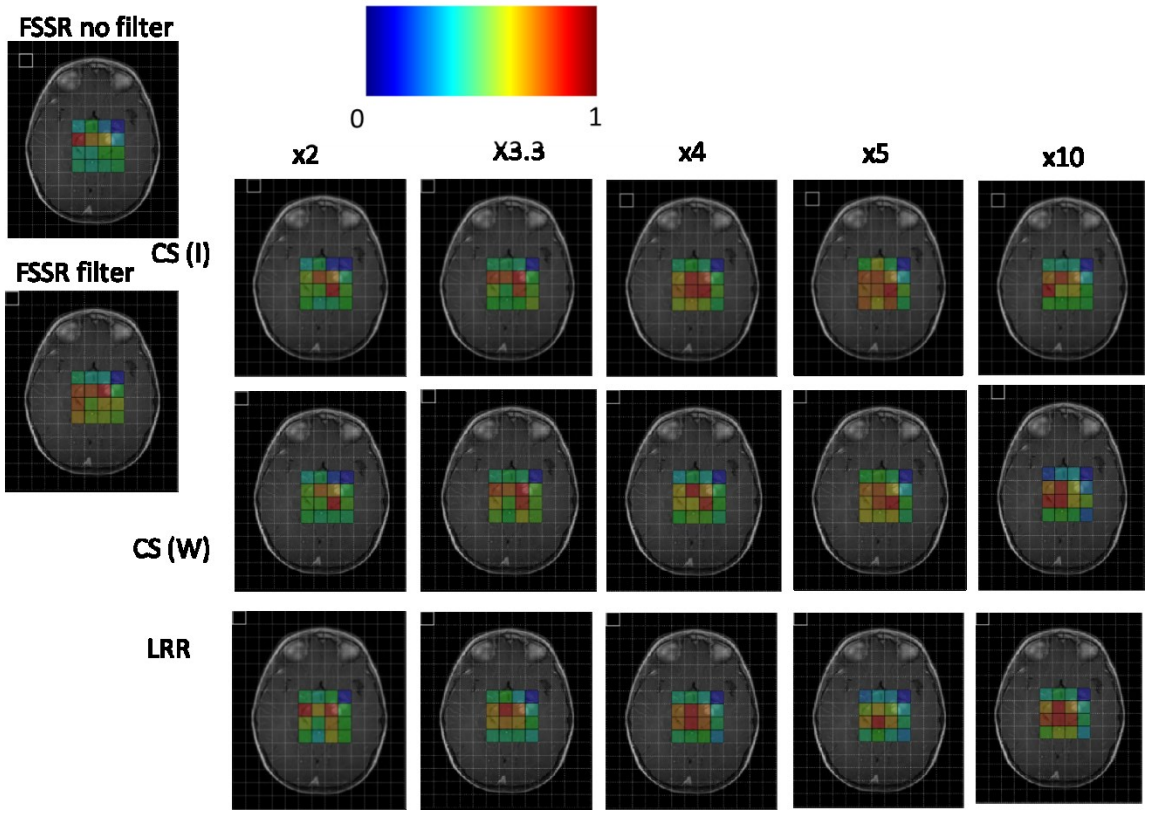

Figure 8-6 - Choline Metabolite maps for the OPG patient MRSI dataset utilising CS-MRSI(identity) and CS-MRSI(wavelets) and the LRR reconstructions as compared to the FSSR with and without filtering. The colour maps are normalised to the highest pixel value.

Since the OPG MRSI dataset is of such low resolution at 13mmx 13mm x13mm voxel size, it is difficult to draw conclusions from the metabolite maps. Each metabolite displays variation between the filtered and non-filtered datasets. Bland-Altman statistics were plotted to provide a quantification of the differences between the reconstructions.

The Bland-Altman plot for NAA, Cr and Cho after reconstruction using CS-MRSI utilising the Identity as the sparse domain, and the equivalent LRR, can be seen in respectively in Figure 8-7, Figure 8-8 and Figure 8-9.

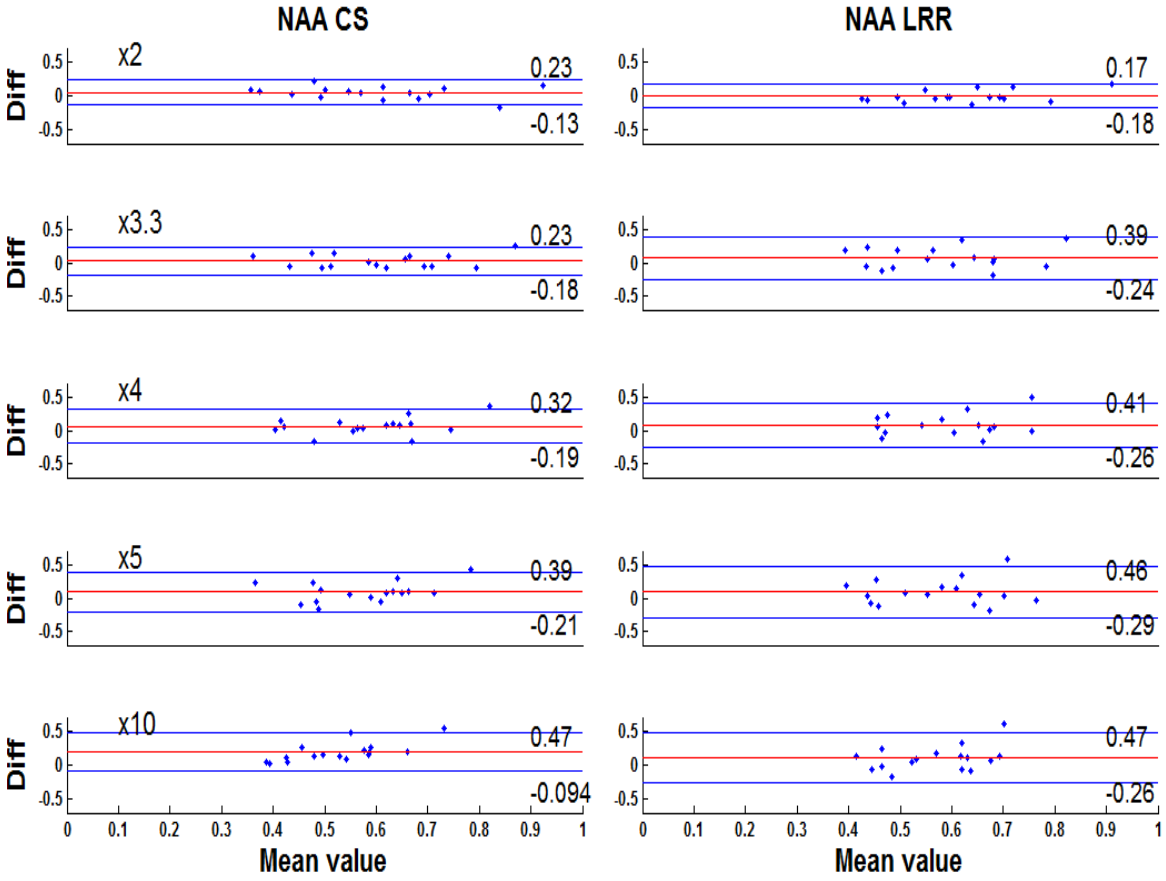

Figure 8-7 Bland-Altman plot of the NAA after reconstruction as compared to the non-filtered FSSR, using CS-MRSI(Identity) and the equivalent LRR at each acceleration factor. The nRMSE is indicated on each plot.

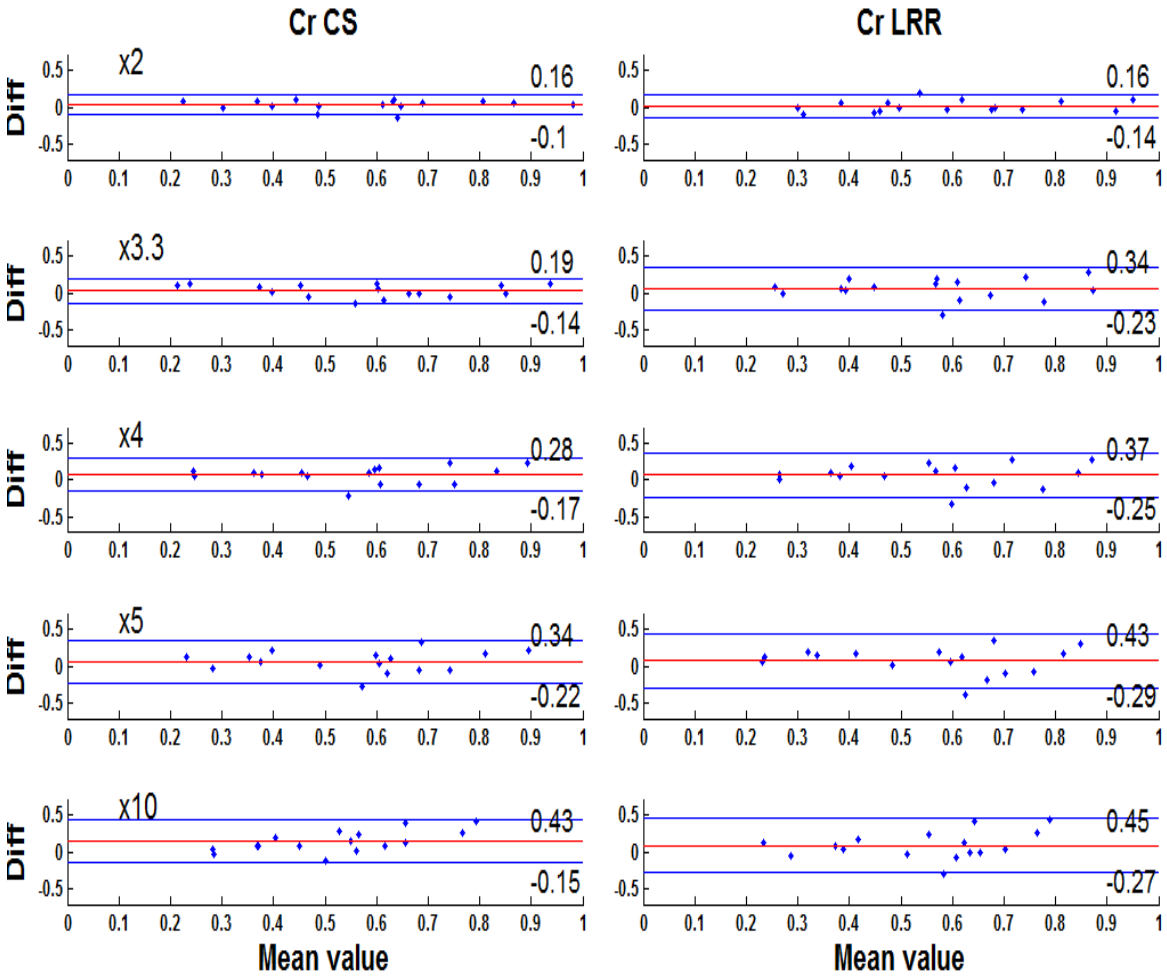

Figure 8-8 - Bland-Altman plot of the Creatine after reconstruction as compared to the non-filtered FSSR, using CS-MRSI(Identity) and the equivalent LRR at each acceleration factor.

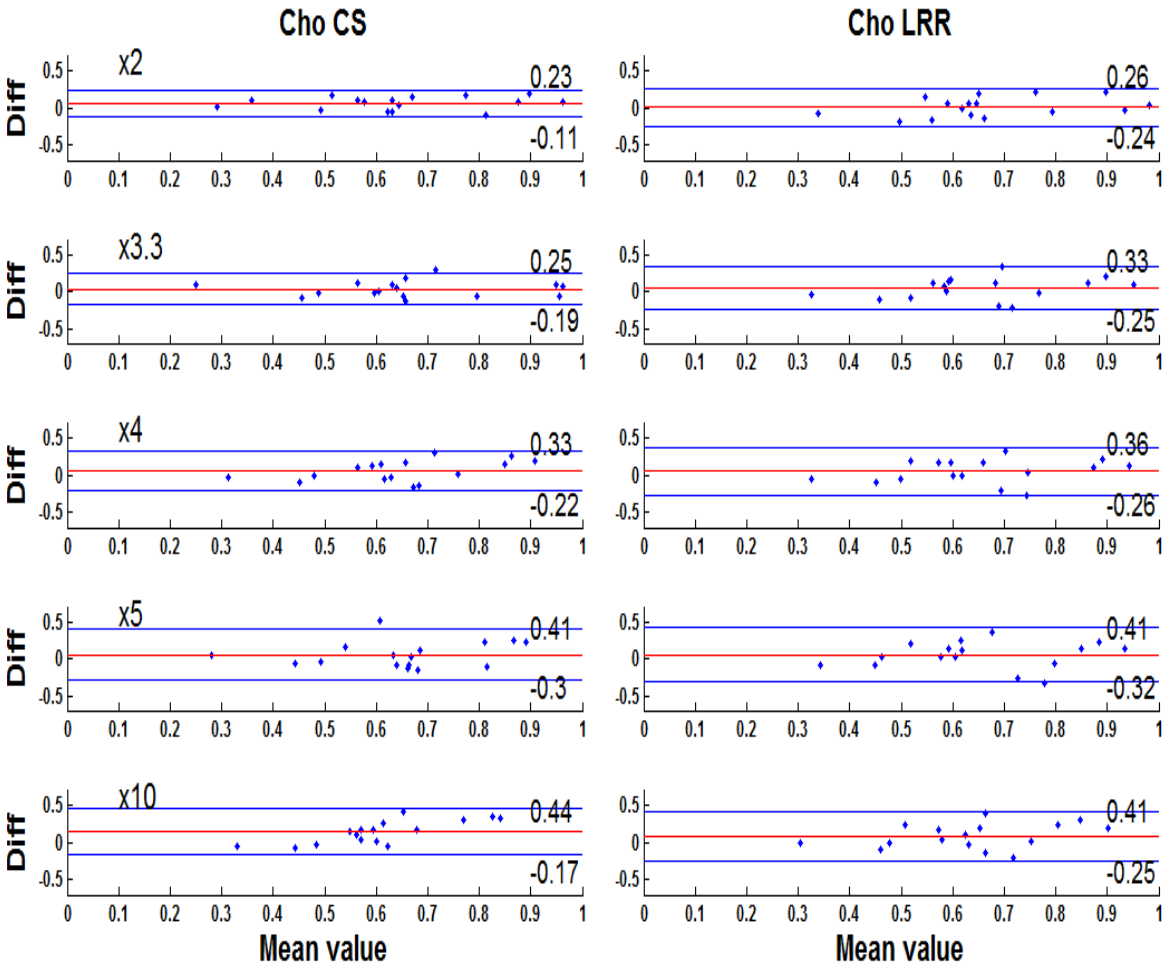

Figure 8-9- Bland-Altman plot of the Choline after reconstruction as compared to the non-filtered FSSR, using CS-MRSI(Identity) and the equivalent LRR at each acceleration factor.

The Bland Altman plots for NAA, Cr and Cho again using acceleration factors x2, x3.3, x4, x5 and x10, can be seen respectively in Figure 8-10, Figure 8-11 and Figure 8-12 for CS-MRSI reconstructed using wavelets as the sparse domain.

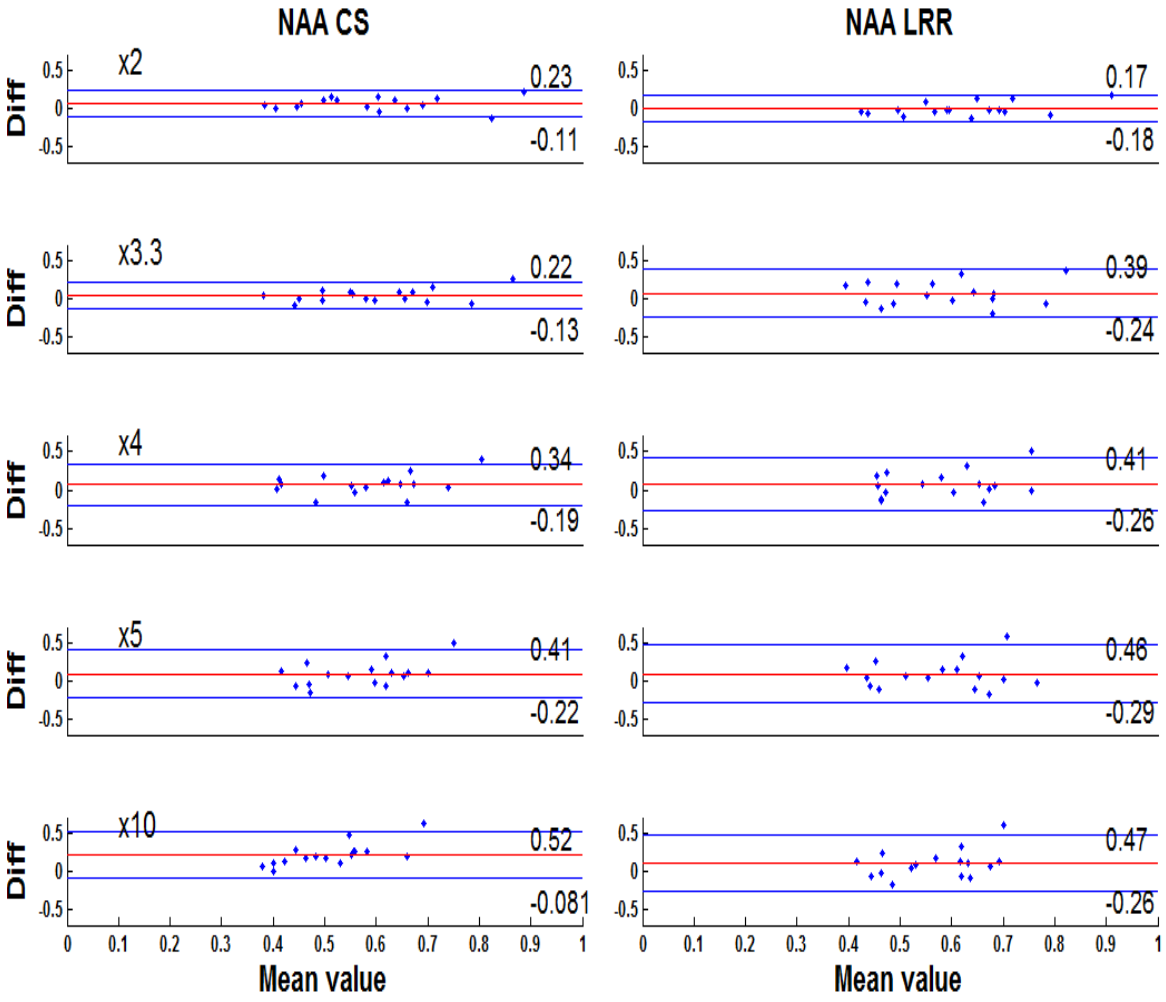

Figure 8-10 - Bland-Altman plot of the NAA after reconstruction as compared to the non-filtered FSSR, using CS-MRS (wavelet) and the equivalent LRR at each acceleration factor.

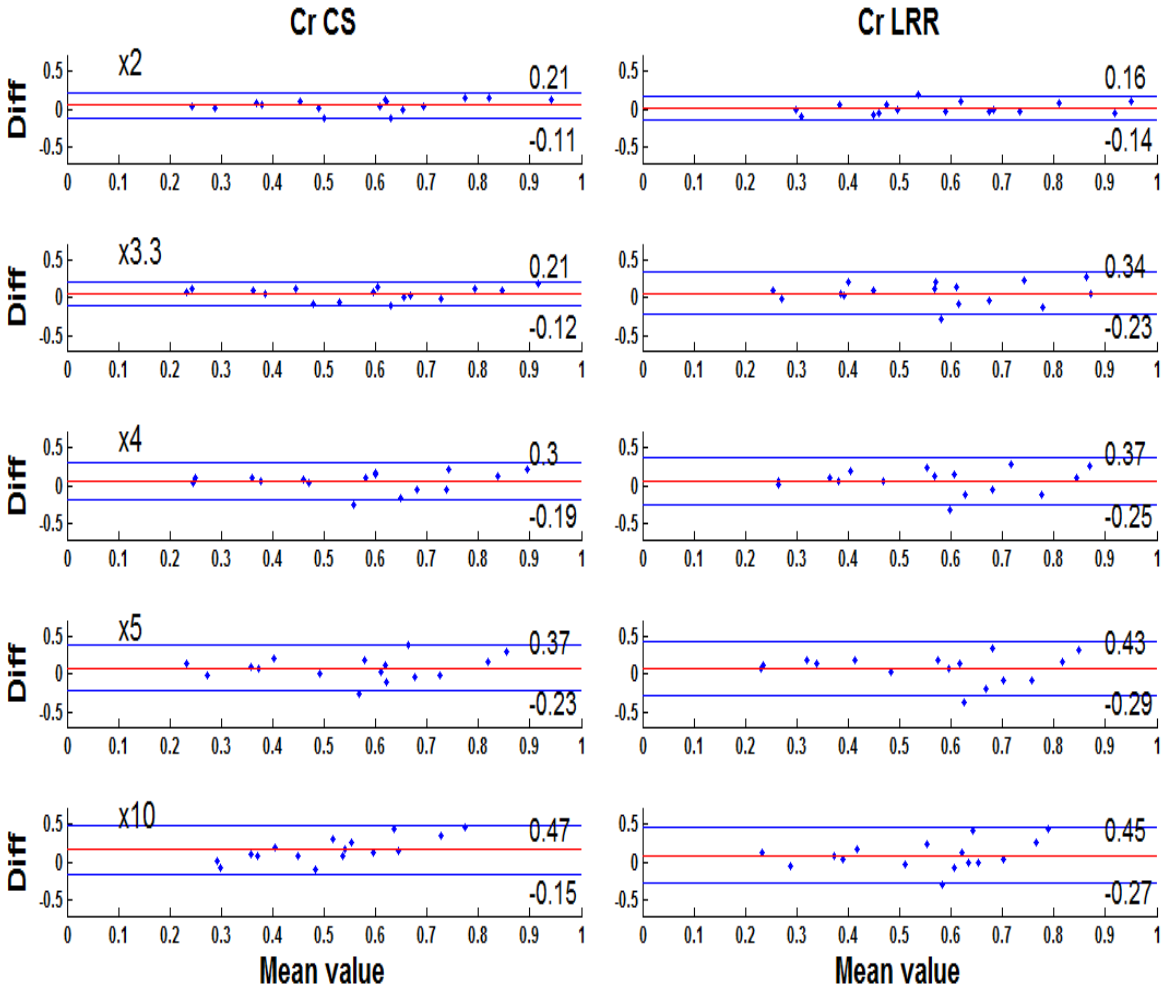

Figure 8-11 - Bland-Altman plot of the Creatine after reconstruction as compared to the non-filtered FSSR, using CS-MRSI(wavelet) and the equivalent LRR at each acceleration factor.

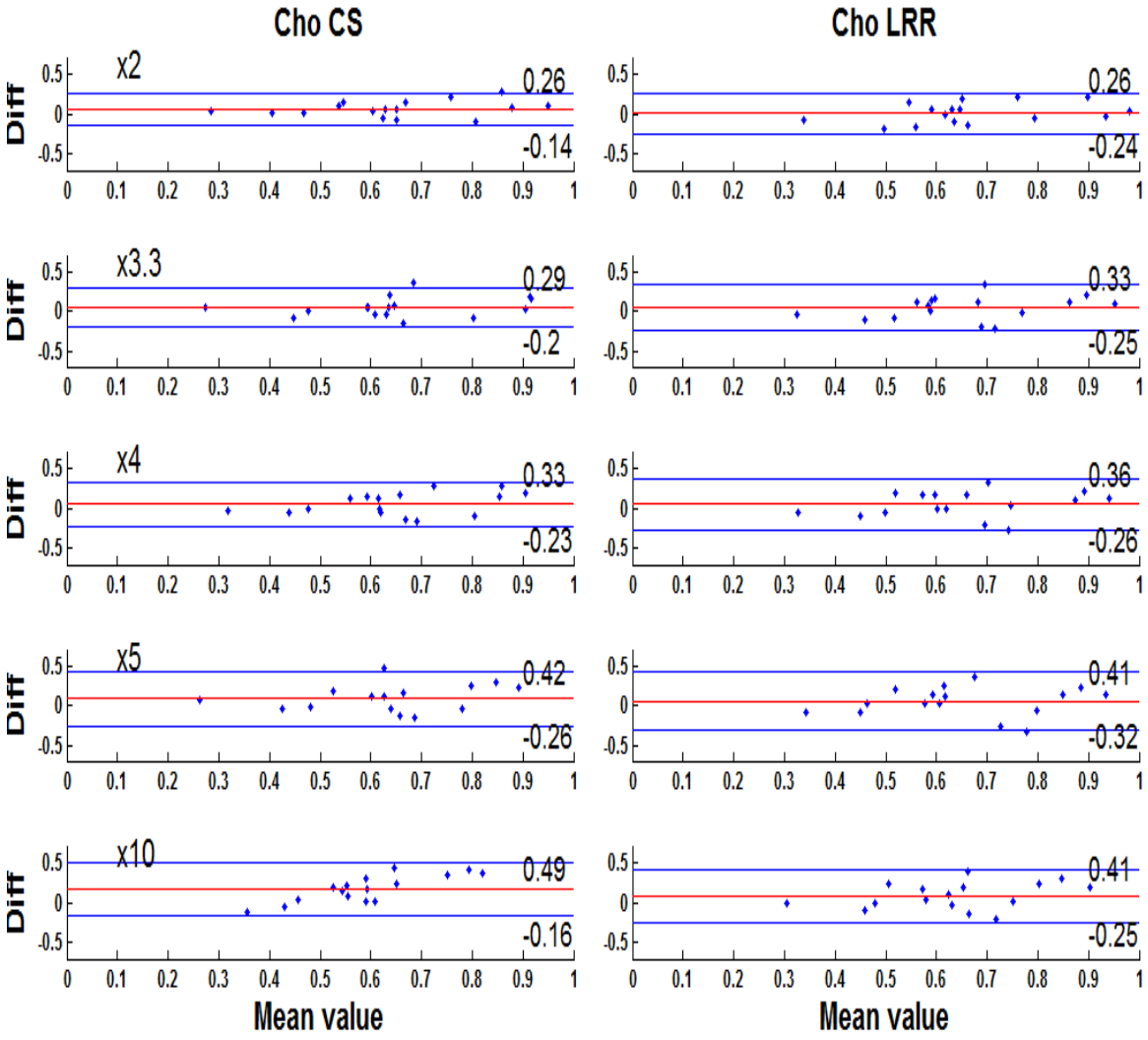

Figure 8-12 - Bland-Altman plot of the Choline after reconstruction as compared to the non-filtered FSSR, using CS-MRSI(wavelet) and the equivalent LRR at each acceleration factor.

The Bland-Altman plots for each metabolite indicate that there is a potential advantage of CS over the LRR reconstructions with a reduction in the standard deviation of the mean difference up to an acceleration factor of x5 for both CS-MRSI(wavelets) and CS-MRSI(identity). The CS reconstructions and the LRR appear to have a consistently positive mean difference indicated by the red line on all plots. This implies that both CS and LRR reconstructions are slightly underestimating the metabolite concentrations relative to the FSSR.

The OPG patient MRSI acquisition is of very low resolution at 13mm x13mm x13mm voxel dimension. This meant that the VOI contained only 16 data points for analysis. A larger matrix size acquisition may greatly help the statistical evaluation of the merits of the CS reconstruction by providing a greater number of data points. This may help determine if there is a significant advantage of CS-MRSI over the LRR at x5 and x10 acceleration factors. Since a real-time acquisition of a high matrix size MRSI dataset is prohibitive due to time constraints, the software simulated digital phantom was utilised for the evaluation of CS in OPG.

8.2.2 Simulations of CS-MRSI in OPG Using Digital Phantoms

The delineation between tumour and healthy tissue is extremely important in the clinical management of brain tumours. Inter-voxel contamination (section 2.3.1) which causes signal to bleed through from one MRSI voxel to another can incorrectly cause the appearance of tumour infiltration. Therefore, it is important that the employed reconstruction technique minimises any possible signal bleed through. To test this in a clinical scenario the digital phantom developed in section 6 was adapted, once to mimic a single, focal OPG tumour and once again to mimic an OPG tumour containing infiltrative disease.

8.2.2.1 Method - Focal OPG Simulation

The digital phantom was created using the methodology outlined in section 6.1. In summary each 1mm x1mm x1mm pixel is assigned a spectrum relevant to its anatomical location to create an MRSI dataset with spatial and frequency dimensions (x,y,f). The spatial resolution is then reduced by the truncation of k-space (section 6.1.3). In this scenario the pixel or voxel size dimension was reduced from (1mm x 1mm x 5mm) to (5mm x5mm x5mm). The FOV was 200mm x 160mm so the new matrix size was (40x32). Real-time acquisition of a 2D phase encoded MRSI dataset with this matrix size would not be feasible due to the long acquisition

time. There was no residual water peak added to the simulated spectra. In reality there is always some residual water which may have an effect upon the quality of the spectral baseline section (2.4.1). It was decided not to add a residual water peak because the residual water signal height in a real-time acquisition is inconsistently distributed. Residual water is usually removed post processing and it may have an influence on the compressed sensing reconstruction (Cao and Wu 2014). In a real-time acquisition scenario, the residual water signal could be removed by scanner software prior to reconstruction. The simulation software also assumes a uniform magnetic shim across the head (section 2.2.2.1). Currently, in a real-time acquisition scenario this is not the case. Future hardware developments may be perfected to reduce shim imperfections. The variation in magnetic field across the head can be hard to predict so completely removing this artefact would improve data comparison. In a real-time acquisition scenario there is often contamination in the spectra from high signal lipid bleed through (section 2.3.1) from subcutaneous fat. Healthy brain tissue does not normally produce a high lipid signal. Clinical protocol utlises the PRESS MRSI sequence (section 2.2.1). MRSI spectra can be improved by placement of the PRESS VOI central in the brain, away from the lipid area around the inside of the skull (section 2.2.5). Therefore, the simulation's VOI was located centrally, encompassing the OPG region. No lipid signal was added to the spectra in areas of healthy grey and white matter. In order to assess the introduction of inter-voxel contamination from the reconstructions into the surrounding healthy brain tissue, a focal tumour with defined edges was initially simulated. An area was defined as an OPG lesion Figure 8-13. Although in reality lesion dimensions associated with OPG are varied, the simulated OPG region was drawn manually and checked by a clinician for authenticity of size and shape.

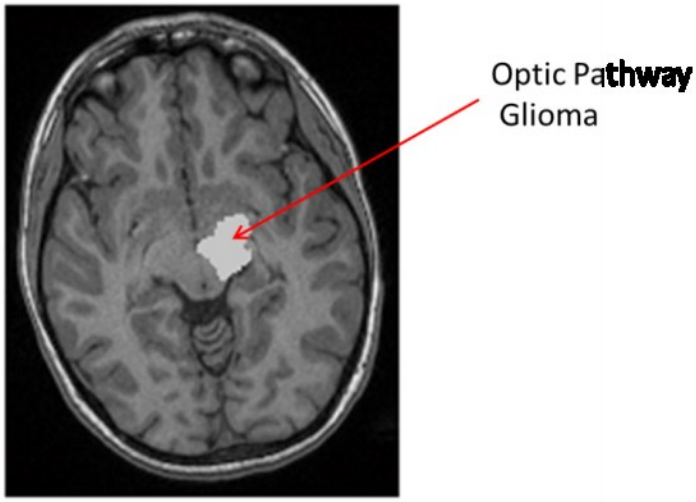

Figure 8-13 – The anatomical MRI template indicating the area of artificial OPG

Each 1mm pixel in the area defined in Figure 8-13 was assigned the spectrum of metabolites consistent with an OPG, before increasing the voxel size. The values of metabolite concentration used in the simulated lesion were those previously quantified using TARQUIN (section 2.4.6) from an existing non-NFI OPG patient, single voxel dataset, previously acquired on the 3T scanner. The 3T basis set utilised in the simulation was weighted according to these quantified concentrations to obtain the simulated OPG spectrum. An example of the simulated spectrum before the addition of noise can be seen Figure 8-14. Random, Gaussian noise was then added to all spectra to provide a clinically relevant level of noise at an SNR of 10.

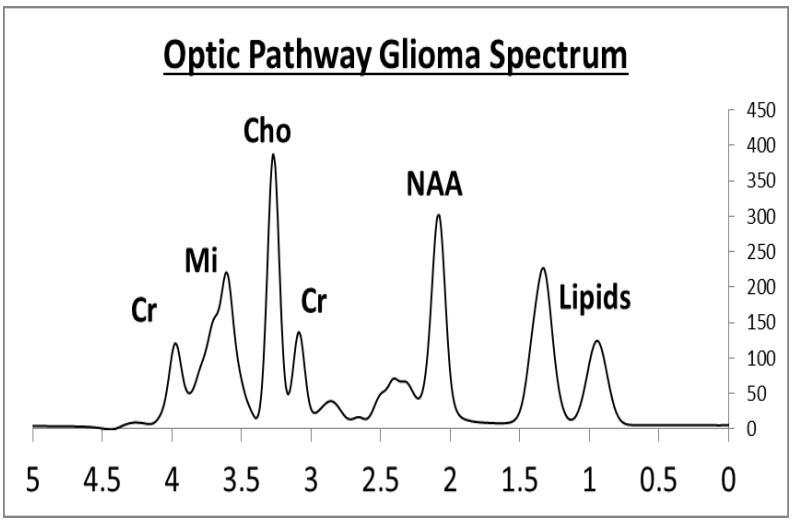

Figure 8-14- Software simulated, OPG Spectrum before the addition of noise.

After the assignment of the appropriate spectrum to each pixel in Figure 8-13, the area shown in Figure 8-15 was defined as the PRESS VOI.

Figure 8-15 The region within the FOV defined as the simulated PRESS acquisition Volume of Interest (VOI).

Once the appropriate spectra were added to each pixel in the anatomical MRI, the voxel size was then increased to (5mm x5mm x5mm) (Section 6.1.3). An FSSR with and without filtration was simulated. The filter was the Hamming filter (section 2.3.1). The reconstructions at each acceleration factor were achieved on the non-filtered dataset since the previous section 7.1.2 indicated that the addition of filtration reduces the maximum spatial resolution of the MRSI.

The CS reconstructions were achieved utilising both the identity and the wavelet transforms. Acceleration factors of x2, x3.33, x4, x5 and x10 were reconstructed. The wavelet transform employed a Daubechie wavelet 1 (Haar wavelet) with level 2. Reconstruction was also achieved for the equivalent LRR at each factor for comparison. After reconstruction the datasets were quantified for relative metabolite level with the TARQUIN software. A region of interest (13x13 voxels) equivalent to the PRESS VOI was quantified Figure 8-16.

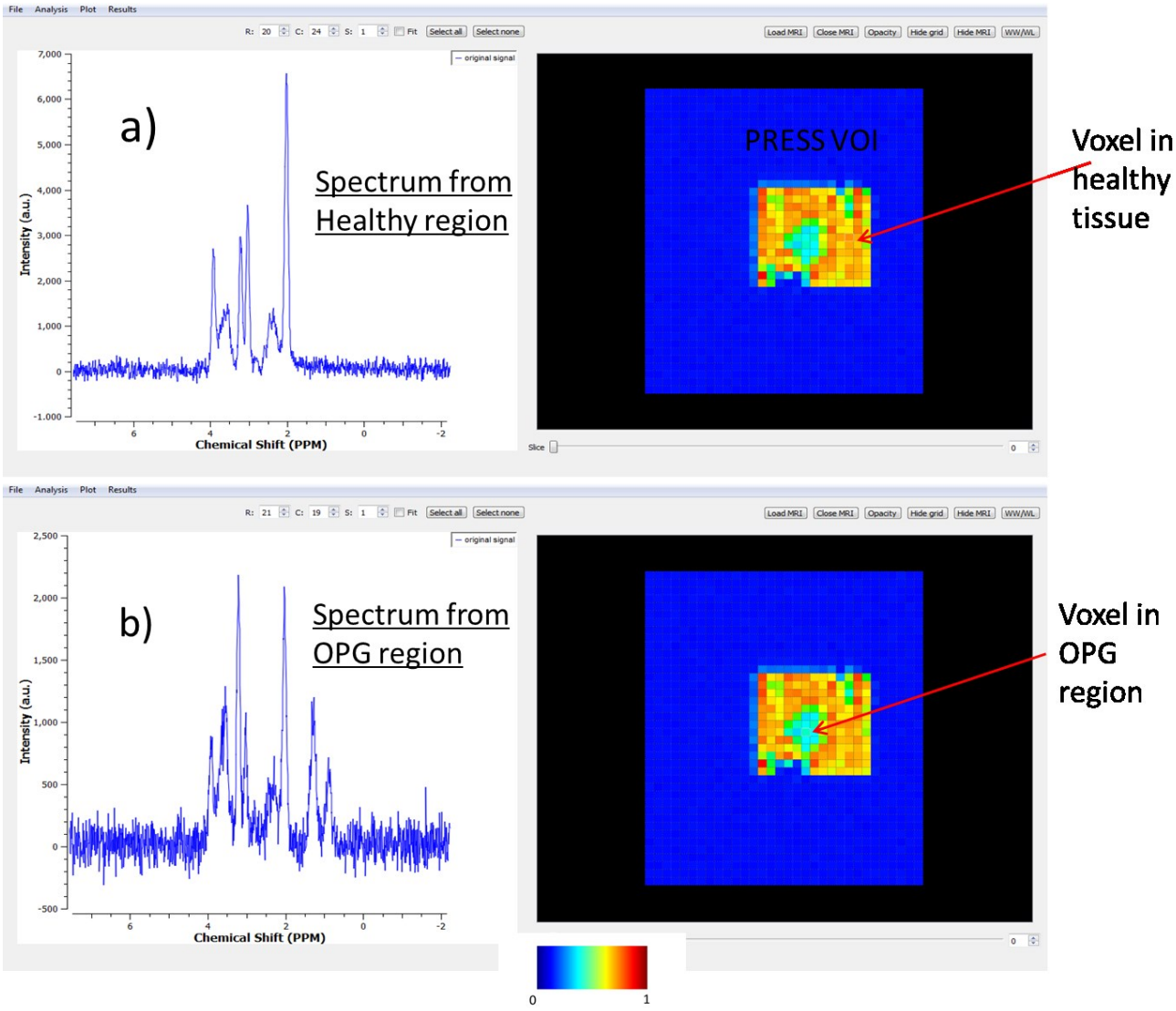

Figure 8-16 – The TARQUIN screenshots depicting the FSSR PRESS VOI used for quantification. A spectrum from the area of healthy tissue is shown in a) and from the OPG region b).

Bland-Altman plots were constructed for NAA, Creatine, Choline and Myo-Inositol metabolites and lipids. Myo-Inositol and lipids were included since these are often elevated relative to healthy tissue in OPG(Orphanidou-Vlachou, Auer et al. 2013). The Bland-Altman statistics were calculated relative to the non-filtered FSSR at each acceleration factor. Plots for the CS-MRSI and the LRR were plotted together for comparison. The Bland-Altman plots were calculated separately for the identity sparse domain, and the wavelet domains, for comparison. The normalised Root mean square (nRMSE) at each acceleration factor was also calculated. Bland-Altman plots were achieved showing the difference from the non-filtered

FSSR against the mean difference for each metabolite for the two different transform domains (Identity and wavelet), and the LRR, at each acceleration factor.

8.2.2.2 Method - Infiltrative OPG Simulation

The exact same methodology as outlined in section (8.2.2.1) was applied to a second OPG simulation. The difference between this and the previous simulation is that there was a simulated 15mm border region around the lesion with a different metabolite profile. Each pixel within the border contained 50% healthy spectra and 50% OPG spectra, Figure 8-17.

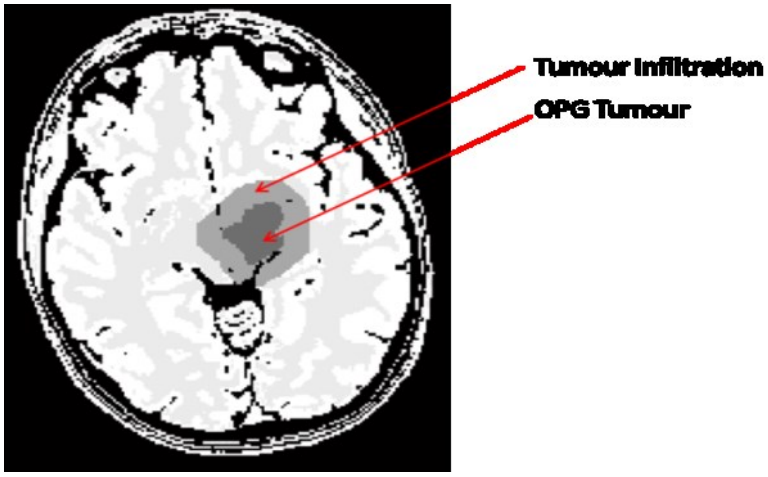

Figure 8-17 – Depiction of the MRSI simulation of an OPG with tumour infiltration into the surrounding healthy tissue.

The data were reconstructed and analysed as described in the previous section.

8.2.2.3 Results – Focal OPG Simulation

Bland Altman statistics were calculated and plotted for the NAA, Creatine, Choline and Myo-Inositol metabolites and lipids based upon the concentrations quantified by TARQUIN. The CS reconstruction using the Identity as the sparse domain are depicted alongside those from the LRR reconstruction, Figure 8-18, Figure 8-19 and Figure 8-20.

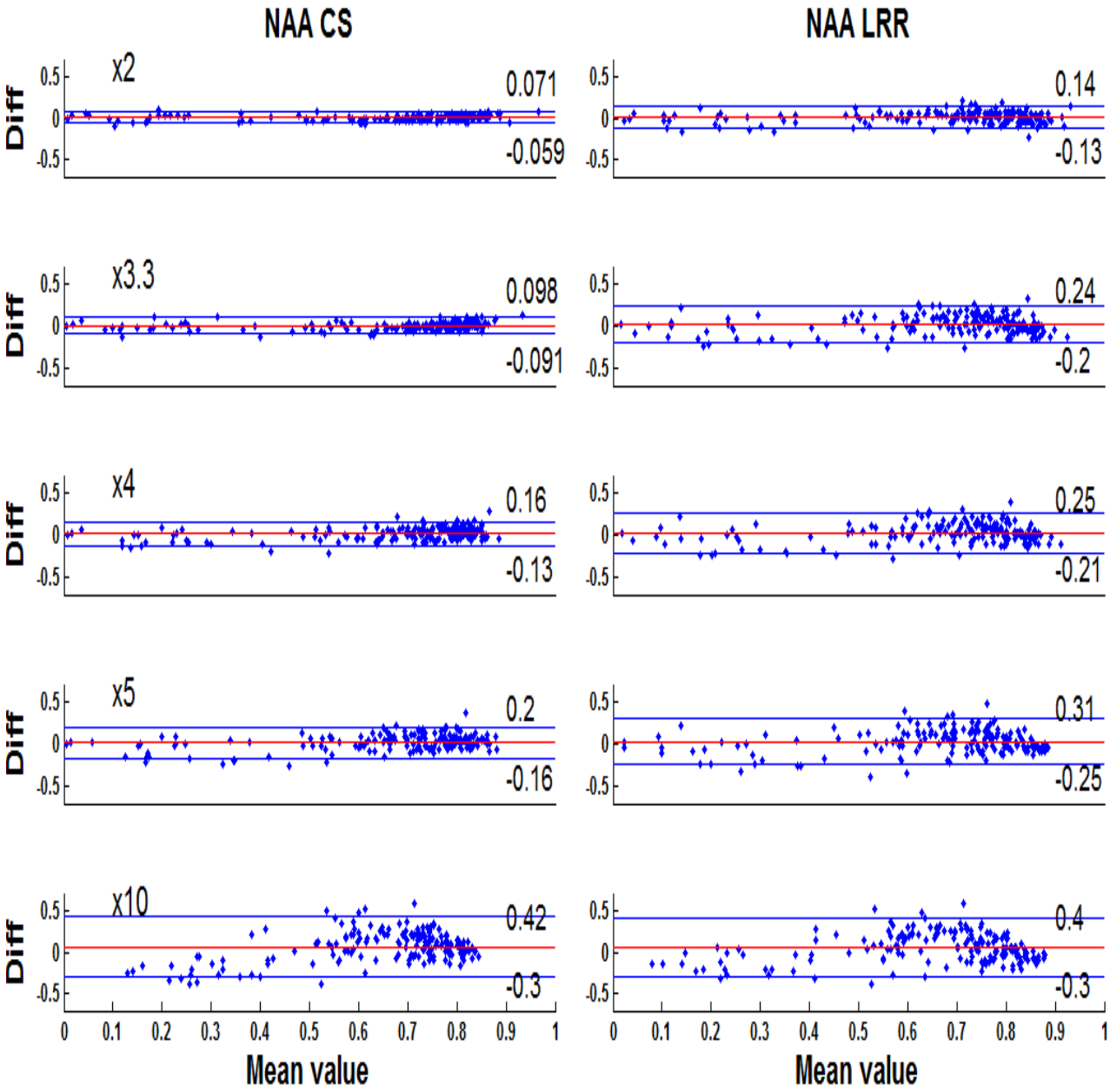

Figure 8-18 – Bland-Altman plots for NAA at each acceleration factor. CS-MRSI(identity) is shown on the LHS and the equivalent LRR on the RHS. (Focal OPG simulation).

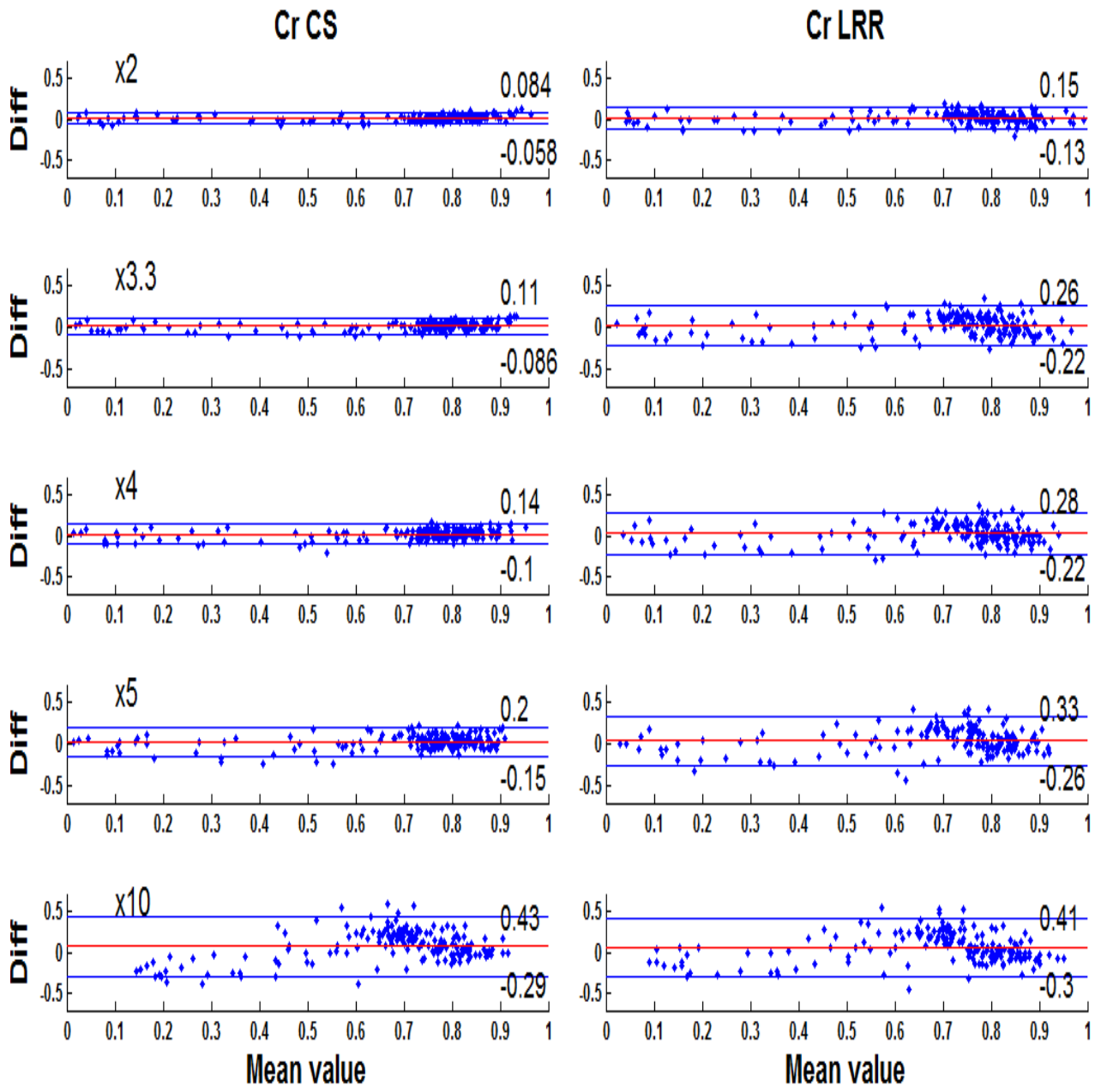

Figure 8-19- Bland-Altman plots for Creatine at each acceleration factor. CS-MRSI(identity) is shown on the LHS and the equivalent LRR on the RHS. (Focal OPG simulation).

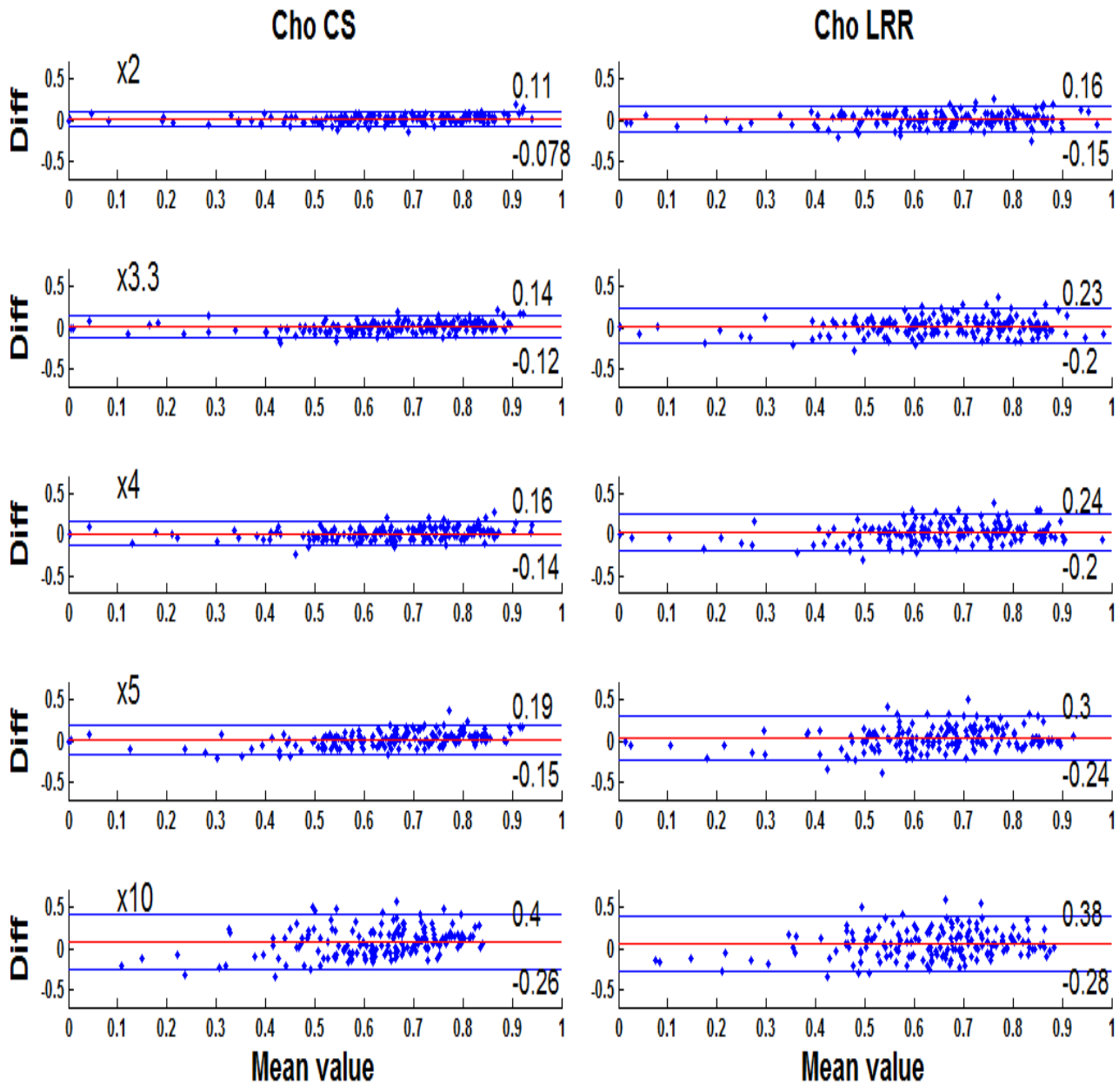

Figure 8-20 - Bland-Altman plots for Choline at each acceleration factor. CS-MRSI(identity) is shown on the LHS and the equivalent LRR on the RHS. (Focal OPG simulation).

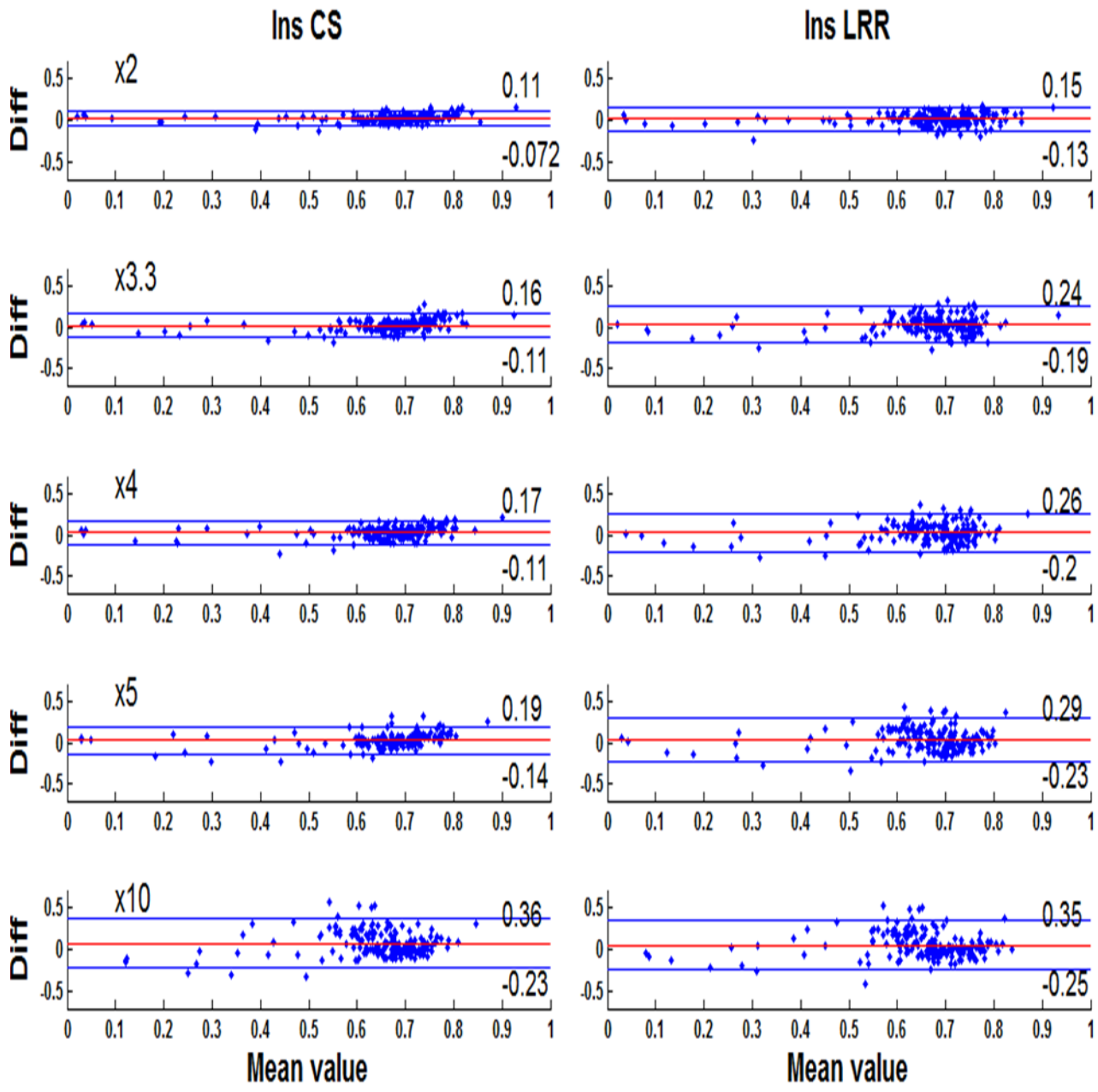

Figure 8-21 - Bland-Altman plots for Myo-Inositol at each acceleration factor. CS-MRSI(identity) is shown on the LHS and the equivalent LRR on the RHS. (Focal OPG simulation).

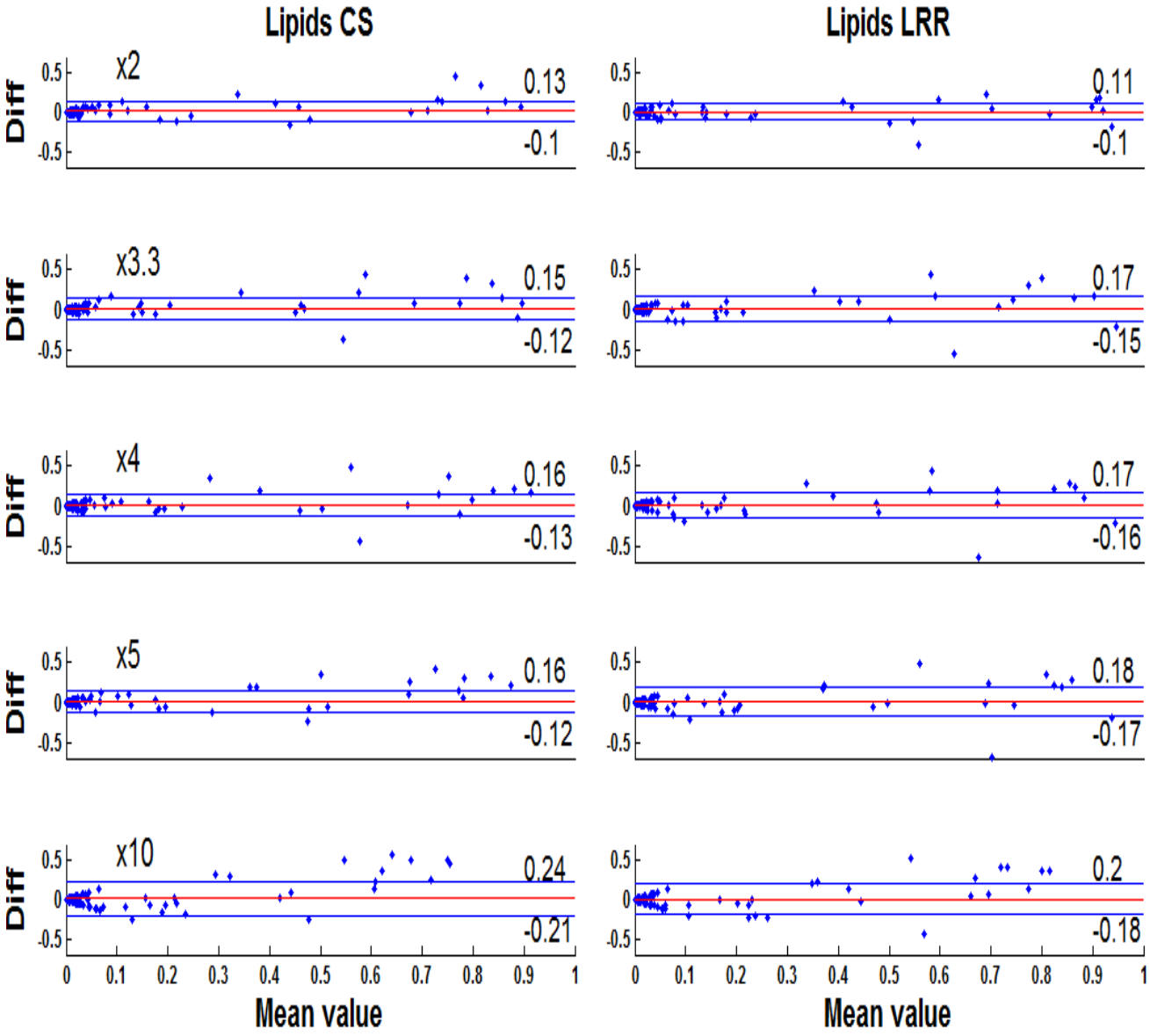

Figure 8-22 - Bland-Altman plots for lipids at each acceleration factor. CS-MRSI(identity) is shown on the LHS and the equivalent LRR on the RHS. (Focal OPG simulation).

The nRMSE, the standard deviation and the mean diff relative to the FSSR (no filtering) for CS-MRSI(identity), CS-MRSI(wavelet) and LRR, were plotted against acceleration factor for metabolites NAA, Creatine, Choline, Myo-Insositol and for lipids Figure 8-23, Figure 8-24, Figure 8-25, Figure 8-26 and Figure 8-27.

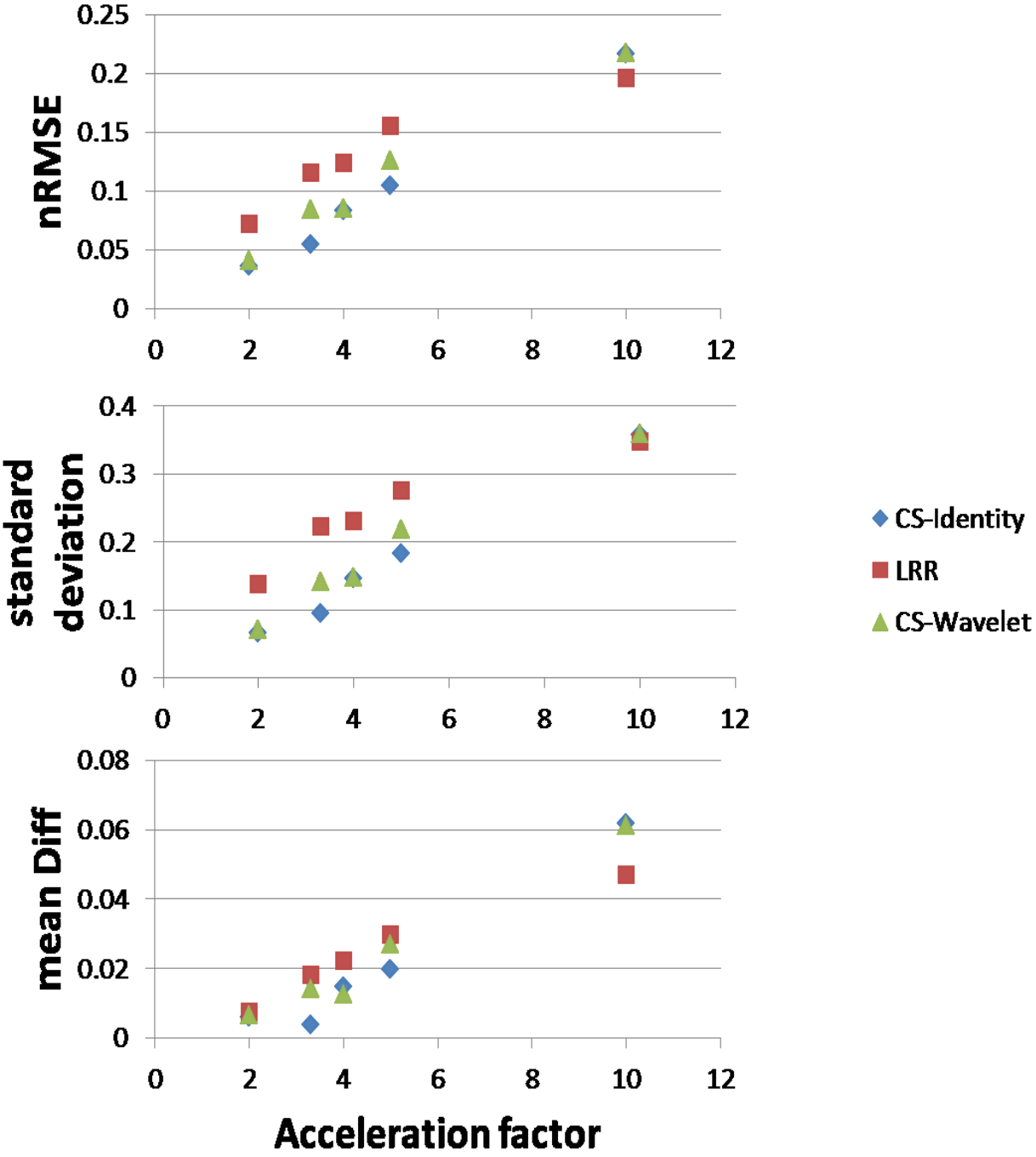

Figure 8-23 – The normalised Root mean square error, the standard deviation and the mean difference between each reconstruction and the non-filtered FSSR.for NAA. (Focal OPG simulation).

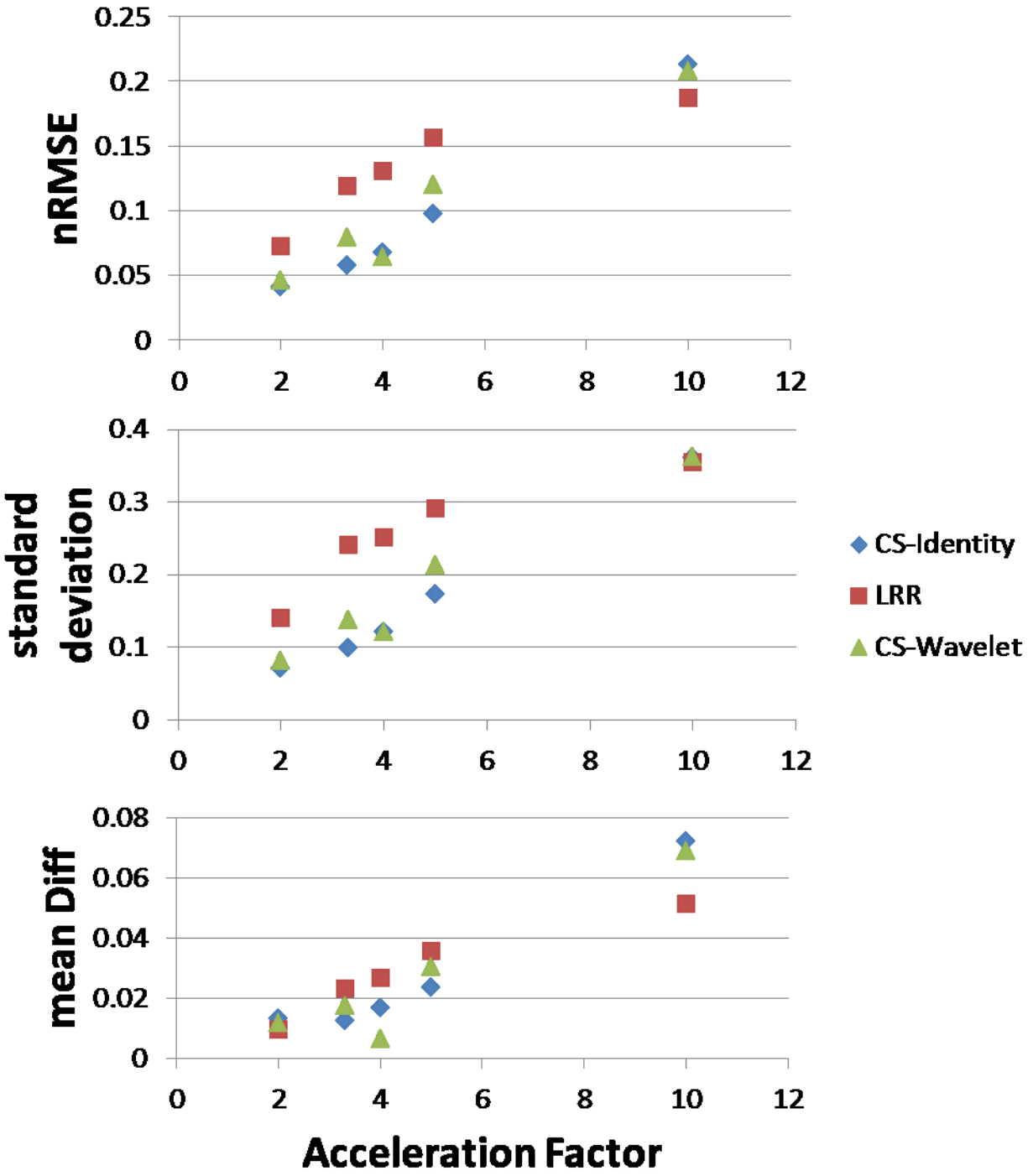

Figure 8-24– The normalised Root mean square error, the standard deviation and the mean difference between each reconstruction and the non-filtered FSSR.for Cr. (Focal OPG simulation).

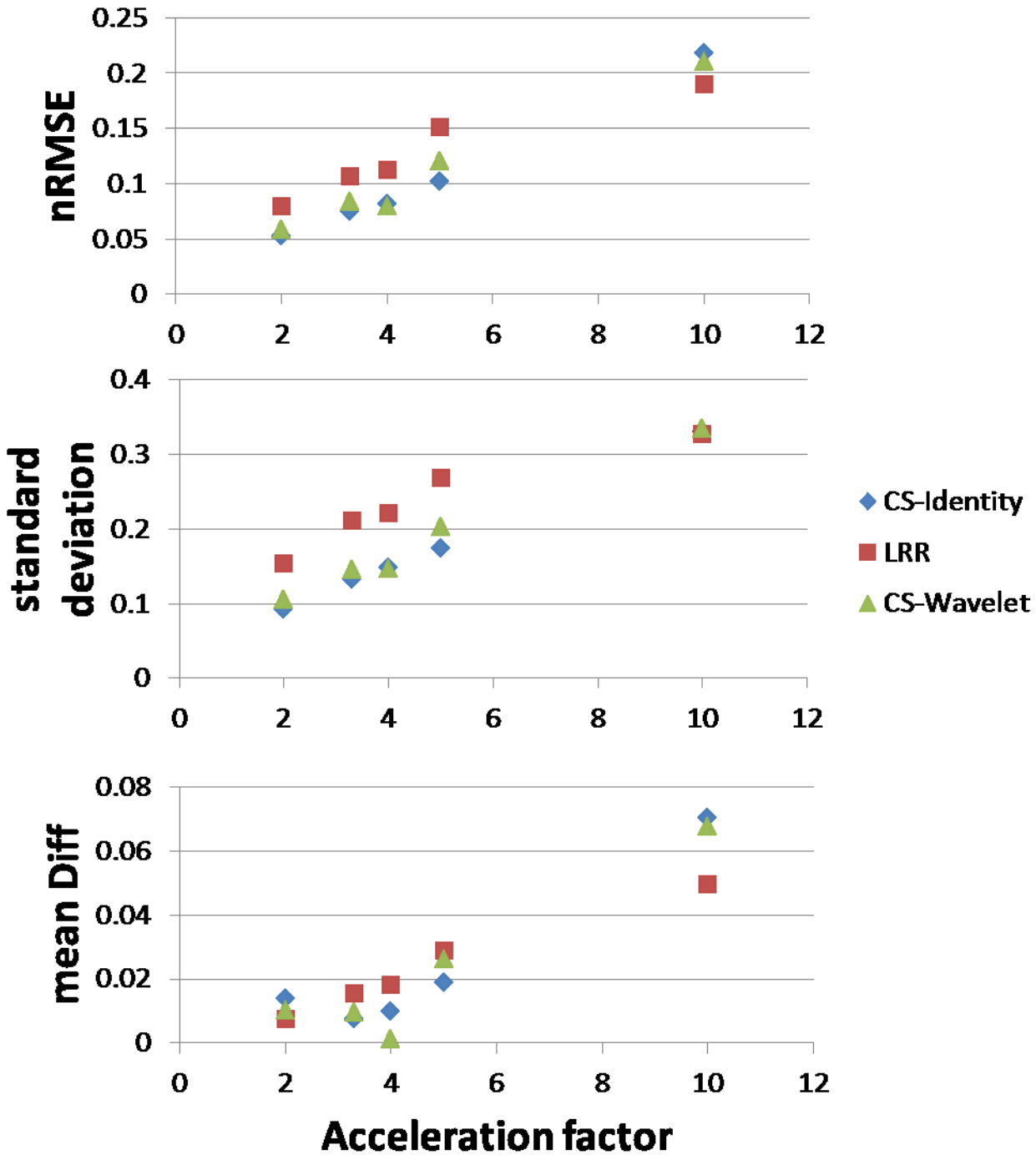

Figure 8-25– The normalised Root mean square error, the standard deviation and the mean difference between each reconstruction and the non-filtered FSSR.for Cho. (Focal OPG simulation).

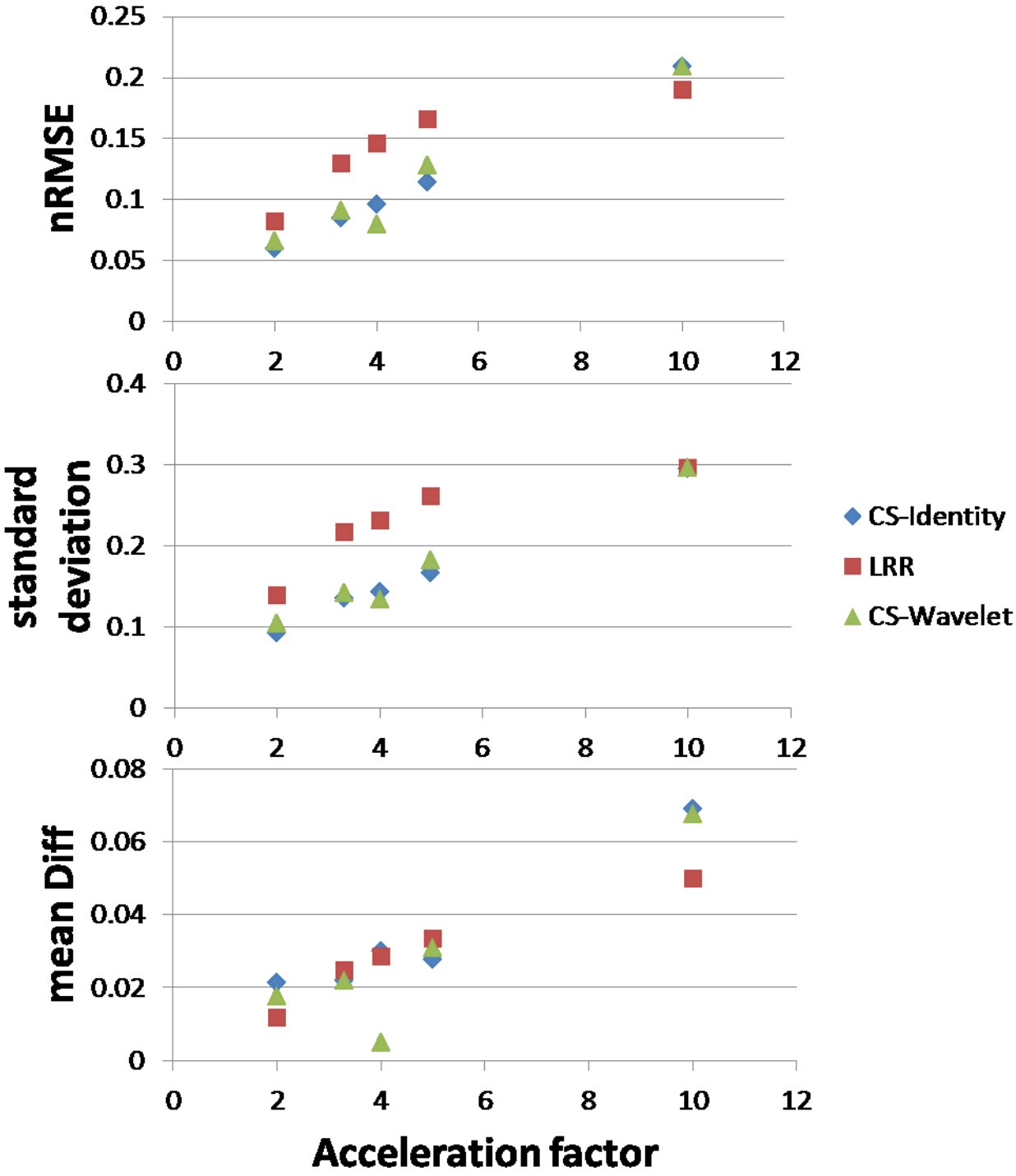

Figure 8-26– The normalised Root mean square error, the standard deviation and the mean difference between each reconstruction and the non-filtered FSSR.for Ins. (Focal OPG simulation).

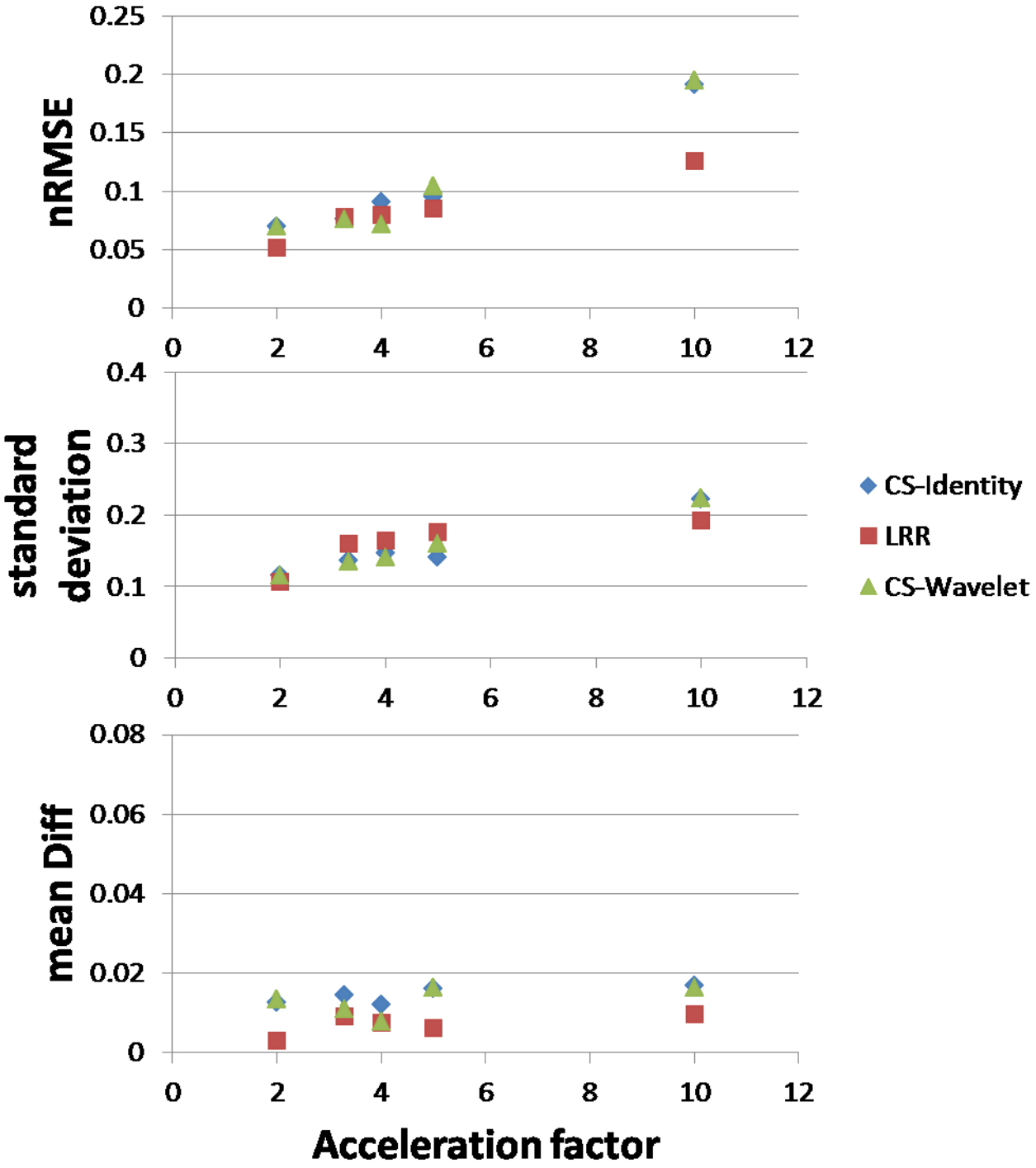

Figure 8-27– The normalised Root mean square error, the standard deviation and the mean difference between each reconstruction and the non-filtered FSSR.for lipids. (Focal OPG simulation).

Metabolite maps calculated by Tarquin are shown in Figure 8-28 for NAA, Figure 8-29 for Creatine, Figure 8-30 for Choline, Figure 8-31 for Myo-Inositol, and Figure 8-32 for lipids.

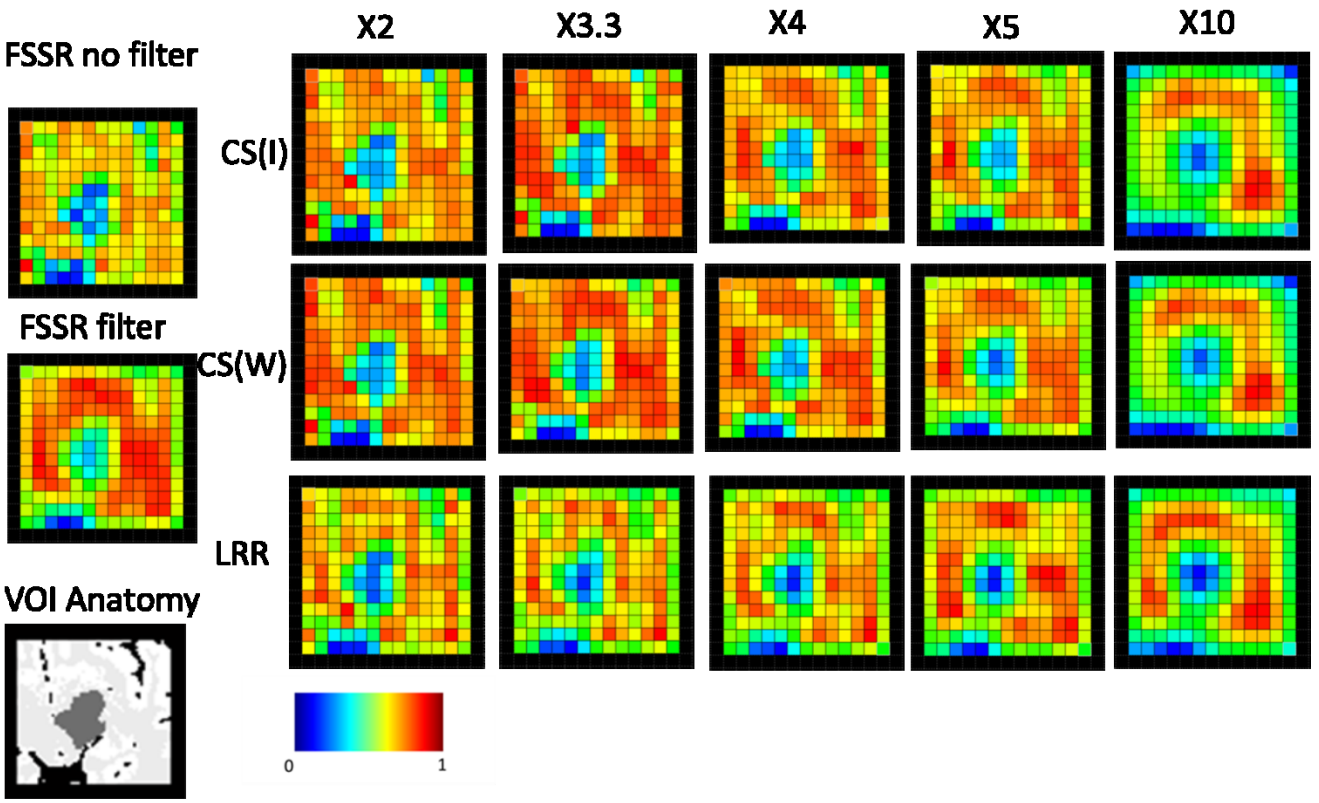

Figure 8-28 – NAA Metabolite maps for the simulations reconstructed with CS-MRSI (identity), CS-MRSI(wavelet) and the LRR as compared to the FSSR with and without filtering. The colour maps are normalised to the highest pixel value. (Focal OPG simulation).

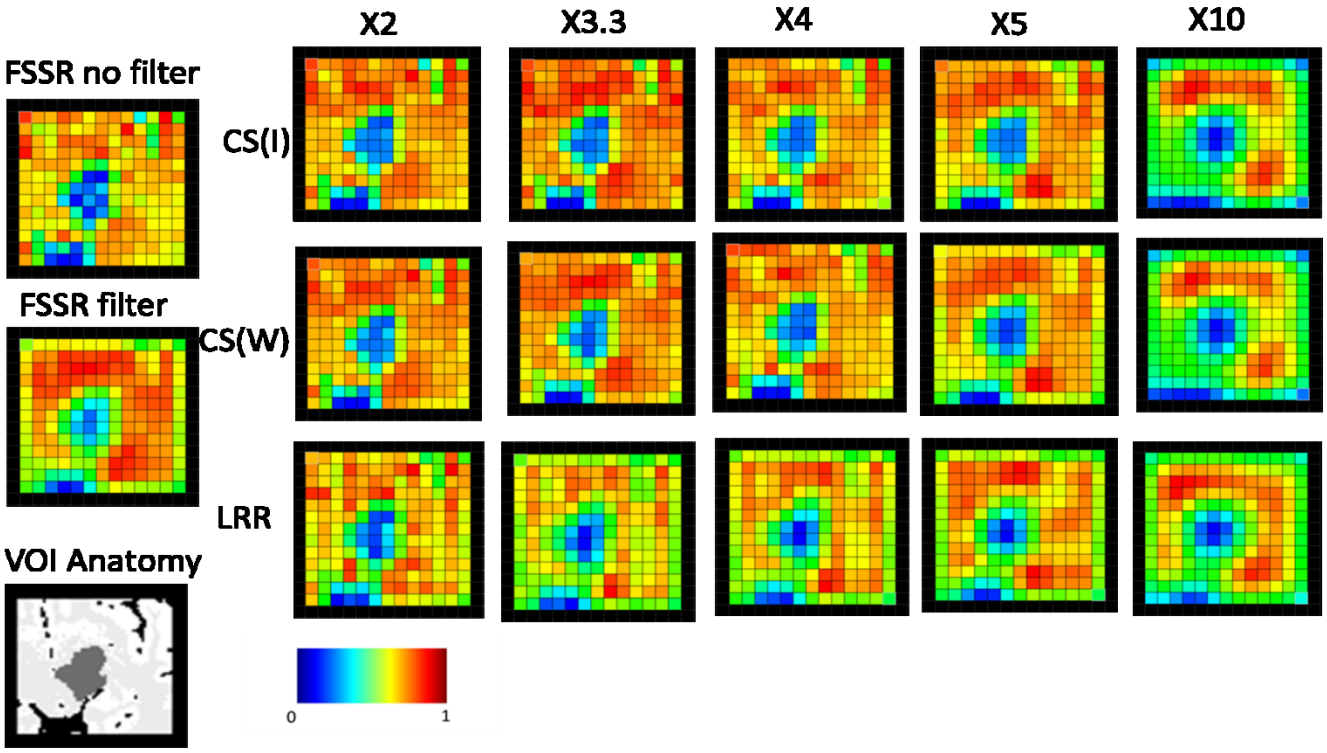

Figure 8-29 - Creatine Metabolite maps for the simulations reconstructed with CS-MRSI (identity), CS-MRSI(wavelet) and the LRR as compared to the FSSR with and without filtering. The colour maps are normalised to the highest pixel value. (Focal OPG simulation).

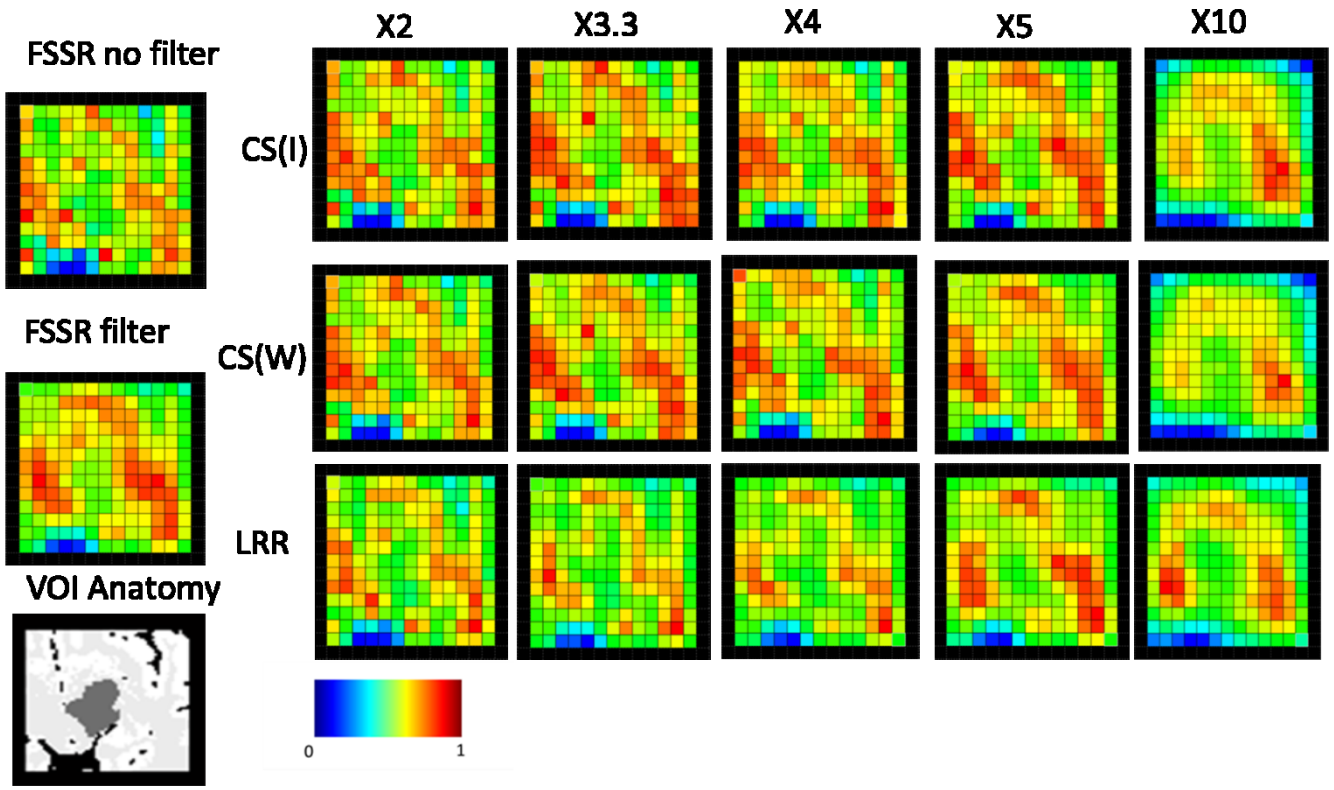

Figure 8-30 - Choline Metabolite maps for the simulations reconstructed with CS-MRSI (identity), CS-MRSI(wavelet) and the LRR as compared to the FSSR with and without filtering. The colour maps are normalised to the highest pixel value. (Focal OPG simulation).

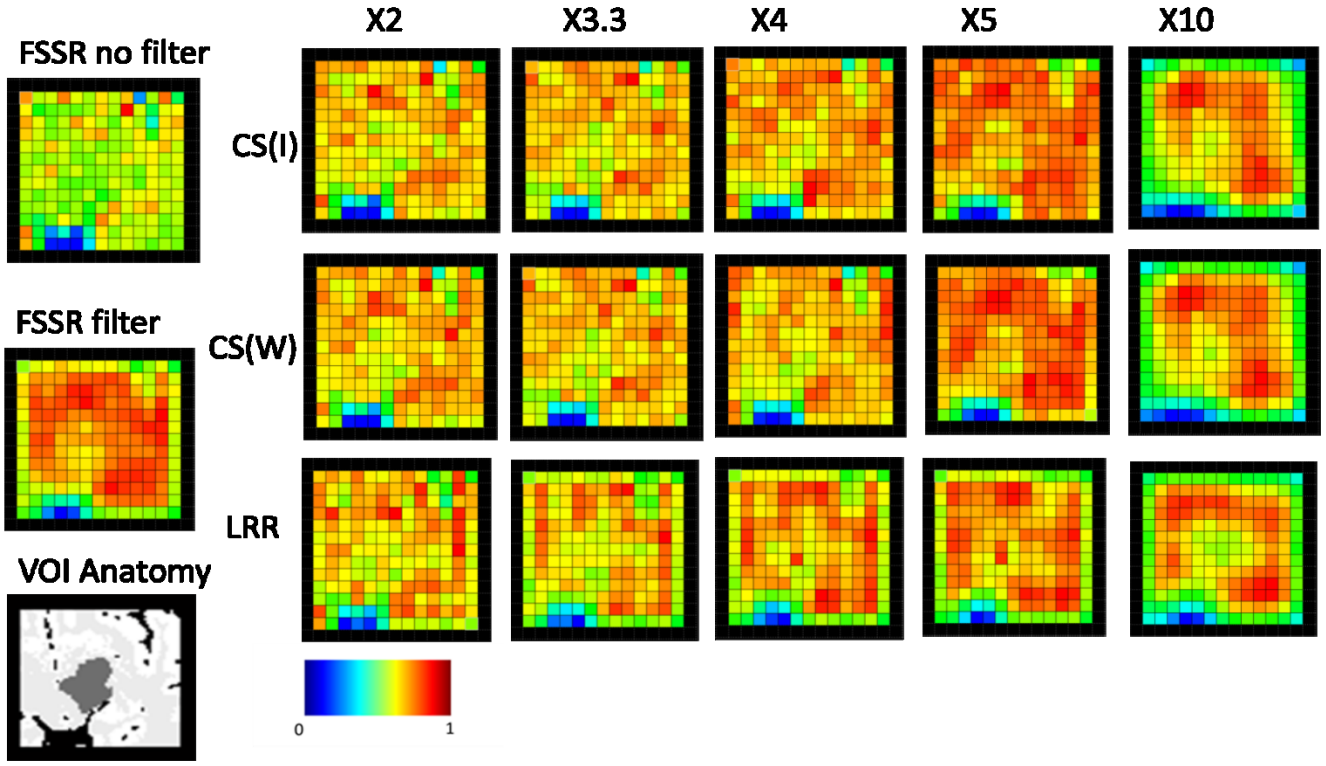

Figure 8-31 - Ins maps for the simulations reconstructed with CS-MRSI (identity), CS-MRSI(wavelet)and the LRR as compared to the FSSR with and without filtering. The colour maps are normalised to the highest pixel value. (Focal OPG simulation).

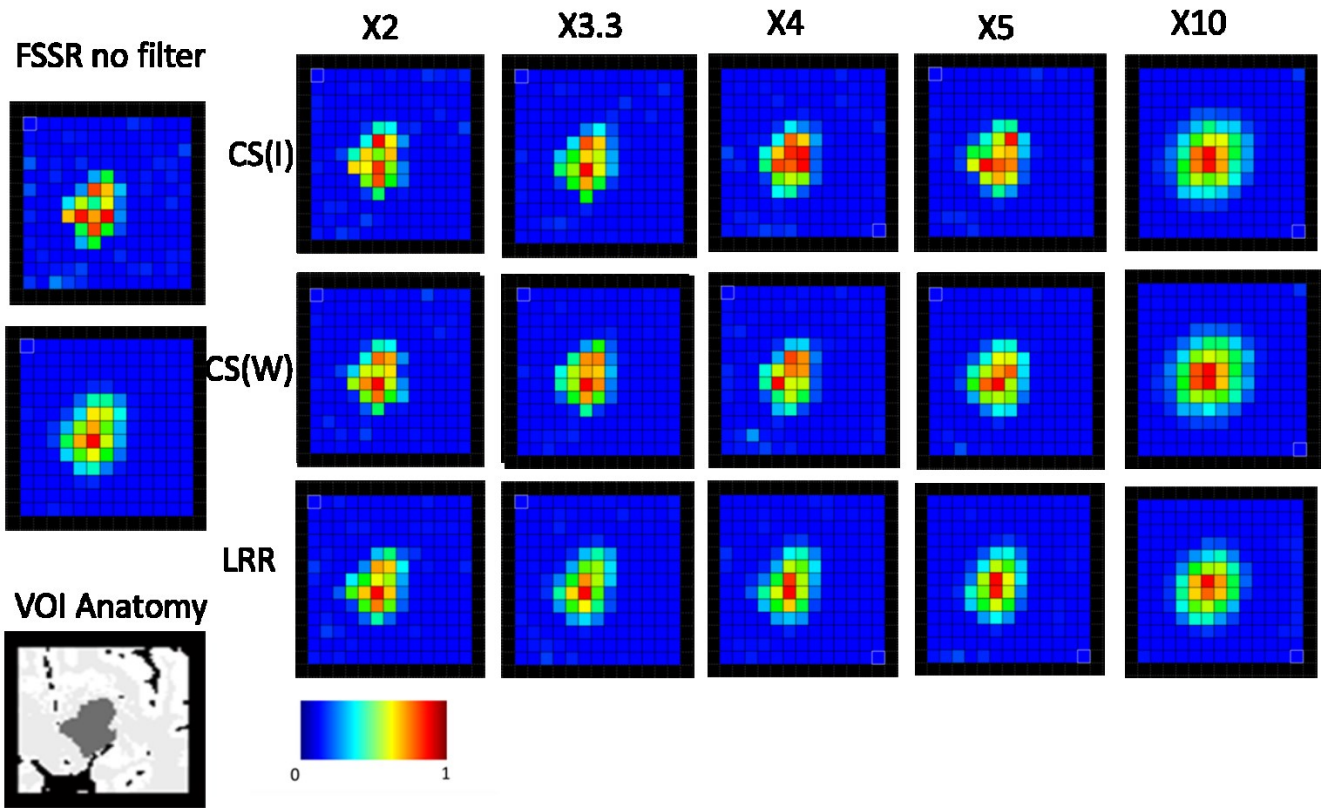

Figure 8-32 – Lipid maps for the simulations reconstructed with CS-MRSI (identity), CS-MRSI(wavelet)and the LRR as compared to the FSSR with and without filtering. The colour maps are normalised to the highest pixel value. (Focal OPG simulation).

8.2.2.4 Results – Infiltrative OPG Simulation

Bland Altman statistics were calculated and plotted for NAA, Creatine, Choline, Myo-Inositol and lipids based upon the metabolite concentrations quantified by TARQUIN. The CS reconstruction using the identity as the sparse domain are depicted alongside those from the LRR reconstruction, Figure 8-33, Figure 8-34, Figure 8-35, and Figure 8-37.

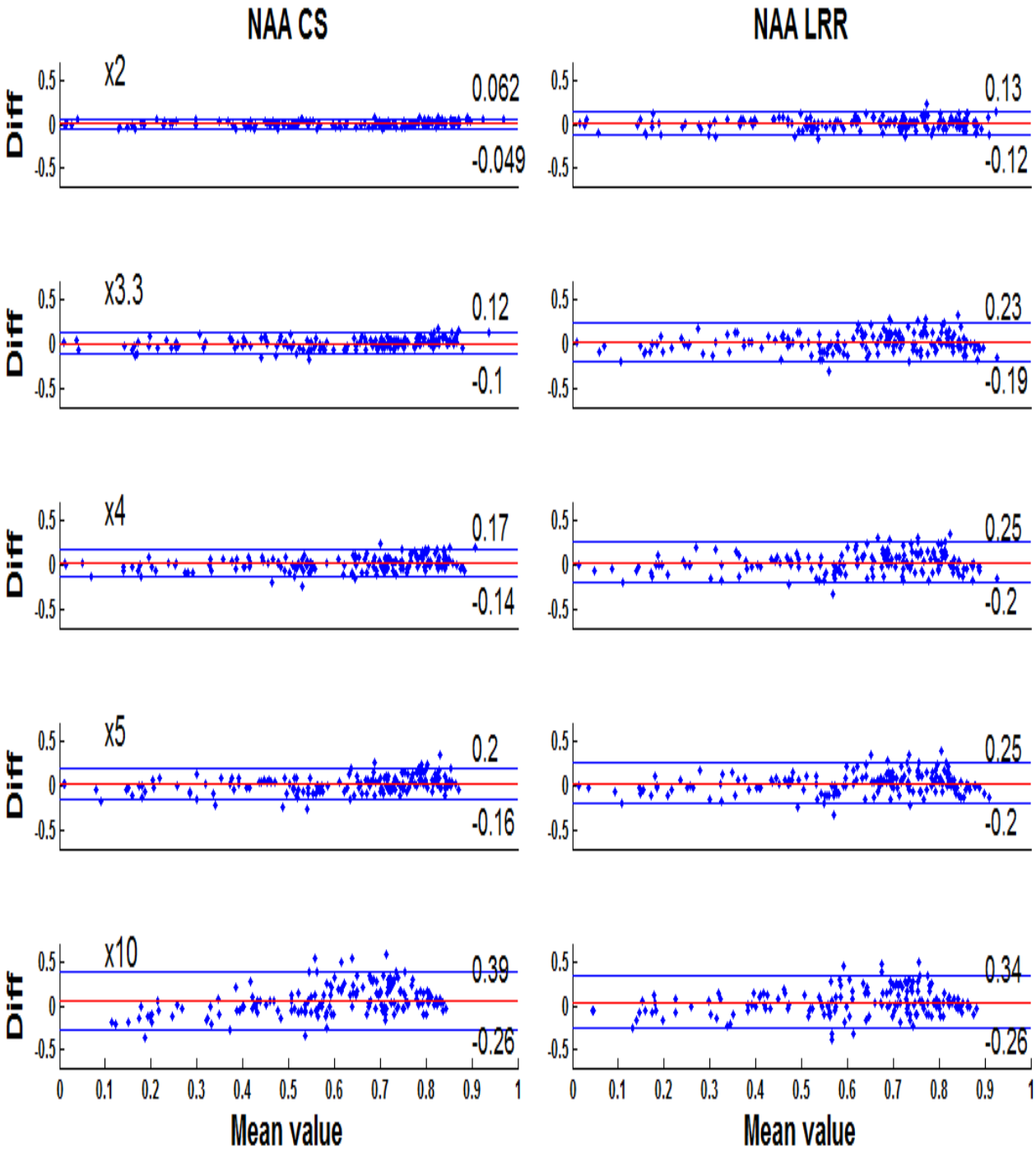

Figure 8-33 - Bland-Altman plots for NAA at each acceleration factor. CS-MRSI(identity) is shown on the LHS and the equivalent LRR on the RHS. (Infiltrative OPG simulation).

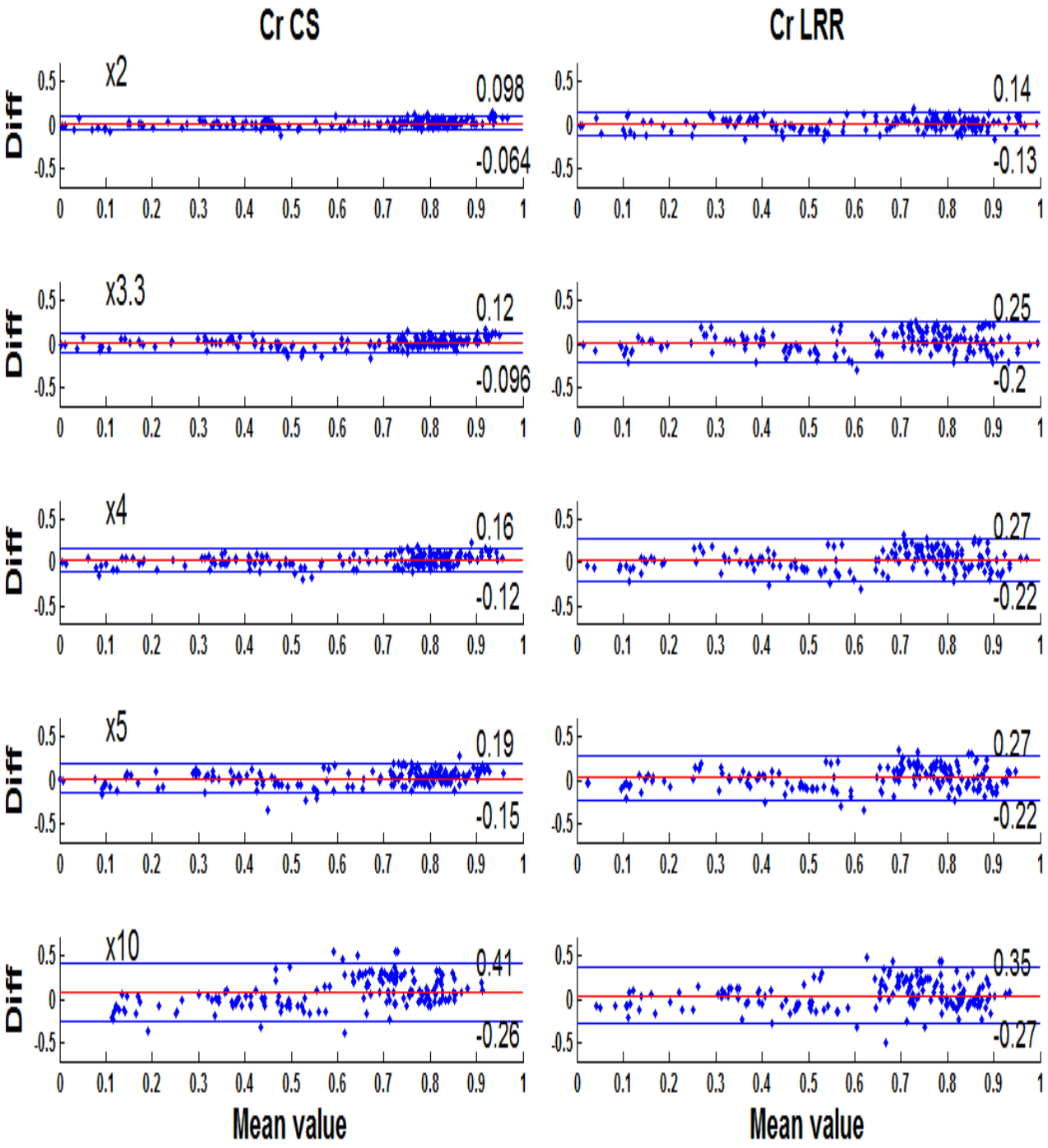

Figure 8-34 - Bland-Altman plots for Creatine at each acceleration factor. CS-MRSI(identity) is shown on the LHS and the equivalent LRR on the RHS. (Infiltrative OPG simulation).

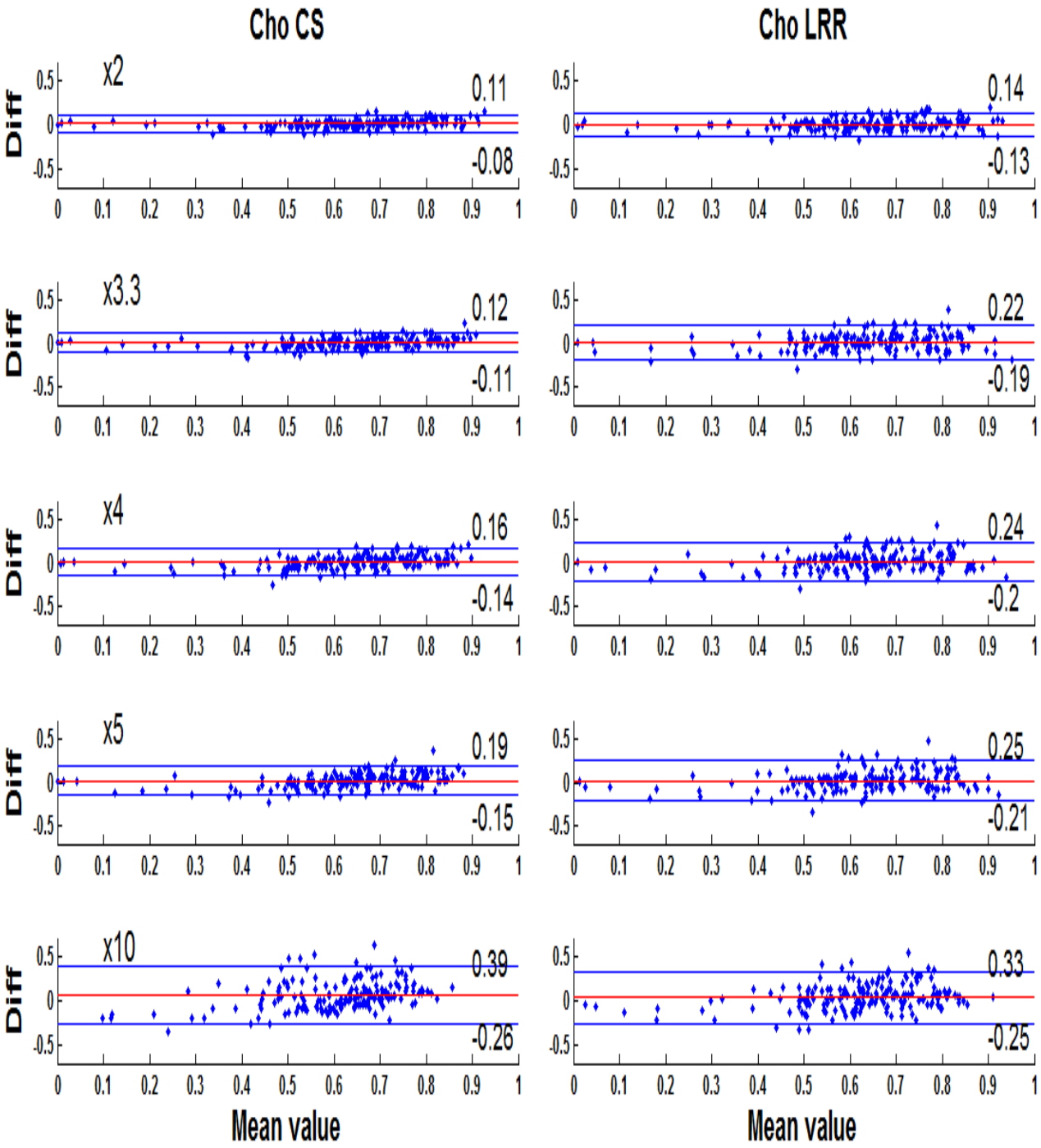

Figure 8-35 - Bland-Altman plots for Choline at each acceleration factor. CS-MRSI(identity) is shown on the LHS and the equivalent LRR on the RHS. (Infiltrative OPG simulation).

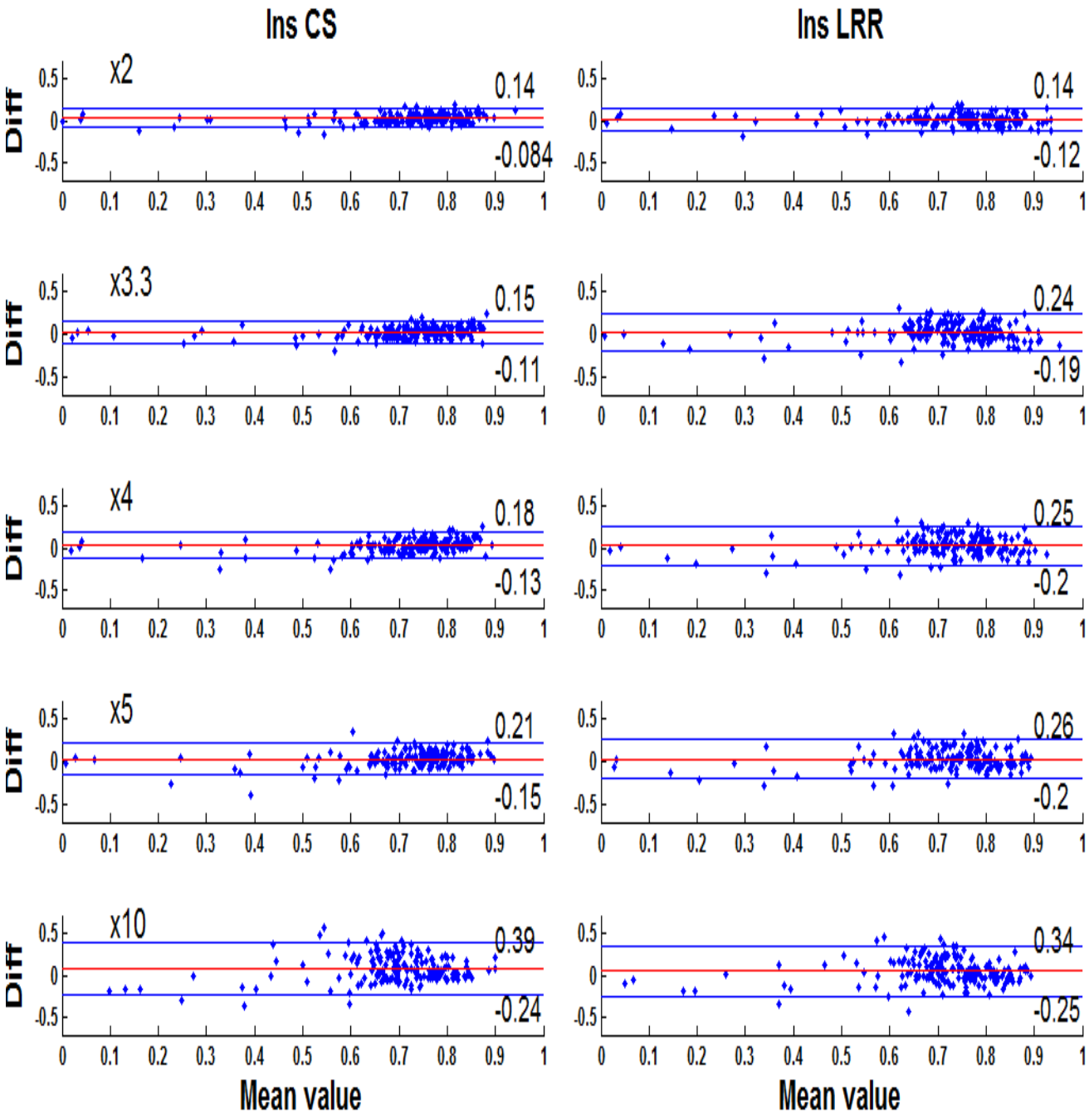

Figure 8-36 - Bland-Altman plots for Myo-Inositol at each acceleration factor. CS-MRSI(identity) is shown on the LHS and the equivalent LRR on the RHS. (Infiltrative OPG simulation).

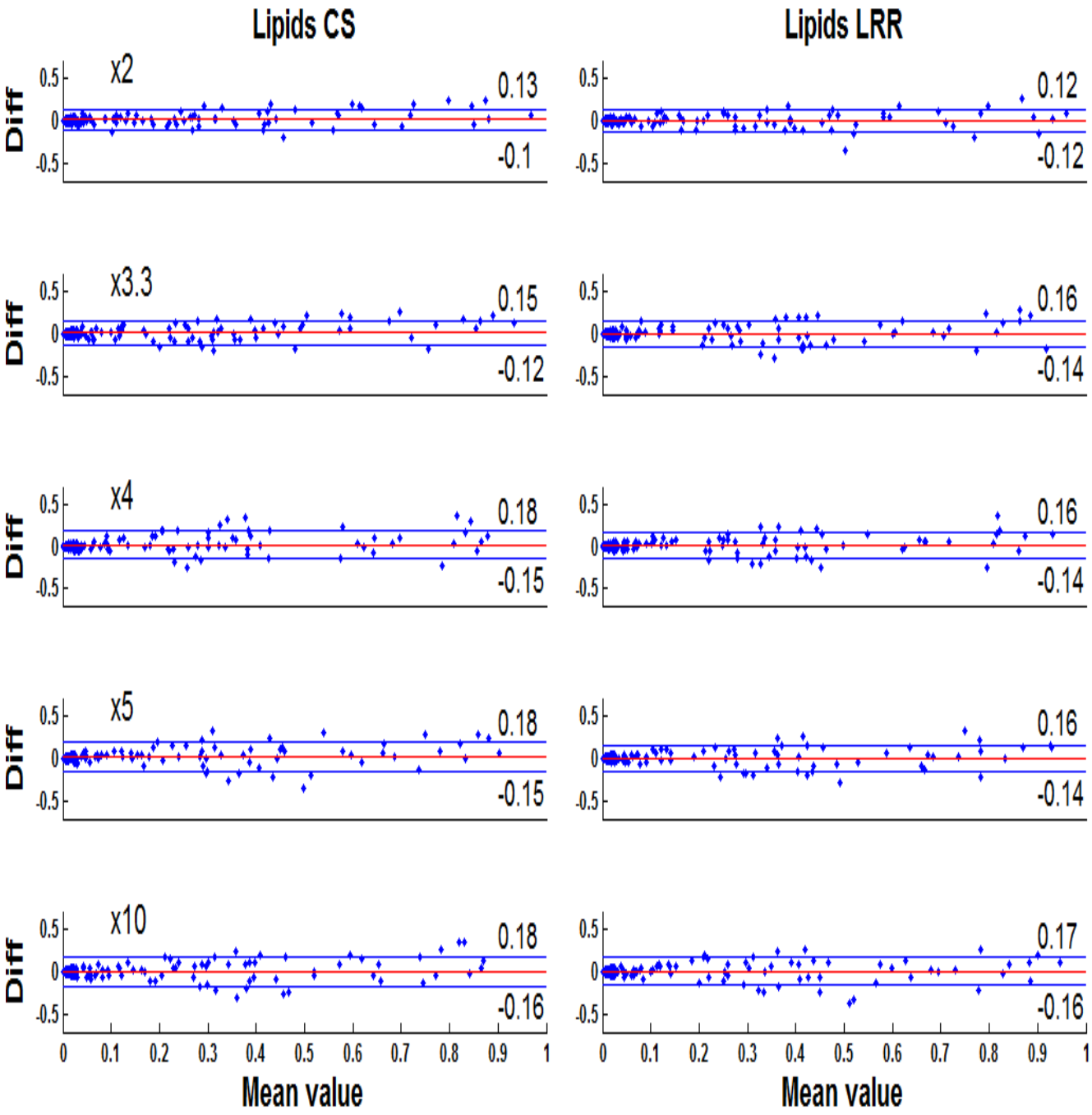

Figure 8-37 - Bland-Altman plots for lipids at each acceleration factor. CS-MRSI(identity) is shown on the LHS and the equivalent LRR on the RHS. (Infiltrative OPG simulation).

The nRMSE, the standard deviation and the mean difference relative to the FSSR (no filtering) for CS identity, CS wavelet and LRR, were plotted against acceleration factor for NAA, Creatine, Choline, Myo-Insositol and lipids Figure 8-38, Figure 8-39, Figure 8-40, Figure 8-41, and Figure 8-42.

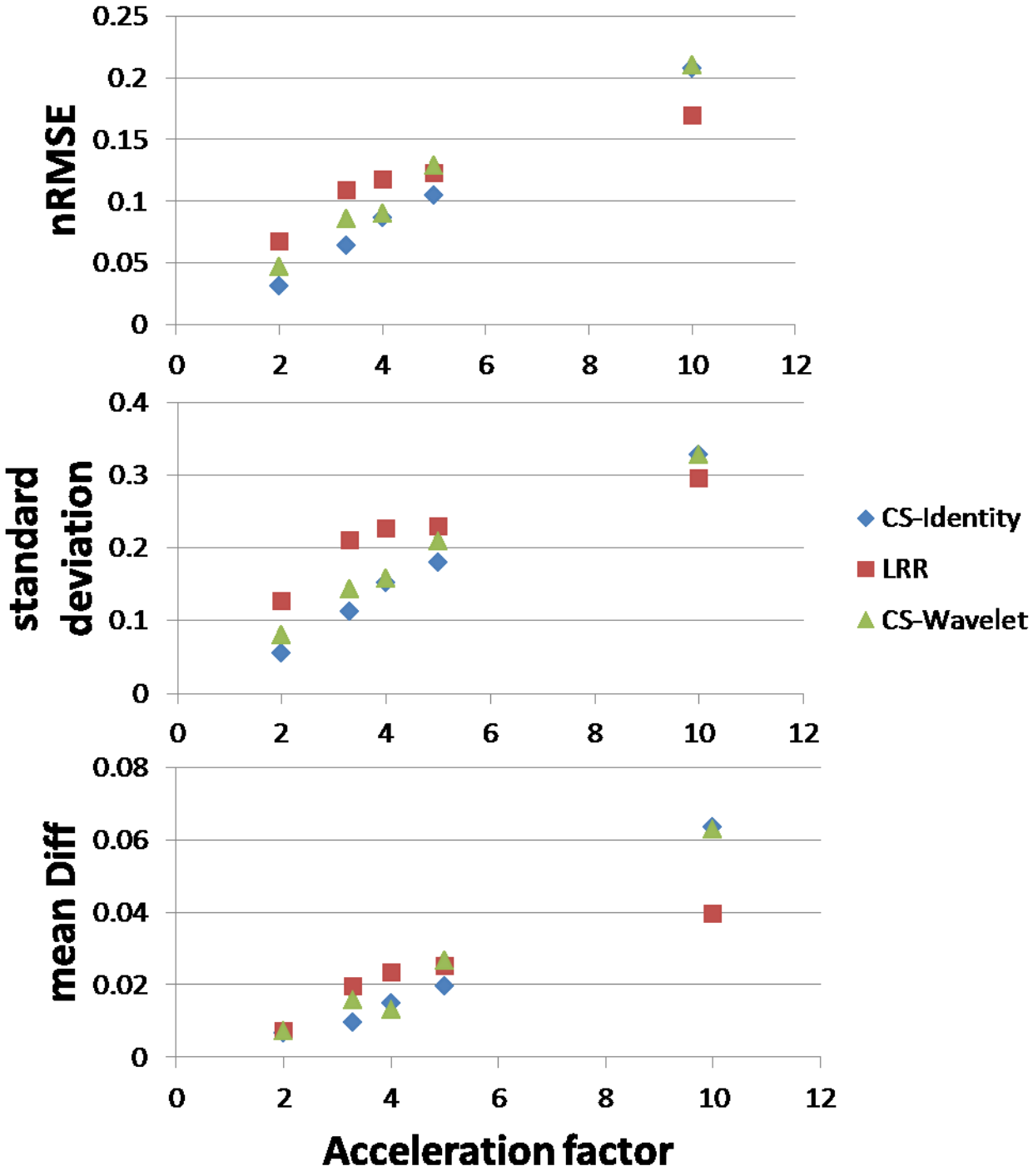

Figure 8-38 - The normalised Root mean square error, the standard deviation and the mean difference between each reconstruction and the non-filtered FSSR, for NAA. (Infiltrative OPG simulation).

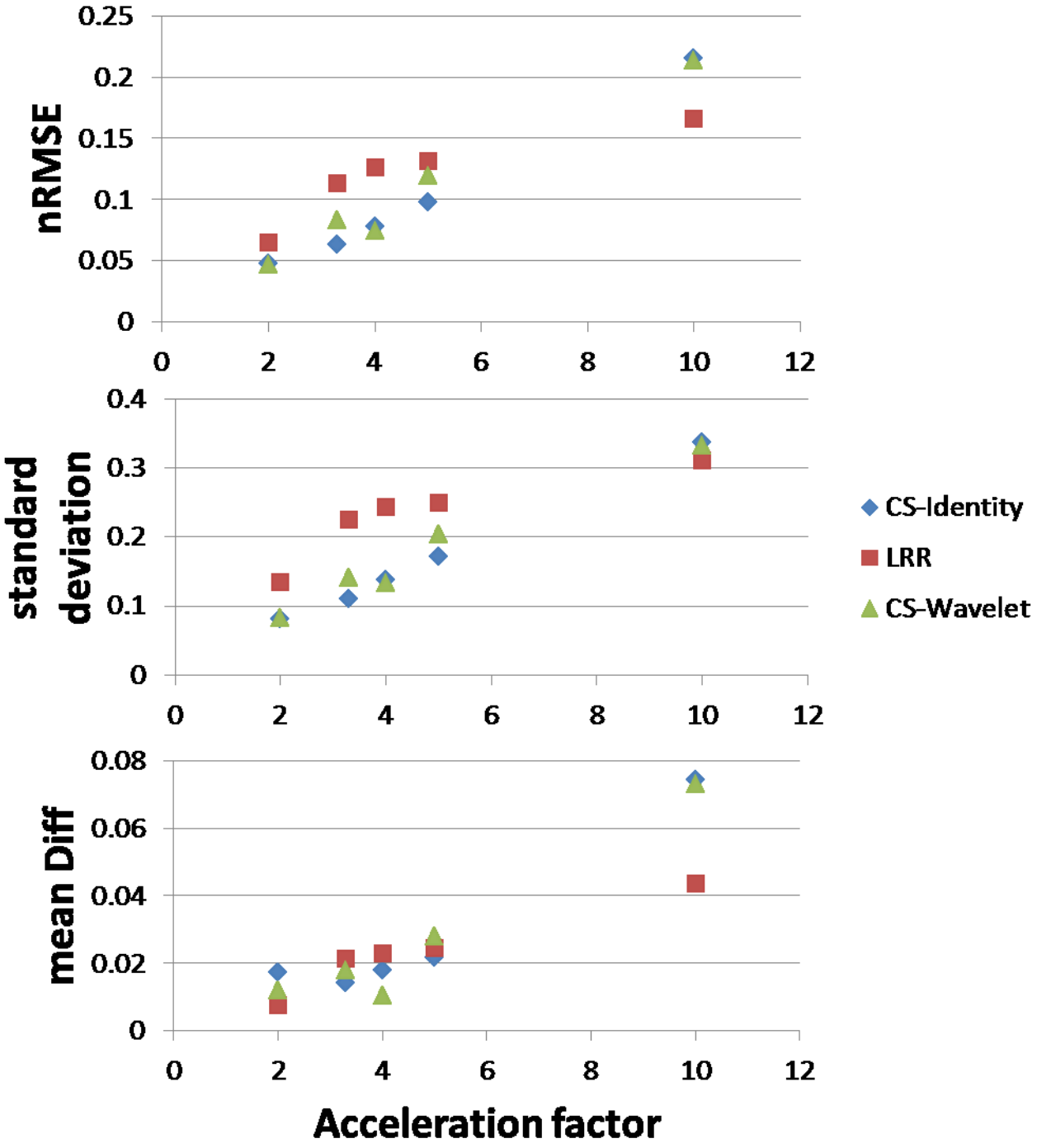

Figure 8-39 - The normalised Root mean square error, the standard deviation and the mean difference between each reconstruction and the non-filtered FSSR, for Cr. (Infiltrative OPG simulation).

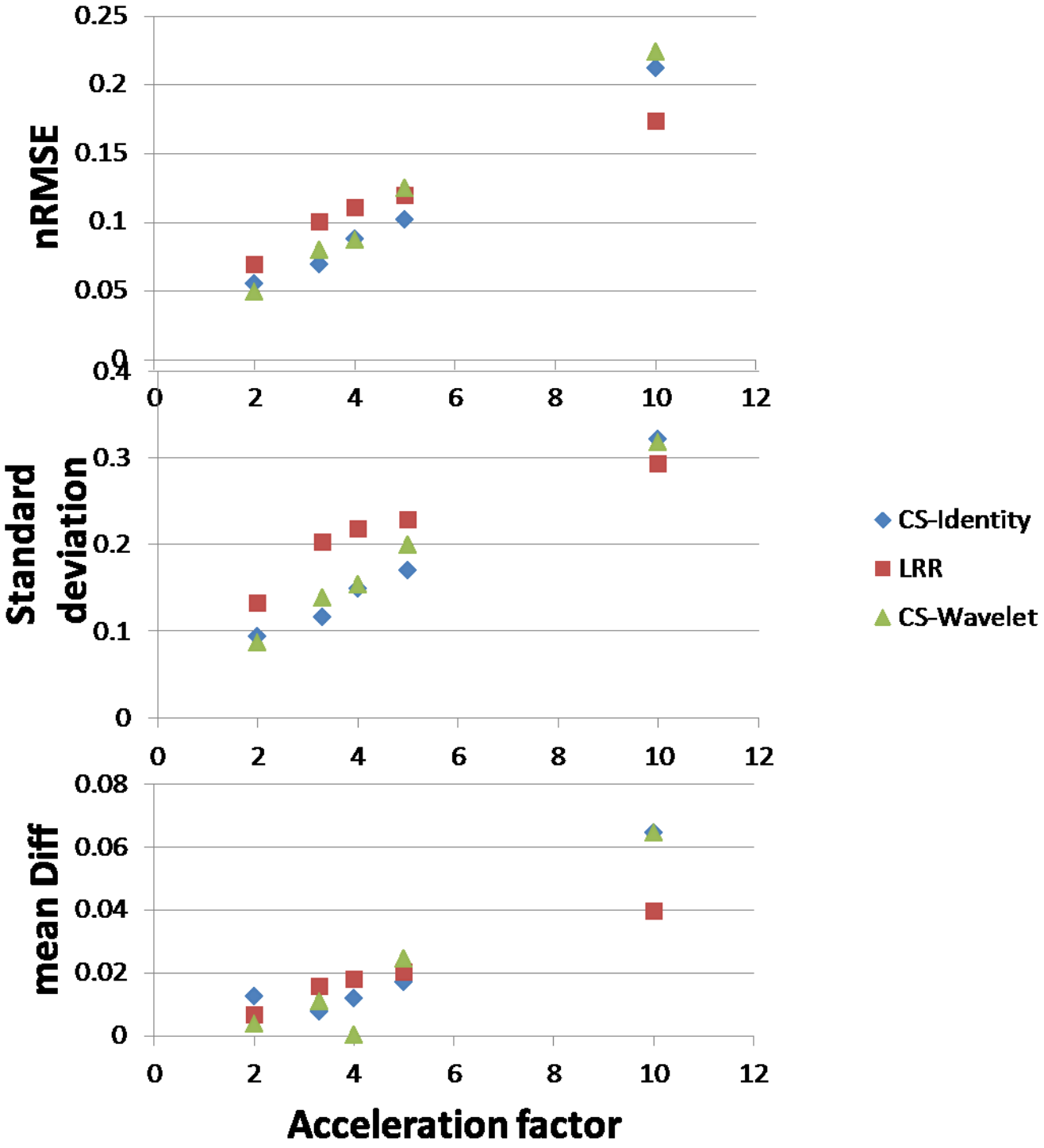

Figure 8-40 - The normalised Root mean square error, the standard deviation and the mean difference between each reconstruction and the non-filtered FSSR, for Cho. (Infiltrative OPG simulation).

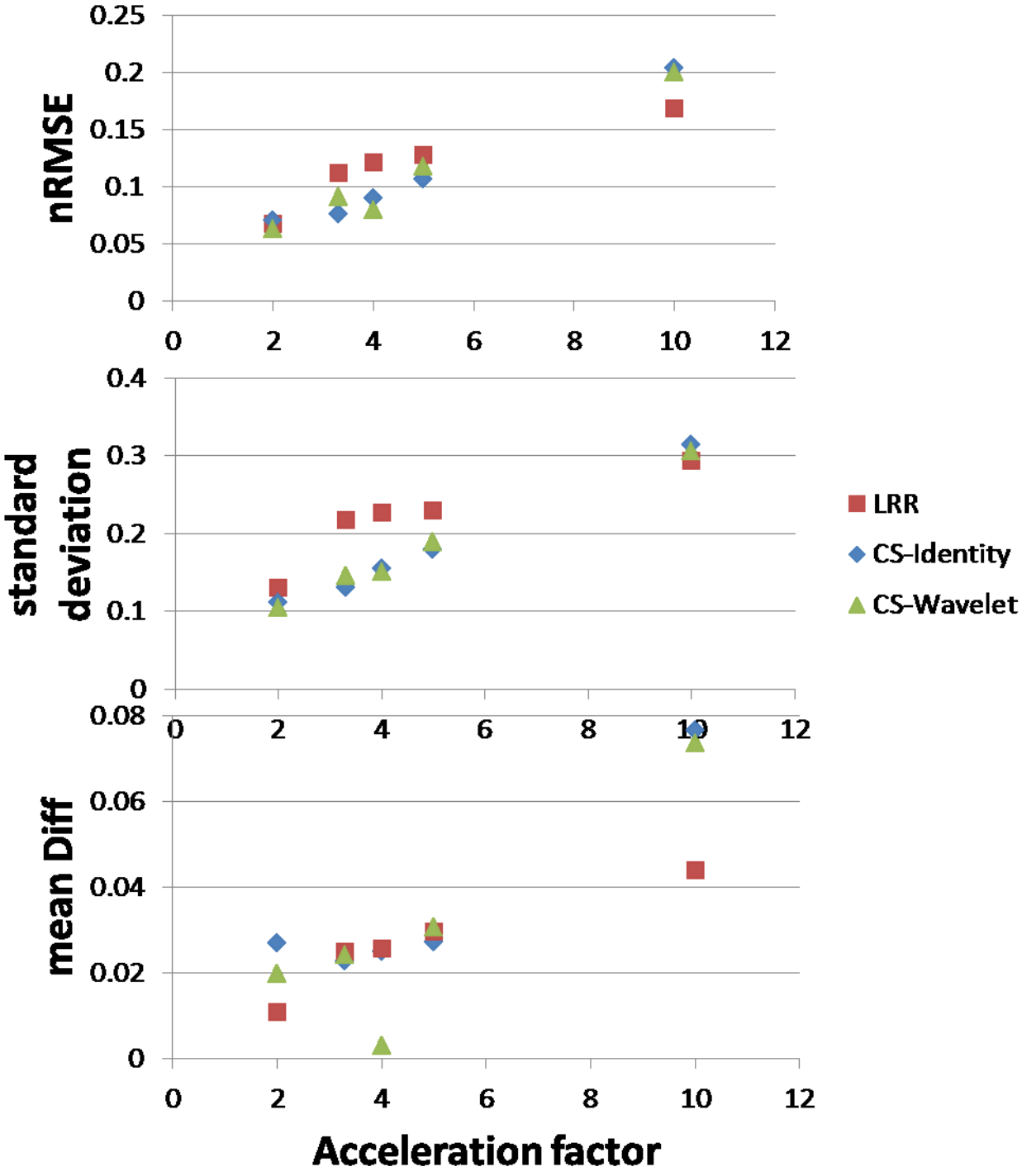

Figure 8-41 - The normalised Root mean square error, the standard deviation and the mean difference between each reconstruction and the non-filtered FSSR, for Ins. (Infiltrative OPG simulation).

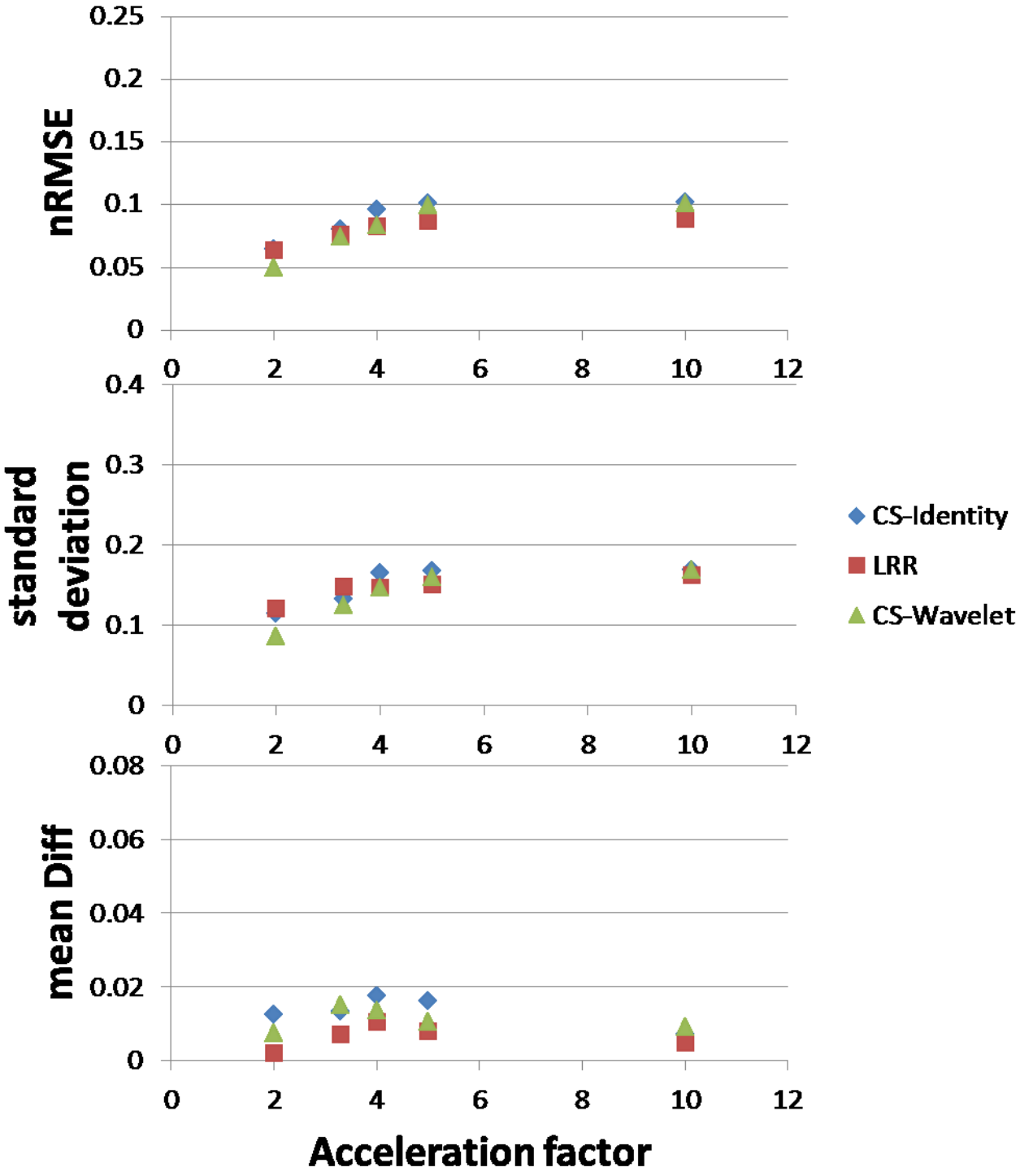

Figure 8-42- The normalised Root mean square error, the standard deviation and the mean difference between each reconstruction and the non-filtered FSSR, for lipids. (Infiltrative OPG simulation).

Metabolite maps as depicted by Tarquin are shown for NAA Figure 8-43, Creatine Figure 8-44 Choline Figure 8-45, Myo-Inositol Figure 8-46 and lipids Figure 8-47.

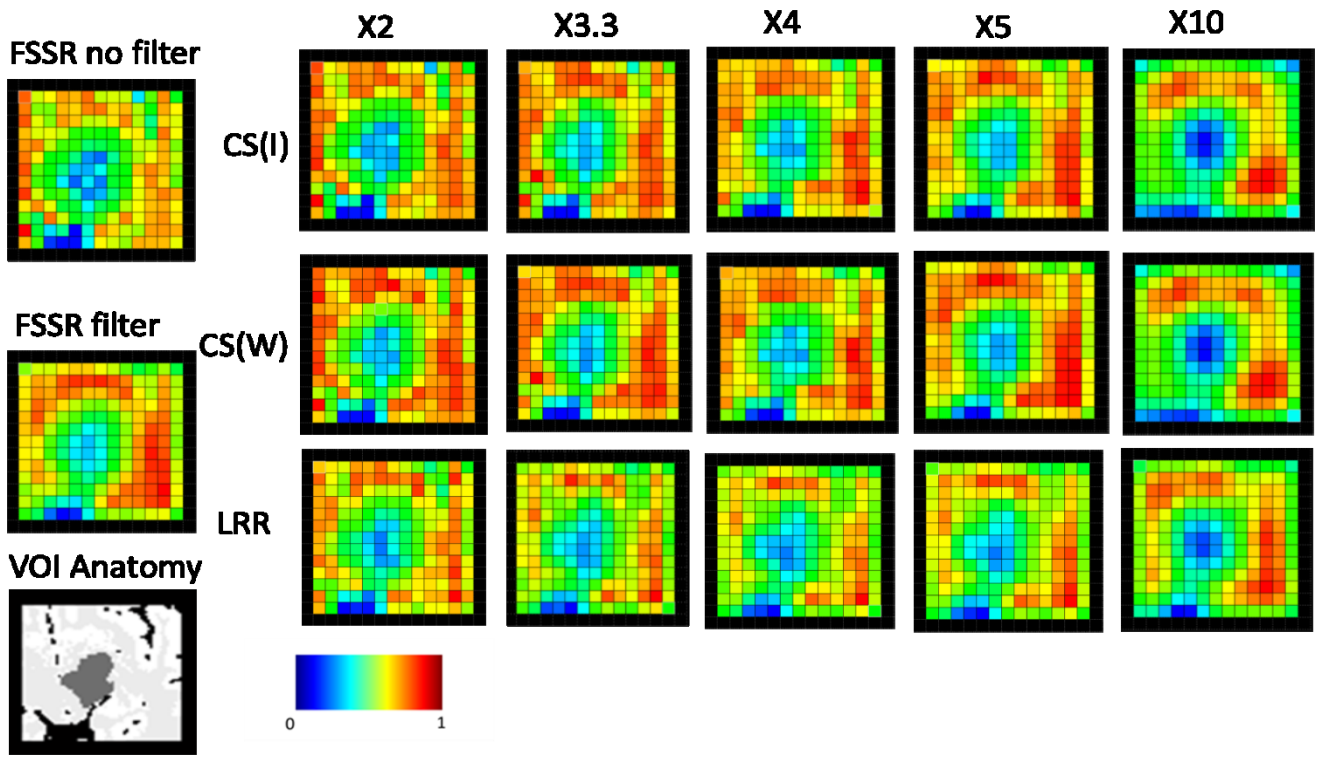

Figure 8-43 - NAA Metabolite maps for the simulations reconstructed with CS-MRSI (identity), CS-MRSI(wavelet) and the LRR as compared to the FSSR with and without filtering. The colour maps are normalised to the highest pixel value. (Infiltrative OPG simulation).

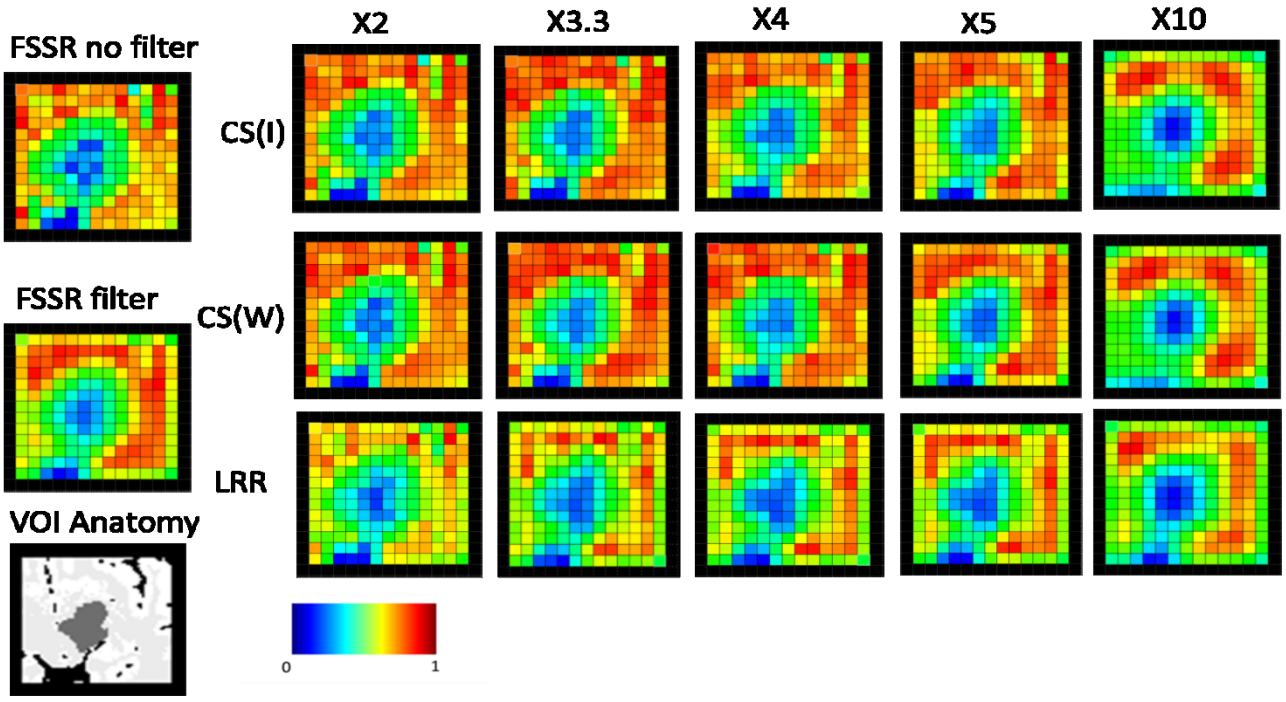

Figure 8-44 - Creatine Metabolite maps for the simulations reconstructed with CS-MRSI (identity), CS-MRSI(wavelet) and the LRR as compared to the FSSR with and without filtering. The colour maps are normalised to the highest pixel value. (Infiltrative OPG simulation).

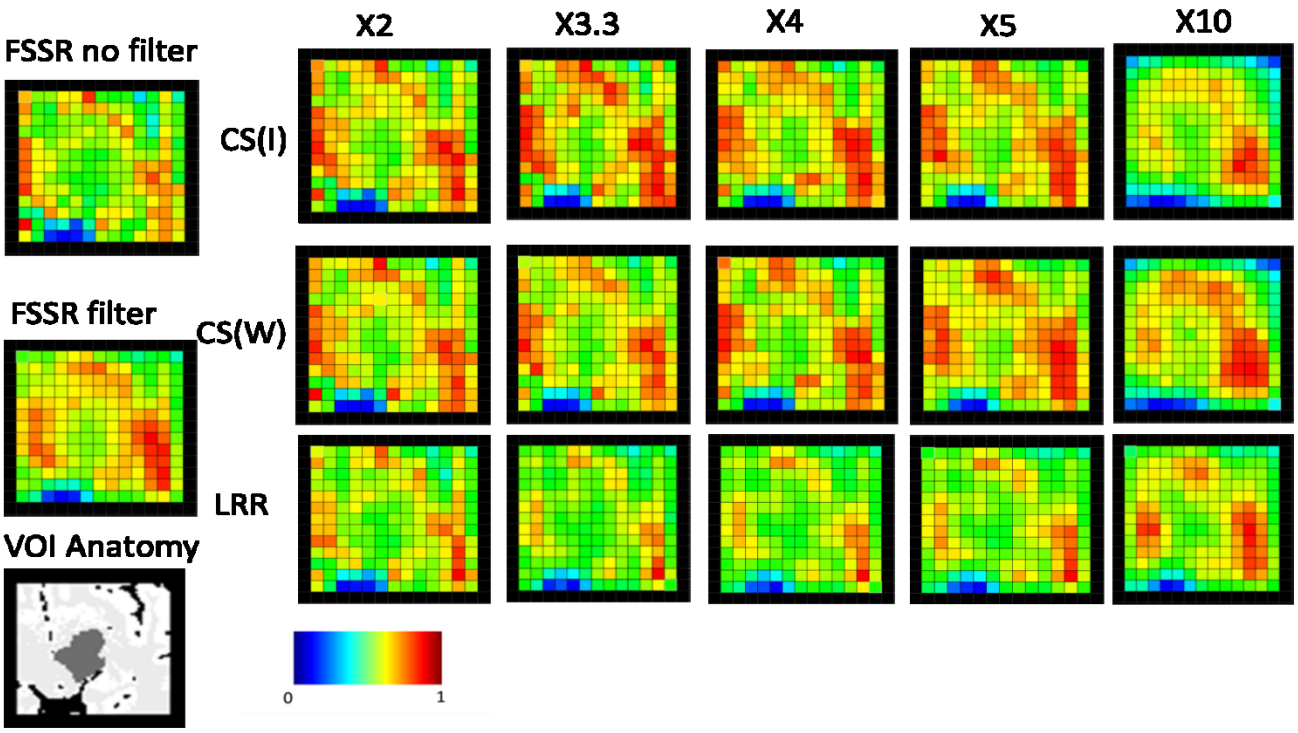

Figure 8-45 - Choline Metabolite maps for the simulations reconstructed with CS-MRSI (identity), CS-MRSI(wavelet) and the LRR as compared to the FSSR with and without filtering. The colour maps are normalised to the highest pixel value. (Infiltrative OPG simulation).

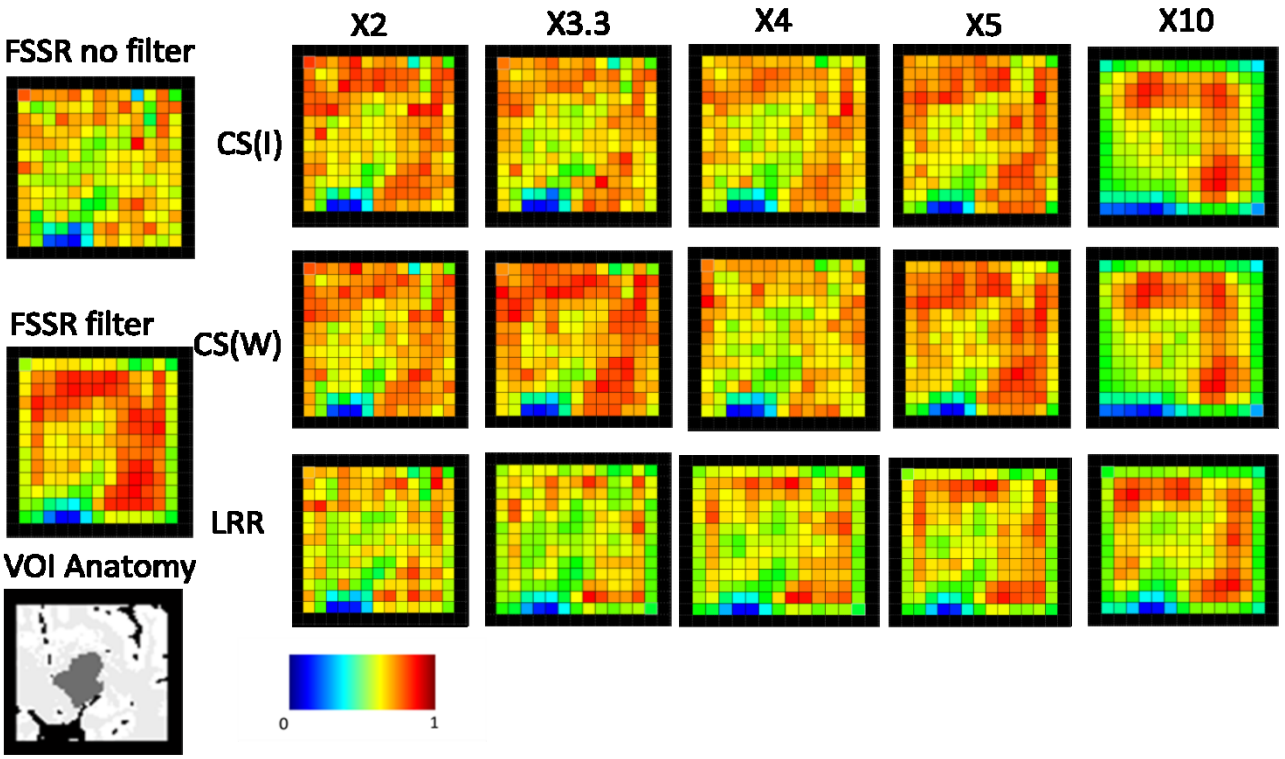

Figure 8-46 – Myo-Inositol Metabolite maps for the simulations reconstructed with CS-MRSI (identity), CS-MRSI(wavelet) and the LRR as compared to the FSSR with and without filtering. The colour maps are normalised to the highest pixel value. (Infiltrative OPG simulation).

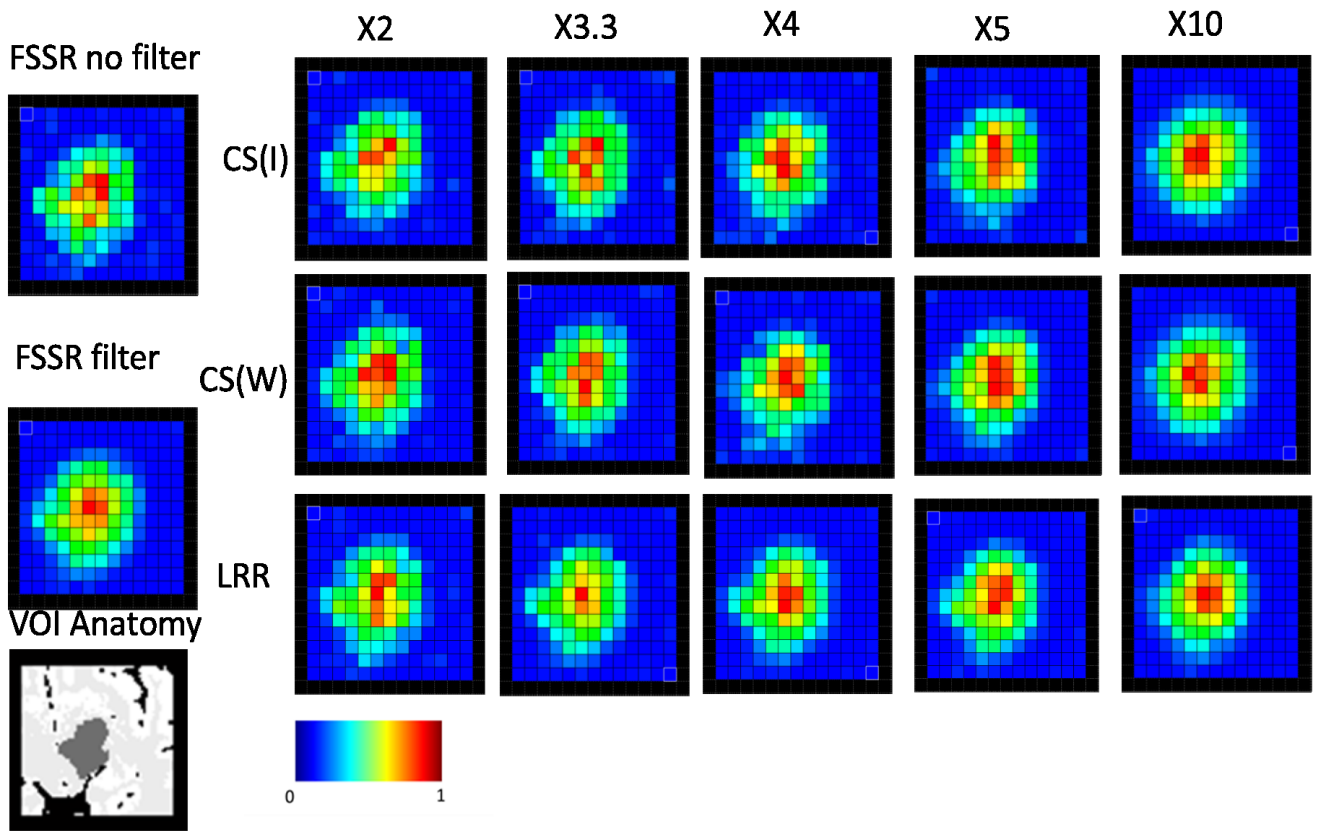

Figure 8-47- Lipid Metabolite maps for the simulations reconstructed with CS-MRSI (identity), CS-MRSI(wavelet) and the LRR as compared to the FSSR with and without filtering. The colour maps are normalised to the highest pixel value. (Infiltrative OPG simulation).

8.2.2.5 Discussion – OPG Simulations

The use of the larger matrix size 40x32 simulated MRSI datasets provides increased data and consistency compared to the real-life OPG (15x13) acquisition. The Bland Altman plots of the real-time acquisition OPG did not indicate as conclusive an advantage of CS-MRSI over LRR as did the simulated focal lesion dataset reconstructions. This may in part be due to the fact that the real-time acquisition OPG patient dataset did not have a clearly defined lesion boundary as had the focal tumour in the simulation. The real-time acquisition OPG MRSI had a large voxel size of 13mm x13mm x13mm which meant an inherently very low spatial resolution. Therefore, the advantages of CS-MRSI noted in previous chapters at maintaining spatial resolution over the LRR reconstructions (section 7.1.2) are not as easily apparent. The real-time acquisition OPG MRSI dataset is subject to baseline distortion from the residual water peak and imperfect shimming (section 2.3). This inevitably affects the quality of the

metabolite TARQUIN quantification (section 2.4.6). The real-time OPG MRSI result therefore demonstrates some of the challenges inherent in the acquisition of real-time MRSI (section 2.3), strengthening the argument for utilising the software simulations in this study.

The focal lesion results and those for which there is tumour infiltration into healthy tissue both indicate that the CS-MRSI reconstruction relative to the non-filtered FSSR provides a lower nRMSE, standard deviation and mean difference for all metabolites, than the LRR, up to an acceleration factor of x5 Figure 8-23 to Figure 8-26 (focal OP lesion), and Figure 8-38 to Figure 8-41 (OPG lesion with infiltration). All values positively correlate with increasing acceleration factor. At x10 acceleration factor this is reversed which may be due to the CS reconstruction not having enough data samples at the centre of k-space at this factor to provide as good a reconstruction as those of the LRR for which sampling is entirely central. The result appears to agree with the results of the digital phantom metabolite edge response investigation, section 7.1.2 where the enhancement in spatial resolution from the CS reconstruction relative to the LRR appeared to break down at x10 acceleration factor. The Bland-Altman plots and the metabolite maps also appear to agree with this result. The nRMSE for NAA, Creatine and Choline for the focal lesion at an acceleration factor of x5, reconstructed with CS-MRSI(identity) was 10%(NAA), 9.7%(Cr) and 10%(Cho) respectively, for the corresponding LRR it was 16%(NAA), 16%(Cr) and 15%(Cho) and CS-MRSI(wavelets) was 13%(NAA), 12%(Cr) and 12%(Cho). The corresponding nRMSE values for the infiltrated lesion with CS-MRSI(Identity) was 10%,(NAA) 9.7%(Cr) and 10%(Cho) respectively, for the LRR was 12% (NAA), 13%(Cr) and 12%(Cho) and for CS-MRSI(wavelets) 12%(NAA), 12%(Cr) and 12%(Cho). Given that there is an approximate 10% error in the TARQUIN reconstruction this may be evidence to suggest that CS-MRSI(identity) could be useful to reduce scan time up to 80%. If the spatial resolution of the OPG patient was doubled so that the matrix size for the FOV increased from (15 x 13) to (30 x 26), the scan time would be increased from 6.5

to 26 minutes. If an acceleration factor of x5 was possible, the high resolution MRSI scan time would reduce from 26 to 5.2 minutes which is clinically more feasible.

A paper in which CS reconstruction using wavelets was investigated on a real-time acquisition claims a nRMSE of less than 5% at this x5 acceleration factor (Geethanath 2012). The paper does not however state the particular metabolite this result refers, or the tumour type the technique was applied. Metabolite spectra vary between tumour type and it is currently unknown if CS-MRSI reconstruction is consistent across all spectral profiles. The metabolite quantification technique utilised in the paper was also different, and k-space filtration had been applied to the MRSI acquisition.

Myo-Inositol and lipids are often elevated relative to healthy tissue in OPG lesions (section 8.2.2.1). The nRMSE and standard deviation for Myo-inositol for CS-MRSI(identity) was 11% and 17% respectively at x5 acceleration factor, for the focal lesion Figure 8-26. The corresponding value for the LRR was 17% and 26%, again showing a potential benefit of CS-MRSI at this factor. The result for the infiltrated lesion also showed an advantage; CS-MRSI (identity) 11% and 18%, and for the LRR 13% and 23% Figure 8-41. The metabolite map for Myo-Inositol appears to show a uniform distribution across the tumour and the grey and white matter. Although Myo-Inositol is usually elevated relative to that of healthy tissue in OPG patients, the particular patient dataset utilised in this study did not exhibit such a marked variation. Myo-inositol has a complex multiplet at around 3.6 ppm at 3T and is also more difficult to evaluate than some of the other metabolites.

The use of CS-MRSI to reconstruct lipid data is yet to be reported in the literature. In this study the CS-MRSI(identity and wavelet) results for nRMSE, standard deviation and mean difference for lipids compared to the LRR in the focal lesion, does not indicate the same advantage of CS-MRSI over LRR as it does for the metabolites. The nRMSE, standard

deviation and mean difference all appear to be comparable for all acceleration factors for the lesion with infiltration Figure 8-42 for both the CS-MRSI and the LRR. The scenario containing the focal lesion shows a marked improvement in the statistics for the LRR over the CS-MRSI at x10 acceleration factor, Figure 8-27. The result implies that for lipids it maybe signal that is important in reconstruction. The lipid peaks are only present in the lesion and are low compared to the metabolite peaks in healthy tissue Figure 8-14 and Figure 8-32. The larger signal peaks of the metabolites in the healthy tissue reconstruct well with CS-MRSI but it may be struggling with the lower signal lipid peaks. For example, the Creatine peaks are also low in the lesion but are comparatively high in healthy tissue. The higher healthy Creatine peaks maybe well reconstructed with CS-MRSI and therefore produce a significant contrast between the healthy and diseased tissues. This is indicated in the metabolite maps Figure 8-29 and Figure 8-32. It could be that the low signal lipid peaks require increased, high signal sampling at the centre of k-space for good CS-MRSI reconstruction. This has implications for the k-space sampling mask which may require optimisation for lipids (section 2.6.6). Also, lipid signal peaks like Myo-Inositol are hard to fit and therefore evaluate on the Tarquin software which may also have an affect upon results.

The CS-MRSI Identity transform results are on average 1% better the wavelet transform results for the metabolites. The similarity in results may be due to the Daubechie (level 1) Haar wavelet which is a step function, producing a similar effect as the identity transform. There is potential for the investigation of a different mother wavelet and level (section 3.3.1). The difference between the two transforms is not as apparent as it is in the measurement of relative spatial resolution (section 7.1.2).

The TARQUIN metabolite maps Figure 8-28 to Figure 8-32 (focal lesion), Figure 8-43 to Figure 8-47 (lesion with infiltration) appear consistent with the Bland Altman, the nRMSE, standard

deviation and mean difference results. On examination of these maps the difference in tumour margin can be clearly visualised between the maps for the focal and infiltrated lesions. It can be seen that the tumour margin deteriorates in all cases at x10 acceleration factor. If the metabolite maps for the tumour infiltration Figure 8-43 to Figure 8-47 are compared to those of the focal lesion the area of infiltration is clearly visible. The maps for the focal tumour for metabolites NAA, Creatine and Choline indicate the CS-MRSI at acceleration factors of x2 to x5, appear to retain the shape of the tumour as depicted in the non-filtered FSSR map but have a degree of smoothing as depicted in the filtered FSSR map. This is because the CS-MRSI as noted in the previous chapter has reduced the appearance of the Gibbs ringing from distant inter-voxel contamination thus smoothing the image whilst retaining the spatial resolution by reducing the adjacent inter-voxel contamination.

The misrepresentation of a tumour boundary appears to be more likely with an LRR than with CS-MRSI. If the Creatine metabolite maps are examined for the focal tumour, Figure 8-29 and the tumour with tissue infiltration Figure 8-44, it can be seen that the LRR reconstructions of the focal tumour of Figure 8-29 at acceleration factors x3.3 to x5 are closer in appearance to the infiltrated, non-filtered FSSR Creatine map of Figure 8-44. The LRR metabolite maps could therefore potentially lead to a misdiagnosis in tumour extent by exhibiting the appearance of tumour infiltration from inter-voxel contamnination.

8.3 Conclusion

The implementation of the digital phantom with larger matrix size (40x32) provided increased data points and therefore increased statistics compared to the real-life OPG (15x13) acquisition. The digital phantoms provided a useful methodology for the assessment of the quality of the CS-MRSI reconstruction and it's comparison with the non-filtered FSSR and uniformly sampled, time equivalent LRR reconstructions with increasing acceleration

factor. The Bland Altman statistic and the metabolite maps appear to correspond well with the results of Chapter 5 in that the CS-MRSI results improved upon those of the LRR up to an acceleration factor of x5. The metabolite maps clearly indicate the difference between the focal and the tumour with an infiltrative border region. The result for lipids is not as conclusive as it is for the metabolites. There does not appear to be any advantage of CS-MRSI over the LRR reconstructions for lipids. This may in part be due to the difficulty in the accurate quantification of lipids and also due to their relatively low signal. The investigation of CS for low signal peaks may warrant further investigation.

In conclusion the use of CS-MRSI could provide up to 80% reduction in acquisition time whilst preserving brain metabolite spatial information. Alternatively, MRSI voxel size could be reduced providing increased spatial resolution for a clinically feasible scan time utilising this acceleration. The reduction in voxel size may have possible implications for SNR which would need confirmation with prospective CS-MRSI, once the k-space acquisition of random under-sampling becomes available on the scanner.

9 Conclusions and Further Work

9.1 First Objective -The development of CS reconstruction software applicable to MRSI.

The first objective was to develop suitable CS reconstruction software applicable to MRSI (CS-MRSI). This was completed by the modification of existing CS software applicable to MRI (section 3). The modification successfully adapted the existing software to allow the CS reconstruction of a dataset containing an additional; third dimension representing the spectral information of MRS. The verification of this newly developed CS software to accurately represent the real MRSI dataset after different degrees of under-sampling was the primary focus of this research.

9.1.1 Future work

The computational optimisation of the CS reconstruction software was not the focus of this work, however the application of different non-linear iterative reconstruction techniques other than conjugate gradient descent (the method utilised in this study), may be of future interest.

The repetition of this analysis with different CS weighting factors λ_1 and λ_2 for the sparse domain and the TV term (Section 3.4) may further optimise the CS.

9.2 Second Objective-Methodology for the assessment of the spatial resolution of MRSI

The second objective was to devise a practical technique providing a measure of relative spatial resolution in MRSI. This was tackled in four ways. The first was the development of an imaging edge phantom (section 4.5). This resulted in the construction of a two-compartment

imaging phantom consisting of two metabolite containing gels separated by a non-permeable polymer membrane. The phantom successfully allowed the assessment of the edge response of MRSI and calculation of the relative edge gradient between the non-filtered FSSR, the CS-MRSI and LRR (section 5) at 10mm x 10mm x10mm voxel dimension. Figure 5-1 b) indicated that the phantom provided an informative measure of MRSI spatial resolution for acceleration factors between x2 and x10.

The second method was to use a saturation band prior to the MRSI acquisition applied perpendicular and central to an axial slice within the brain of a healthy volunteer. This provided a means to assess the inter-voxel contamination of each reconstruction by examination of the relative contrast between the saturated and unsaturated regions. Figure 5-5 a) and Figure 5-4 indicate that by saturating out the metabolites from within a band of two voxels wide the CS-MRSI and the LRR maintain an equivalently high mean contrast up to a factor of x5. This suggests that the relatively low metabolite spatial frequency variation imposed by this technique is only relevant for testing spatial frequencies greater than half the maximum spatial frequency of the full MRSI dataset.

The phantom work was found to be constrained by the low matrix size available on real-time acquisitions, so a digital phantom to simulate MRSI datasets at higher matrix size was developed (section 6). The validation of the simulation (section 6.2) indicated that the nRMSE between the acquired dataset from the two-gel phantom and the fully sampled simulation was a maximum of 4%. The adaptation of this phantom to contain an angled, metabolite edge allowed the assessment of a more highly sampled edge response (section 7.1 and section 6.3). The simulated angled metabolite edge allowed measurement of the relative spatial responses of non-filtered FSSR MRSI data with the filtered FSSR, CS-MRSI and LRR at acceleration factors of x2,x3.3,x4,x5 and x10 (section 7.1.2). Further adaption of the

digital phantom allowed the same investigation but with application to two clinical scenarios. One for which the digital phantom contained a single simulated focal OPG lesion and another simulated lesion without a clear border between diseased and healthy tissue.

The fourth method of spatial resolution assessment investigated in this research was the calculation of the Modulation Transfer Function (MTF). The MTF can be calculated from the edge response of an imaging system and so was applied to the simulated angled edge. This methodology worked well for MRSI datasets without noise (section **Error! Reference source not found.**) however the addition of noise rendered difficulties in the required differentiation of the edge response. This therefore hinders the use of the calculation of the MTF in MRSI with a metabolite edge that contains noise.

9.2.1 Future Work

A previous study calculated the MTF of MRSI utilizing an imaging phantom containing Perspex wedges arranged in a fan pattern within a metabolite containing solution (Heikal, Wachowicz et al. 2013). Square waveform profiles were obtained at differing radii from arc profiles across this spatial variation. The MTF was calculated by comparing the resultant profiles to the idealized square wave profile at a particular radius. It may therefore be a useful exercise to develop a software simulation of this phantom and calculate the MTF using this methodology instead of the angled edge scenario.

9.3 **Third Objective –** Exploration of the limits of CS-MRSI by comparison of the spatial resolution of CS-MRSI at different acceleration factors.

The calculation of the relative spatial resolution from both the imaging, two-compartment gel phantom (section 5.1.2) and those of the digital phantom which contained the angled

metabolite edge (section 7.1.2) both indicate that the spatial resolution degrades with increasing acceleration factor.

Both scenarios agree that the CS-MRSI provides a superior resolution relative to that of the LRR up to a factor of x5. The digital phantom is the more reliable measurement since the gradient of the edge response contains a higher number of samples relative to the imaging phantom. The two-compartment gel phantom results revealed a relative spatial resolution of 78% ± 14% of that of the non-filtered FSSR respectively for NAA at an acceleration factor of x5. This is compared to 50% for the LRR. For the digital phantom these values were 68% ± 5% for CS-MRSI and 44% for the LRR. The filtered FSSR produced a relative value of 48%. In current MRSI the use of a k-space ringing filter is standard. One of the most interesting outcomes of this work is that the CS-MRSI results imply not only a reduction in ringing but a spatial resolution consistently higher than that of the filtered FSSR, with the added benefit of reducing acquisition time by up to 80%. This means that for a conventional, clinical 2D phase encoded MRSI acquisition, for which duration is around 5 minutes with a relatively low spatial resolution of 48%, using CS-MRSI results suggest that the acquisition can be reduced to 1 minute with a relative spatial resolution of 68% ± 5%, and a reduction in Gibbs ringing. This is not only advantageous in terms of patient throughput but will reduce possible movement artefacts. The higher spatial resolution will also aid in correct diagnosis and management of disease in particular in the delineation of tumour boundaries with healthy tissue.

If the acquisition time of 2D phase encoded MRSI can be reduced this implies that the acquired MRSI spatial resolution could also be increased. This may however have implications for SNR since the SNR is proportional to the acquired voxel volume. If the resolution is doubled in conventional 2D phase encoded MRSI, scan time is quadrupled, and

SNR is reduced. The NSA can be increased but at the cost of scan time. Higher field strength would also improve SNR but currently most clinical scanners are 3T and below. In order to improve the spatial resolution there is future work to be done.

The effect of CS-MRSI on the SNR is interesting to note. The results of section 5.2.2, Figure 5-5 b) implies that CS has a de-noising effect exhibiting a higher SNR than the fully sampled MRSI dataset for NAA. A possible explanation for this is that the variable density k-space sampling scheme results in fewer acquired data points at the periphery of k-space which have a lower SNR than the fully sampled centre of k-space. The CS-MRSI reconstruction estimates the large proportion of missing data points in the periphery of k-space by minimising the differences between the estimated fit and the sampled data points. In conjunction with a TV penalty (section 3.4) this results in an inherent smoothing effect which reduces certain components of the noise. However, the possible de-noising of the CS reconstruction may also smooth out the less prominent metabolites peaks as well as the noise peaks. The effect on relative SNR will vary between different metabolites, since those such as Myo-Inositol have smaller peaks than others such as NAA, however the potential de-noising quality of CS-MRSI may be an advantage over other fast MRSI techniques which negatively impact on SNR. For example, the very short scan times of PEPSI (section 2.6) result in reduced SNR. In SENSE-MRSI, whilst SNR has been improved with the use of phased array head coils, it is inherently dependent upon coil geometry resulting in a spatially varying SNR which is usually poorest at the centre of the FOV.

This work implies that there is potential in the use of CS-MRSI in the clinic to accelerate MRSI acquisition by up to 80% without detriment to the spatial resolution of MRSI with possible benefits in SNR.

9.3.1 Future Work

The cut-off in the ability of CS-MRSI to retain MRSI spatial integrity between acceleration factors x5 and x10 is yet to be determined.

So far CS-MRSI has been applied to retrospective data sets because current clinical scanners do not have the software to acquire MRSI data in a random pattern as required by CS. Philips has a 'patch' available to allow the acquisition of random MRSI datasets, but currently do not have the software to perform the CS reconstruction. If the patch were applied to the scanner it could allow a true assessment of the quality of CS-MRSI in practise and indicate how the SNR fares at smaller voxel sizes. Unfortunately, in order to be given this patch the department at BCH requires a research contract with Philips. A research contract has just recently been granted to the department, but not within the time scale of this research and permission to apply the patch is pending.

The reduction in acquisition time could be advantageous for the increased coverage of current 2D MRSI by allowing the acquisition of multiple slices in the same time scale, or indeed when combined with 3D MRSI.

The combination of CS-MRSI and other fast MRSI techniques is also a possibility to further reduce the acquisition time(Thomas, Nagarajan et al. 2014). The simplest combination would be CS-MRSI and reduced FOV (section 2.6.2) which could be simulated in software as a starting point. CS has previously been combined in a pre-clinical study with an echo-planar MRSI sequence (section 2.6.4) which was shown to have successful application to 13C MRSI (Hu, Lustig et al. 2010). The use of echo planar spectroscopy at BCH is not currently an option but may soon be available.

9.4 **Fourth Objective –** Comparison of different sparse data representations

The use of CS-MRSI so far in the literature has only employed wavelets as the sparse domain. The identity function was investigated in this work due to its simplicity of calculation and the fact that an MRSI dataset is itself relatively sparse. The results so far in this work from the calculation of the metabolite edge gradient (section 7.1.2) tend to suggest that the use of the identity function in the CS-MRSI reconstruction provides a 10% increase in average relative spatial resolution for NAA and for Choline compared to wavelets. The application of both sparse domains to CS-MRSI reconstructions of a simulated OPG scenario indicate that there is on average a slight advantage (1%) in using the identity function. It may be concluded from the current results that the use of the identity function will give the best CS-MRSI reconstruction, however the use of a different wavelet may provide a more sparse representation of the data.

9.4.1 Future Work

An investigation of different wavelet types and levels would be of interest as a comparison with the use of the identity function in this study. Different sparse representations may also be of interest for example the discrete cosine or the FREBAS transform which have also been employed in conventional MRI reconstruction (Lustig, Donoho et al. 2007; Ito 2011).

9.5 **Fifth Objective –** Application of CS-MRSI in OPG

The OPG simulations in a digital phantom for both a focal and an infiltrating lesion provided a framework to investigate the effect of CS-MRSI on tumour margin delineation. It can be seen from the results (section 8.2.2.3) that the CS-MRSI provided superior delineation as compared to the LRR up to acceleration factor of x5 for NAA, Cr, Cho and Ins. This advantage was not apparent for the reconstruction of lipids. However, the standard deviation, nRMSE and mean difference were all relatively low. The lipid maps for all reconstructions clearly

indicate the tumour outline at all accelerations, which as expected is more clearly defined for the focal lesion Figure 8-32 compared to the case where the tumour exhibits infiltration Figure 8-47.

9.5.1 Future Work

Investigation into the resulting lack of advantage of CS over LRR in lipid signal reconstruction is of particular interest to determine if this is due to the difficulty in quantification of lipids or if it is due to CS having difficulty in reconstructing low level signals.

The work was limited to the use of a single lesion which was useful for investigation of the delineation of tumour margins. Patients exhibiting OPG often have multiple diffuse lesions and cysts. The simulation of such cases and their subsequent reconstructions would also be beneficial in the validation of CS-MRSI. The current OPG simulations do not have any lipid contamination from subcutaneous fat which is another challenge in MRSI (section 8.2.2.1). The use of fat saturation bands placed over these areas are designed to reduce lipid bleed through but they are not always effective if the VOI is located near such areas. The effect of lipid contamination on the reconstructions would therefore be of interest. Application of CS-MRSI to different tumour profiles is also a relevant future simulation.

9.6 Summary

The results of this research appear to suggest that implementation of CS-MRSI can potentially speed up data acquisition by up to 80% for 2D phase encoded MRSI whilst providing a reduction in inter-voxel contamination. In comparison to the uniformly sampled, time equivalent LRR, CS-MRSI provided greater improvement in the reduction of inter-voxel contamination by maintaining spatial resolution and reducing the side lobes of the PSF. This is of particular relevance in the context of current clinical MRSI in which a ringing filter is implemented for the reduction of the PSF side lobes. This research suggests that the use of a

Hamming filter reduces the MRSI spatial resolution by up to 50%, which is commonly expected for post-processing filtration (Barker and Lin 2006). CS-MRSI however, not only appears to also reduce the side lobes of the PSF, but maintains a spatial resolution consistently higher than the filtered FSSR with the added benefit of reducing acquisition time by up to a factor of 5. The implementation of CS-MRSI on prospective 2D phase encoded MRSI data would therefore be an interesting area for future research as the application of CS-MRSI may greatly enhance the clinical utility of MRSI. The reduction in acquisition time reduces the potential of movement artefacts and improves patient throughput. CS-MRSI may be beneficial in aiding brain tumour diagnosis and management since the inter-voxel contamination present in current MRSI leads to poor image integrity. This presents challenges particularly in the delineation between a tumour and it's boundary with healthy tissue. The acceleration of phase encoded MRSI acquisition permitted by CS-MRSI may allow improvement in spatial resolution by allowing a corresponding reduction in voxel dimension within the same time frame. This may however have to be tempered with a corresponding loss of signal. The combination of CS-MRSI with other fast imaging techniques may improve on any signal loss and further reduce scan times. For standard voxel volume MRSI, this work indicates the potential of CS-MRSI to aid in enhanced delineation between normal and infiltrative diseased tissue when compared to the current filtered, clinical MRSI with the added benefit of reduced scan time.

10 References

Antoniou, A. (2006). Digital signal processing, McGraw-Hill Toronto, Canada:.

Ashwal, S., T. Babikian, et al. "Susceptibility-Weighted Imaging and Proton Magnetic Resonance Spectroscopy in Assessment of Outcome After Pediatric Traumatic Brain Injury." Archives of Physical Medicine and Rehabilitation **87**(12): 50-58.

Askin, N. C., B. Atis, et al. (2012). Accelerated phosphorus magnetic resonance spectroscopic imaging using compressed sensing. Engineering in Medicine and Biology Society (EMBC), 2012 Annual International Conference of the IEEE.

Barker, P. (2014). Diagnosis and Characterization of Brain Tumors: MR Spectroscopic Imaging. Functional Brain Tumor Imaging. J. J. Pillai, Springer New York**:** 39-55.

Barker, P. B. and D. D. M. Lin (2006). "In vivo proton MR spectroscopy of the human brain." Progress in Nuclear Magnetic Resonance Spectroscopy **49**(2): 99-128.

Bonekamp, D., M. A. Smith, et al. (2010). "Quantitative SENSE-MRSI of the human brain." Magnetic Resonance Imaging **28**(3): 305-313.

Bostock, M., D. Holland, et al. (2012). "Compressed sensing reconstruction of undersampled 3D NOESY spectra: application to large membrane proteins." Journal of Biomolecular NMR **54**(1): 15-32.

Cao, P. and E. X. Wu (2014). "Accelerating phase-encoded proton MR spectroscopic imaging by compressed sensing." Journal of Magnetic Resonance Imaging: n/a-n/a.

Chang, C.-H. and J. Ji (2010). "Compressed sensing MRI with multichannel data using multicore processors." Magnetic Resonance in Medicine **64**(4): 1135-1139.

Chard, D. T., C. M. Griffin, et al. (2002). "Brain metabolite changes in cortical grey and normal-appearing white matter in clinically early relapsing–remitting multiple sclerosis." Brain **125**(10): 2342-2352.

Chartrand, R. (2009). Fast algorithms for nonconvex compressive sensing: MRI reconstruction from very few data. Biomedical Imaging: From Nano to Macro, 2009. ISBI '09. IEEE International Symposium on.

Child, T. F. and N. G. Pryce (1972). "Steady-state and pulsed NMR studies of gelation in aqueous agarose." Biopolymers **11**(2): 409-429.

de Graaf, R. (2007). in vivo NMR Spectroscopy Principles and Techniques, John Wiley and sons, Ltd.

de Kok, W. (2007). "Application tips on fast spectroscopic imaging." NetForum Community Retrieved 2012, from http://clinical.netforum.healthcare.philips.com/us_en/Operate/Application-Tips/MRI/Application-tips-on-fast-spectroscopic-imaging.

Dreher, W., C. Geppert, et al. (2003). "Fast proton spectroscopic imaging using steady-state free precession methods." Magnetic Resonance in Medicine **50**(3): 453-460.

Dreher, W. and D. Leibfritz (2000). "A new method for fast proton spectroscopic imaging: Spectroscopic GRASE." Magnetic Resonance in Medicine **44**(5): 668-672.

Dydak, U. M., D Lamerichs,R and Boesiger,P (2006). "Trading Spectral Separation at 3T for Acquisition Speed in Multi Spin-Echo Spectroscopic Imaging." Am J Neuroradiol **27**: 1441-1446.

Dydak, U. W., M Pruessmann, PK Meier,D and Boesiger,P (2001). "Sensitivity-Encoded Spectroscopic Imaging." Magnetic Resonance in Medicine **46**: 713-722.

Edden, R. A. E., M. Schär, et al. (2006). "Optimized detection of lactate at high fields using inner volume saturation." Magnetic Resonance in Medicine **56**(4): 912-917.

Farahani, K., U. Sinha, et al. (1990). "Effect of field strength on susceptibility artifacts in magnetic resonance imaging." Computerized Medical Imaging and Graphics **14**(6): 409-413.

Friedman, S. D., W. M. Brooks, et al. (1999). "Quantitative proton MRS predicts outcome after traumatic brain injury." Neurology **52**(7): 1384.

Fujita, H., D. Y. Tsai, et al. (1992). "A simple method for determining the modulation transfer function in digital radiography." Medical Imaging, IEEE Transactions on **11**(1): 34-39.

Furuyama, J. W., NE Burns,BL Nagarajan,R Margolis,DJ and Thomas,MA (2012). "Application of Compressed Sensing to Multidimensional Spectroscopic Imaging in Human Prostate." Magnetic Resonance in Medicine.

Geethanath, S. (2011). Novel Applications of Compressed Sensing to Magnetic Resonance Imaging and Spectroscopy. Texas, The University of Texas at Arlington. **Doctor of Phillosophy:** 148.

Geethanath, S., Baek,H and Kodibagkar,V.D (2010). "Retrospective analysis of application of compressive sensing to 1H MR metabolic imaging of the human brain." Proc. SPIE 7626.

Geethanath, S. and V. D. Kodibagkar (2013). "Acceleration of H-1 MR Metabolic Imaging with Compressed Sensing Response." Radiology **266**(2): 686-687.

Geethanath, S. B., H Ganji,SK Ding,Y Maher,EA Sims,RD Choi,C Lewis,MA Kodibagkar,VD (2012). "Compressive Sensing could Accelerate 1H MR Meatbolic Imaging in the Clinic." Radiology **262**(3): 985-994.

Golay, X., J. Gillen, et al. (2002). "Scan time reduction in proton magnetic resonance spectroscopic imaging of the human brain." Magnetic Resonance in Medicine **47**(2): 384-387.

Golder, W. (2004). "Magnetic Resonance Spectroscopy in Clinical Oncology." Oncology Research and Treatment **27**(3): 304-309.

Govindaraju, V., K. Young, et al. (2000). "Proton NMR chemical shifts and coupling constants for brain metabolites." NMR in Biomedicine **13**(3): 129-153.

Haase, A., J. Frahm, et al. (1985). "1H NMR chemical shift selective (CHESS) imaging." Physics in medicine and biology **30**(4): 341.

Haifeng, W., L. Dong, et al. (2009). Pseudo 2D random sampling for compressed sensing MRI. Engineering in Medicine and Biology Society, 2009. EMBC 2009. Annual International Conference of the IEEE.

Heikal, A. A., K. Wachowicz, et al. (2013). "MTF behavior of compressed sensing MR spectroscopic imaging." Medical Physics **40**(5): 052302.

Hoffman, H. J., R. P. Humphreys, et al. (1993). "Optic Pathway/Hypothaiamic Gliomas: A Dilemma in Management." Pediatric Neurosurgery **19**(4): 186-195.

Horská, A. and P. B. Barker (2010). "Imaging of brain tumors: MR spectroscopy and metabolic imaging." Neuroimaging clinics of North America **20**(3): 293.

Hu, S., M. Lustig, et al. (2010). "3D compressed sensing for highly accelerated hyperpolarized 13C MRSI with in vivo applications to transgenic mouse models of cancer." Magnetic Resonance in Medicine **63**(2): 312-321.

Hu, X., D. N. Levin, et al. (1988). "SLIM: Spectral localization by imaging." Magnetic Resonance in Medicine **8**(3): 314-322.

Ito, S. M., K and Yamada,Y (2011). MR Compressed Sensing Using FREBAS Transform. International Society Magnetic Resonance in Medecine.

Jakob, P. M., A. Ziegler, et al. (1995). "Echo-Time-Encoded Burst Imaging (EBI): A Novel Technique for Spectroscopic Imaging." Magnetic Resonance in Medicine **33**(4): 573-578.

Judy, P. F. (1976). "The line spread function and modulation transfer function of a computed tomographic scanner." Medical Physics **3**(4): 233-236.

Kirchner, T., A. Fillmer, et al. (2015). "Reduction of voxel bleeding in highly accelerated parallel 1H MRSI by direct control of the spatial response function." Magnetic Resonance in Medicine **73**(2): 469-480.

Lange, T. D., U, Roberts,TPL, Rowley,HA, Bjeljac,M, Boesiger,P (2006). "Pitfalls in Lactate Measurements at 3T." Am. J. Roentgenol. **27**: 895–901.

Larson, P. E. Z., S. Hu, et al. (2011). "Fast dynamic 3D MR spectroscopic imaging with compressed sensing and multiband excitation pulses for hyperpolarized 13C studies." Magnetic Resonance in Medicine **65**(3): 610-619.

Lazareff, J. A., K. H. J. Bockhorst, et al. (1998). "Pediatric Low-grade Gliomas: Prognosis with Proton Magnetic Resonance Spectroscopic Imaging." Neurosurgery **43**(4): 809-817.

Leach, M. O., D. J. Collins, et al. (1995). "Quality assessment in in vivo NMR spectroscopy: III. Clinical test objects: Design, construction, and solutions." Magnetic Resonance Imaging **13**(1): 131-137.

Lin, F. T., S Otazo,R Caprihan,A Wald,LL Belliveau,JW and Posse,S (2007). "Sensitivity-Encoded (SENSE) Proton Echo-Planar Spectroscopic Imaging (PEPSI) in the Human Brain." Magnetic Resonance in Medicine **57**: 249–257.

Louis, D. N., H. Ohgaki, et al. (2007). "The 2007 WHO classification of tumours of the central nervous system." Acta neuropathologica **114**(2): 97-109.

Lustig, M., D. Donoho, et al. (2007). "Sparse MRI: The application of compressed sensing for rapid MR imaging." Magnetic Resonance in Medicine **58**(6): 1182-1195.

Lustig, M., D. L. Donoho, et al. (2008). "Compressed Sensing MRI." Signal Processing Magazine, IEEE **25**(2): 72-82.

McRobbie, D. W., E. A. Moore, et al. (2007). MRI From Picture to Proton, Cambridge University Press.

Muñoz Maniega, S., V. Cvoro, et al. (2008). "Changes in NAA and lactate following ischemic stroke: A serial MR spectroscopic imaging study." Neurology **71**(24): 1993-1999.

Nelson, S. J. (2001). "Analysis of volume MRI and MR spectroscopic imaging data for the evaluation of patients with brain tumors." Magnetic Resonance in Medicine **46**(2): 228-239.

Novak, J., M. Wilson, et al. "Clinical protocols for 31P MRS of the brain and their use in evaluating optic pathway gliomas in children." European Journal of Radiology **83**(2): e106-e112.

Orphanidou-Vlachou, E., D. Auer, et al. (2013). "1H magnetic resonance spectroscopy in the diagnosis of paediatric low grade brain tumours." European Journal of Radiology **82**(6): e295-e301.

Philips (2011). Application Guide Volume - 4 Spectroscopy. P. M. Systems, Philips. **Achieva Release 3.2 series**.

Pijnappela, W. W. F. V. D. B., De Beer,R. and Van Ormondt,D. (1992). "SVD-Based Quantification of Magnetic Resonance Signals." JOURNAL OF MAGNETIC RESONANCE **97**: 122-134.

Pizzo, P. A., D. G. Poplack, et al. (2006). Principles and practice of pediatric oncology, Lippincott Williams & Wilkins Philadelphia, PA:.

Posse, S., R. Otazo, et al. (2013). "MR spectroscopic imaging: Principles and recent advances." Journal of Magnetic Resonance Imaging **37**(6): 1301-1325.

Poullet, J.-B., D. M. Sima, et al. (2007). "An automated quantitation of short echo time MRS spectra in an open source software environment: AQSES." NMR in Biomedicine **20**(5): 493-504.

Pouwels, P. J. W. and J. Frahm (1998). "Regional metabolite concentrations in human brain as determined by quantitative localized proton MRS." Magnetic Resonance in Medicine **39**(1): 53-60.

Provencher, S. W. (2001). "Automatic quantitation of localized in vivo1H spectra with LCModel." NMR in Biomedicine **14**(4): 260-264.

Reynolds, G. (2008). Magnetic Resonance Spectroscopy Methods for Paediatric Brain Tumour Classification. Electrical, Electronic and Computer Engineering. Birmingham, Birmingham. **Phd:** 167.

Samei, E., M. J. Flynn, et al. (1998). "A method for measuring the presampled MTF of digital radiographic systems using an edge test device." Medical Physics **25**(1): 102-113.

Scheenen, T. W. J., D. W. J. Klomp, et al. (2008). "Short echo time 1H-MRSI of the human brain at 3T with minimal chemical shift displacement errors using adiabatic refocusing pulses." Magnetic Resonance in Medicine **59**(1): 1-6.

Schuff, N., A. A. Capizzano, et al. (2003). "Different patterns of N-acetylaspartate loss in subcortical ischemic vascular dementia and AD." Neurology **61**(3): 358-364.

Skoch A, J. a. F., Bunke J (2008). "Spectroscopic imaging: Basic principles." European Journal of Radiology **67**: 230–239.

Spratlin, J. L., N. J. Serkova, et al. (2009). "Clinical Applications of Metabolomics in Oncology: A Review." Clinical Cancer Research **15**(2): 431-440.

Stadlbauer, A., T. Hammen, et al. (2012). "Differences in Metabolism of Fiber Tract Alterations in Gliomas: A Combined Fiber Density Mapping and Magnetic Resonance Spectroscopic Imaging Study." Neurosurgery **71**(2): 454-463 410.1227/NEU.1220b1013e318258e318332.

Steckner, M. C., D. J. Drost, et al. (1994). "Computing the modulation transfer function of a magnetic resonance imager." Medical Physics **21**(3): 483-489.

Steen, R. G., J. S. Taylor, et al. (2001). "Prospective Evaluation of the Brain in Asymptomatic Children with Neurofibromatosis Type 1: Relationship of Macrocephaly to T1 Relaxation Changes and Structural Brain Abnormalities." AJNR Am J Neuroradiol **22**(5): 810-817.

Thomas, M. A., R. Nagarajan, et al. (2014). "Multidimensional MR spectroscopic imaging of prostate cancer in vivo." NMR in Biomedicine **27**(1): 53-66.

Träber, F., W. Block, et al. (2004). "1H metabolite relaxation times at 3.0 tesla: Measurements of T1 and T2 values in normal brain and determination of regional differences in transverse relaxation." Journal of Magnetic Resonance Imaging **19**(5): 537-545.

Tsaig, Y. and D. L. Donoho (2006). "Extensions of compressed sensing." Signal Processing **86**(3): 549-571.

Vikhoff-Baaz, B., G. Starck, et al. (2001). "Effects of k-space filtering and image interpolation on image fidelity in 1H MRSI." Magnetic Resonance Imaging **19**(9): 1227-1234.

Vikhoff-Baaz, B. L., M Starck,G Forssell-Aronsson,E J¨Onsson,L Alpsten,M AND Ekholm,S (1999). "Performance of 2D 1H Spectroscopic Imaging of the Brain: Some Practical considerations regarding the Measurement procedure." Magnetic Resonance Imaging **17**: 919–931.

Walter, A. and J. Hilden (2004). "Brain tumors in children." Current Oncology Reports **6**(6): 438-444.

Williams, W. H. (1991). "The Physics of Medical X-Ray Imaging." Investigative Radiology **26**(7): 702.

Wilson, M., G. Reynolds, et al. (2011). A Constrained least-squares approach to the automated quantitation of *in-vivo* ^{1}H MRS data. Birmingham, Cancer Sciences, University of Birmingham**:** 1-34.

Wilson, M. R., G (2011). TARQUIN User Guide Birmingham.

Yahya, A. and B. G. Fallone (2009). "Detection of glutamate and glutamine (Glx) by turbo spectroscopic imaging." Journal of Magnetic Resonance **196**(2): 170-177.

Yoshimura, K., H. Kato, et al. (2003). "Development of a tissue-equivalent MRI phantom using carrageenan gel." Magnetic Resonance in Medicine **50**(5): 1011-1017.

Zhi-pei, L. and P. C. Lauterbur (1991). "A generalized series approach to MR spectroscopic imaging." Medical Imaging, IEEE Transactions on **10**(2): 132-137.

Zierhut, M. L., E. Ozturk-Isik, et al. (2009). "1H spectroscopic imaging of human brain at 3 Tesla: Comparison of fast three-dimensional magnetic resonance spectroscopic imaging techniques." Journal of Magnetic Resonance Imaging **30**(3): 473-480.